Grant agreement no.: FCH-JU-325386

Support to Safety Analysis of Hydrogen and Fuel Cell Technologies

Guide to Best Practice in Numerical Simulations

The SUSANA project is co-funded by the European Commission within the 7th Framework Program

Co-Authors

Alexandros Venetsanos (NCSRD)

Ilias Tolias (NCSRD)

Stella Giannissi (NCSRD)

Vladimir Molkov (UU)

Dmitry Makarov (UU)

James Keenan (UU)

Volodymyr Shentsov (UU)

Simon Coldrick (HSL)

Olaf Jedicke (KIT)

Ke Ren (KIT)

Alexei Kotchourko (KIT)

Daniele Baraldi (JRC)

Daniele Melideo (JRC)

Shane Slater (EE)

Franck Verbecke (AREVA)

Audrey Duclos (AREVA)

Content

0. Introduction

0.1 Purpose of this document

The purpose of this document is to develop a comprehensive guide to Best Practice Guidelines (BPG) in numerical simulations for FCH (Fuel Cells and Hydrogen) applications. These BPG focus on the practical needs of engineers in consultancies and industry faced with undertaking Computational Fluid Dynamics (CFD) simulations in support of hazard/risk assessments of hydrogen facilities, and the needs of regulatory authorities.

The guidelines have been drawn together by team with extensive experience of relevant FCH simulations. The objective is that the reader of this document will improve their knowledge in the sector and improve the quality of their hydrogen-safety simulations. The reader will be introduced to the appropriate practice (modelling approach) and by following this, improve the accuracy and fidelity of their modelling.

A number of BPG for CFD applications are available. ERCOFTAC developed a general BPG for industrial CFD simulations (ERCOFTAC, 2000). The reader is recommended to advise this BPG too. BPG for CFD simulations that focus on specific applications have also been developed, for example for flows in urban environment (COST, 2007), for the use of CFD in nuclear reactor safety applications (OECD, 2007) and for the design and assessment of ventilation and gas dispersion in gas turbine enclosures (Ivings et al., 2003).

In the context of FCH risk assessments, it is possible that many scenarios may have to be simulated, accounting for release location, orientation and hydrogen release aperture size, ignition location, effects of wind speed and direction, etc. for example, see Middha and Hansen (2009), Angers, et al., (2011). Therefore, to be useful, CFD modelling approaches need to allow for the large number of simulations which have to be undertaken. This need has been taken into consideration in drafting these BPG.

This being the case, the BPG focus is on modelling approaches which are currently and in the near-future most likely to be commonly-employed in addressing the needs of industry within the context of hazard/risk assessments. These include models based on RANS (Reynolds-Averaged Navier Stokes) and VLES (Very Large Eddy Simulation) methodologies. Nevertheless, more advanced LES (Large Eddy Simulation) approaches are also referenced in the BPG, as these may form the next generation of models available to industry. Also, it is important that the user is informed of the potential benefits and drawbacks of such models in relation to simpler approaches.

The BPG aims also to deal with the fact that several different users can produce different results for the same problem, using the same CFD code (Hall, 1997). Thus, BPG are a way of reducing variability between users.

A basic knowledge of fluid dynamics and numerical methods is expected of the reader, in order to fully comprehend the document and to correctly apply the proposed guidelines.

0.2 Introduction to CFD for safety analysis of FCH installations/technology

The simulation of real problems concerning many aspects of our lives is a practice that is being used for several decades. Combined with experiments, simulation is used to give insight

into physical phenomena in a wide range of industrial and non-industrial application areas. The tools that are used for the simulations can be either analytical or numerical.

The last decades CFD has entered the research and industrial community, and is considered as a very useful and promising tool that can predict with high accuracy many phenomena of practical interest even in very complex systems. The main advantages of CFD simulation method are: the lower cost compared with the experiments, and the capability to test many parameters of the same problem without significant extra cost.

CFD is a part of fluid mechanics that uses numerical methods and algorithms to analyze and solve problems that involve fluid flows, heat transfer and associated phenomena with the help of computers. The first use of computer to model and solve fluid flow is probably dated back in 1957 and was made from a group at Los Alamos National Lab (T3 group) (Harlow, 2004).

All problems related to fluid flows are described by the conservation equations (mass, momentum, energy conservation equations). Only some very simplified forms of these equations have analytical solutions. However, most practical problems in engineering and fluid mechanics are very complex. Therefore, in order to solve these equations numerical methods are employed. CFD does exactly that: the technique solves the conservation equations using numerical approximations. The complex continuous partial differential equations (which cannot be solved directly) are replaced by a large number of simpler equations evaluated at a finite number of points within the physical and time domain. This process that continuous problems are replaced by a discrete problem whose solution is known to approximate that of the continuous problem is called *discretization*.

In CFD using the control volume approach (other approaches also exist such as finite elements), the computational domain is discretized into control volumes (usually called cells) which tessellate to form a grid which covers the physical domain. The solution of the flow problem is defined at a node inside each cell, which usually lies at the cell geometrical center. The number of cells (grid size) strongly influences the accuracy of the CFD solution. In general, the finer the grid is the higher the accuracy is, but the computational cost in terms of calculation time and the necessary computer hardware is also increased significantly.

Governing equations such as the Navier-Stokes may be solved in this way. However for unsteady / turbulent flow, where there is a mean (time averaged) and fluctuating part, the fluctuations still appear in the Reynolds Averaged equations. An additional model relating to this turbulence is required to close (solve) the set of equations. These models/equations can be either algebraic or partial differential equations. Depending on the model one or more equations may need to be solved. Details about the available turbulence models related to hydrogen safety simulations can be found in (SUSANA D2.1, 2016).

In general, CFD is a useful tool and has been used for several years to study safety issues in hydrogen and FCH application. However, CFD models are only a representation of reality, and errors may be introduced which reduce the fidelity of the numerical outputs to the case under examination. The user should first study and be fully aware of the underlying physics and the fundamentals of the numerical methods and algorithms. The intention of this document is to provide all the necessary information and to set the guidelines for the proper use of the CFD in hydrogen and FCH applications. The guidelines aim to assist the user in choosing the appropriate model for his problem, but continuous validation of these choices plays a key role and should be performed.

0.3 CFD software requirements

Today, there are a wide variety of CFD programs. Some of them are commercial and some of them are available for free. Many of the free CFD packages distribute also the source code of the program (open source programs). Moreover, many universities and research centres develop their own “in-house” CFD codes. As a result, a question arises: which CFD program is more appropriate for safety analysis of FCH installations and technology? The general requirements that a CFD code has to meet are:

- Verification: The CFD program should have been verified. Verification is the process where we check the correctness of the equations’ solution. We do not examine if the governing equations are appropriate to solve the problem but we only examine if the equations are solved correctly. Incorrect solution of the equations can be caused for example from the discretization of the equations, the solver and the numerical scheme. Programming errors (bugs) also can be revealed at this stage. Verification may be achieved by simulating problems which have analytical solutions.
- Validation: The models of the CFD program should have been validated. Validation is the process where we examine if the mathematical model predicts (with sufficient accuracy) the physical phenomena of interest. Validation of a code is performed after the verification. In verification we take care that the equations are solved correctly whereas in validation we take care that we solve the correct equations. Validation is normally accomplished by comparing the numerical outputs with the experimental ones.
- Robustness: The CFD program needs to be robust, i.e. always provide accurate solutions in a reasonable computational time.
- Easy process chain: The CFD program needs to provide in a convenient way all the necessary tools of a CFD simulation, i.e.
    - CAD tool in order to construct and visualize the geometry of the problem.
    - Meshing tool for the grid generation.
    - User friendly interface for the CFD solver options.
    - Convergence overview as the simulation progresses.
    - Post-processing capabilities and visualisation of the results.

Verification and Validation procedures are described thoroughly in (SUSANA D4.2, 2016). In the next paragraphs, the necessary features that a CFD program needs to have in order to simulate problems for safety analysis of FCH installations and technology will be described in details. We will describe the necessary equations that need to be solved and the necessary modelling that needs to be done. We will also give guidelines on how to set up a problem and the appropriate numerical options.

1. Hydrogen releases and dispersion

1.1 Introduction

This Chapter focuses on hydrogen release and dispersion problems. Both compressed and liquid storage conditions, and thus single and two phase releases, are considered. The Chapter consists of two main parts. In the first part the physical models are described, i.e. the mathematical formulation and the modelling approaches that are used in order to describe the physical phenomena are presented. In the second part the simulation set up is described. Useful guidelines for choosing domain size, imposed boundary and initial conditions, and mesh generation are given, in order to improve accuracy of the computational results. Detailed information is provided to the reader by the references given in Chapter 5, the reading of which could assist the reader in attaining an advanced level in CFD hydrogen applications.

1.2 Selection of physical models

In the next paragraphs, we will present the equations which describe hydrogen release and dispersion phenomena. These equations are necessary to be solved numerically in the CFD program in order to achieve accurate and reliable results. The equations will be presented by using the Einstein summation convention, i.e. when an index variable appears twice in a single term it implies summation of that term over all the values of the index.

1.2.1 Conservation equations

The fundamental equations which describe fluid motion are the continuity equation and the Navier-Stokes equations. The Favre averaged equations will be presented next to account for turbulence modelling.

The continuity equation shows that mass is a conserved quantity, i.e. cannot be created from nowhere or cannot disappear to nowhere. The equation which describes this law is:

$$\frac{\partial \bar{\rho}}{\partial t} + \frac{\partial}{\partial x_j}\left(\bar{\rho}\tilde{u}_j\right) = 0 \tag{1.2.1}$$

where t is the time, ρ is the density u is the velocity vector and x is the distance. The first term of the above equation expresses the rate of change of mass per unit volume in a fluid element and the second the net flow of mass out of the element across its boundaries (convection term).

The Navier-Stokes equations are derived from applying Newton's second law of motion to fluid elements, i.e. the rate of increase of momentum of fluid particles is equal to the sum of the forces on the fluid particles. The forces are in two categories, surface forces and body forces. The surface forces which act on a fluid element are pressure and viscous forces. The only important body force for hydrogen release and dispersion phenomena, which cannot be omitted, is the gravitational force. Thus, the governing equations are ($i = 1, 2, 3$):

$$\frac{\partial \bar{\rho}\tilde{u}_i}{\partial t} + \frac{\partial}{\partial x_j}\left(\bar{\rho}\tilde{u}_j\tilde{u}_i\right) = -\frac{\partial \bar{p}}{\partial x_i} + \frac{\partial}{\partial x_j}\left(\left(\mu + \mu_t\right)\left(\frac{\partial \tilde{u}_i}{\partial x_j} + \frac{\partial \tilde{u}_j}{\partial x_i}\right)\right) + \bar{\rho} g_i \tag{1.2.2}$$

where p is the pressure, g_i is the acceleration of gravity in i direction, μ the laminar viscosity and μ_t the turbulent viscosity. The last term of the right hand side of the above equation expresses the gravitational force per unit volume. This term is the driven force in buoyant gases. Hydrogen is a highly buoyant fluid due to its low density and as a result this term must not be omitted.

In hydrogen dispersion applications, an additional equation should be solved for hydrogen conservation. We usually solve for the hydrogen mass fraction Y which is defined as the ratio of hydrogen mass to the total mass. The general conservation equation of a species k is:

$$\frac{\partial \bar{\rho}\tilde{Y}_k}{\partial t}+\frac{\partial}{\partial x_j}\left(\bar{\rho}\tilde{u}_j\tilde{Y}_k\right)=\frac{\partial}{\partial x_j}\left(\left(\bar{\rho}\bar{D}_k+\frac{\mu_t}{Sc_t}\right)\frac{\partial \tilde{Y}_k}{\partial x_j}\right) \tag{1.2.3}$$

The left hand side of this equation expresses the rate of increase of the hydrogen mass fraction in a fluid particle. The right hand side predicts how diffusion causes the concentration to change with time, according to Fick's law. Turbulent diffusion is also included in the right hand side. D_k is the diffusion coefficient of species which has units m^2/s and $\mathrm{Sc_t}$ is the dimensionless turbulent Schmidt number (usually equal to 0.7). Hydrogen is a highly diffusive gas. Its diffusion coefficient in air is equal to 6.1e-005 m^2/s at temperature 293 K and pressure 1 atm.

For non-isothermal flows, the equation for the conservation of energy is also required to be solved. Energy equation is derived from the first law of thermodynamics which states that the rate of change of energy of a fluid particle is equal to the sum of the rate of heat addition to the particle and the rate of work done on the particle. The forces which do work on a particle are:

- Pressure
- Viscous stresses

The mechanisms which transfer heat to a fluid particle are:

- Heat diffusion expressed by Fourier's Law
- Diffusion of species with different enthalpies

Conservation of energy exists in many forms, such as conservation of enthalpy, total enthalpy, energy, total energy and temperature. For example, the conservation equation of the enthalpy H of the mixture is:

$$\frac{\partial \bar{\rho}\tilde{H}}{\partial t}+\frac{\partial}{\partial x_j}\left(\bar{\rho}\tilde{u}_j\tilde{H}\right)=\frac{D\bar{p}}{Dt}+\overline{\tau_{ij}\frac{\partial u_i}{\partial x_j}}+\frac{\partial}{\partial x_j}\left(\bar{\lambda}\frac{\partial \tilde{T}}{\partial x_j}+\sum_{i=1}^{N}\bar{\rho}\bar{D}_i\tilde{H}_i\frac{\partial \tilde{Y}_i}{\partial x_j}\right)+\frac{\partial}{\partial x_j}\left(\frac{\mu_t}{\mathrm{Pr}_t}\frac{\partial \tilde{H}}{\partial x_j}\right) \tag{1.2.4}$$

where T is the temperature, Pr_t the turbulent Prandlt number (usually equal to 0.7) and $\mathrm{H_i}$ is the enthalpy of component i. The second term in the right hand side represents the heat production due to viscous stresses. The third term expresses the heat diffusion (Fourier's law) and the laminar diffusion of species with different enthalpies. The forth terms is the turbulent diffusion of enthalpy.

1.2.2 Turbulence modelling

A number of different approaches are currently being used by numerical modellers in order to simulate turbulent flows. These approaches can be grouped in three broad categories:

- Reynolds-Averaged Navier-Stokes (RANS). In RANS (Reynolds, 1895) simulations the instantaneous quantities are decomposed into the time-averaged and fluctuating parts. Decomposition of the Navier-Stokes equations results in introduction of a number of additional variables, which means that the solution of RANS equations requires additional equations, known as turbulence closure equations. A number of RANS models have been proposed, including $k-\varepsilon$ (Launder and Spalding, 1974), $k-\omega$ (Wilcox, 2008), Shear Stress Transport (SST) (Menter, 1994), etc. RANS simulations are the least computationally expensive and are frequently found in simulations of practical problems, but their capability to accurately predict turbulent flow behaviour is limited.
- Large Eddy Simulation (LES). In LES, originally proposed by Smagorinsky (1963), the turbulent motion is divided into large and small scales, the former of which are explicitly resolved, while the later are modelled. The separation of large and small scales is achieved by filtering the governing equations (Favre averaging being the most popular form of filtering used by CFD researchers). Scales smaller than the filter width, known as Sub Grid Scales (SGS), are not resolved and modelled by separate SGS models. A number of different SGS models had been proposed over years, including Smagorinsky (1963), Smagorinsky-Lilly (Lilly, 1992), Monotone Integrated LES (MILES, Boris, 1990), Germano et al., (1991), etc. LES often provides a good compromise between good predictive capability and acceptable, if still high, computational resources requirements.
- Direct Numerical Simulation (DNS). In DNS Navier-Stokes equations are explicitly resolved on all scales without application of any special turbulence model. DNS provides the most accurate results at the expense of very high computational resources requirements driven by the necessity to resolve the flow field down to Kolmogorov scales. This requirement usually made DNS unsuitable for simulation of flows of practical interest which usually involve complex geometries and/or large scale flows.

The choice of the appropriate turbulence model depends on the specific problems and physical phenomena to be modelled, available computational resources and required degree of accuracy. One particular difficulty in the modelling of hydrogen releases, especially in confined spaces, is that the flow may not be fully turbulent at all locations, and may even be laminar in some regions outside the jet or plume (which can be assumed to be turbulent). Many turbulence models, especially those for RANS (Reynolds Averaged Navier Stokes) approaches, assume that the flow is fully turbulent. The renormalization group (RNG) sub-grid model in conjunction with RANS is capable to reproduce not only turbulent, but also transitional and laminar flows. At low Reynolds numbers the effective viscosity becomes equal to molecular viscosity. This allows the model to perform better in the vicinity of walls. In principle, LES (Large Eddy Simulation) is better able to model such flows, but this comes at the cost of greatly increased computer resources and much longer run times.

The most widely used turbulence model is the standard k-ε model. It is a robust turbulence model with low computational cost. However, it is appropriate for fully turbulent flows rather than laminar and transitional flows, while in complex flows involving separation regions and severe pressure gradients its applicability is narrowed down. The k-ε model has been successfully used for atmospheric flows for several years. In general, for simulations related to hydrogen release and dispersion in open environment the k-ε model performs satisfactorily (A. Venetsanos and Bartzis, 2007), (Giannissi et al., 2014). However, a modification with extra buoyancy terms (Markatos and Pericleous, 1984) is used and it is recommended in

hydrogen applications. A model that performs better in flow with separation regions is the k-ω turbulence model. Some variations of this model exist which allow for a more accurate near wall treatment with an automatic switch from a wall function to a low-Reynolds number formulation based on grid spacing. In addition, this model can be used for transitional flows. However, it requires high mesh resolution near wall. SST k-ω model is a combination of the k-ε and k-ω model. It transits from k-ε model in the free stream to k-ω model in near wall regions. It makes use of the advantages of both models dependent on the flow region. LES models resolve the unsteady fluctuations and can capture well the larger eddies and recirculation areas. It tends to reproduce more accurately and consistently the solution and it predicts better the turbulent mixing in these areas. The main advantage of the LES model is its applicability to reproduce the regimes throughout the whole range of flows, including laminar, transitional and turbulent as well as the flows where both laminar and turbulent zones exist simultaneously. However, the LES model is in general computationally more expensive because it requires finer grid and smaller time step compared to RANS models. Finally, laminar models have to be applied to laminar flows only. The use of laminar models in turbulent or transitional flows can lead to inaccurate results.

Several numerical inter-comparison exercises have compared various numerical codes utilizing different turbulence models to assess the predictive capabilities of each. These provide a set of results which can be used to make an informed selection of an appropriate numerical approach and turbulence model. The main inter-comparison exercises along with critical analysis of turbulence models are presented in (SUSANA D2.2, 2016). Inter-comparison exercises have also been performed within the SUSANA project (SUSANA D5.2, 2016), (SUSANA D5.3, 2016).

It should be pointed out that turbulence models should be accompanied with the appropriate numerical options (see Sections 1.3 and 1.4), in order to ensure that they are unaffected by numerical errors. Even if only one of the requirements is not satisfied, e.g. a CFL number value is above the best practice limit or the mesh quality is poor, then the predictive capability of such simulations can be unsatisfactory and its accuracy/fidelity to the hydrogen safety case can be questionable. Section 6.2 and (SUSANA D5.3, 2016) present a simulation of a low speed hydrogen release inside a closed garage. The results from this CFD analysis provide a good example of misleading results because of inappropriate numerical choices (grid, CFL number etc).

The following BPG is derived from a number of sources, but chief amongst these are the ERCOFTAC Best Practice Guidelines (2000) and the ERCOFTAC QNET-CFD Knowledge Base (http://www.ercoftac.org/products_and_services/wiki/).

- The spreading rate of a round momentum jet is 15% lower than for a two-dimensional plane jet. However, the standard *k-ε* turbulence model (Jones and Launder, 1972) predicts that the spreading rate for round jets is 15% higher than that for plane jets (Pope, 1978). If the momentum-dominated region of a round jet release is important, turbulence model modifications should be employed to counter this limitation, or more sophisticated models employed (e.g. non-linear *k-ε* models).

- For a round buoyant plume, use of the standard *k-ε* model will probably over-predict mean parameters (concentration, velocity) on the centreline of the plume and will under-predict plume spreading rate. More accurate predictions can be obtained with a *k-ε* model by using a Generalized Gradient Diffusion Hypothesis instead of the Standard Gradient Diffusion Hypothesis. More sophisticated models may lead to further improvements (Rodi, 1982).

- Do not use the Boussinesq approximation in the modelling of hydrogen releases, as this is only applicable to very small density differences.
- In the context of the k-ε model and its variants, source terms should be included in the ε-equation to account for the effects of buoyancy (Rodi, 1982).
- In general, strongly buoyant flows (such as releases of hydrogen), flows with strong curvature of the mean streamlines and some aspects of flow impingement (especially heat transfer), are poorly predicted by the standard k-ε model and its variants. Instead the use of more sophisticated RANS models could be considered, such as non-linear k-ε models or Second Moment Closure Models. See Hanjalic and Launder (2011). Alternatively, the user should be aware of the limitations of the standard k-ε model and its variants (ERCOFTAC, 2000; Hanjalic and Launder, 2011).

Finally, the following points should be highlighted:

- There is no universal turbulence model which is accurate in all hydrogen release and dispersion problems.
- The user should reference a similar simulation case (if available) from the literature in order to check which model performs well.
- LES-based approaches can give good results for hydrogen releases, including for mixed laminar-turbulent flow conditions, but require significant user knowledge and expertise, as well as large computer resources and long run times. LES does not always produce better results that RANS models, e.g. see (SUSANA D5.3, 2016).
- In the Smagorinsky-Lilly LES model, a Smagorinsky coefficient (Cs) value approximately equal to 0.1 has been shown to give good agreement with experiment, whereas high values such as 0.2 are not recommended because they produce laminar-like flow (Koutsourakis et. al 2012a, Koutsourakis et. al 2012b, Zhang et. al, 2010). Alternatively, the dynamic Smagorinsky-Lilly LES model (Germano et. al, 1991) can be used. This model calculates the value of Cs based on the local flow field and has been used successfully in (Molkov and Shentsov, 2014).
- If it is possible, different turbulence models should be tested to identify the most appropriate.
- It is crucial to follow the Best Practice Guidelines which are presented in this document in order to ensure the validity of the turbulence model results.

1.2.3 Physical properties

The reference equation of state (EoS) for hydrogen is given by (Leachman et al., 2009) see also (NIST, 2016). This modern formulation is explicit in the Helmoltz free energy, being a function of density and temperature. All other thermo-physical properties can be derived from the Helmoltz free energy. The above equation covers both liquid and vapour phases. A revised standardized equation for hydrogen gas densities, based on the virial series was provided in (Lemmon et al., 2008).

A comparative study of eleven equations of state in predicting the thermodynamic properties of hydrogen was performed by (Nasrifar, 2010). The author recommends the cubic Redlich-Kwong-Mathias-Copeman EoS for most applications connected with hydrogen and for the whole range of conditions (including saturated and supercritical).

The ideal gas approximation is often made. At ambient temperature significant departure from the ideal gas behaviour occurs at high pressures (the relative error of gas density using the ideal gas equation of state is approximately 10% at 20MPa and 20% at 35 and 70MPa). Departure from ideal gas behaviour also occurs at ambient pressure near the saturation temperature (approximately 10% for gas density at 20 K).

Regarding saturation curves (required in two-phase simulations) as well as other specific physical properties (e.g. specific heats), correlations can be found in (NIST, 2016) and (Poling and Prausnitz, 2004). The user should be very careful, in order to use the appropriate formula and constants which best fit within the temperature range of their problem.

In case of mixtures, the "ideal mixture" assumption is usually made. Then, the mixture properties are defined as the sum of the product of each component property and its mass fraction; except for mixture density where volume fractions are used instead.

$$\varphi = \sum_i q_i \varphi_i \tag{1.2.5}$$

where φ is the mixture property, q_i the mass fraction of i-component and φ_i the property of i-component.

In two-phase mixtures, the mixture properties are the sum of the product of each phase of each component property and its mass fraction. Accordingly, the mixture density is derived. Approaches to calculate the mass fraction of each phase (phase distribution) are given in Section 1.2.6 in (SUSANA D2.1, 2016).

A special treatment should be taken for the calculation of the mixture molecular viscosity, if solidification is modelled (e.g. of humidity in case of LH2 releases), since equation (1.2.5) can produce unphysical very high values due to the very high (infinite) viscosity of solids. Other approaches are more appropriate to use in such cases, for example:

$$\frac{1}{\mu_{mix}} = \sum_i \frac{\alpha_i}{\mu_i} \tag{1.2.6}$$

where α is the volume fraction and the index i stand for each phase of each component.

Each CFD program can use different formulas for the calculation of the physical properties and different default values. The user should always refer to the code documentation (manual) in order to retrieve this information.

1.2.4 Two phase flow modelling

Liquid hydrogen (LH2) releases result in two-phase mixtures of hydrogen with air at least near the release. Far from the release liquid hydrogen has evaporated and a vapour phase mixture exists.

One approach to model this two phase flow is to assume that vapour and liquid phases are in thermodynamic and hydrodynamic equilibrium (i.e. share the same temperature, pressure and velocity), solve the conservation equations for the mixture and a conservation equation for hydrogen (vapour + liquid) and obtain the phase distribution using Raoult's law.

Another approach is to solve separate conservation equations for each phase. If separate equations are used for momentum, then hydrodynamic non-equilibrium is implicitly assumed. If one assumes thermodynamic non-equilibrium then separate energy equations have to be

solved for each phase. Attention should be given to the coupling between phases of course (evaporation rates and friction). This approach has obviously a higher computational cost compared to the previous one. According to the authors knowledge this approach to its full extent (full non-equilibrium) has never been applied to LH2 dispersion.

Combination of the two above approaches has been reported, see e.g. (Giannissi et al., 2014), where hydrodynamic non-equilibrium was applied using algebraic slip modelling.

An alternative approach is to separate the two-phase region from the vapour region. Then a two-phase model (CFD or simpler model) could be applied within the two-phase region and a CFD vapour model within the vapour region. An example is the case of a liquid hydrogen release close to ground. Then one could consider the pool as the vapour source and use a pool model for the pool and a CFD model for the vapour phase region, see Par.1.2.6 in (SUSANA D2.1, 2016). The main difficulty in this approach is the separation of the two-phase and vapour regions and their interaction (e.g. pool evaporation rates and pool feed rates). The advantage of this approach is that single phase (vapour) CFD simulations are faster compared to two-phase.

Under the thermodynamic equilibrium assumption the phase distribution is obtained using Raoult's law as mentioned above. The procedure often called "PT-flasher" provides the phase distribution, with inputs the temperature, pressure and species total mass fractions. In pressure-based solvers (see Section 1.4.1) which also solve for mixture enthalpy a procedure called "PH-flasher" is applied. This procedure provides the temperature and the phase distributions with inputs the pressure, the mixture enthalpy and the species total mass fractions.

Accurate conditions at the source are important for the simulation for any kind of hydrogen release. For LH2 release modelling see section 1.2.5.

In LH2 releases near ground (or water) the heat transfer from the ground (or water) is very important, see (Verfondern, 2008 and Statharas et al., 2000) and should be considered.

Where LH2 spills onto ground, one needs to solve the temperature conservation (heat conduction) equation inside the ground to obtain the heat flux from the ground to the hydrogen air mixture or pool. Usually a transient one-dimensional equation with respect to depth inside the ground is solved assuming temperature at the interface between ground and hydrogen equal to the pool temperature and temperature at the underground boundary equal to ambient. With these boundary conditions the in-ground temperature equation has an analytical solution provided ground physical properties are considered constant.

During the beginning of an LH2 release on non pre-cooled ground, film boiling phenomena occur between the ground and the spilled hydrogen as the ground temperature is much higher than 20K (the saturation temperature of H2 at ambient pressure). These phenomena do not last for long as the ground temperature drops rapidly. The approximation described in the previous paragraph is therefore reasonable. If one wants to include such phenomena then the boundary condition at the ground hydrogen interface should be the following heat flux balance:

$$k\frac{\left(T_g - T_i\right)}{\Delta z} = h\left(T_i - T_p\right) \tag{1.2.7}$$

where k is the thermal conductivity of the ground, h the heat transfer coefficient, the indexes g, i and p are for the ground, interface and pool, respectively. The heat transfer coefficient,

h, should be calculated based on the correlations of the hydrogen boiling curve (Par.1.1.13 in (SUSANA D2.1, 2016)).

In cases where the release is above water, it is usually assumed that the water temperature remains constant. In this case film boiling is an important mechanism which must be accounted for.

Ambient air humidity affects hydrogen dispersion in various ways. The low temperatures near the LH2 release result in condensing and/or freezing of the water. Two counteracting effects occur at the same time. The resulting solid water particles tend to decrease the buoyancy of the cloud. The heat released during solidification on the other hand tends to increase the buoyancy of the cloud.

If the generated solid particles become large enough they might start falling to the ground (violation of the hydrodynamic equilibrium approach). In this case one could use slip (or drift) CFD models, see (Giannissi et al., 2014).

1.2.5 Release modelling

Hydrogen releases can occur either accidentally or under normal operation. Accidental releases may be due to failure of particular system components (e.g. holes/cracks in piping, activation of pressure relief devices (PRDs), etc.) or loss of connection between components (e.g. flanges failure, hose disconnection during refuelling, etc.). Normal operational hydrogen releases may occur due to permeation in pressurized gaseous storage and boil-off in liquefied hydrogen storage (if a boil-off management system is not installed).

Hydrogen release modelling comprises the physical models and computational methodology to provide the correct mass, momentum, energy and turbulence sources into the computational domain.

When carrying out simulations, the source can be treated (depending on the software/code) in two basic ways: either as a volumetric source in one or more control volumes of the computational domain or as an area source located exactly at one of the faces of a given control volume. In the second approach the jet exit area (source area) could be either the full area of the face or a part of it, if the software/code permits to characterize part of the face as “blocked” by defining the “face area porosity”. The volumetric source in one cell has been applied e.g. in Statharas et al., 2000. For the volumetric distributed source (more than one cells) see Molkov et al., 2009a and SUSANA D2.1, 2016.

Source area approach is recommended for most cases because it is a more realistic implementation of the inlet boundary. However, in some cases, such as blowdown simulations (SUSANA D2.1, 2016), the volumetric source approach can be applied more easily.

The following is recommended:

- If the software/code provides different means of source treatment the user is recommended to perform a sensitivity study.
- The computational methodology for the source should reproduce the correct inflow of mass, momentum and energy into the computational domain. For this, the user is strongly recommended to monitor the supplied sources with time to verify that the actual source into the domain is as intended.

The physical modelling of the source will generally differ depending on the hydrogen storage conditions (compressed or liquefied hydrogen). This is discussed separately in the sections below.

1.2.5.1 Compressed hydrogen

When the storage pressure is above 1.9 times the atmospheric pressure, the flow at the break is choked. The pressure at the jet exit is above atmospheric (under-expanded jet) and expands to atmospheric at a short distance downstream through one or more expansion shocks.

In such cases mesh resolution of 32 to 64 control volumes (CV) per nozzle diameter may be required to adequately resolve the under-expanded region and to ensure grid independence (Cumber et al., 1995), see also Section 1.3.2.6. This requirement, coupled with the large disparity of scales, with under-expanded jets extending over tens of meters and the nozzle diameter typically measured in millimetres, would demand prohibitively high computation resources.

Therefore, several modelling approaches have been developed introducing the notional nozzle (or fictitious diameter) approach, in order to minimize the computational demands. The most widely used notional nozzle approaches are those described by (Birch et al., 1984), (Birch et al., 1987), (Ewan and Moodie 1986) and (Schefer et al., 2007). In these modelling approaches the main assumption is that isentropic expansion occurs at the nozzle. Birch et al. (1984) developed the concept of an effective source diameter, based on the area which would be occupied by the same mass flow rate at ambient pressure and temperature with a uniform sonic velocity. Birch et al. (1984) showed that the behaviour of under-expanded jets is similar to classical subsonic free jets provided that an appropriate scaling factor is employed to describe the effective size of the jet source. Birch et al. (1987) proposed an improved approach of Birch et al. (1984) based not only on the conservation of mass (as Birch et al., 1984) but also in the conservation of momentum through the expansion area. The values of the notional diameter and the velocity that are computed by applying the modelling approach are set on the source boundary.

While the Birch et al. (1984) model remains one of the most frequently cited, this model is based on the ideal gas equation of state and thus becomes less applicable to gas storage pressures above 10 MPa when effects of gas non-ideality must be accounted for. The first theory of under-expanded jets that accounts for non-ideal behaviour of highly compressed hydrogen has been published by Schefer et al. (2007). The notional nozzle diameter calculations by Schefer et al. (2007) are similar to Birch et al. (1984) except for the Abel-Noble equation (Chenoweth, 1983) being applied instead of the ideal gas equation of state, and the assumption by Birch et al. about the speed of sound at the notional nozzle being relaxed. As a result the theory of Schefer et al. (2007) predicts uniform super-sonic velocities at the notional nozzle exit at high storage pressures.

Molkov et al. (2009a) developed an alternative to the Schefer et al. (2007) under-expanded theory which is based on mass and energy conservation equations rather than mass and momentum (Schefer et al., 2007). Similar to Birch et al. (1984) the model developed by Molkov and colleagues is based on the assumption of uniform sonic flow through the notional nozzle. Molkov and Bragin (2009) provided an extension of this model to account for the effect of losses. Details about the formulation of the models can be found in (SUSANA D2.1, 2016).

The above approaches can be utilized for modelling highly under-expanded jets when the explicit (resolved) modelling of the shock barrels Mach disks is not necessary or not practical and allows significant reduction of required grid resolution and time step and therefore computational time. Furthermore, these methods can be used with an incompressible modelling approach because the explicit simulation of the highly compressible region is avoided. Therefore, the modelling of the release in a typical setting where external air is quiescent or has low velocity is significantly facilitated.

The notional nozzle diameter depends on storage pressure. If storage pressure decreases during release (in case of blowdown) then the notional diameter also decreases. Computational modelling of a time varying notional diameter can be done using either a transient volumetric source approach or a transient area source approach.

Besides the above, one should bear in mind that leak holes are associated with values of the discharge coefficient less than one. Assuming a value of one for the discharge coefficient will overestimate the release rate and in some cases, this may result in conservative predictions. If a specific value of the discharge coefficient is not available, it should ideally be treated as an uncertain model input and the sensitivity of the simulations to its value should be determined.

Comparison of release models and critical analysis are presented in (SUSANA D2.2, 2016). To sum up, the following guidelines regarding release modelling of compressed hydrogen should be followed:

- For practical applications involving high pressure releases (above 1.9 times atmospheric pressure) notional nozzle approaches, are recommended. Notional nozzle approaches give reasonable results avoiding the high computational cost of resolving directly the complex flow structure near the nozzle.
- In general, for low storage pressures the approach of Birch et al. (1987) can be applied, whereas for high storage pressures (above 10-20 MPa) where the ideal gas assumption becomes less valid, the Schefer et al. (2007) or Molkov et al. (2009) are recommended.
- Modelling of blowdown release requires a transient volumetric or transient area source approach.
- If no specific information is provided on the value of the discharge coefficient, the sensitivity of the results to its value should be examined.

1.2.5.2 Liquid hydrogen

In a liquefied hydrogen system flashing occurs at the leak location, as the pressure drops from storage pressure to atmospheric. This results in a two-phase hydrogen jet at temperature approximately 20K (saturation temperature of hydrogen at 1bar), whose void fraction is an important parameter to be estimated, since it affects the density at the source.

Two approaches are usually followed: either isentropic or isenthalpic expansion. For isentropic expansion see (Statharas et al., 2000). For isenthalpic see (Venetsanos and Bartzis 2007), (Giannissi et al., 2014)). Isenthalpic expansion produces more hydrogen in vapour phase and therefore results in higher jet momentum for the same mass flow rate. In an expansion from 2 bar to 1 bar a 10% increase in jet momentum is estimated with isenthalpic flash. Another option is to perform a sensitivity study on the void fraction as suggested by (Ichard et al., 2012).

At temperatures as low as 20K the ideal gas approximation for hydrogen vapour leads to approximately 10% under-estimation of hydrogen vapour density. More accurate release calculations require use of more sophisticated equation of state models: see Leachman (2009) and Nasrifar (2010).

If droplets are accounted for in the CFD model then an estimation of droplet diameter at the source is required. One approach is to estimate the droplet diameter using the Weber mechanical breakup criterion (We = 12), although this might not be appropriate where there is break up due to flashing. In this case, a more sophisticated approach is required (see Johnson and Woodward, (2010) for example). The necessity to account for droplets in the source and their effect in the near field and far field is still an open issue.

As for compressed hydrogen, liquid releases through holes and cracks will be dependent on the value of the discharge coefficient, and the sensitivity of the results to its value should be examined. The user should keep in mind that values as low as 0.6 have been reported (Ichard, 2012).

Turbulence conditions at the jet source may be important. Turbulence intensity in the range 1-15% can be assumed. If no information is available a sensitivity study can be performed.

Computational implementation of a two-phase jet can be performed either using the volumetric source approach or the area source approach, provided that the CFD code can handle flow and dispersion of two-phase mixtures.

When the hydrogen leak source is sufficiently close to the ground (or water) such that a liquid evaporating pool is formed then one could assume that the pool is the source and only vapour hydrogen is introduced into the computational domain. This approach has been found attractive in the past since one can use a CFD model only for vapour phase hydrogen and vapour phase air, implicitly neglecting of course solidification of air and related humidity. Examples of this approach are the works of (Sklavounos, S., Rigas 2005) and (Luketa-Hanlin et al., 2007).

The pool approach requires information about pool area and pool evaporation rates. A pool model should be applied if available in the software/code. The simplest approach is to assume a circular pool and given evaporation rate and calculate transient pool area by mass balance between the hydrogen mass flow into the pool (from the jet) and the pool evaporation rate.

Computational implementation of vapour release from a transient pool can be performed either using the volumetric source approach or the area source approach.

In recent study involving liquefied natural gas release, Giannissi et al. (2013) concluded that the two-phase source provides better results than the evaporating pool. Moreover, fewer assumptions are required in the two-phase source compared to the evaporating pool. However, more research has to be conducted on this issue with focus on hydrogen.

Finally, a comparison of release models and critical analysis are presented in (SUSANA D2.2, 2016). Summing up, the following guidelines regarding release modelling of liquid hydrogen should be followed:

- The two-phase jet approach is recommended compared to the evaporating pool approach based on evidence from liquefied natural gas releases.
- The void fraction at the source can be estimated with either isenthalpic or isentropic expansion. A sensitivity on the void fraction could be performed

- If no specific information is provided on the value of the discharge coefficient, the sensitivity of the results to its value should be examined.

1.2.6 Interaction with walls

During hydrogen releases, it is likely that the hydrogen-air mixture comes in contact with the ground or with the walls (in general with any obstacle in the flow path). Either way there is an interaction with solid surface that affects the flow. In near-wall boundaries the velocity reduces to zero and gradients in some flow variables become large. To resolve these gradients a very fine mesh is required close to the wall. Furthermore, the Reynolds number ($\mathrm{Re} = \mathrm{u} \cdot \mathrm{y} / \mathrm{v}$) in near wall region based on y (normal distance from wall) decreases to zero. This implies that the viscous forces dominate over the inertial forces. At distances from the wall before y reaches zero there is a range of y values for which Reynolds number is of the order of 1. At this distance from the wall and closer to the wall, viscous forces are equal in order of magnitude to the inertia forces or larger. To sum up, there is a thin layer within which viscous effects are important, while turbulent fluctuations are suppressed. This implies that many standard turbulence models do not predict accurately the near wall variables. A reliable way to simulate the near wall layer is high grid resolution and low Reynolds models. However, this is very expensive, particularly in 3-D problems. Thus, special wall modelling procedure is required. The most commonly used procedure is the wall functions (see below, equation (1.2.12)). When wall functions are used there is no need in resolving explicitly the near wall region.

In general, the boundary layer above a solid surface is divided in three regions. The first region close to the surface ($0 < \mathrm{y} < 0.01\delta$ where δ is the boundary layer height) is called laminar boundary layer, and as its name reveals, the dominant shear stress is the laminar one. Within this region the turbulent shear stress can be neglected. The dimensionless velocity is equal to:

$$\mathrm{u}^{+} = \mathrm{y}^{+} \tag{1.2.8}$$

where u^{+} is the dimensionless velocity, y^{+} is the dimensionless distance from the wall. The dimensionless velocity and distance are derived by:

$$\mathrm{u}^{+} = \frac{\mathrm{u}}{\mathrm{u}_{\tau}} \tag{1.2.9}$$

$$\mathrm{y}^{+} = \frac{\mathrm{y} \cdot \rho \cdot \mathrm{u}_{\tau}}{\mu} \tag{1.2.10}$$

u is the velocity, y is the normal distance from the wall, ρ the fluid density, μ the fluid viscosity and u_{τ} is the friction velocity which is defined as followed:

$$\mathrm{u}_{\tau} = \left(\tau_{\mathrm{w}} / \rho\right)^{1/2} \tag{1.2.11}$$

where τ_{w} is the wall shear stress.

As equation (1.2.8) reveals, in the laminar sub-layer there is a linear velocity distribution and it is valid for $\mathrm{y}^{+} < 5$.

In approximately $y^+ = 30$ the turbulent boundary sub-layer (log layer) begins. In this region, the turbulent shear stress is dominant, while the laminar shear stress is neglected, and the velocity follows a logarithmic profile:

$$u^+ = \frac{1}{\kappa}\ln\left(y^+\right) + B = \frac{1}{\kappa}\ln\left(Ey^+\right) \tag{1.2.12}$$

where κ is the von Karman constant equal to approximately 0.41 and B is a constant equal to approximately 5.5 (or E=9.8). The turbulent sub layer is valid for $30 < y^+ < 500$. Between the two sub-layers the buffer layer exists (transition region between the viscous sub-layer and the log layer).

For rough walls, y^+ is replaced by y/z_0, where z_0 is the surface roughness length. Those were the standard wall functions which are based on the proposal of Launder and Spalding (Launder and Spalding, 1974).

In flows along solid surfaces, besides the convective boundary layer there is also the thermal boundary layer, which is highly affected by the surface if there is temperature difference between the fluid and the surface. As in the case of the convective boundary layer, the thermal boundary layer is also divided in three regions: the laminar sub-layer close to the wall, the turbulent sub-layer at a distance away from the wall, and the buffer layer in the transition area between the laminar and turbulent sub-layer.

In flows with heat transfer the resolution of the sub layer should be very accurate, because across this layer most of the temperature changes are occurred. Once again, the accurate resolution is very expensive, and therefore, temperature wall functions are used instead. Based on the analogy between momentum and energy transfer the standard temperature wall function is the semi-logarithmic temperature profile:

$$T^* = \frac{\left(T_w - T_p\right)\rho c_p u_\tau}{\dot{q}} = Pr_t\left[\frac{1}{\kappa}\ln\left(Ey^+\right) + P\right] \tag{1.2.13}$$

where T_w is the temperature of the solid wall, T_p is the first grid temperature, $\dot{q}$ is the convective heat flux, Pr_t is the turbulent wall Prandtl number, and P is a function of the ratio of the molecular to the turbulent Prandtl number.

The friction velocity in (1.2.13) is replaced by the square root of turbulent kinetic energy in the first near-wall grid cell. This leads to the dimensionless number $y^* \equiv \rho c_\mu^{3/4} k_p^{1/2} y_p / \mu$ (k_p is the turbulence kinetic energy, c_μ a constant and μ the dynamic viscosity) and the temperature wall function is given by (FLUENT, 2004),

$$T^* = \frac{\left(T_w - T_p\right)\rho c_p c_\mu^{1/4} k_p^{1/2}}{\dot{q}} = Pr_t\left[\frac{1}{\kappa}\ln\left(Ey^*\right) + P\right] \tag{1.2.14}$$

The above temperature wall function is adopted for convective heat transfer modelling. The logarithmic temperature profile may only be valid for forced convection flows when the grid cells lie in the fully-turbulent boundary layer, i.e., 30<y*<300.

Wall functions have been also developed for the turbulence variables, e.g. k and epsilon (Versteeg and Malalasekera, 2007).

To sum up, the specific guidelines on near wall modelling in real case scenarios with gas release and dispersion indoors or outdoors are,

- The use of wall functions is a good approximation without requiring a large number of mesh points in the region close to the wall.
- Check the lower limit of y^+. The grid should be constructed in such way that the value of y^+ is only slightly above the recommended lower limit, typically between 20 and 30. In case of separation or reattachment zones the value of y^* instead of y^+ should be checked.
- Even when using wall functions mesh refinement near the ground, walls and any obstacle may be required, for example in cases with heat transfer from the walls.
- In rough walls, the user should check that the correct roughness length is used by the CFD code. Its value depends on the problem's terrain. Several tables are available in the literature, which give typical values of the roughness length for several surfaces, in case where its value cannot be calculated based on experimental data. As an approximation, the roughness length is one-tenth of the height of the surface roughness elements.
- The distance of the center of the wall-adjacent cells from the wall should not be less than the roughness length.
- Finally, in cases where the wall interaction is the main feature in the simulation, e.g. heat transfer through impinging jet, the fine resolution without the wall functions could be preferred, if the computational time is acceptable.

1.3 Problem setup

1.3.1 Domain design

In a CFD problem setup, domain design refers to the process where we determine

- the geometry of the problem (e.g. solid surfaces)
- the size of the computational domain, i.e. the volume in which the variables of interest will be calculated.

The geometry of the problem must include all the obstacles that are expected to affect the flow such as walls, fences etc. Vents play an important role in hydrogen release indoors and as a result their geometry needs to be described as accurately as possible. Grid size limits the accuracy at which the geometry of the problem needs to be described. Therefore, obstacles with size smaller than the grid size are usually not included in the geometry of the problem. Fine geometrical details may also be omitted or be approximated if they are not expected to influence the flow. In the case of an outdoor hydrogen release and dispersion, the terrain profile should be included.

The size of the computational domain should be carefully chosen. Domain boundaries should be located far enough from the area of interest in order to minimize the impact of the boundary conditions on the results. For example, Figure 1.3-1 shows the computational domain (orthogonal parallelepiped of white edges) in a case of hydrogen release in a vented room. In this problem, the aim is to predict the hydrogen concentration distribution inside the enclosure. Hydrogen is released at the left side of the floor at a flow rate of $9.44 \cdot 10^{-4}$ m^3/s for a period of 1200 sec. The computational domain should be extended beyond the enclosure. Vents are areas of great importance with complex flow around them, thus it is necessary to ensure that the boundary conditions have no impact on them. In the case of Figure 1.3-1 the domain was extended outside the building 1.01 m in the x direction, 0.78 m in the z direction

and 0.35 m at each side of the building in the y direction. Sensitivity tests showed that the above domain size does not influence the results inside the enclosure (Koutsourakis et. al, 2012b).

In cases of flows in urban environment including ambient wind, according to Franke et al. (2007) in the presence of a building/obstacle with height H a distance of 5H between the inflow boundary and the building/obstacle is recommended if the approach flow profiles are well known. If the approach flow profiles are not available, then an even larger distance is recommended to allow for a realistic flow establishment (Bartzis et al., 2004). The domain behind the building/obstacle should be extended at least 15H (Cowan et al., 1997, Bartzis et al., 2004). In the vertical and lateral direction the domain should be extended by 5H (Hall 1997, Cowan et al., 1997). However, the influence of the lateral boundaries on the flow and dispersion in the region of interest are case-dependent. Therefore, it is recommended to test at least two different distances from the obstacle. Furthermore, the domain extension depends on the boundary conditions which are applied. Although the presented guidelines can be applied to similar cases, a good practice is to always examine the domain extension effect.

When we design the domain of a problem, we should also be careful not to include areas which are of minor significance for the examined phenomenon. By extending the domain too far or by including areas which can be omitted may result in unnecessary excessive computational time. For example in the case of Figure 1.3-1, the areas at the sides of the enclosure aren't expected to influence the flow field at the areas of interest. In the case of a multi-block mesh, these areas can easily be excluded from the domain. In the case of a non multi-block mesh, these areas can be omitted by introducing solid volumes, as Figure 1.3-1 shows. Simulations with and without these blocked areas showed that the solution isn't affected (Koutsourakis et al., 2012b).

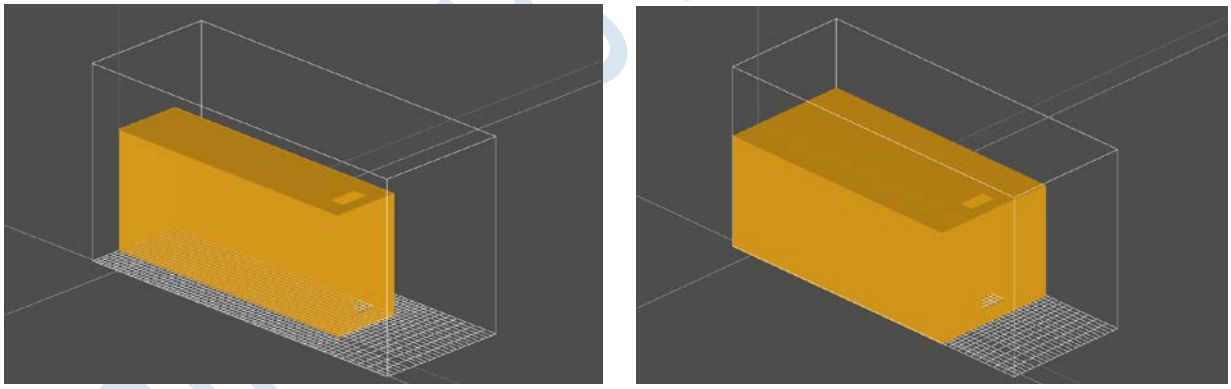

Figure 1.3-1. Computational domain for a hydrogen release in a vented room case with and without the inclusion of extra solid volumes.

When a new problem is designed a domain sensitivity study is recommended to be carried out to ensure that the domain is extended enough. To perform such an analysis the user should extend the domain in the directions that the flow is likely to exhibit complex structure (like recirculation areas). An initial simulation can be performed to identify the flow structure, in case that the user cannot guess it a priori. In this simulation a coarse mesh can be used to save computational time and the domain extension can be quite large in all directions. Then, the domain can be less extended in order to examine the effect on the results. The decrease should be progressively, for instance each time the user can take the half of the previous domain extension. An alternatively strategy for domain size sensitivity analyses is to start from small

domain extension (based on user's experience) and progressively increase the extension. The extension of the domain can be made at all directions simultaneously or not. The extension across the directions which the flows mainly occur is more significant and should be studied more thoroughly.

To sum up, the guidelines for the domain design are,

- Domain size sensitivity study should be performed in order to ensure that the area of interest is unaffected by the location of boundaries.
- The user can be advised by similar cases regarding the domain extension that it is required in order to use it as a reference point for the sensitivity study.
- Larger domain extension would probably be required along the direction of the flow.
- The domain analysis can be performed using a relatively coarse mesh (not too coarse however).
- The computational cost can be reduced by excluding areas that are not expected to influence the flow. In the case of a multi-block mesh, these areas can easily be excluded from the domain. In the case of a non multi-block mesh, these areas can be omitted by introducing solid volumes.

An example of domain size sensitivity study can be found in (SUSANA D5.3, 2016). Another example is presented in the following paragraph.

1.3.1.1 Numerical assessment of domain expansion impact

An extensive analysis of the domain sensitivity study in a release case is presented next, in order to define the exact domain extension sufficient to provide accurate results with the minimum computational cost. This analysis reveals the directions along which grid extension is more critical, and also provides an example of the amount of the extension that is necessary for hydrogen releases inside vented facilities.

For the sensitivity study a test from a series of experiments related to helium release inside an almost one cubic meter enclosure with one vent was considered. The experiments were carried out by CEA and the details of the experiments can be found in (Cariteau and Tkatschenko 2013). In the sensitivity study the case with one vent of 1620 cm^2 area was examined and with release rate equal to 60NL/min. The enclosure has a square base with 0.93m side and 1.26m height. The extension is essential in the directions where the inflow or outflow occurs. In the examined case, where the released gas is buoyant, it flows upwards as soon as it passes through the vent. Therefore, it can be assumed a priori that the directions where the extension is significant are the x and z-direction (see Figure 1.3-2). However, a case with extension in the y direction was also considered to examine its effect.

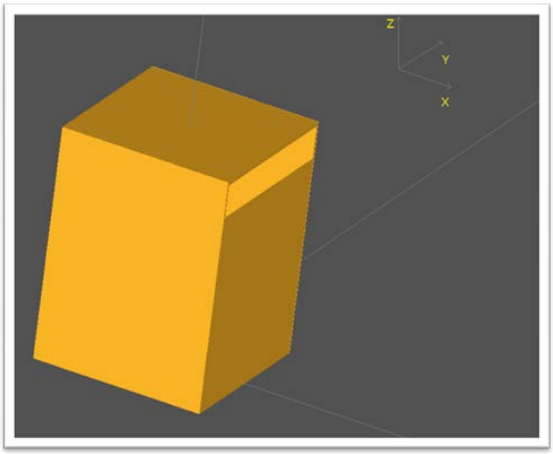

Figure 1.3-2. The GAMELAN enclosure with the vent on the right wall.

Table 1.3-1 indicates a summary of the test cases and their abbreviation. The extension size is in terms of boxes' dimension, and specifically in terms of the side of the square base (1L = 0.93m).

Table 1.3-1. The examined test cases with their abbreviation (1L = 0.93m).

Name	Description
NE	Not extended
X 1L	1L extension only in x direction
XZ 1L-0.5L	1L extension in x and 0.5L in z direction
XYZ 1L-0.25L-0.5L	1L extension in x, 0.25L in y and 0.5L in z direction
XYZ 1L-0.25L-1L	1L extension in x, 0.25L in y and 1.0L in z direction
XYZ 1L-0.25L-0.25L	1L extension in x, 0.25L in y and 0.25L in z direction

First, a non-extended domain was tested. Figure 1.3-3 shows that the prediction with no domain extension exhibits poor agreement with the experiment and did not reach the steady state. It seems that helium accumulates on the top, and no flow through the vent occurs. This highlights the significance of the domain extension.

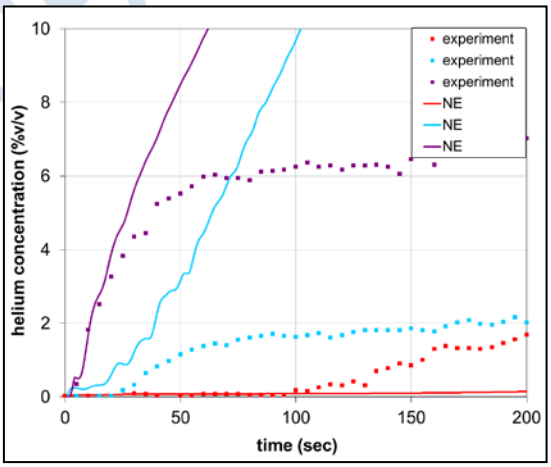

Figure 1.3-3. The measured and predicted helium concentration with no domain extension.

Then, simulations were carried out with domain extension only in x direction, in x and z direction and in all three directions, in order to confirm to which directions it is necessary to

extend the domain. The flow occurs mainly along the x direction (outflow through the vent), thus a larger domain extension was applied in the x direction equal to 1L, while to the rest directions the half extension was applied. The results are illustrated in Figure 1.3-4.

It can be observed that independent results are obtained using a domain extension in the x and z directions. The extension in the y direction is not that significant. This can be justified by the fact that flow does not occur along that direction. However, it was observed that the extension in all three directions assisted the convergence behaviour (case XZ 1L-0.5L exhibited slower convergence compared with the XYZ 1L-0.5L-0.5L case). Thus, domain extension in all directions is preferred for the rest of the analysis. In the case where the vent is smaller in size and its edges are not close to walls, the lack of extension in y direction might not create convergence problems and thus extension in y direction might be unnecessary.

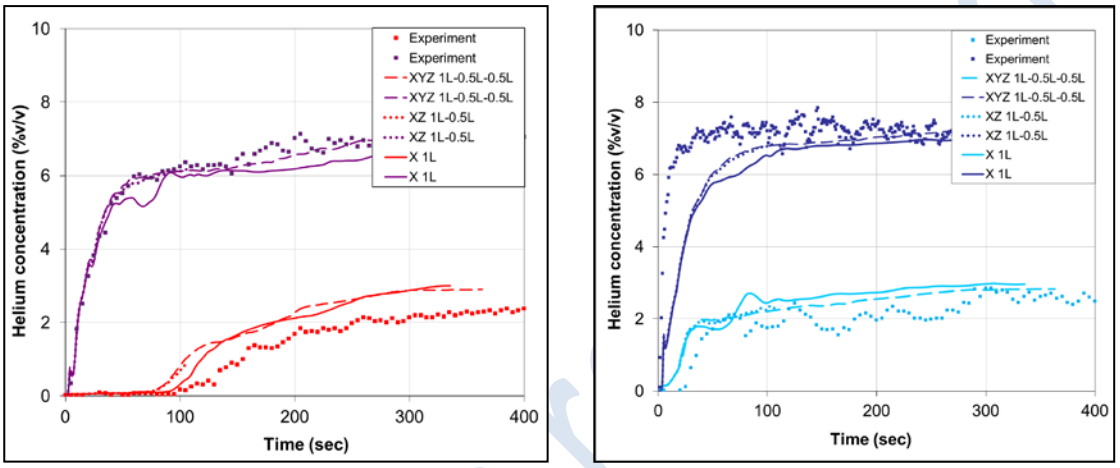

Figure 1.3-4. Measured and predicted helium concentration with domain extension in the x direction, in the x-and z-direction and in all three directions.

In the next stage several extension along x direction were examined: 0.5L, 1L and 2L. In all sensors the results with the 1L and 2L were identical. The results with 0.5L were practically similar with the others at most of sensors. However, there were some discrepancies at some sensors. Therefore, the 1L size extension along x direction is considered necessary.

Since the domain extension in the y direction showed little discrepancy compared with the case without y extension, smaller y extensions were tested to minimize the computational cost without convergence problems. An extension equal to 0.25L found to be sufficient.

In the final stage of the sensitivity study the independent size of domain extension in x and y direction were applied and the effect of the extension in the z direction was examined. Domain extensions in the z direction equal to 0.25L, 0.5L and 1L size were tested. All size extensions provided almost identical results.

Consequently, the independent domain extension that was obtained through this study is 1L in x, 0.25L in y and 0.25L in z direction respectively.

1.3.2 Meshing

1.3.2.1 Mesh design considerations

Utilization of an adequately refined and high quality mesh is an important step in ensuring accuracy and performance of numerical simulation. A number of factors need to be considered in the generation of a high quality mesh, such as:

- Resolution.
- Expansion factor.
- Cell aspect ratio.
- Cell skewness.

The choice of mesh resolution is to a large degree governed by the turbulence model employed in the simulation. DNS requires resolution of the whole range of spatial and temporal scales of the turbulence, down to the smallest dissipative scales (Kolmogorov microscales, $\eta = \left(\nu^3/\varepsilon\right)^{1/4}$, where ν is the kinematic viscosity and ε is the rate of kinetic energy dissipation). This requirement makes utilization of DNS impractical in the majority of engineering problems, and restricting its application primarily to relatively simple and low Reynolds number flows. LES has less stringent requirements on mesh resolution. Pope (2004) suggested that LES can be considered well-resolved when 80% of the turbulent kinetic energy is resolved over the grid (with the remainder represented by the sub-grid model). This condition still requires a very large grid for the majority of practical simulation and the exploration of the minimum resolution required to obtain accurate results remains an active area of research (see, e.g., Moin and Kim (1982), Hoyas and Jimenez (2006), Moser et al., (1999), Davidson (2009), etc.). LES using an under-resolved grid, i.e., such that less than 80% of turbulent kinetic energy is resolved, is often referred to as Very Large Eddy Simulation (VLES, Pope, 2004).

In addition to providing adequate resolution, grid should also satisfy other quality criteria. The aspect ratio of a high quality mesh should be kept as low as practical in order to prevent appearance of unphysical preferential directions, with cubical or tetrahedral cells providing the optimal results. It is particularly important in LES, where cell size commonly doubles as the turbulence filter width. Utilization of a mesh with cells with large aspect ratios will result in different turbulent scales being resolved in different spatial directions, creating artificial turbulence anisotropy. Similarly, a large expansion factor between neighbouring cells can result in significant variation of resolved scales which can lead to undesirable effects, such as artificial turbulence dissipation. An optimal grid, therefore, should be as close to uniform as practically possible. Practical considerations, particularly in the cases of complicated geometry and/or wide range of physical scales, however, often require utilization of non-uniform, stretched and skewed grids, in which case investigation of the grid influence is highly desirable in order to achieve acceptable accuracy. If it is impractical to make the entire grid uniform, it is particularly important to keep the grid as close to uniform as practical in the area of particular interest and in the regions where high gradients are expected. Increased refinement of the grid in the areas of high gradients is another common technique aimed at increasing simulation accuracy while maintaining acceptable overall mesh size.

1.3.2.2 General guidelines about expansion ratio, aspect ratio and skewness

Cell **expansion ratio** is the ratio between the characteristic length of the adjacent cells. For example, according to Figure 1.3-5 the expansion ratio for rectangular parallelepiped cells is defined as $\Delta x_{i+1}/\Delta x_i$. This is applied in all directions. A sudden change in size of the

adjacent cells is not recommended specifically in areas where complex flow phenomena take place, in order to avoid convergence problems and inaccuracies (loss of precision). Therefore, the expansion ratio should be kept low with maximum change in grid spacing <20%. An expansion ratio less than 1.2 is satisfactory and is not expected to pose problems to the solution.

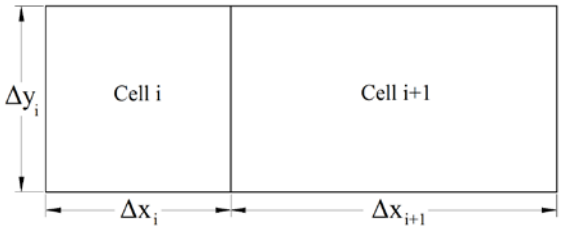

Figure 1.3-5. Schematic representation of two adjacent grid cells.

Cell **aspect ratio** is defined as the ratio of the longest edge length to the shortest edge length. Based on Figure 1.3-5 the aspect ratio is equal to $\Delta y_i / \Delta x_i$. The ideal value for an equilateral square or triangle is equal to 1. For example in Figure 1.3-5 the cell i has aspect ratio equal to 1 and the cell i+1 greater than 1. The cell aspect ratio should be near one in regions where flow is multidimensional. Aspect ratios of 2-3 are considered satisfactory, especially if the flow direction is parallel to the longest side of the cell.

The last primary quality indicator for a mesh is the cell **skewness**. Skewness determines how close to ideal (i.e., equilateral or equiangular) a face or cell is. The range of skewness is [0,1] with ideal value equal to 0 and the worst value equal to 1. In Table 1.3-2 the skewness range and the corresponding cell quality are displayed. For hexahedral, quadrilateral and triangles cells the skewness value should not exceed 0.85, for tetrahedral cells the skewness value should not exceed 0.9.

Table 1.3-2. Skewness range and cell quality (FLUENT, 2004).

Value of Skewness	Cell quality
0-0.25	excellent
0.25-0.5	good
0.5-0.75	acceptable
0.75-0.9	poor
0.9-0.99	bad (sliver)
1	degenerate

There are three methods to determine the skewness of a grid. The first one is based on the equilateral volume**.** The skewness is defined as (see Figure 1.3-6):

$$\text{skewness} = \frac{\text{optimal cell size} - \text{cell size}}{\text{optimal cell size}} \qquad (1.3.1)$$

Optimal cell size is the equilateral cell. This method applies only to triangles and tetrahedra, and usually is the default method in CFD codes.

The second method is based on the deviation from normalized equilateral triangle. This method applies to all cell and face shapes and is almost always used for prisms and pyramids. For a pyramid, the cell skewness will be the maximum skewness computed for any face. An

ideal pyramid is one in which the 4 triangular faces are equilateral (and equiangular) and the quadrilateral base face is a square.

$$\text{skewness (for a quad)} = \max\left(\frac{\theta_{max} - 90}{90}, \frac{90 - \theta_{min}}{90}\right) \quad (1.3.2)$$

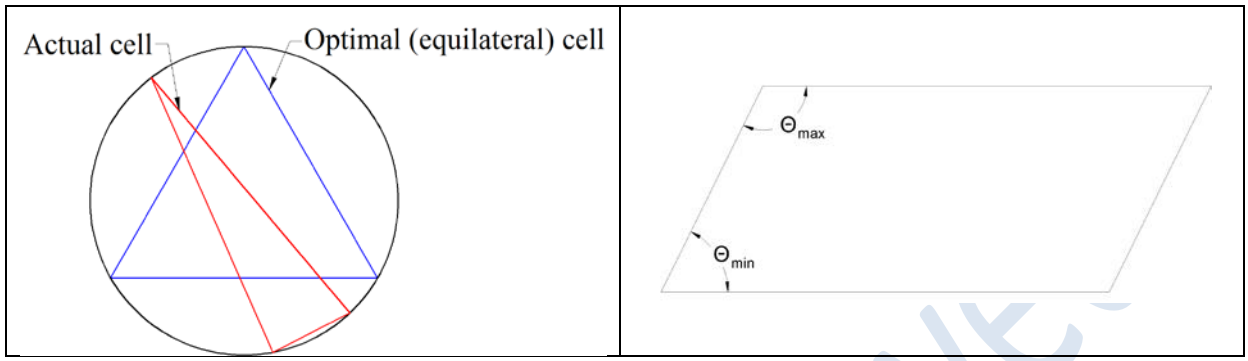

Figure 1.3-6. Skewness based on equilateral volume (left) and based on a quadrilateral (right).

where θ_{max} is the largest angle in face or cell, θ_{min} is the smallest angle in a face or cell (see Figure 1.3-6). The third method is based on equiangular skew. This is defined as

$$\text{Equiangle skew} = \max\left(\frac{\theta_{max} - \theta_e}{180 - \theta_e}, \frac{\theta_e - \theta_{min}}{\theta_e}\right) \quad (1.3.3)$$

where θ_e is the angle for an equi-angular face or cell i.e. 60 degrees for a triangle and 90 for a square.

1.3.2.3 Grid density

The suitable grid density is estimated by grid independency study. Several grids are tested with different number of cells until the results are not affected significantly. Grid independency study is very important because results with coarse grid can be misleading. In Figure 1.3-7 the grid independency study performed by Koutsourakis et al., 2012b is shown at four positions inside the enclosure where experimental data is available. Geometry of the problem is depicted in Figure 1.3-1. We observe that at sensors 1, 3 and 4 there are coarse grids which gave results closer to the experimental than the results of grid-independent finest grid. Another example of misleading results due to coarse grid is presented in Section 6.2 and in (SUSANA D5.3, 2016). Thus, grid independency should always be performed in order to assure that the chosen grid doesn't affect the solution.

For the grid independency study refinement should be performed and at least three grids should be tested. The results are compared with each other, and graphs similar to Figure 1.3-7 can be produced. If two grids provide similar results the coarser grid is the independent one.

A measure to compare two different computational results obtained with different grid is the relative error, ε, between them.

$$\varepsilon = \frac{C_{coarse} - C_{fine}}{C_{fine}} \quad (1.3.4)$$

The relative error is calculated in all sensors in all time steps and the maximum error is recorded. Zero relative error indicates that grid independency has been achieved. However, zero values are usually difficult to be achieved. Therefore, small values, e.g. 10% are assumed to provide sufficient grid independency.

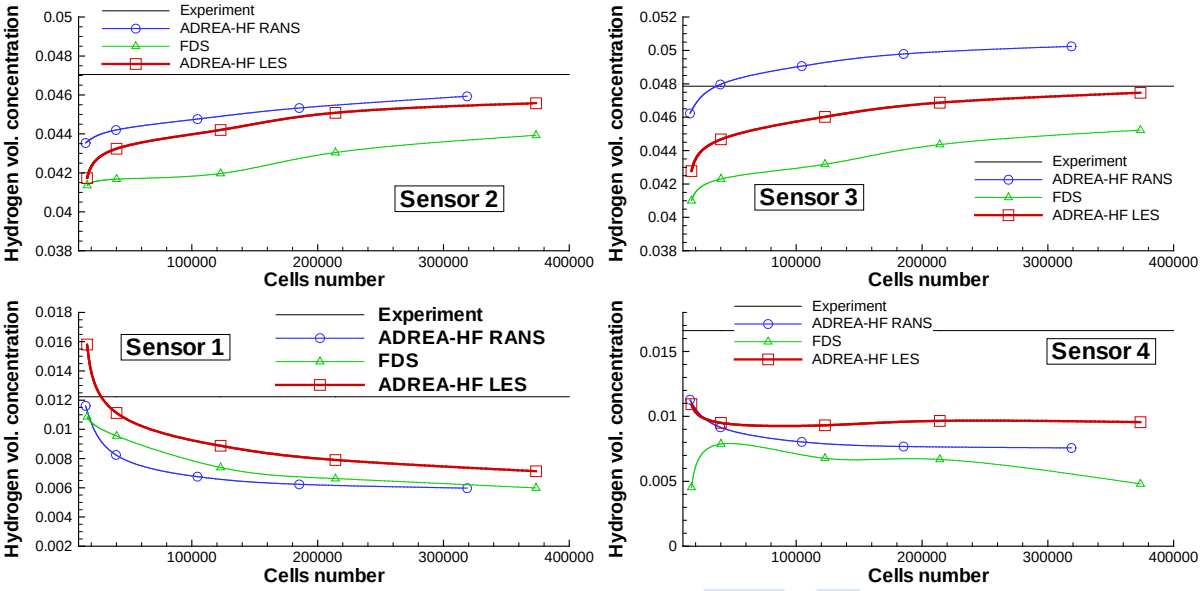

Figure 1.3-7. Grid independency study for three computational models (ADREA-HF RANS, ADREA-HF LES and FDS) at the four sensors of the experiment (Koutsourakis et al., 2012b).

Refinement should be made in regions of interest and with high gradients. A methodology for grid independency study could be to design a coarse grid with refinement in the appropriate regions (e.g. hydrogen inlet) and perform an initial simulation. Then, decrease the minimum cell size (which is most likely be at hydrogen inlet) without changing expansion ratios. This will result in a finer grid in the whole domain. At least one more even finer grid should be tested as mentioned earlier, in order to be able to perform the grid sensitivity study. The sensitivity study continues until convergence is achieved.

Alternatively, if the computational cost is very high, the fine grids may be constructed by changing the expansion ratios and keeping the minimum cell size constant, assuming that the minimum cell size that is used is satisfactory based on guidelines for the examined case. The refinement can also be performed only in regions where high gradient are occurred rather than in the entire domain, in order to minimize the number of cells.

Finally, a quick way to find out whether the initial grid is satisfactory without testing other grid sizes, and consequently without raise the computational time much, is to use higher order numerical schemes. If the results with the higher order schemes are similar to those with the first order scheme it means that the numerical diffusion due to the coarse grid is minimum. However, the most reliable method for the grid independency study is to test several grids.

A thorough grid independency study has been performed and presented in (SUSANA D5.3, 2016). Part of this analysis is presented also in Section 6.2 of the current document. For the study a low speed release and dispersion inside a closed garage (Gupta et al., 2009) has been simulated. One significant conclusion from the analysis is that the user should perform a new grid sensitivity study whenever they change the grid type. Furthermore, it is suggested to perform a grid sensitivity study for every different turbulence model that is used, especially when these turbulence models belong to different categories (see Section 1.2.2).

An example with grid independency study is. CFD benchmark has been performed within the SUSANA project (SUSANA D5.3, 2016) based on the GARAGE experiment (Gupta et al., 2009). Several sensitivity studies have been carried out according to the guidelines that are developed and presented by the current document.

Quantitative grid verification can be performed using the grid convergence index (GCI). Let's suppose that we have a coarse grid with number of cells equal to N_{coarse} and a fine grid with number of cells equal to N_{fine}. The grid refinement ratio r is defined as the cubic root of the ratio between the number of cells/elements in the fine and coarse meshes.

$$r = \left(\frac{N_{fine}}{N_{coarse}} \right)^{\frac{1}{3}} \tag{1.3.5}$$

According to (Celik et al., 2008) this parameter should be greater than 1.3 to allow discretization error to be separated from other sources of error (D'Agostino and Congedo, 2014). Based on Richardson extrapolation (Richardson 1911; Richardson 1927), the GCI for the fine grid solution helps to estimate the grid convergence error (Roache, 1994). The GSI is defined as

$$GCI^{fine} = F_s \frac{\varepsilon}{r^p - 1} \tag{1.3.6}$$

where F_s is a safety factor equal to 1.25 when comparing more than three grids (Celik et al., 2008), and p is the order of convergence, which is calculated from

$$p = \frac{\ln \left| \frac{f_{coarse} - f_{medium}}{f_{medium} - f_{fine}} \right|}{\ln r} \tag{1.3.7}$$

The variable ε is the relative error between the coarse (f_{coarse}) and the fine (f_{fine}) grid solution (eq. (1.3.4).

The GCI parameter may be applied to any variable in CFD solution, e.g. hydrogen concentration, temperature etc.

1.3.2.4 Refinement regions

In hydrogen release and dispersion simulations the flow is almost always non-uniform, i.e. different flow characteristics are exhibited in different areas. Thus, in some areas the grid is chosen to be finer than other areas (refinement areas) and a uniform grid is rarely preferred. The refinement areas should be selected wisely based on the problem geometry. Refinement usually is performed near boundaries and general in regions where high gradients are expected, recirculation areas etc. At solid boundaries the grid should not be too coarse even in the case where wall functions are used. In hydrogen releases, the area near the hydrogen inlet boundary and the source area itself are of primary significance. Furthermore, when the release takes place in confined area with openings, mesh refinement should be examined over the opening, because complex flow may occur in this region (e.g. bidirectional flow).

The first step in generating a "good" grid is to define the number of cells that would enclose the inlet area. Usually, one cell with a projected area equal to the source area is not enough. Higher resolution should be tested (more cells along the source area). Previous studies have

been conducted within the HYINDOOR project which examined effect of the number of cells along the source diameter on the results. With the help of a GAMELAN experiment (Cariteau, 2010) related to upwards helium (as a surrogate for hydrogen) release in an enclosed box three different grid sizes were examined. The grid characteristics are shown in Table 1.3-3. Each grid has a different number of cells along the source diameter; consequently the minimum cell size is different along the horizontal directions, in which the source is located, and it expands at the boundaries with expansion ratio 1.12. All the other characteristics, e.g. the minimum cell size in the third direction (z axis) are the same for the three grids. Figure 1.3-8 displays the source discretization with one cell over the entire source area and 8 cells.

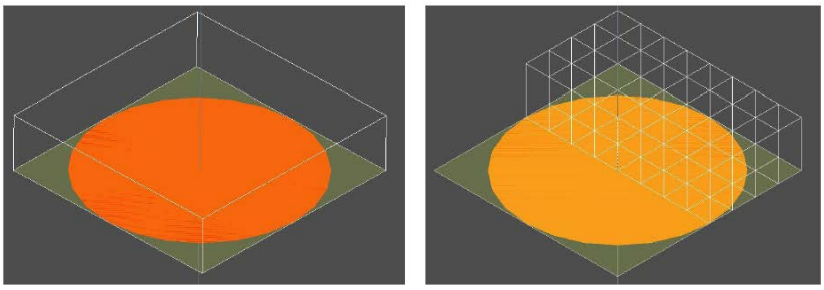

Figure 1.3-8. The source discretization with one cell (left) and 8 cells (right).

Table 1.3-3. The grid characteristics for the tested cases.

Source along the source area	Minimum horizontal cell size	Number of cells	Cells distribution
2	1	43 387	44 x 20 x 53
4	0.5	79 053	58 x 27 x 53
8	0.25	125 410	72 x 34 x 53

The results show that the number of cells used to discretize the source area strongly affects the predictions along the source axis, but only close to the source (see Figure 1.3-9 and Figure 1.3-10). Far enough from the source (near the ceiling and at the other lateral locations, e.g. the sensor mast) the results are practically unaffected, as shown in Figure 1.3-11 with both laminar and standard k-ε turbulence model.

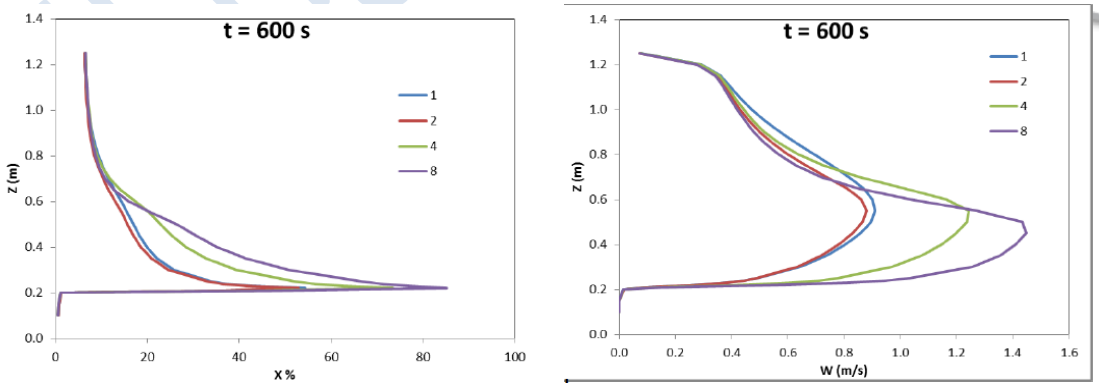

Figure 1.3-9. The axial profile of the hydrogen concentration (left) and vertical velocity (right) above the source with the k-ε model.

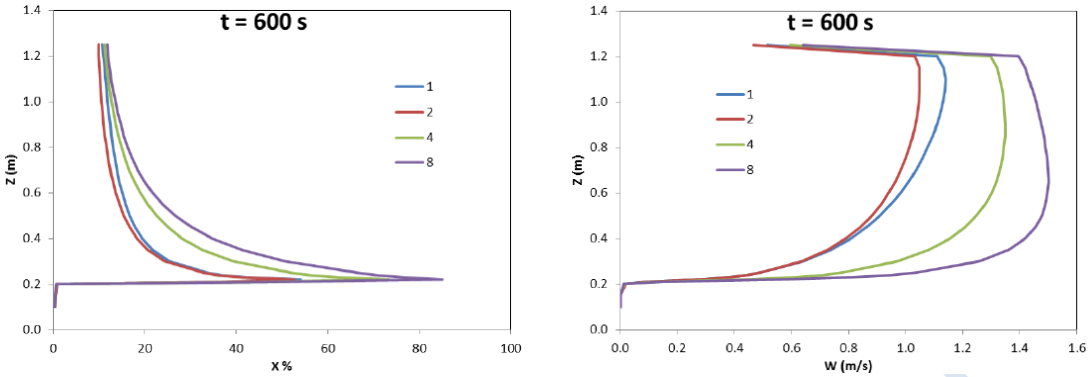

Figure 1.3-10. The axial profile of the hydrogen concentration (left) and vertical velocity (right) above the source with the laminar model.

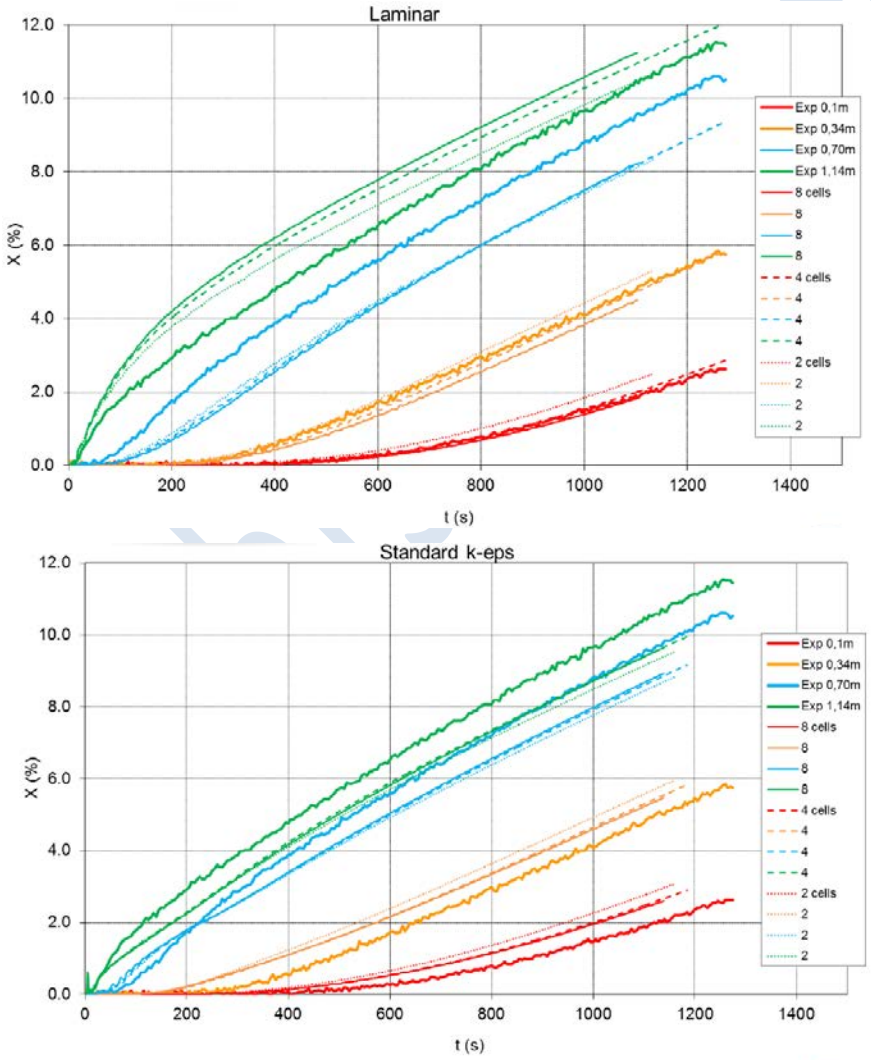

Figure 1.3-11. The time series of the hydrogen concentration with the laminar model (top) and with the k-ε model (bottom).

In real situations with hydrogen release in an enclosure the sensors are usually placed near the ceiling. Therefore, for CFD “risk assessment” predictions it is considered reasonable to limit the number of cells along the source area, in order to reduce the computational cost without loss of accuracy.

Another grid characteristic that affects the results is the number of cells in the vertical direction above the source. The grid around the source and in the direction of the release should be fine in order to capture the concentration gradients.

A simulation of another experiment (Cariteau and Tkatschenko, 2013) showed that the number of cells along the source diameter affects the results. In this experiment hydrogen is released upwards in a partially enclosed box with one opening near the ceiling and with higher release rate than the above investigated case. The prediction with the higher number of cells across the source gives results closer to the experiment, even at the sensors near the ceiling away from the source (Figure 1.3-12).

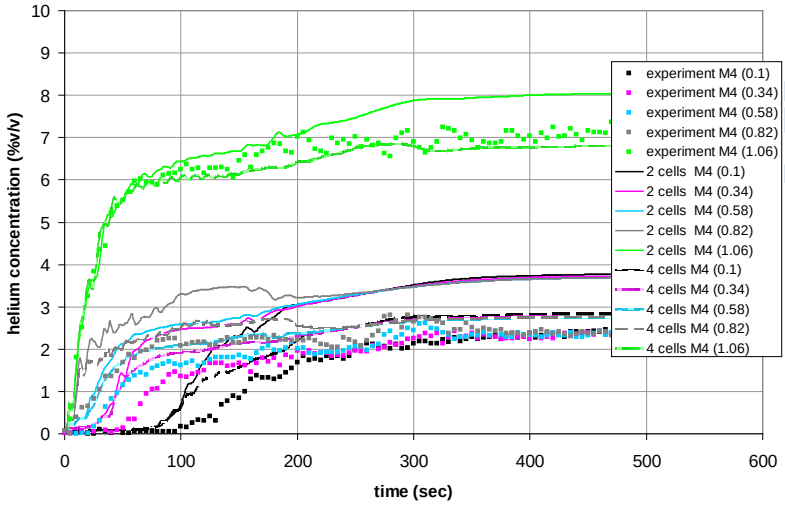

Figure 1.3-12. Comparison of the experiment and the predictions with the different number of cells along the source diameter.

A possible reason for that discrepancy between the two studies is the different release rate. Higher release rates may demand more cells along the source area. This finding reveals the need to make a relevant sensitivity study in cases with different release conditions, in order to assess the effect of the source resolution in the results.

1.3.2.5 LES numerical assessment of mesh quality impact

A study of the physical and numerical requirements for simulation of hydrogen release in the enclosure carried out by the University of Ulster included an assessment of the mesh impact on the performance of the simulation of (Molkov and Shentsov, 2014). The simulation concerned subsonic hydrogen release in an enclosure with a single vent. The computational domain included both the enclosure and a part of the surrounding space in order to avoid boundary conditions being imposed directly at a vent. To decrease CPU time, block-structured hexahedral computational grids had been chosen as way to decrease a total number of control volumes (CVs) by 6 times compared to unstructured tetrahedral grids with the same characteristic cell size. Figure 1.3-13 illustrates one of the meshes developed for this simulation with a mesh inside of the enclosure and outside just beyond the circular opening in the wall located 1 cm above the floor level (the opening itself is not shown). This mesh will be subsequently referred to as Grid 1. Two other grids (Grid 2 and Grid 3, Figure 1.3-14 and Figure 1.3-15) had significantly larger external elements completely surrounding the enclosure in the form of hexahedron of size H×W×L=2.5×3.0×2.5 m (see Figure 1.3-14) and H×W×L=3.0×3.0×4.5 m (see Figure 1.3-15) respectively. Figure 1.3-16 shows 3-D view of

all three grids. The larger extent of external domains in Grids 2 and 3 compared to Grid 1 is necessary due to the presence of a significantly larger vent at the top of the enclosure wall and the two-way character of the flow through the vent. This flow characteristic prompts the removal of the domain boundaries as far as reasonably practical from the enclosure in order to exclude the effect of boundary conditions on the numerical solutions.

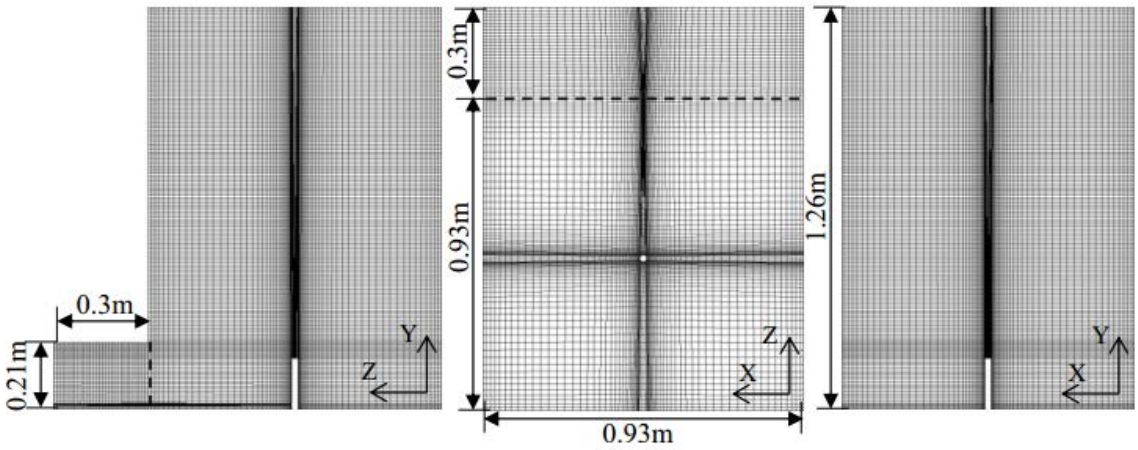

Figure 1.3-13. Grid 1 cross-sections in three cardinal directions. (Molkov and Shentsov, 2014).

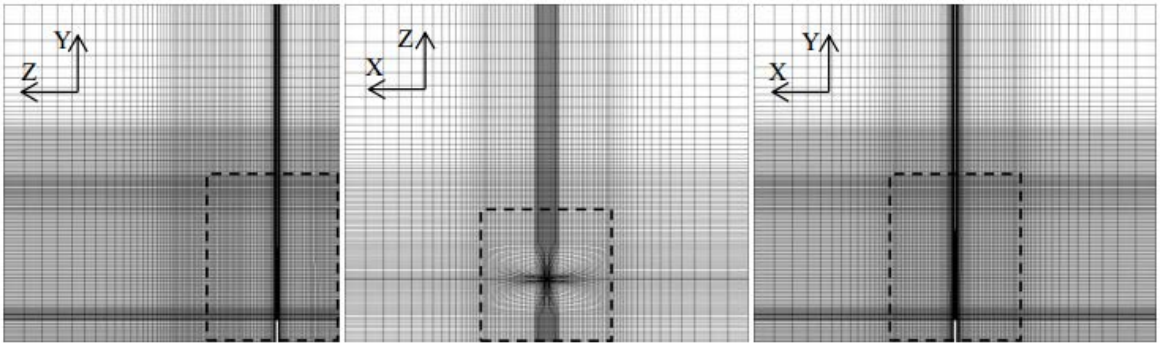

Figure 1.3-14. Grid 2 cross-sections. Dashed lines show the location of the enclosure. (Molkov and Shentsov, 2014).

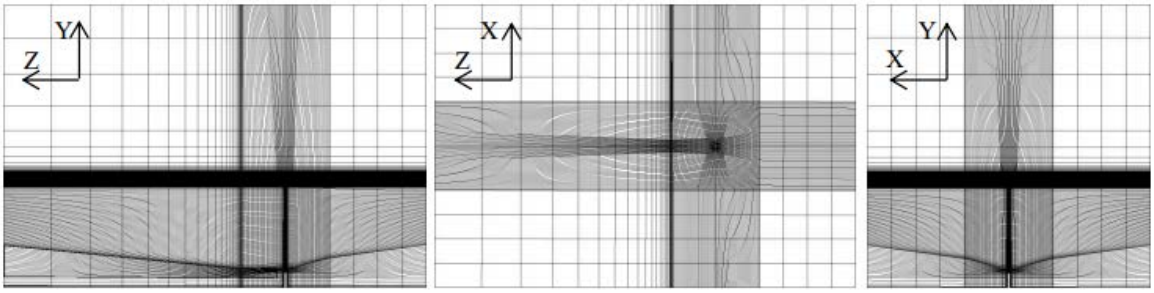

Figure 1.3-15. Grid 3 cross-sections (Molkov and Shentsov, 2014).

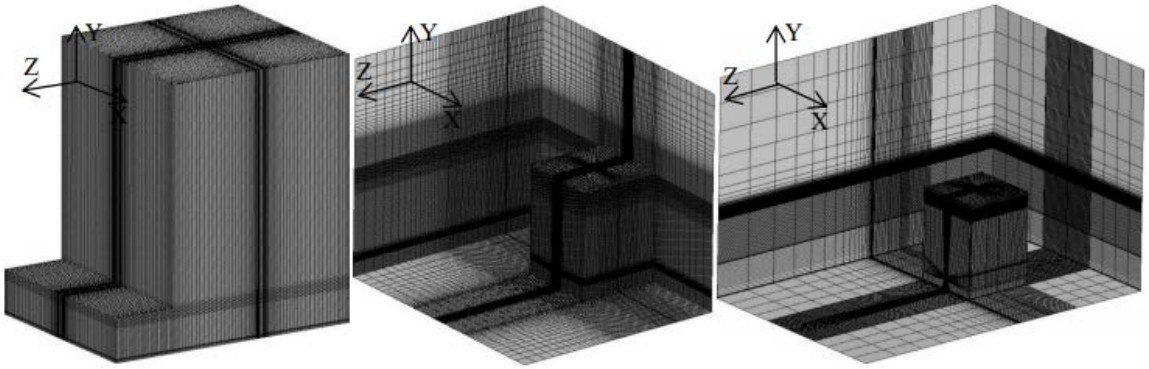

Figure 1.3-16. 3-D views of grid 1 (left), 2 (centre) and 3 (right). (Molkov and Shentsov, 2014).

The jet inflow boundary is a polygon inscribed in a circle with 18 control volumes (CVs) across the pipe diameter (for a total 68 CVs through a pipe cross-sectional area) for the simulation with a 20 mm diameter pipe, and 8 CVs across pipe diameter (20 CVs through the cross-section area) for the 5 mm diameter pipe. The polygon cross-section area is equal to the cross-section area of the enclosure of the corresponding pipe (either 5 mm or 20 mm). The inflow boundary is located inside the release pipe at distance 5 cm from the pipe exit. There are 10 cells along the pipe axis from the inflow boundary to the pipe exit for all grids.

Grid 1 was generated as follows. The vertical size (height) of CVs at the pipe exit was 5 mm (the same as inside the pipe). Expansion ratio of 1.05 was applied to the following 8 cells in the upward direction, until the cell size reached 7.3 mm. Subsequent cells in the upward direction maintained uniform height until the top of the enclosure. There were total 170 CVs along the height of the enclosure. The total number of CVs in the enclosure in Grid 1 is 915,486 with 991,436 CVs contained in the entire domain. 1 cm diameter vent was resolved by 9 cells across the diameter, with the total number of CVs in the cross-section equal to 45. The expansion ratio applied in all horizontal directions from the release point was 1.05 (unless the mesh from walls was encountered). The expansion ratio applied from the walls towards the release point and outside the enclosure was 1.10.

Grid 2 was generated in a fashion similar to Grid 1 following best practice recommendation of grid generation from ANSYS Fluent User Guide. Figure 1.3-14 shows that the mesh of Grid 2 has a uniform distribution of cell heights at the ceiling and the vent area of the domain with vertical CV size equal to 7 mm. The expansion ratio of 1.05 was applied both downwards from this area, and upwards from the release source, reaching maximum vertical cell size (height) of 9.2 mm in 6 steps from the top and in 13 steps from the bottom. The following cells were kept at uniform height equal to 9.2 mm. The total number of cells along the height of the enclosure in Grid 2 was 155, or 15 less as compared to Grid 1. The total number of CVs in the enclosure is 834,710, with 2,338,620 CVs contained in the entire domain. Grid 2 was prepared in two versions, designated 2A and 2B, distinguished by the vent size, which in case of Grid 2A measured H x W= 90 x 18 cm (resolved by 26 x 69 cells), and in case of Grid 2B H x W = 18 x 18 cm (resolved by 26 x 31 cells). The expansion ratio applied in each horizontal direction out of the release source and from the walls towards the release point and in the external to enclosure area of the domain was the same as for Grid 1.

Grid 3 (see Figure 1.3-15, and Figure 1.3-16, right) was built in the largest domain yet contained the smallest number of CVs equal to 437,150 in the enclosure and 812,644 CVs in

the entire domain. The 1 cm diameter vent was meshed exactly as in Grid 1. The expansion ratio applied in each direction from the release point was 1.20. The expansion ratio applied from the walls towards the release point and outside the enclosure was 1.50. Grid 3 was generated with deviations from the recommended best practice in order to assess how strongly these deviations will affect the predictive capability of simulation results.

In addition to adequate resolution, mesh quality is an important parameter determining the accuracy and performance of a numerical simulation. The (Molkov and Shentsov, 2014) simulation utilized the ANSYS FLUENT software as an engine for numerical simulations. Similar to other software it requires high quality mesh to avoid numerical diffusion (ANSYS 2009). In order to improve the accuracy of a numerical solution the mesh quality parameters such as an orthogonal quality, an aspect ratio, and a skewness should be evaluated and controlled. The orthogonal quality varies in a range of 0-1, where value 0 is the worst and value 1 is the best. The recommended best practice is to use grids with the minimum value of the orthogonal quality of not less than 0.1. In (Molkov and Shentsov, 2014) the orthogonal quality was above 0.4 for Grid 1 and 2, and 0.25 for Grid 3.

Maximum value of the aspect ratio in the entire domain was equal to 40 for Grid 1, 431 for Grid 2 (due to a large vertical size of cells in the external region above the narrow [in horizontal direction] cells in the pipe), and 353 for Grid 3. The best practice per FLUENT manual recommendation (ANSYS 2009) is not to exceed the value of 40, but the importance of its observance is dependent on a flow characteristics and a location of particular cells with respect to the flow with relatively high velocity. Aspect ratio values were significantly better in the mesh sub-domain contained within the enclosure, where the most significant flows are expected. Within the enclosure the maximum aspect ratio is equal 40 for Grid 1, 29 for Grid 2 and 37 for Grid 3.

Another parameter to be considered during mesh generation is a cell size change or an expansion factor. ANSYS FLUENT User Guide (ANSYS 2012) recommends to keep it between 1 and 2. The larger the value of the expansion factor, the higher is the numerical diffusion. A poor mesh quality may result in an inaccurate solution and a slow convergence.

A comparison of numerical results of LES simulations performed using “high quality” Grid 1 with experimental data obtained by Cariteau and Tkatschenko of CEA for helium release in the enclosure (Cariteau, and Tkatschenko, 2011), (Cariteau 2010) showed a good agreement in both transient and steady-state helium concentration values (Figure 1.3-17, left) for the upper portion of the enclosure where the highest helium concentrations were observed. In order to assess the impact of grid quality, the same simulation was repeated using “low quality” Grid 3 using the same LES model and close CFL number (25 *versus* 28 used in case of Grid 1). Grid 3 was intentionally designed with the orthogonal quality, aspect ratio and skewness close to the lower edge of recommended values and the expansion factor applied exceeding that of Grids 1 and 2.

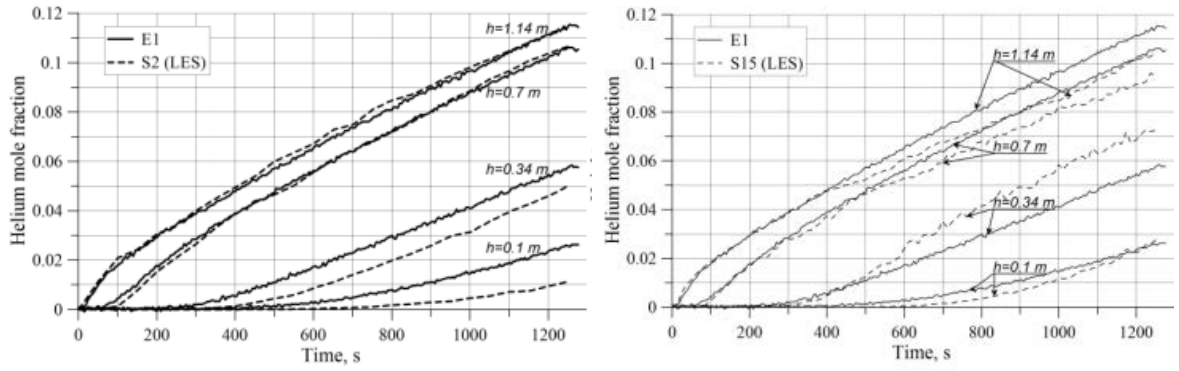

Figure 1.3-17. Comparison of experimental data (solid lines marked E1) with numerical results obtained by the LES model on a “high-quality” (Grid 1, dashed lines) mesh (left) and “low-quality” (Grid 3, dashed line) mesh (right).

Figure 1.3-17 (right) shows a comparison of the transient helium concentrations between the experiment (solid curve marked E1) and simulation performed on a “low-quality” Grid 3 (dashed curve marked S15) at location of sensors 1, 3, 6, and 10. Both simulations reasonably closely reproduce experimental data until approximately 400 s after start of the release. For the rest of release duration until its termination at 1275 s, simulation using Grid 3 consistently under predicts concentration value in the upper part of the enclosure by about 10% and over predicts by 20-30% at the height of h = 0.34 m above the floor. It can be concluded that the “low-quality” of Grid 3 is responsible for the decreased capability of the LES model to reproduce experimental data. It appears that the higher numerical diffusion is a reason for a faster “transport” of helium from the upper part of the enclosure to its lower part.

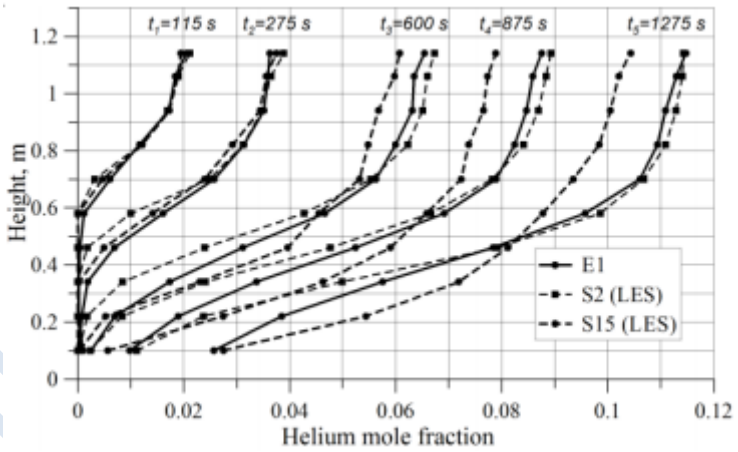

Figure 1.3-18. Comparison of experimental data of helium concentration at 10 sensors locations at five different moments of time (solid lines) and numerical simulation predictions obtained on “high-quality” (Grid 1, marked S2 on the figure) and “low-quality” (Grid 3, marked S15 on the figure) meshes.

Figure 1.3-18 further compares helium distribution along the enclosure height at five different moments of time (t_1 = 115 s, t_2 = 275 s, t_3 = 600 s, t_4 = 875 s and t_5 = 1275 s) calculated using “high quality” Grid 1 and “low-quality” Grid 3, as well as experimental data. It can be seen that the deviation from experimental data (under-prediction of concentration in the upper part of the enclosure and over-prediction in the lower part) grow with time, which can be once

again attributed to the non-physical numerical diffusion generated by the “low-quality” mesh. Numerical experiments discussed in this sub-section illustrate the effect of mesh quality on simulation results. Simulations on the under-resolved mesh in which lower number of cells is compensated by the increase of the expansion factor indicated significantly increased numerical viscosity, leading to artificially increased dispersion of gas concentration and under prediction of maximum concentration near the ceiling.

1.3.2.6 Two stage approach to under-expanded jet release modelling

Many practical engineering problems involve phenomena exhibiting a wide range of spatial scales. A typical example is gas release from a high pressure storage tank resulting in the under-expanded jet. The length of the resulting jet can be several orders of magnitude larger than the characteristic scales defining physical processes in the immediate vicinity of the nozzle.

As it was highlighted in Section 1.2.5 when a high pressure release occurs at pressures above 1.9 times atmospheric pressure, the flow is supercritical at the exit. Under-expanded supersonic jets are formed immediately after a physical exit. As the flow leaves the exit it rapidly accelerates and expands to atmospheric pressure through one shock at a very high pressure or a series of expansion shocks. Modelling of under-expanded jets therefore presents a considerable problem due to a large disparity of spatial and velocity scales in the vicinity of the release origin and in the far field, which makes simulations of the entire jet in a single computational domain prohibitively CPU-expensive. On one hand, a presence of the under-expanded jet shock structure associated with high flow velocities in a near field and a small aperture of the nozzle would dictate utilization of a very fine mesh in the vicinity of release origin. Cumber et al., (1995), suggested that adequate resolution of under-expanded region may require as many as 32 to 64 cell volumes (CV) per nozzle diameter. On the other hand, an under-expanded jet extent can often reach tens of meters, making development of a grid covering an entire domain without violating best practice recommendations regarding cell expansion ratio difficult or impossible. Furthermore, slow velocities at the end of the jet necessitate relatively long physical characteristic timescales which need to be covered by simulation, while the requirement of keeping CFL number sufficiently low dictates very short time step due to the fine refinement of the mesh near the jet origin, resulting in prohibitively high number of time steps required for a typical simulation. This makes simulation of the problem in one computational domain impractical.

This problem can be circumvented by utilization of the two-stage or two-domain approach to the simulation, in which the phenomena with significantly different characteristic scales are simulated on different grids connected through the interface on which the outflow conditions of one domain are interpolated into inflow conditions of the other. Simulations in these domains can utilize different numerical approaches, suitable for modelling of respective physical phenomena. Illustration of such approach can be found, e.g., in Xu et al. (2005) and Makarov and Molkov (2013a).

Xu et al. (2005) used it for simulation of a highly under-expanded hydrogen jet released from the high pressure vessel at 20 MPa. The highly under-expanded jet near the orifice (50D in diameter and 80D in axial extent) was simulated using RANS approach on unstructured grid with 200,000. Subsequent hydrogen jet was modelled using LES approach within 160D×160D×300D box using 60×60×120 clustered grid.

A similar approach was used in simulation of under-expanded jet release problem at University of Ulster. It involved separation of the computational domain into two

subdomains, one describing the compressible region near the nozzle exit, while the other covered the far-field region where the flow was essentially incompressible (Makarov and Molkov, 2013a). Reduction of the computational effort is achieved through the modelling of the under-expanded jet problem in two separate stages. In the first stage the compressible flow in the near-to-nozzle field is simulated, with the results used as boundary conditions for the second stage, simulating essentially incompressible flow in the far-from-nozzle field.

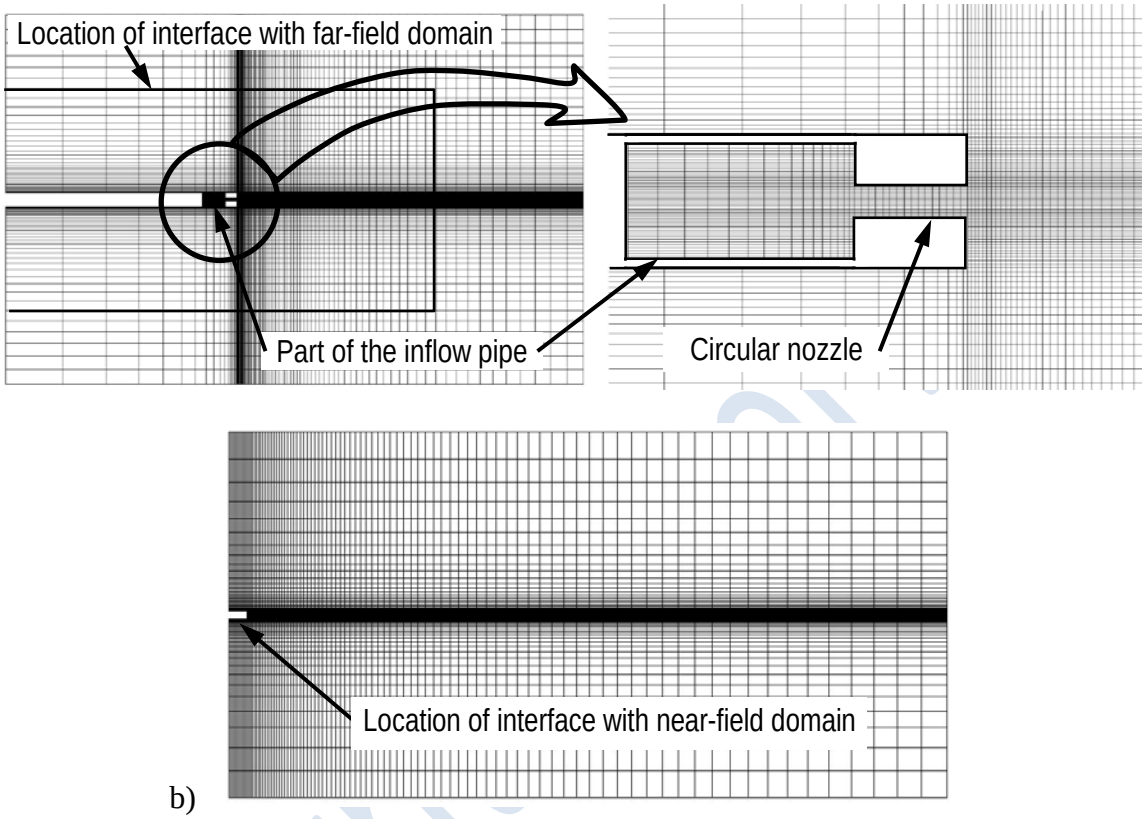

Figure 1.3-19. Illustration of two sub-domain approach to under-expanded jet modelling (from (Makarov and Molkov, 2013a)) showing near-field (a) and far-field (b) meshes relative dimensions and interaction.

Figure 1.3-19 illustrates the two subdomain approach as was applied in (Makarov and Molkov, 2013a). In that case the jet originated from the 1 mm diameter round nozzle. In order to simulate a flow field in the vicinity of release origin, the inner subdomain was created with dimensions L (length) × D (diameter) = 0.1625×0.104 m. It was discretized using 412,736 hexahedral control volumes (CVs) with 20 CVs across the nozzle diameter. The far field subdomain had much larger dimensions of L×D = 7.8×2.0 m and was discretized using 356,868 hexahedral CVs. Subdomains connected through the interface boundary, with simulation results at the outer (interface) boundaries of the near-field sub-domain used as boundary conditions for the far-field sub-domain. The interface was located far from the compressible boundary to minimize potential effect of its numerical approximation errors onto the incompressible stage boundary conditions. Meshes were designed to optimize simulation of the phenomena occurring in the respective domains. The inner mesh was designed to be uniform in the expected location of Mach disk in order to minimize numerical dissipation in the area of maximum gradients. The other mesh was designed with the outer boundary removed to a far field which is a design typically used in RANS in order to ensure that simulation would not be affected by boundary effects.

Note that the near- and far-field grids, used for compressible and incompressible simulation stages respectively, did not have identical cells distribution at the sub-domain's interface. An interpolation of simulation results was therefore required at the inflow boundary of the incompressible stage domain. This had a potential to cause deterioration of the accuracy of calculation results. Special attention is therefore necessary to verify that the key flow parameters at the interface between compressible and incompressible domains are matching each other and there are no significant discontinuities across the interface.

1.3.3 Boundary conditions

The choice of the boundary conditions is of great significance to the accuracy of the computational results. There are several options available for boundary conditions and the user must decide the most appropriate boundary conditions for the application. The objective of this section is to present the most widely used boundary conditions in problems regarding hydrogen dispersion and introduce the user to the main features of the several boundary conditions. Typically, the boundaries can be divided in 6 categories: inlet, outlet, top, sides, wall and ground. Regarding the application all of some of the below boundaries may exist.

Outlet

The outlet boundary of the computational domain, as stated in Section 1.3.1 should be placed far enough, in order to ensure that the flow is undisturbed and is not influenced by obstacles and high gradients. Outlet is an open boundary and for open boundary the most common boundary conditions that are applied are a) constant pressure and b) zero gradient for all variables, except pressure. According to (Versteeg and Malalasekera, 2007) the constant pressure condition is used for flows where details for the flow distribution are unknown. Typical flows that this boundary condition is appropriate to are external flows, around objects, buoyancy driven flows, such as natural ventilation and internal flows with multiple outlets. The zero gradient condition can be applied in cases where the outlet boundary is placed far from geometrical disturbances and a fully developed flow is reached with no changes in the flow direction. Based on the above recommendations the constant pressure boundary condition seems the most appropriate in hydrogen dispersion problems. However in LES approach, the non-reflecting boundary condition (Givoli, 1991) can also be applied (Koutsourakis et. al, 2012b). Especially, for the boundary condition of the mass fraction of the hydrogen and the temperature a zero gradient condition can be applied, if outflow occurs, and a given value (equal to the initial value) if inflow occurs. With this boundary condition hydrogen is not allowed to re-enter the outlet boundary.

Inlet

Inlet refers to boundaries through which hydrogen enters the domain and boundaries where inflow occurs, e.g. wind. In the inlet boundaries of the computational domain Dirichlet conditions are specified for all variables. A Dirichlet condition means that the values of the variables on the boundaries are given.

In hydrogen inlet (source), special treatment is required in the case of compressed or liquefied hydrogen in order to estimate the boundary values. Details are given in Section 1.2.5.

For the k and ε variables, if their values are unknown, they can be estimated from the following relations (Versteeg and Malalasekera, 2007):

$$k = \frac{3}{2}\left(U_{ref} \cdot T_i\right)^2 \tag{1.3.8}$$

$$\varepsilon = c_{\mu}^{3/4} \frac{k^{3/2}}{0.07D} \quad (1.3.9)$$

where U_{ref} is the velocity, T_i is the turbulent intensity, $c_{\mu} = 0.09$ and D is the characteristic length scale.

In open environment releases it is likely that wind will be present. In that case, the values of the wind velocity (and the turbulent characteristics, e.g. k and ε values), can be obtained from a 1-D simulation that would produce the vertical profile (Giannissi et al., 2014). Alternatively, for the wind velocity the power law profile can be used. More details for producing the wind profile in non-stagnant environment are providing in Section 1.3.4.

In LES approach, the choice of the appropriate inlet boundary conditions requires considerable expertise. When LES turbulence model is used, the fluctuating velocity, u′, should also be imposed in the inflow boundary, in order to generate turbulence in the flow field. The values of the fluctuating velocity can be estimated following two main methodologies:

1. Impose certain values in the inflow boundary. These values can be given/derived by experimental measurements. If such information is unavailable or if the simulation is not replication of a specific experiment, then the user can assume values based on similar applications.
2. Cyclic (periodic) boundary conditions in the 3D problem. Air flow is simulated initially with zero fluctuating velocity in the inflow boundary. In the next time steps the outflow boundary conditions are set as inflow boundary conditions, etc. In this way the generated by the Navier-Stokes turbulence inside the domain is imposed as inflow conditions (Lund et al., 1998). This simulation continues until a statistically steady state solution is achieved.

However, the choice of the appropriate inlet conditions in LES approach is still an open issue and requires an experienced user.

Top

The top boundary is usually an open boundary and boundary conditions similar to the outlet could be applied. However in the presence of wind, Dirichlet and symmetry boundary condition are usually preferred (Luketa-Hanlin et al., 2007). In symmetry boundary condition, no flow crosses the plane boundary and no scalar flux occurs through it. Thus, the normal component of velocity is set to zero and in all other variables zero gradient condition is imposed. The top boundary must be placed sufficiently far away in order the zero gradient boundary not be violated (typically 10 times the height of any obstacle). In several studies (Chan et al. 2002, Hertwig et al. 2012, Rakai et al. 2013) regarding urban flow fields and dispersion of pollutants in street canyon, in the top boundary fixed velocity and turbulence characteristics is imposed (Dirichlet condition) according to the measured value at that height. This boundary condition can also be used in hydrogen dispersion problems in open environment providing that the top boundary is placed high enough and it is unaffected by the release.

Sides

Similar to the top boundary the side boundaries are open boundaries. The constant pressure condition can be applied. However, as in the top boundary Luketa-Hanlin et al. (2007)

recommended the symmetry condition in these boundaries too, because a constant pressure condition could lead not to the desired velocity profile and consequently excessive mixing will be introduced into the domain.

Wall

The wall is specified with no-slip condition. Wall functions are used for the velocity and the temperature, in order to avoid resolving the boundary layer near the wall. Zero gradient condition is applied for hydrogen mass fraction.

Ground

Similar to wall boundary a no-slip condition is specified on the ground and wall functions are employed. For adiabatic ground, zero gradient condition should be applied for temperature. When heat transport from the ground should be accounted for, a Dirichlet condition for ground temperature or ground heat flux should be imposed. The given values (of temperature or heat flux) on the ground can be either constant or transient depending on the physical problem. For instance, in case of cryogenic releases, where the ground comes in contact with the cold cloud, temperature drops as time passes. In such cases, an underground temperature conservation equation can be solved at each time step and its solution is set as temperature boundary condition on the ground-cloud interface. More details about cryogenic releases can be found in Section 1.2.4. For hydrogen mass fraction zero gradient condition is applied similar to wall boundary.

1.3.4 Initial conditions

The conservation equations that are solved to simulate the real problem require initial conditions. Initial conditions define the values of all variables in the domain before the beginning of the investigated problem, e.g. before the hydrogen release.

1.3.4.1 Initial conditions for velocity

In problems where the release takes place in quiescent environment (in closed geometries, such as boxes and garages) the initial values are set equal to zero, which is usually the default value in the CFD codes. However in LES approach, initial perturbations in velocities could be given (e.g. this is the default option in the FDS code (FDS, 2016)).

In problems in open environment in the presence of wind the specification of initial conditions is more complicated. The wind field should be reproduced. First the vertical velocity 1D profile should be calculated. This vertical profile will be used for the calculation of the initial and boundary condition in the 3D simulation as it will be described next. Two main approaches are used to compute the velocity profile: 1D steady state problem solution and use of empirical expressions.

In the first approach the procedure is the following: A 1D steady state problem is solved with the help of a turbulence model and with Dirichlet velocity boundary condition on the top. If there are available data (e.g. from experiment) for the wind speed at a given height these data can be used in order to predict accurately the velocity at that height by adjusting the top boundary condition. The result of this 1D simulation is the vertical velocity profile and the vertical profiles of k and ε variables in the case where k-ε turbulent model is used.

In the second approach the user can use mathematical expressions to calculate the velocity profile along the height of the domain. The two most common expressions that approximate

the variation of the mean speed from the ground to the gradient height are the logarithmic law and the power law. Both expressions can be applied in turbulent flows.

The logarithmic law describes the vertical distribution of horizontal mean wind speed and it is generally limited in the lowest part of the surface layer of the atmospheric boundary layer (i.e. 100 m):

$$u_z = \frac{u_*}{\kappa}\left[\ln\left(\frac{z}{z_0}\right) + \psi_m\left(z, z_0, L\right)\right] \tag{1.3.10}$$

where u_z is the velocity at height z, u_* is the friction velocity (see also §1.2.6), z_0 is the roughness length, ψ_m is a stability function (in neutral conditions is zero), and L the Monin-Obukhov stability parameter. Definitions and details about the friction velocity, the roughness length, the stability function and the Monin-Obukhov parameter can be found in Section 1.1.3 in (SUSANA D2.1, 2016). Although this expression is considered reliable for estimating the vertical velocity profile, some difficulties are encountered in its use related to the friction velocity and the surface heat flux (for definition of the atmospheric stability class) values that are required, yet they are not usually measured and cannot be readily derived. However, as mentioned in Section 1.1.3 in (SUSANA D2.1, 2016) in many dispersion modelling applications, the user can roughly estimate the stability from simple observed quantities and produce the velocity profile.

The wind power law relationship is:

$$\frac{u_z}{u_r} = \left(\frac{z}{z_r}\right)^a \tag{1.3.11}$$

where u_r is the velocity at the reference height z_r. To use this expression the user should know the velocity at a height above the ground (reference height). The exponent a is an empirically derived coefficient dependent on the stability class of the atmosphere. For neutral stability conditions, a is approximately $1/7$, or 0.143 (Tominaga et al., 2008).

Apart from the above approaches, if the wind speed is available from measurements at several heights, an approximation of the wind profile can be made by fitting the data. This approach is used by (Giannissi et al., 2013) in order to reproduce the exact velocity and temperature profiles based on the experimental data. Finally, a simple approach is to consider uniform velocity along height equal to the measured velocity at a height (Sklavounos and Rigas, 2005). This approach can be used if there is lack of information about the stability class, the surface roughness, etc. However, the logarithmic law or the power laws are recommended for more accuracy.

When the 1D wind field has been produced with one of the above approaches, it can be used as initial condition by applying it in every vertical column of cells in the grid of the 3D release problem. In cases with complex geometry, in order to account for the obstacles in the domain and their effect on the flow field, a 3D steady state problem (without release) for the calculation of the 3D wind field should be solved using the velocity profile from the 1D problem as initial and inflow boundary conditions. Then, the 3D problem is used as initial and inflow boundary condition for the release problem.

Finally in LES approach, in order to estimate the initial 3D wind field a common practice is to initialize the problem with the solution obtained by a RANS simulation. Then, special treatment for the inlet boundary conditions is required for the LES (see Section 1.3.3).

1.3.4.2 Initial conditions for other variables

Initial conditions need to be specified for other variables too (i.e. temperature and turbulence quantities). In problems with heat exchange the initial temperature distribution is likely to be significant. The user can consider uniform temperature in the entire domain equal to the ambient temperature. However, in atmospheric dispersion applications a temperature profile based on the lapse rate should be used instead (in Section 1.1.3 of (SUSANA D2.1, 2016)), which for neutral conditions is equal to 0.98.

Alternatively, similar to the logarithmic velocity profile there is also a logarithmic potential temperature profile which can produce the temperature vertical distribution:

$$\theta_z = \theta_0 + \frac{\theta_*}{\kappa}\left[\ln\left(\frac{z}{z_0}\right) - \psi_h\left(\frac{z}{L}\right)\right] \tag{1.3.12}$$

where θ_z is the temperature at height z, θ_0 is the potential temperature and ψ_h a stability function.

The ambient temperature (T) is related to the potential temperature and the pressure (P) by:

$$T = \theta\left(\frac{P}{P_0}\right)^{\frac{R}{C_p}} \tag{1.3.13}$$

where R is the gas constant, C_p is specific heat of air, and P_0 is the standard reference pressure (equal to 1 bar). In general, the ambient temperature and the potential temperature in the atmospheric surface layer (~100m) do not vary by more than 10% (Arya, 2001).

For the turbulence quantities the user can use the equations described in Section 1.1.3 of (SUSANA D2.1, 2016), dependent on the atmospheric stability class. In problems where the stability class is unknown usually neutral conditions are assumed. Alternatively, the user can perform a sensitivity analysis.

Finally for the pressure, the hydrostatic pressure is used. Usually this initial condition is set by default from the CFD software.

1.4 Numerical options

1.4.1 Solver type

Solvers can be distinguished based on whether they use a partial differential equation to calculate the pressure (pressure-based) or the density (density-based). In pressure-based solvers the density is obtained from the Equation of State (EoS). In density-based solvers the EoS is used to calculate the pressure.

Another classification of solvers is based on whether the density is considered a function of pressure or not. The mixture density (mixture of hydrogen with air) is generally a function of pressure, temperature and species mass fractions. In incompressible solvers the mixture density is a function of temperature and species concentrations only. This is achieved by

using the static pressure (or a fixed reference pressure) in the EoS. In compressible solvers the mixture density depends also on the actual pressure. In general incompressible solvers are considered as computationally faster. Another advantage of an incompressible solver is that by eliminating the pressure-density dependence it eliminates the possibility of pressure waves travelling at sonic speed through the computational domain, which can create oscillations and deteriorate numerical convergence.

A third classification of solver is based on whether time discretization of the conservation equations is explicit or implicit. In explicit solvers calculation of the solution at the next time step is very fast. Explicit solvers though require very small time steps to satisfy convergence (CFL<1). Implicit solvers on the other hand need iterations within each time step but may accept larger time steps without loss of convergence. If the physical phenomena to be captured by the simulation require a very small “physical” time step, then use of an explicit solver is preferred from the point of view of computational cost.

Compressible solvers must be used in regions of the flow where density is severely dependent on pressure. In regions of the flow where the density weakly depends on pressure one can use either a compressible or a (faster) incompressible solver and an associated sensitivity analysis could be performed on the predicted results.

An example of a strongly compressible region is the field near the nozzle of an under-expanded gaseous hydrogen release. Far from the nozzle the flow is weakly compressible and the pressure is approximately atmospheric.

In a recent study by (Makarov and Molkov, 2013a) the near and far field under-expanded jet problem was modelled in two stages (see also Section 1.3.2.6): first the compressible flow in the near-to-nozzle field was simulated using a compressible density-based explicit solver, and then the results were used as boundary conditions for the far-from-nozzle field simulations, which were performed using a pressure-based implicit incompressible solver. This approach allowed saving the simulation time while preserving the physics of the phenomena.

In the case when the resolution of the near nozzle shock structure is not of interest the notional nozzle approach (Molkov et al., 2009) can be applied and an incompressible solver can be used similar to (Brennan et al., 2009).

For simulation of hydrogen dispersion the numerical and physical requirements of simulations of sub-sonic release and dispersion of light gas in an enclosure with one vent are described and discussed in recent paper (Molkov and Shentsov, 2014). Numerical details applied in this paper employed incompressible solver calculations with pressure velocity coupling through the SIMPLE scheme, a second-order upwind scheme for spatial discretization, and a second-order implicit scheme for time stepping. An incompressible solver with the LES turbulence model was capable of reproducing with good accuracy all experimental data, including laminar, transitional, and turbulent flow releases from a pipe either 5 mm or 20 mm diameter.

1.4.2 Spatial discretization schemes

In the finite volume method, which is usually employed in CFD methodology, the differential equations are integrated over computational cells. The values of the variables are stored at the center of the cells (nodes). However, during the discretization process the values of the variables at the cell surfaces are required. The calculation of these values is of great importance, especially for the case of the discretization of the convective term of the equations.

The order of accuracy of a spatial discretization scheme is an important factor in CFD simulations. First-order accurate schemes such us the upwind scheme may introduce numerical diffusion into the solution where there are flow gradients. This results in artificial mixing and reduction in the spatial gradients of flow variables. Numerical diffusion can be reduced by using higher-order schemes, such as QUICK, FROMM and CUBIC. However, high-order schemes may introduce unphysical oscillations of flow variables and unbounded results. This can be a great drawback especially for variables which must not exceed certain values, such as species mass fraction. Especially, the Central Differences numerical scheme should not be used as it requires very small grid cells in order avoid production of oscillations in the solution (Versteeg and Malalasekera, 2007). High-order schemes which have the Total Variation Diminishing (TVD) (Waterson and Deconinck, 2007), (Versteeg and Malalasekera, 2007) property should be preferred. Classical 2nd order TVD schemes such as Van Leer, MUSCL, SMART and Bounded Central Differences have been used successively in hydrogen dispersion problems.

In RANS modelling, even though an upwind scheme can be used, a grid independency study should be done which may require an unrealistically large number of computational cells. In general, high-order schemes require larger cells to achieve the same accuracy as first order schemes. As a result high order schemes can achieve a grid independent solution using fewer numbers of cells. In LES modelling, high-order schemes are a prerequisite and first-order schemes are not recommended.

An example of the importance of high order schemes is given in (Tolias and Venetsanos, 2015) where hydrogen impinging jet was simulated. When the impinging jet hits the ground, a circulating velocity field is expected to be formed. It was shown that the CFD simulation of hydrogen impinging jets suffers from numerical errors resulting in a non-physical velocity and hydrogen concentration field with a butterfly like structure. In order to minimize the numerical errors and to avoid the butterfly effect, high order schemes need to be used. Fifteen numerical schemes were tested in order to access their capability to reproduce a physical correct solution. In Figure 1.4-1 hydrogen mass fraction near the ground are presented for the Upwind and the MUSCL scheme and for 3 different grid sizes. We observe that a butterfly like structure of the contours appears when the Upwind scheme was used. Furthermore, the Upwind scheme fails to achieve a grid independent solution. Even for a 9 cell discretization of the source the shape of the contours lines deviate from circular. However the butterfly structure seems to be smoothed out as the number of cells increases. The convergence to a grid independent solution seems to be very slow, probably because of the low order accuracy (1st order) of the Upwind scheme. On the other hand for the MUSCL scheme a near grid independent solution is achieved with the 9 cells discretization. Furthermore, a physical shape of the contours is achieved even with the 4 cells discretization.

Upwind - 1 cell discretization

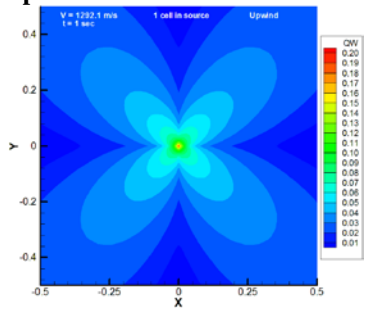

Upwind - 4 cells discretization

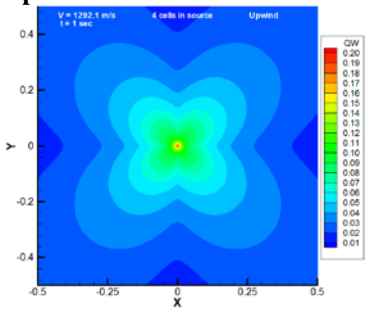

Upwind - 9 cells discretization

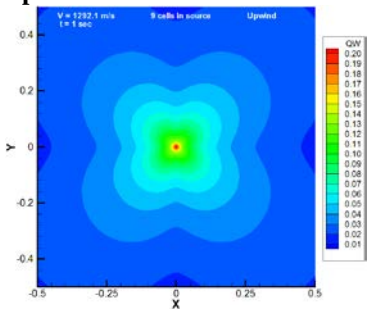

MUSCL - 1 cells discretization

MUSCL - 4 cells discretization

MUSCL - 9 cells discretization

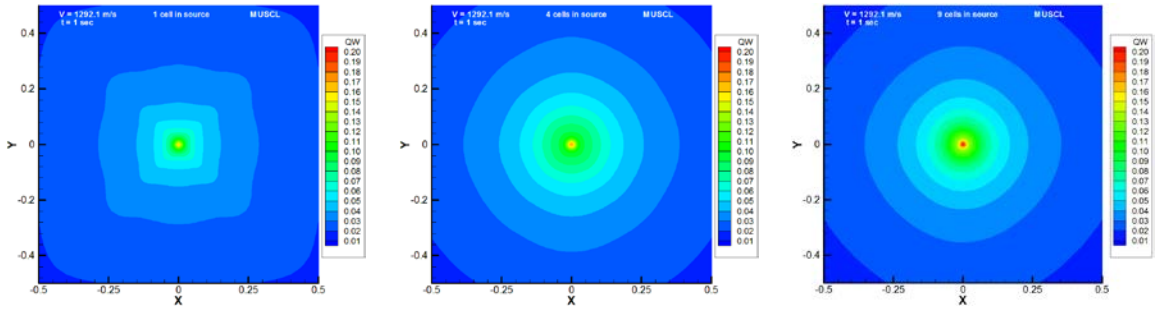

Figure 1.4-1. Hydrogen mass fraction contours at z=0.005 m above the ground for Upwind and MUSCL scheme for 1, 4 and 9 cells discretization of the source

To sum up, the following guidelines regarding temporal discretization schemes should be followed:

- High order schemes which have the Total Variation Diminishing (TVD) property should be preferred. First order schemes (e.g. Upwind) should be avoided especially for complex flows with strong gradients.
- In LES modelling, high order schemes are a prerequisite and first order schemes should not be used.

1.4.3 Temporal discretization schemes

In hydrogen release and dispersion problems the related physical phenomena usually have strong transient characteristics. As a result transient numerical simulations are required.

In transient simulations the term $\partial f/\partial t$ exists in transport equations and needs to be discretized, where f is the transport quantity e.g. $f=\rho u$ (where ρ the density and u a component of the velocity).

Temporal discretization schemes are categorized in two major categories: explicit and implicit schemes. In the explicit scheme discretization, the unknown variables in the new time-step are calculated based on the values of the variables at the previous time-step. In this case, the variables are estimated by algebraic equations without the need of solving system of equations. On the other hand, in implicit formulation the unknown variables in a point of the grid are coupled with the (unknown) values of the variables of neighbour points at the new time-step. As a result a system of equations should be solved in order to calculate the variable in the new time-step. Even though explicit schemes are simpler and require less computational time per time step, they have stability issues and thus require very small time-steps. The Courant-Friedrichs-Lewy (CFL) number is defined in a computational cell by the equation:

$$CFL=\frac{U\cdot\Delta t}{\Delta x} \qquad (1.4.3.1)$$

where U is the velocity, Δt the time-step and Δx the length of the computational cell. In the explicit formulation the restriction $CFL<1$ needs to be imposed.

In hydrogen safety applications, the duration of the relative phenomenon is often large. As a result an explicit formulation may require an extensively large number of time-steps. Furthermore, explicit formulation may not be appropriate in flows of high Reynolds number. In that case, the velocity U will be high and as a result a very small time-step will be required

in order to satisfy the restriction $CFL < 1$ (see equation (1.4.3.1)). In an implicit formulation, CFL number can be in theory be very large. In practice, a maximum value of the CFL number should be imposed for two reasons:

- Numerical stability. Too large CFL number may result in convergence issues of the overall algorithm (solver).
- Accurate prediction of the transient phenomenon. The proper time step depends on the time scales of the examined flow. If the time step is bigger than the time scales which drive the phenomenon, the simulation may fail to capture the correct physics and as a result may produce wrong solution.

The upper value of the CFL number that should be set depends strongly on the specific case. As a result a specific value cannot be suggested. Good practice is to review the manual of the specific CFD program that will be used, search in the bibliography for successive simulations of a similar case and to test different values of the CFL number in order to see how the convergence behaves and how the results change.

An example of sensitivity study of the CFL number has been performed within the SUSANA project (SUSANA D5.3, 2016), and is presented next for the k-ε turbulence model. The simulation is based on the GARAGE experiment (Gupta et al., 2009). Three different CFL numbers have been tested, CFL=5, CFL=10 and CFL=20. These values correspond to a time step of 0.3, 0.62, 1.25 s, respectively during the release period and to about 1.26, 2.5, 5 s, respectively, after the release has stopped. The analysis was performed using the independent grid. The results are presented in Figure 1.4-2.

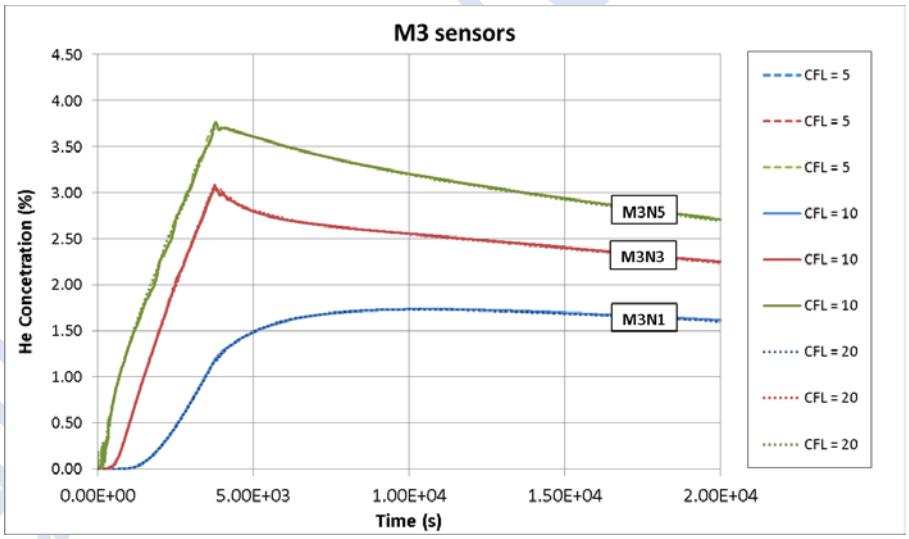

Figure 1.4-2. The results from the CFL sensitivity study.

It can be noticed that the results are identical. However, convergence issues were observed during the diffusion phase when CFL=20 was used. Therefore, a CFL number equal to 10 is considered independent.

Usually a CFL number value has its maximum at the release point and decays quickly with a distance from a release pipe, since the release inflow velocity is usually the highest in the computational domain and maximal near the release origin, but quickly drops with the

distance from the nozzle. The smaller the CFL number in a particular area of a domain, the better the resolution of the flow structures can be achieved in this area.

It should be pointed out, however, that for a given mesh the reduction of CFL number can only be accomplished through reduction of the time step, which can result in impractically long time required to complete simulation. Accordingly, a study had been performed within (Molkov and Shentsov, 2014) in order to assess the impact of CFL number on simulation accuracy. A comparison had been performed between the LES simulations of transitional flow release with Re=2863 and a large (90 x 18 cm) vent using the same mesh (Grid 2) but with significantly different CFL numbers (26 and 520). Figure 1.4-3 compares the experimentally measured steady-state concentrations at different heights within enclosure with the results of LES simulations with CFL=26 and CFL=520. It can be seen that the difference between two simulations is marginal and lies within 10% limit acceptable for hydrogen safety engineering. It can be noted, however, that the simulation with a higher CFL number did not reproduce the level of uniformity at the top layer of helium, predicting a steeper concentration distribution gradient near the ceiling, which can be considered a “cost” paid for the 20 times shorter simulation time of the simulation with large CFL number. In (Molkov and Shentsov, 2014) a CFL sensitivity study was also performed for the laminar model for a laminar flow release with Re=39. The laminar model found to be quite sensitive to the CFL number value. The results with CFL number equal to 26 gave unacceptable results not matching experimental data at all whereas CFL equal to 5.2 gave results with good agreement with the experiment.

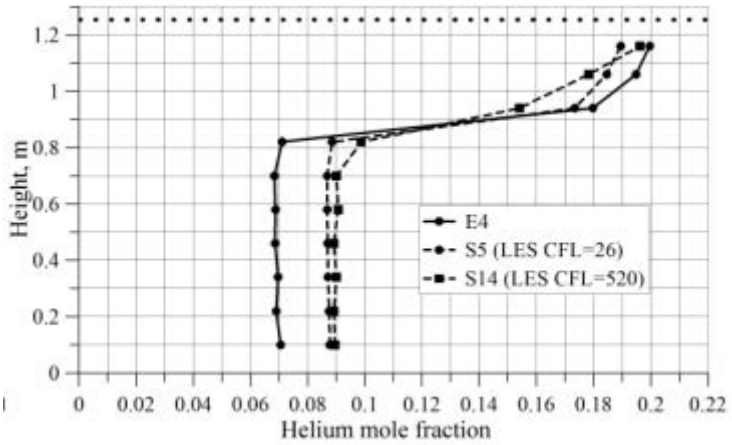

Figure 1.4-3. Comparison of experimentally measured steady-state concentrations at all 10 sensors locations (solid line marked E4 in the figure) with the results of simulations using LES model with CFL=26 (marked S5 in the figure) and CFL=520 (marked S14 in the figure).

Both explicit and implicit schemes can be of 1st or higher order of accuracy depending on the formulation. In either case, a time-step sensitivity study needs to be carried out in order to verify that the results are time-step independent. In RANS modelling, first-order accuracy can give good results whereas in LES modelling high-order time discretization should always be employed (for example see Giannissi et al., 2015).

The formulation of various temporal discretization schemes can be found in (Ferziger and Peric, 2002).

To sum up, the following guidelines regarding temporal discretization schemes should be followed:

- A time-step (or CFL) sensitivity study should be performed in order to ensure that the results are independent of time-step.
- In explicit formulation CFL<1 should be used. In implicit formulation the proper CFL choice is case-dependent. However, even in the implicit formulation case the CFL number should not be too large for numerical stability and accuracy.
- In RANS modelling 1st or higher order approaches could be used. In LES modelling only 2nd or higher order schemes should be used.
- An implicit formulation is preferred in simulations of large time duration and in simulations of large Reynolds number, in order to save computational time.

1.4.4 Convergence criteria

Hydrogen release and dispersion usually requires transient CFD simulations. In general, in transient simulations two type of convergence criteria are usually necessary:

- Convergence inside a single time-step, in order to move to the next one.
- Convergence of the iterative method for the solution of the system of equations (if the solver results in a system of equations and in the case that an iterative method is used for the system).

Regarding the convergence of the iterative method for the solution of the system of equations, a high-accuracy solution is usually required, especially for the solution of the pressure equation (in the case where the solver results in a pressure equation). In general, the default convergence criteria of the CFD code can be used with safety.

The main method to check the convergence of a time-step is to check if the values of the main variables (velocity components, hydrogen concentration, etc.) converge. To do this, a single representative number (error) should be computed for each variable. This number can be a type of norm of the variable, e.g. the maximum of the absolute values of the variable in the entire domain, the sum of the absolute values of the variable or the Euclidean norm. Different CFD codes may use different definitions for the error and as a result different criteria for convergence, i.e. how small the error needs to be in order to consider that the variable has been converged.

The user should always refer to the manual of the CFD code in order to understand the definition of the errors and the recommended maximum values for those errors. A sensitivity study for the maximum errors should be conducted in a representative problem in order to assess the accuracy of the calculations. Once the maximum errors have been determined in the representative problem, the same values can be used at similar simulations.

Besides the convergence of the flow main variables, the conservation of total mass, of hydrogen mass and of energy (in the case of non-isothermal flows) should be also checked. These conservations can be checked either globally (in the whole domain) or locally (inside each computational cell). Once again the user should advise the manual of the CFD code to see how these balances can be monitored.

A numerical inter-comparison exercise within the European Network of Excellence HySafe by Gallego et al. (2007) highlighted the problem of observed mismatch of hydrogen mass between the experiment and the simulations. This problem presumably affected the accuracy of calculations (after 1 min of hydrogen release in the experiment a long period of 250 min of

hydrogen “diffusion” was simulated). Analysis of simulations demonstrated that the hydrogen mass balance problem occurred when time step was too high. One of the conclusions of Gallego et al. (2007) study was the necessity of exercising close monitoring and control over mass balance of released gas during simulations.

Numerical simulation of a subsonic hydrogen release and dispersion in a large scale enclosure can require substantial (and potentially unaffordable) calculation time. This could result in an attempt to increase a simulation time step. Unfortunately, the increase of time step (and therefore CFL number) usually leads to decreased accuracy of simulation results. Another example of convergence control using monitoring of helium mass balance is given in Molkov and Shentsov (2014). A theoretical value of released helium mass, calculated by multiplication of the mass flow rate from the pipe by the release time was compared against a numerically integrated mass of a gas released in a simulation within a calculation domain calculated at each time step as

$$m_N(t) = m_d(t) + \sum \dot{m}_b(t) \cdot \Delta t\,, \tag{1.4.2}$$

where $m_N(t)$ is the total numerical integrated mass of gas released in simulation, $m_d(t)$ is the mass of gas in the domain at time t, $\dot{m}_b(t)$ is the mass flow rate of gas though the outflow boundary of the calculation domain, and Δt is the time step. Figure 1.4-4 shows comparison in time of the theoretical and the simulated values of released mass for one of the laminar simulation with CFL equal 5.2 performed within the study (Molkov and Shentsov, 2014).

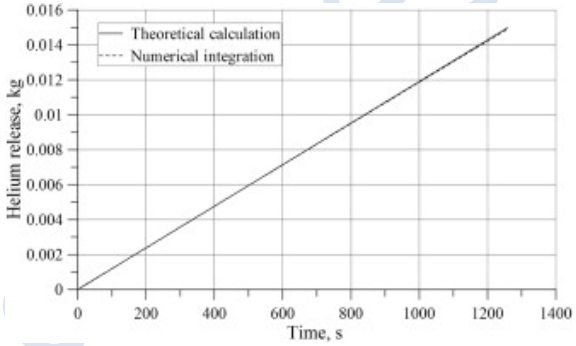

Figure 1.4-4. Simulated versus theoretical mass of released helium. Data for laminar simulation with CFL = 5.2. (Molkov and Shentsov, 2014).

The deviation of the simulated from the theoretical value was calculated as $\Delta m/m = (m_T - m_N)/m_T$ where m_T is the theoretical value. It can be seen to increase linearly (Figure 1.4-4) reaching its maximum of $\Delta m/m = 0.0055_T$ =0.0055, i.e. 0.55%, at the end of the simulation (at 1275 s). The value of the deviation depended on the specific simulation parameters and model used, reaching up to 1.7% in one of the simulations with CFL = 26. Simulation with CFL= 175 for laminar model exhibited maximum deviation of 5.6% at the end of simulation. At the same time a k-ε model in a simulation with CFL=178 gave a deviation of about 1.2% for the same physical duration of simulation. The computational time of the simulations varied for different models and release conditions from 52 days (deviation 5.6%) to 27 days (deviation 1.2%). This indicates accumulation of numerical error with increase of total time of simulations. LES simulations often exhibiting under-prediction of simulated helium mass compared to theoretical value, reaching values of 1.7, 1.9 and 2.2 % at the end of simulations with different conditions.

To sum up, the following guidelines regarding convergence criteria should be followed:

- The default maximum errors of the CFD code can be used. However it is good practice to perform a sensitivity analysis regarding convergence errors on a representative problem, in order to examine the desirable level of convergence for the target variables.
- Always refer to the manual of the CFD program in order to understand how the convergence criteria are defined.
- Always monitor the conservation of total mass balance, hydrogen mass balance and energy mass balance in order to ensure that you do not have mass or energy imbalance.
- Ensure that hydrogen mass fraction values are always bounded between 0 and 1.
- Ensure that turbulent kinetic energy k and turbulent dissipation ε are always positive.
- In the case where convergence is difficult to be achieved,
    - Reduce the time-step (or CFL number) and/or the under-relaxation factors.
    - Check the grid quality at the areas where convergence is difficult to be achieved.
    - Consider using different boundary conditions which comply better with the physics of the problem.

1.5 Analysis of the simulation results

1.5.1 Validation and sensitivity of the results

CFD validation is essential and it is undertaken by comparison of CFD results to reliable and appropriate experimental data or analytical solutions, if available. It is highly recommended that the user has validated their code/model against several experiments before using the code to perform any kind of study. It is significant that the code/model has been tested and validated in applications similar to those that the user would like to simulate, in order to assess the code performance and the range of inaccuracies that it provides.

The basic guidelines on validation are:

- For the validation process, the user should utilize data from experiments that have been performed under controlled conditions. At the beginning, start with simple test cases and then proceed with cases involving complex flows, i.e. external flows exposed to wind (where higher input data uncertainties are expected).
- The user should check elementary physical flow features. For example, the hydrogen mass balance should be satisfied, the temperature should not vary if the system is adiabatic and no work is added to the system, the velocity vectors should form a physical flow field etc.
- The measurements should be reliable and the experimental errors and inaccuracies should be reported. The quality of the experimental data in terms of both input data and output results should provide a satisfactory level of confidence. Moreover, it is significant that the monitoring variables (e.g. hydrogen concentrations) are measured at several points downwind and lateral to the release, in order to provide an image of the full (three dimensional) flow structure.

- If a model parameter is calibrated, in order to predict better a specific experiment, then this parameter should be used only in similar applications. For more generic use, a value of the model parameter should be found that provides good results for most of the cases and it is independent of the validation data set.
- The validation simulations should be carried out in accordance with the guidelines that this document provides. The CFD results for the validation process should be the independent ones (after performing the sensitive studies outlined in the above Sections).

More extensive analysis about the validation procedure of the model/code can be found in (SUSANA D4.2, 2016). In (SUSANA D4.2, 2016) the quantitative criteria for the model evaluation, the source and the level of uncertainties and approaches to treatment of uncertainty are reported. Moreover, some worked examples are presented and reference to other protocols that have been developed in the previous years is made.

As mentioned already several sensitivity studies (grid, domain, boundary conditions etc.) should be performed to ensure that prediction is unaffected by numerical errors. However, sensitivity studies on the input data for the simulations should also be carried out if there are uncertainties. In particular,

- In external flows the wind field (wind velocity, direction and turbulence) involves uncertainties. Sensitivity of the CFD results to the inlet wind field can be carried out.
- In liquid hydrogen releases the sensitivity of the CFD results on the hydrogen inlet boundary conditions that are applied based on isenthalpic or isentropic process can be conducted.
- In expanded or under-expanded releases the sensitivity of the CFD results on the release conditions should be checked. For instance, the effect of pipe losses on the pipe exit conditions can be tested, or the effect of resolving the flow inside the pipe before the hydrogen emerges into the domain.
- Check the effect of turbulence intensity at source on the results.
- In semi-confined releases and dispersion the effect of the wall thickness can be tested. Based on experience the wall thickness affects the predicted exchange flow rate through openings.
- All sensitivity studies should be based on experience of the fluid dynamics of the case under consideration. First, study the physical phenomenon and identify the parameters that are most likely to exhibit sensitivity on the results. The document D2.2 “Critical analysis and requirements to physical and mathematical models” (SUSANA D2.2, 2016) would help for the physical understanding of the flow in hydrogen applications.
- Because it is very time consuming to perform all the appropriate sensitivity studies in complex cases, the user can conduct them not for each particular application, but for some similar applications. The same modelling approach can then be used for the similar classes of applications.
- It is recommended to document the results of the sensitivity studies and show to what extent the CFD results depend or not on the parameter settings.

1.5.2 Interpretation of the results

The CFD results should be interpreted in terms of physical validity regardless the existence of experiment to be compared against or not. There are a wide variety of visualisation tools that can be used to interpret the numerical flow field. Dependent on the physics of the application under consideration several plots can be made. Experience with similar simulations is a good guide which plots to make. In hydrogen release and dispersion the basic options are:

- Plot the concentration and temperature contours (in non-isothermal applications) on the plane parallel with the release.
- Plot of the contours of concentration (and temperature) on cross-sections through the flow at several distances downwind the release point.
- In jet impingements, plot concentration contours on the solid surface (wall or ground) that the jet impacts on. The contour plots would help the user to check any unphysical behaviour, such as the butterfly effect that has been detected in jet impingement using low order numerical schemes (see Section 1.4.2).
- Plot the velocity vectors along solid surfaces, at the source and at regions where flow and vortices are expected, e.g. vents, around obstacles in order to detect any unphysical behaviour.
- Plot time series of the variables of interest (e.g. concentration) at several points downwind the release in unsteady flows. Check the trend of hydrogen distribution in the domain and check if it is in accordance to what it is physically expected. For instance, in releases inside closed facilities if the volumetric Richardson number is too small (see SUSANA D2.1, 2016) a homogeneous mixture is expected to be formed based on physics and experience.
- When experimental results are available a comparison of the concentration time series or the steady state concentration between simulation and experiment could also provide useful information. For instance, if the concentration is under-predicted at all sensors, then it is most likely that mass is lost; therefore, the mass error during simulations should be checked.
- Produce video sequences of unsteady simulations.
- Do not rely on one or two monitoring points for only one variable. The interpretation of the results should be performed by monitoring several points in the domain. Three dimensional plots would be also helpful.
- Check the concentration contours and the velocity vectors near open boundaries. This kind of plots could indicate if the domain is extended enough and if the appropriate boundary conditions are imposed.

2. Ignition and Jet fires

2.1 Introduction

Similarly to the turbulence modelling for non-reacting releases, a number of combustion models are available depending on the specifics of the case and phenomena to be modelled and available computational resources. The models most often used in practical applications for simulation of non-premixed (diffusion) combustion include:

- Eddy Break Up (EBU) model. The EBU model was originally proposed by Spalding (1971) and further developed by Mason and Spalding (1973). EBU represents an example of the so-called "mixed-burned" models. It assumes that the chemical kinetics rates are much faster than the flow rates, and the combustion rate is therefore determined by the turbulent mixing rate, delivering fresh reactants to the reaction zone. This model was later generalized by Magnussen and Hjertager (1976), who proposed using mean concentrations of intermittent quantities instead of concentration fluctuations used in the original Spalding model. This version of the model became known as Eddy Dissipation Model (EDM). The advantage of the EBU/EDM models lies in the simplicity of their implementation and relatively low computational cost. They have therefore become popular with engineering CFD models, particularly where large scale/long duration reacting flows are needed to be modelled, as the computational cost is often critical for these applications. Among the shortcomings of EBU type models is their inability to model a model a full range of physical phenomena associated with fires, e.g., flame lifting, and the limitation on their applicability to the flows where the reactions are fast and the system can be considered to be purely mixing limited. An additional feature of EBU type models is that due to their "mixed-burned" nature they do not require an artificial ignition source in order to initiate combustion, as the reaction starts as soon as both reactants mix (in the most software realisations).
- The Laminar Flamelet model is based on the view of a turbulent diffusion flame as an ensemble of stretched laminar flamelets proposed by Williams (1975). Flamelet equations based on the mixture fraction as independent variable, using the scalar dissipation rate for the mixing process, were independently derived by Peters (1980) and Kuznetsov (1982). Flamelets are thin reactive-diffusive layers embedded within an otherwise non-reacting turbulent flow field. Once ignition has taken place, chemistry accelerates as the temperature increases due to heat release. When the temperature reaches values that are of the order of magnitude of those of the close-to-equilibrium branch, the reactions that determine fuel consumption become very fast. Since the chemical time scale of this reaction is short, chemistry is active only within a thin layer. Flamelet models typically take intermediate place between EBU and EDC models in terms of both computational cost and the range of combustion phenomena they are able to accurately model. They allow better prediction of reaction rate and "intermediate" species, but not suitable for modelling of flame lift-off and underventilated combustion.
- The Finite Rate Chemistry model. This model is usually applied to situations where the chemical time scale is rate-limiting, requires fine mesh for resolution of flame front thickness (or adjustment of model constants) The most comprehensive combustion model describing whole range of combustion phenomena (including flame lifting, underventilated and self-extinguishing fires, production of intermediate

species, etc.). It is typically the most CPU-expensive model.

- The Eddy Dissipation Concept (EDC) model (not to be confused with EDM) was proposed by Magnussen (1981). It is based on the assumption that reaction occurs in small turbulent structures known as the fine scales. The EDC model can be coupled with detailed finite rate chemistry, providing a highly accurate tool for modelling of fires. The advantage of EDC model is its flexibility and ability to model wide range of physical phenomena, including, e.g., flame lifting and problems with chemical kinetics rate comparable with the flow rates. It is significantly more computationally expensive than the EBU or flamelet models listed above. The EDC model often requires artificial initiation of reaction through patching of ignition source in the reaction zone.

2.2 Selection of physical models

2.2.1 Conservation equations

The governing equations for turbulent combustion flows may be expressed in different forms; however, they normally are represented as transport equations for overall continuity, momentum and additional scalars that can be used to spatially- and temporally- resolve the thermodynamic state of the mixture (Echekki and Mastorakos, 2011). These equations are augmented by initial and boundary conditions, as well as constitutive relations for atomistic processes (e.g. reaction, molecular diffusion, equations of state). Therefore, in addition to density, transport equations for the evolving momentum and composition (e.g. mass or mole fractions, species densities or concentrations) and a scalar measure of energy (e.g. internal energy, temperature, or enthalpy). For illustration purposes, we present the compressible form of the instantaneous governing equations in non-conservative form for the mass density, momentum, species mass fractions and internal energy. A more detailed discussion on the various forms and their equivalence, especially for the energy equation can be found in the textbooks by Williams (1994) or Poinsot and Veynante (2011).

• Continuity

$$\frac{\partial \rho}{\partial t} + \nabla \cdot \rho \vec{u} = 0 \quad , \tag{2.2.1}$$

• Momentum

$$\rho \frac{D\vec{u}}{Dt} = \rho \frac{\partial \vec{u}}{\partial t} + \rho \vec{u} \cdot \nabla \vec{u} = -\nabla p + \nabla \cdot \tau + \rho \sum_{k=1}^{N} Y_k \vec{f}_k \quad , \tag{2.2.2}$$

• Species continuity (k=1,⋯,N)

$$\rho \frac{DY_k}{Dt} = \rho \frac{\partial Y_k}{\partial t} + \rho \vec{u} \cdot \nabla Y_k = \nabla \cdot (-\rho \vec{V}_k Y_k) + \omega_k \quad , \tag{2.2.3}$$

• Energy

$$\rho \frac{De}{Dt} = \rho \frac{\partial e}{\partial t} + \rho \vec{u} \cdot \nabla e = -\nabla \cdot \vec{q} - p \nabla \cdot \vec{u} + \tau \times \nabla \vec{u} + \rho \sum_{k=1}^{N} Y_k \vec{f}_k \cdot \vec{V}_k \quad , \tag{2.2.4}$$

In the above equations, ρ is the mass density; $\vec{u}$ is the velocity vector; p is the pressure; $\vec{f}_k$ is the body force associated with the k-th species per unit mass; τ is the viscous stress tensor; $\vec{V}_k$ is the diffusive velocity of the k-th species, where the velocity of the k-th species may be expressed as the sum of the mass-weighted velocity and the diffusive velocity, $\vec{u}+\vec{V}_k$; ω_k is the kth species production rate; e is the mixture internal energy, which may be expressed as $e=\sum_{k=1}^{N} h_k Y_k - p/\rho$; $\vec{q}$ is the heat flux, which represents heat conduction, radiation, and transport through species gradients and the Soret effect.

As can be seen, a number of terms in the governing equations are not explicitly expressed in terms of the solution vector and must rely on constitutive relations, equations of state or any additional auxiliary relations. These terms include expressions for the viscous stress, the species diffusive velocities, the body forces, the species reaction rate and the heat flux. The bulk of these terms have their origin in the molecular scales, and therefore, the role of constitutive relations is to represent them in continuum models. In fact, the use of constitutive equations is the first level of multiscale treatment for the modelling of turbulent combustion flows.

2.2.2 Turbulence modelling

All three main groups of turbulent models, RANS, LES and DNS are used in turbulent combustion modelling.

- DNS is usually considered prohibitively expensive for fire modelling, but is widely used in ignition modelling where its high accuracy presents a significant advantage. Also, the requirement for very fine mesh resolution can be met as high mesh fidelity is typically required for all types of ignition simulations for adequate modelling of ignition driving processes, such as shock heating. Due to the very high computational requirements DNS is restricted to 2-D problems.
- LES is widely used for both fire and ignition modelling, providing good accuracy and adequate modelling of physical processes with affordable computational costs. It is used in conjunction with a range of combustion models.
- RANS is often used for modelling of large scale fires and in the engineering problems requiring calculation of complex geometries and large computational domains using modest computational resources. It is used with a variety of combustion models including EBU, flamelet and EDC models.

2.2.3 Ignition modelling

A sudden release of hydrogen gas from a high pressure reservoir often leads to the so called spontaneous diffusion ignition phenomenon. Numerical modelling of hydrogen autoignition presents significant computational challenges. The consensus among researchers is presently turning toward shock heating as the primary cause of hydrogen spontaneous ignition, which means that numerical methods seeking to model autoignition have to be able to simulate shocks, small scale turbulent mixing and shock wave/vortex interactions. In practical terms it means that the ignition model would require a combination of highly resolved mesh with highly accurate numerical method. Many researchers sought to avoid prohibitively high

computational resources requirements by reducing problem to two or even one dimension, developing a diverse selection of models covering the full range from 1-D to fully 3-D.

1-D models have obvious limitations in terms of predictive power and are used primarily for phenomenological studies, such as evolution of the shock wave development following hydrogen release. An example of such approach can be found in (Maxwell and Radulescu, 2011).

2-D models, particularly developed for modelling of the axisymmetric geometry, provide an opportunity to perform simulations of more realistic release scenarios, which can be directly compared with experimental data. The importance of shock wave interaction and small scale turbulent mixture processes encouraged many researchers to choose a DNS approach, made possible by dramatic reduction of mesh size due to reduction of the problem to two dimensions. Despite this reduction, however, most DNS simulations of hydrogen autoignition utilize meshes with resolution on order of 15-20 μm with overall number of control volumes (CV) in millions or tens of millions and relatively small computational domains. DNS simulations usually use highly detailed chemical kinetics for modelling of combustion processes. An alternative approach is to utilize LES, which allows modelling of significantly larger and more complex geometries and reduces necessary computational resources. An example of such approach, using Implicit LES (ILES) is presented by (Xu et al., 2007). A shortcoming of all 2-D models, in addition to being inherently limited to simplified axi-symmetrical geometry, is compromised simulation of turbulence, which is an inherently 3-D phenomenon.

Fully 3-D approaches allow researchers to both capture the appropriate physics of turbulent mixing and to investigate more realistic geometries (e.g., T-shaped pressure relief device (PRD) simulated at University of Ulster (Bragin et al., 2013)). Since performing 3-D DNS would be prohibitively expensive, 3-D models LES with accurate combustion models, such as EDC plus detailed chemistry (Bragin et al., 2013) compensating for inevitably more coarse mesh. The following is the description of several representative examples of the various strategies of ignition modelling listed above:

The desire to obtain the most accurate result drove the development of DNS approaches, used, among others, in works by (Pinto et al., 2007), (Yamada et al., 2009), (Lee and Jeung, 2009). The very high computational cost of DNS, is driven by the very high resolution requirements necessary to resolve the Kolmogoroff scale which is inversely proportional to $Re^{3/4}$ (Dimotakis, 2005). Currently, therefore, these approaches are limited to 2-D simulations with relatively simple geometries. Furthermore, high-order numerical schemes designed for DNS (e.g. spectral or high-order finite-difference) are incapable of capturing shock containing flows due to Gibbs oscillations (Wen et al., 2009). It is impossible to fully resolve shocks with typical length scale of less than one micron in a macroscopic simulation.

Alternative approach was proposed by Xu and colleagues (Xu et al., 2007), (Wen et al., 2009), (Xu et al, 2009), (Xu and Wen 2012), opting to use implicit large eddy simulation (ILES) to solve the compressible Euler equations for supersonic turbulent mixing flows to avoid resolving all the spatial scales and small scale interactions. In LES, the large scale motions of turbulent flow are solved directly, while the effect of the unresolved smaller universal scales is modelled, significantly reducing computation requirements.

Following (Drikakis, 2003), Wen and colleagues argued that ILES is more suitable to simulate supersonic flows with shock waves than explicit LES. ILES is based on the hypothesis that the action of sub-grid scale (SGS) on the resolved scale is equivalent to a

strictly dissipative action. Therefore, no explicit SGS model is required in the ILES approach. Here the Navier–Stokes equations are implicitly filtered by the discretization and the implicit dissipative truncation error from the numerical scheme for the convection terms is regarded as an adaptive numerical dissipation to model the unresolved small scales in the same manner as an explicit sub-grid scale model in LES (Wen et al., 2009).

Although the LES approach utilized by (Xu et al., 2007) allowed significant reduction in computational cost, it remained sufficiently high to force the researchers to use a 2-D approximation of the problem, which remained significant limitation of the method. Wen (Wen et al., 2009) argued that for the ignition simulation, involving only the early stage of the jet leaving the tube, the turbulence is not yet fully developed and mainly generated by large scale flow development and shock interactions. The flow in this stage behaves more in a two-dimensional manner due to the large scale geometry-related flow development and dominance of large scale geometry-related turbulence which is less prone to 3-D vortex stretching, it is possible to reduce problem to 2-D formulation taking advantage of symmetric nature of the problem.

A mixture-averaged multi-component approach (Kee et al., 1989) was used for the calculation of molecular transport with consideration of thermal diffusion which is important for non-premixed hydrogen combustion. Although the diffusion flame was directly resolved, such ‘‘direct” approach was still classified as large eddy simulation as the flow field has not been fully resolved (Norris and Edwards, 1997). Due to the presence of strong under-expansion and shock/combustion interaction, a detailed chemistry allowing for the pressure dependent reaction rate is essential to accurately predict chemical reaction rates. For autoignition chemistry, Saxena and Williams’ detailed chemistry scheme (Saxena and Williams, 2007) which involves 21 elementary steps among eight reactive chemical species was used. The scheme was previously validated against a wide range of pressures up to 33 bar.

The 2-D approach used in previously described methods presents serious limitations for modelling realistic geometries of practical interest. Furthermore, it fails to capture the inherently three-dimensional nature of turbulence. For example, a recent DNS study of non-premixed flame extinction in a methane-air jet with reduced chemistry by Pantano (2004) using highly resolved mesh with nearly 100 million grid pointsdemonstrated that two-dimensional turbulence behaves differently from real three-dimensional turbulence where straining of vortices in the third direction is possible, leading to the existence of very small-scale turbulence (Pantano, 2004). Accordingly, the University of Ulster implemented a fully 3-D LES model of spontaneous ignition using eddy dissipation concept (EDC) model with detailed chemistry (Bragin and Molkov, 2009), (Bragin et al., 2013). The renormalization group (RNG) theory (Yakhot and Orszak, 1986) was used for the closure of turbulent terms in the filtered LES equations. The advantage of RNG models is that they are capable of reproducing not only turbulent, but also transitional and laminar flows. At low Reynolds numbers the effective viscosity becomes equal to molecular viscosity. This allows the model to perform better in the vicinity of walls (Shah et al., 2001). RNG calculates the effective viscosity μ_{eff} as

$$\mu_{eff} = \mu\left[1 + H\left(\mu_s^2\ \mu_{eff} / \mu^3 - 100\right)\right]^{1/3}, \tag{2.2.5}$$

where $\mu_s = \overline{\rho}\left(C_{RNG}\ V_{CV}^{1/3}\right)^2 \sqrt{2\widetilde{S}_{ij}\ \widetilde{S}_{ij}}$ and $H(x)$ is Heaviside function.

In highly turbulent regions of the flow where $\mu_{eff} \approx \mu_s$,the RNG model reduces to the Smagorinsky model, while in laminar flow regions the argument of the Heaviside function becomes negative and the model recovers molecular viscosity, $\mu_{eff} = \mu$. The effective Prandtl and Schmidt numbers are calculated following the RNG theory by purely theoretical equations (Yakhot and Orszak, 1986)

$$\left|\frac{1/N_{eff} - 1.3929}{1/N - 1.3929}\right|^{0.6321} \left|\frac{1/N_{eff} + 2.3929}{1/N + 2.3929}\right|^{0.3679} = \frac{\mu}{\mu_{eff}}, \tag{2.2.6}$$

where N stands for laminar Prandtl or Schmidt numbers. Laminar Prandtl and Schmidt numbers are calculated according to kinetic theory.

The University of Ulster model used the EDC model (Magnussen, 1981) with updates incorporating detailed Arrhenius chemical kinetics in turbulent flames as the combustion sub-model. The EDC model gives an expression for a combustion rate based on an assumption that chemical reactions occur in the small scale structures on the Kolmogorov's scale where the dissipation of turbulence energy takes place.

In the EDC model a source term in the species transport equation is modelled as

$$R_m = \frac{\rho(\xi^*)^2}{\tau^*\left[1-(\xi^*)^3\right]}\left(Y_m^* - Y_m\right), \tag{2.2.7}$$

where R_m is a net rate of production of specie m by chemical reactions, ξ^* is the length fraction of the fine scale turbulent structures where the reaction occurs, Y_m^* is the fine scale species mass fraction (specie m) after reacting over the time τ^*, Y_m is a species mass fraction for specie m in the surrounding fine scales state. The multiplier in (2.2.7) with a square of the length fraction of fine scales represents the mass exchange between the surrounding and fine structure regions. The length fraction of fine structures is evaluated in this LES model is similar to EDC RANS model as

$$\xi^* = C_\xi u_\eta / u_{SGS}, \tag{2.2.8}$$

where the volume fraction constant is taken as C_ξ = 2.1377 similar to RANS. The upper limit ξ^* = 1 is applied when the fine scales velocity is larger than residual SGS velocity.

The scale of a LES residual velocity at the sub-grid scale (SGS) level is

$$u_{SGS} = \mu_t / (\rho \cdot L_{SGS}), \tag{2.2.9}$$

where μ_t is turbulent viscosity, and the SGS length scale is determined as

$$L_{SGS} = C_{RNG} V^{1/3}. \tag{2.2.10}$$

The Kolmogorov's velocity u_η is

$$u_\eta = \left(\frac{\mu \cdot u_{SGS}^3}{\rho \cdot L_{SGS}}\right)^{1/4}, \tag{2.2.11}$$

where μ is laminar viscosity.

Characteristic sub-grid eddy and Kolmogorov's timescales are respectively

$$\tau_{SGS} = L_{SGS} / u_{SGS}, \text{ and} \tag{2.2.12}$$

$$\tau_{\eta} = \left(\frac{\mu \cdot L_{SGS}}{\rho \cdot u_{SGS}^3} \right)^{1/2}, \tag{2.2.13}$$

The volume fraction of the fine scales is calculated as ξ^{*3} and species are assumed to react in the fine structures over a time scale

$$\tau^* = C_{\tau} \tau_{\eta}, \tag{2.2.14}$$

where a time scale constant is taken equal to C_{τ} = 0.4082 similar to that in the EDC RANS model.

Magnussen (Magnussen, 1989) assumes that all the fine scales in the cell are perfectly stirred reactors with a residence time τ^*. Combustion at the fine scales is assumed in this model to take place as a constant-pressure reactor. The reactor type is determined by the choice of a mixing rate $1/\tau^*$ and a time-step Δt. The initial conditions at the constant pressure reactor are taken as the current species and temperature in the cell. Arrhenius reactions governed by equation (2.2.15) proceed over the time scale τ^*.

All of the reactions considered in the chemical mechanism involved are elementary (reversible). For reversible reaction the molar rate of creation or destruction of species *i* in reaction *r* is given by equation (2.2.15)

$$\hat{R}_{m,R} = \Gamma \left(\nu''_{m,r} - \nu'_{m,r} \right) \left(k_{f,r} \prod_{n=1}^{N} \left[C_{n,r} \right]^{\nu'_{m,r}} - k_{b,r} \prod_{n=1}^{N} \left[C_{n,r} \right]^{\nu''_{m,r}} \right), \tag{2.2.15}$$

where N is number of chemical species in the system; $\nu'_{m,r}$ is stoichiometric coefficient for reactant m in reaction r; $\nu''_{m,r}$ is stoichiometric coefficient for product m in reaction r; $k_{f,r}$ is forward rate constant for reaction r; $k_{b,r}$ is backward rate constant for reaction r. Γ represents the net effect of third bodies on the reaction rate and is given by

$$\Gamma = \sum_{n=1}^{N} \gamma_{n,r} C_n, \tag{2.2.16}$$

where $\gamma_{m,r}$ is the third-body efficiency of m-th species in the r-th reaction.

The forward rate constant for reaction r without pressure dependency is computed in conventional form of Arrhenius equation

$$k_{f,r} = A T^{\beta_r} \exp\left(-E_r / RT \right). \tag{2.2.17}$$

All reactions are reversible, the backward rate constant for reaction r is calculated from the forward rate (2.2.17) and the equilibrium constant K_r using the equation

$$k_{b,r} = k_{f,r} / K_r. \tag{2.2.18}$$

The equilibrium constant K_r computed as

$$K_r = \exp\left(\frac{\Delta S_r^0}{R} - \frac{\Delta H_r^0}{RT}\right) \cdot \left(\frac{P_{atm}}{RT}\right)^{\sum_{i=1}^{N}\left(\nu''_{m,r} - \nu'_{m,r}\right)}, \quad (2.2.19)$$

where P_{atm} denotes atmospheric pressure (101,325 kPa). The term within the exponential function represents the change in Gibbs free energy and its components are computed as

$$\frac{\Delta S_r^0}{R} = \sum_{i=1}^{N}\left(\nu''_{m,r} - \nu'_{m,r}\right)\frac{S_m^0}{R}, \quad (2.2.20)$$

$$\frac{\Delta H_r^0}{RT} = \sum_{i=1}^{N}\left(\nu''_{m,r} - \nu'_{m,r}\right)\frac{h_m^0}{RT}, \quad (2.2.21)$$

where S_m^0 and h_m^0 are entropy and enthalpy respectively of the m-th species respectively evaluated at temperature T and atmospheric pressure.

Specific heats of mixtures were approximated as piecewise-polynomial functions of temperature with polynomial coefficients calculated according to mass-weighted mixing law.

University of Ulster self-ignition model (Bragin et al., 2013) utilized the detailed 21-step chemical reaction mechanism of hydrogen combustion in air employing 37 elementary reactions is applied (Gutheil et al, 1993). The effect of nitrogen chemistry is taken into account by considering detailed mechanism of nitrogen oxide (NO) formation. The specific reaction rate constants are given in Table 2.2-1. The forward reaction rate constants are presented in the table, and backward rates for reversible reactions are calculated through the equilibrium constants.

Table 2.2-1. Specific reaction rate constants (Gutheil et al., 1993).

No.	**Reactions**	***A*, KJ/mol**	***β*r,**	***E*r, mol/m^3**
1	H+O2=OH+O	2.00E+14	0.00	70.30
2	H2+O=OH+H	1.80E+10	1.00	36.93
3	H2O+O=OH+OH	5.90E+09	1.30	71.25
4	H2+OH=H2O+H	1.17E+09	1.30	15.17
5	H+O2+M=HO2+M	2.30E+18	-0.8	0.00
	Third-body chaperon efficiencies H2/1./ H2O/6.5/ O2/0.4/ N2/0.4/			
6	H+HO2=OH+OH	1.50E+14	0.00	4.20
7	H+HO2=H2+O2	2.50E+13	0.00	2.93
8	OH+HO2=H2O+O2	2.00E+13	0.00	4.18
9	H+H+M=H2+M	1.80E+18	-1.00	0.00
	Third-body chaperon efficiencies H2/1./ H2O/6.5/ O2/0.4/ N2/0.4/			
10	H+OH+M=H2O+M	2.20E+22	-2.00	0.00

	Third-body chaperon efficiencies H2/1./ H2O/6.5/ O2/0.4/ N2/0.4/			
11	HO2+HO2=H2O2+O2	2.00E+12	0.00	0.00
12	H2O2+M=OH+OH+M	1.30E+17	0.00	190.38
13	H2O2+OH=H2O+HO2	1.E+13	0.00	7.53
14	O+HO2=OH+O2	2.E+13	0.00	0.00
15	H+HO2=O+H2O	5.E+12	0.00	5.90
16	H+O+M=OH+M	6.2E+16	-0.60	0.00
	Third-body chaperon efficiencies H2O:5, others 1			
17	O+O+M=O2+M	6.17E+15	-0.50	0.00
18	H2O2+H=H2O+OH	1.E+13	0.00	15.02
19	H2O2+H=HO2+H2	4.79E+13	0.00	33.26
20	O+OH+M=HO2+M	1.E+16	0.00	0.00
21	H2+O2=OH+OH	1.7E+13	0.00	200.0
	Nitrogen Chemistry			
22	O+N2=N+NO	1.82E+14	0.00	319.02
23	O+NO=N+O2	3.8E+09	1.00	173.11
24	H+NO=N+OH	2.63E+14	0.00	210.94
25	NO+M=N+O+M	3.98E+20	-1.50	627.65
26	N2+M=N+N+M	3.72E+21	-1.60	941.19
27	N2O+O=NO+NO	6.92E+13	0.00	111.41
28	N2O+O=N2+O2	1.E+14	0.00	117.23
29	N2O+N=N2+NO	1.E+13	0.00	83.14
30	N+HO2=NO+OH	1.E+13	0.00	8.31
31	N2O+H=N2+OH	7.6E+13	0.00	63.19
32	HNO+O=NO+OH	5.01E+11	0.50	8.31
33	HNO+OH=NO+H2O	1.26E+12	0.50	8.31
34	NO+HO2=HNO+O2	2.E+11	0.00	8.31
35	HNO+HO2=NO+H2O2	3.16E+11	0.50	8.31
36	HNO+H=NO+H2	1.26E+13	0.00	16.63
37	HNO+M=H+NO+M	1.78E+16	0.00	203.7

2.2.4 Jet fire modelling

Jet fire modelling presents a different set of challenges compared to ignition modelling. Unconfined fires with velocities below 100 m/s (M<0.3) are typically modelled using incompressible approaches since the pressure variation is usually negligible compared to atmospheric pressure.

While typically presenting less stringent requirements for very high fidelity resolution and accurate handling of strong shocks, jet fires, particularly originating from under-expanded jets, often present a problem with a very wide range of scales. Indeed, on one hand the release origin is typically measured in millimetres, and in case of under-expanded supersonic release may require large number of CV across the nozzle to properly capture flow dynamics and shock structure. On the other hand, jet fires often extend for many meters of tens of meters, requiring employment of a very large domain. DNS approach would require excessive computational resources to be practical, and therefore jet fires are usually modelled using LES or RANS approaches. It should be noted that practically all combustion occurs at subgrid scales, since there are practically no resolved combustion reactions. This means that in fire modelling using LES, combustion modelling depends almost entirely on SGS modelling (Pope, 2004).

Modelling of jet fires can be performed using a wide range of combustion models, from simplified EBU/EDM to flamelet and EDC with detailed chemistry, depending on a problem conditions and requirements. More precise models such as EDC can provide more accurate modelling of physical phenomena at the expense of significantly larger computational requirements. The choice of the combustion model should also be determined by specific phenomena to be modelled. EBU is primarily limited to modelling of well-ventilated fires. It is not suitable for simulation of phenomena such as flame lift-off fires due to its underlying assumption of chemical rates being much faster than the mixing/flow rates. The flamelet approach provides slightly better treatment of chemistry. Accurate modelling of underventilated fires requires inclusion of consideration of chemical kinetics (Molkov et al., 2014).

The following is a description of three characteristic simulations conducted at University of Ulster illustrating utilization of a wide range of models, including EBU, EDC and probability density function (PDF)/flamelet combustion models and LES and RANS numerical approaches.

The Eddy Break-Up (EBU) combustion model (Magnussen and Hjertager, 1976) was employed for combustion modelling of under-expanded round and plane jets performed at University of Ulster (Makarov and Molkov, 2013a). Simulation of the under-expanded jets in unconstrained environment necessitated utilization of a large scale domain. Accordingly, to reduce computational costs, less demanding RANS $k-\varepsilon$ turbulence model and EBU combustion model had been selected for this simulation.

In the EBU model the hydrogen source term (mass burning rate per unit volume) was modelled as

$$S_{H_2} = -C\bar{\rho}\frac{\bar{\varepsilon}}{k} = \min\left\{\tilde{Y}_{H_2}, \frac{\tilde{Y}_{O_2}}{s}\right\}, \qquad (2.2.22)$$

where $C = 4.0$ is the empirical coefficient, $\tilde{Y}_{H_2}$ is the mass fraction of hydrogen, $\tilde{Y}_{O_2}$ is the mass fraction of oxygen and $s = 8.0$ is the stoichiometric coefficient for hydrogen–oxygen

reaction. Symbol “overbar” here stands for Reynolds averaged parameters and “tilde” for Favre averaged parameters.

The EBU combustion model assumes that the reaction rate is infinitely fast and combustion is controlled by turbulent mixing only, hence it is unable to predict, for example, the lift-off of turbulent flames. In this simulation, however, the focus was on the prediction of axisymmetric and plane turbulent nonpremixed flame lengths, and the relatively insignificant effect of lift-off on the jet flame length had been neglected. Indeed, the observed flame length reached 1.0 – 2.6 m (Mogi and Hariguchi, 2009) while the lift-off distance of hydrogen flames is not more than 0.08 m (Mogi et al., 2005a).

Flamelet/Probability Distribution Function (PDF) model provides a more universal alternative to the EBU approach at the expense of higher computational cost. An example of mixture fraction/PDF model application to fire modelling is provided in (Brennan et al., 2009). This study was aimed at the modelling of the large scale high pressure under-expanded hydrogen-jet flame. The simulation uses Very Large Eddy Simulation (VLES) version of LES approach, better suited to modelling of non-stationary release (blowdown) than RANS, coupled with mixture fraction/PDF combustion model using a pre-calculated flamelet library.

The flamelet model takes advantage of the hierarchy problem appearing in turbulent combustion, namely, the fact that on one hand, the turbulence structures cover a spectrum of scales and, on the other hand, the typical thickness of a flame is on the low end of that spectrum. This hierarchy decouples the mixing of the species that is operated by the turbulent cascade from the chemistry that happens exclusively in the flame. The above section on the diffusion flame solution has illustrated this through a typical relationship:

$$\dot{\omega} = \rho\chi \frac{d^2T}{dZ^2}, \tag{2.2.23}$$

where Z – mixture fraction, which may be seen as relative fuel concentration, i.e. Z=1 in the fuel stream and Z=0 in oxidiser stream. This explains that the reaction rate is determined by contributions coming from different hierarchies: the turbulent mixing ($\rho\chi$), and the reaction occurring in the structure of the flame $\frac{d^2T}{dZ^2}$, (the profile of T versus Z is completely linked to the chemistry and its strength).

The simulation uses LES with larger than the grid size flow features solved explicitly, whereas flow structures which are smaller than the grid size (e.g., sub-grid scale, SGS) are modelled. The Lilly (1992) dynamic SGS model is used for the closure of turbulence terms in (Brennan et al., 2009). Rather than solving conservation equation for each species a mixture fraction approach is used (Bilger, 1976). The approach is based on the assumption that the diffusivity of all species is equal. It allows simplification of calculations by decoupling simulation of the flow and complex reaction chemistry. The mixture fraction is introduced as:

$$Z = \frac{sY_F - Y_o + Y_o^0}{sY_F^0 + Y_o^0}, \tag{2.2.24}$$

where Y_F^0 and Y_o^0 are the mass fractions of fuel in the pure fuel stream and oxidizer in the pure oxidizer stream respectively, Y_F and Y_o are the values at the position Z as calculated, s is the mass stoichiometric ratio and $s = \left(Y_o / Y_F\right)_{st}$ at stoichiometric conditions. It can be shown (Poinsot and Veynante, 2005) that the species equations can be replaced by a single

conservation equation for the mixture fraction Z with no source term (hence Z is a conserved scalar). The unfiltered equation for the mixture fraction is:

$$\frac{\partial \rho Z}{\partial t} + \frac{\partial}{\partial x_j}(\rho u_j Z) = \frac{\partial}{\partial x_j}\left(\rho D \frac{\partial Z}{\partial x_j}\right), \tag{2.2.25}$$

where ρD denotes the molecular diffusion. The filtered transport equation for the mixture fraction is:

$$\frac{\partial \overline{\rho}\overline{Z}}{\partial t} + \frac{\partial}{\partial x_j}(\overline{\rho u}_j \overline{Z}) = \frac{\partial}{\partial x_j}\left(\overline{\rho D}\left(\frac{\partial \overline{Z}}{\partial x_j}\right)\right), \tag{2.2.26}$$

In the case of chemical equilibrium (assumption of infinitely fast chemistry) all thermo-chemical scalars i.e. the species fractions, density, and temperature depend solely on the instantaneous mixture fraction. If the chemistry is not infinitely fast, and instead occurs in a very narrow reaction zone, then assumptions must be made about the turbulent flame structure so that temperature and species concentration may be calculated.

In Brennan et al., (2009), the laminar flamelet approach, which is well developed for application to non-premixed flames (see, e.g., Peters, 1986), was used. The approach assumes that the turbulent flame brush can be approximated as a system of instantaneous laminar flamelets, where species concentrations and temperature are described as a function of mixture fraction (Poinsot and Veynante, 2005). The flamelet equations solved are as follows (Poinsot and Veynante, 2005):

$$\rho \frac{\partial Y_k}{\partial t} = \dot{\omega}_k + \frac{1}{2}\rho\chi \frac{\partial^2 Y_k}{\partial Z^2}, \tag{2.2.27}$$

$$\rho \frac{\partial T}{\partial t} = \frac{1}{2}\rho\chi \frac{\partial^2 T_k}{\partial Z^2} - \frac{1}{c_p}\sum_k H_k \dot{\omega}_k + \frac{1}{2c_p}\rho\chi\left[\frac{\partial c_p}{\partial Z} + \sum_k c_{p,k}\frac{\partial Y_k}{\partial Z}\right]\frac{\partial T}{\partial Z}, \tag{2.2.28}$$

where $\chi = 2D\left(\partial Z/\partial x_j\right)^2$ is scalar dissipation representing the flame stretch. The scalar dissipation varies along the axis of the flamelet and the inverse of χ can be interpreted as the characteristic diffusion time across the flame. In adiabatic systems the laminar flamelets are completely parameterised by χ_{st} (value of flame stretch at flame location) and Z, and can hence be used to determine instantaneous values of species mass fraction and mixture temperature. The density-weighted mean species mass fractions and temperature can then be determined from the probability density function (PDF) of χ_{st} and Z (described below), therefore for adiabatic cases the energy equation is not solved explicitly at each time step.

The effect of turbulence on the chemistry should be accounted for. PDF approach is used here as a closure model for these effects. The averaged values of species mass fraction, temperature and density are a function of both their instantaneous values and the joint PDF of Z and χ_{st}:

$$\overline{\phi}_i = \iint p(Z,\chi_{st})\phi(Z,\chi_{st})dZd\chi_{st}, \tag{2.2.29}$$

where $\overline{\phi}_i$ represents the averaged value of ϕ_i which can be the species mass fraction or temperature. The shape of the PDF needs to be specified in order to determine the local mean

fluid state at all points in the flow field. The PDF describes SGS temporal fluctuations in the properties which are obtained from the flow field, i.e. the mixture fraction and the scalar dissipation. Z and χ_{st} are assumed to be statistically independent and so there are separate PDF functions for each. In practice this PDF is unknown and is modelled as a mathematical function that approximates the actual PDF shapes that have been observed experimentally. Equation (2.2.29) can therefore be rewritten as:

$$\bar{\phi}_i = \iint p(Z)\, p(\chi_{st})\phi(Z,, \chi_{st}) dZ d\chi_{st} . \tag{2.2.30}$$

In practice $p(Z)$ is unknown and must be modelled based on experimentally observed PDF shapes. The sub filter PDF of a conserved scalar can be approximated by a beta function (Richardson, Howard and Smith, 1952). The b-function PDF is a function of Z and its SGS variance Z

$$p(Z) = \frac{Z^{\alpha-1}(1-Z)^{\beta-1}}{\int Z^{\alpha-1}(1-Z)^{\beta-1} dZ}, \tag{2.2.31}$$

where $\alpha = \bar{Z}\left[\left(\bar{Z}(1-Z)/Z'^2\right)-1\right]$, $\beta = \left(1-\bar{Z}\right)\left[\left(\bar{Z}(1-Z)/Z'^2\right)-1\right]$, and $\overline{Z'^2}$, the mixture fraction variance, is modelled using

$\overline{Z'^2} = C_{\text{var}} L_s^2 \left|\nabla \bar{Z}\right|^2$ where C_{var} is computed dynamically in the same way as C_s, and $L_s = \min(kd, C_s V^{1/3})$.

Brennan et al. (2009) used Fluent as a CFD engine, which implementation of the flamelet model ignored fluctuations in χ_{st} so that the PDF of χ is a delta function $p(\chi) = \delta(\chi - \bar{\chi})$. The mean scalar dissipation $\overline{\chi_{st}}$ was modelled using formula $\overline{\chi_{st}} = C_\chi(\mu_t + \mu/\rho\sigma_t)\left|\nabla Z\right|^2$ where $C_\chi = 2$.

Numerical investigation of the different regimes of hydrogen non-premixed combustion in an enclosure (Molkov et al., 2014) utilized a combination of the Reynolds averaged Navier-Stokes (RANS) model with the eddy dissipation concept (EDC) combustion model coupled with the 18-step reduced chemical mechanism. Simulation covered several distinct flame regimes including well ventilated (Figure 2.2-1) and under ventilated external fire (Figure 2.2-2).

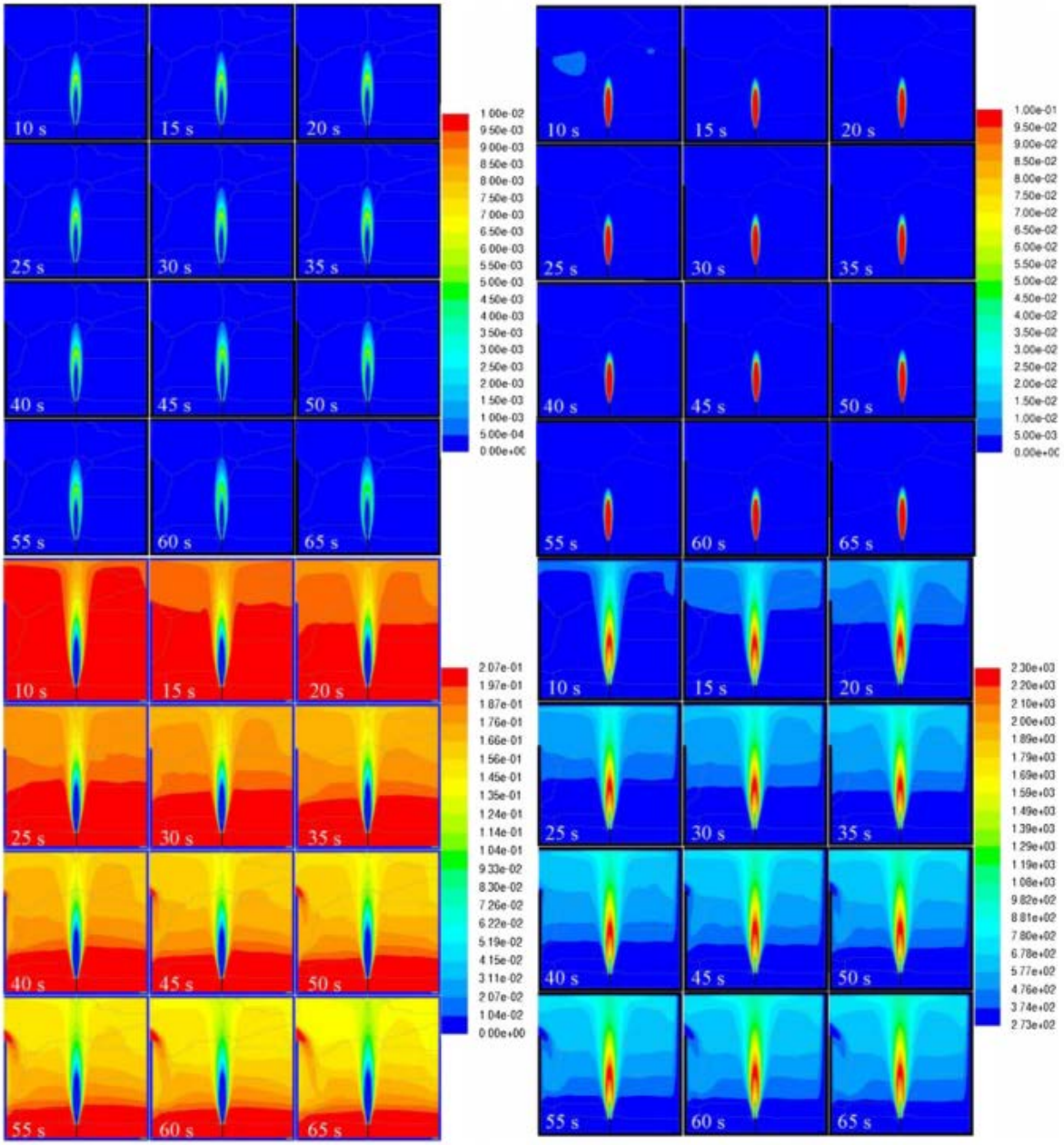

Figure 2.2-1. Mole fractions of OH (top left), H_2 (top right), O_2 (bottom left), and temperature (bottom right) in a 2D slice along the enclosure centre-line in simulation of well-ventilated fire (Molkov et al., 2014).

The model was based on the renormalization group (RNG) k-ε turbulence model (Yakhot and Orszag, 1986), (Orszag et al., 1993). The main difference between the RNG and standard k-ε model lies in the additional term in the ε equation given by

$$R_\varepsilon = \frac{C_\mu \rho \eta^3 (1-\eta/\eta_0)}{1+\beta\eta^3}\frac{\varepsilon^2}{k}, \qquad (2.2.32)$$

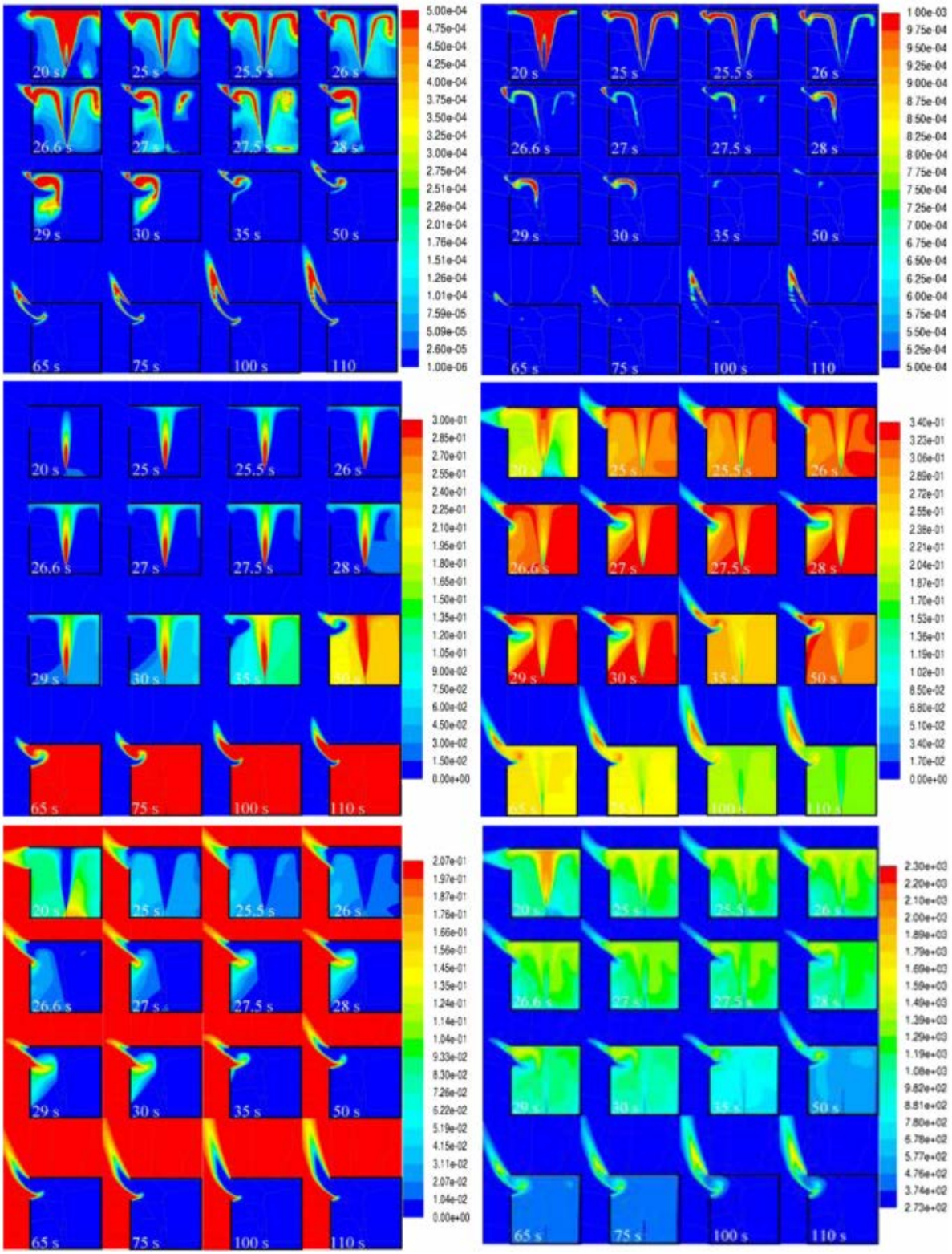

Figure 2.2-2. Mole fractions of OH in the range 1E-06 ~ 5E-04 (top left) and OH in the range $5 \cdot 10^{-4}$ ~ $1 \cdot 10^{-3}$ (top right), H_2 (middle left), H_2O (middle right), O_2 (bottom left) and temperature (bottom right) in a 2D slice along the enclosure centre-line in simulation of under ventilated fire resulting in the external flame (Molkov et al., 2014).

with $\eta = S\frac{k}{\varepsilon}$, $\eta_0 = 4.38$ and $\beta = 0.012$ where k is the turbulence kinetic energy, ε is the turbulent energy dissipation rate, S is mean rate of strain tensor $S = \sqrt{2S_{ij}S_{ij}}$, $C_\mu = 0.0845$ and $\beta = -(\partial\rho/\partial T)/\rho$ is the expansion coefficient.

EDC combustion model (Magnussen, 1981) is similar to the one described in the ignition section, supplemented with the 18-step reduced chemical reaction mechanism of hydrogen combustion in air that is a subset of the Peters and Rogg's mechanism (Peters and Rogg, 1993) that excludes H_2O_2 formation and consumption is applied taking into account the conclusion of (Fairweather and Woolley, 2003) as well. Indeed, for the reactants at room temperature and not very large pressures up to 4 MPa, the H_2O_2 concentration is very low and does not play an important role in the structure of the flame (Trevino and Mauss, 1993). The reduced mechanism counts eight reactive species (H_2,O_2, H, O, OH, HO_2, H_2O, N_2). The effect of nitrogen chemistry is not taken into account and nitrogen plays a role of the third body only. The forward reaction rate constants are presented in Table 2.2-2, and backward rates for reversible reactions are calculated through the equilibrium constants.

Table 2.2-2. Specific reaction rate constants (Peters and Rogg 1993)

No.	Reactions	A_r *	β_r	E_r, kJ/mol
H_2/O_2 Chain Reactions				
1	O2+H=OH+O	2.00E+14	0.00	70.30
2	OH+O=O2+H	1.568E+13	0.00	3.52
3	H2+O=OH+H	5.06E+04	2.67	26.30
4	OH+H=H2+O	2.222E+04	2.67	18.29
5	H2+OH=H2O+H	1.00E+08	1.60	13.80
6	H2O+H=H2+OH	4.312E+08	1.60	76.46
7	OH+OH=H2O+O	1.5E+09	1.14	0.42
8	H2O+O=OH+OH	1.473E+10	1.14	71.09
HO_2 Formation and Consumption				
9	O2+H+M=HO2+M	2.3E+18	0.80	0.00
	Third-body chaperon efficiencies H2O/6.5/ O2/0.4/ N2/0.4/			
10	HO2+M=O2+H+M	3.19E+18	-0.80	95.39
	Third-body chaperon efficiencies H2O/6.5/ O2/0.4/ N2/0.4/			
11	HO2+H=OH+OH	1.5E+14	0.00	4.20
12	HO2+H=H2+O2	2.5E+13	0.00	2.90
13	HO2+OH=H2O+O2	6.E+13	0.00	0.00
14	HO2+H=H2O+O	3.E+13	0.00	7.20
15	HO2+O=OH+O2	1.8E+13	0.00	-1.70

Recombination Reactions				
16	H+H+M=H2+M	1.8E+18	-1.00	0.00
	Third-body chaperon efficiencies H2O/6.5/ O2/0.4/ N2/0.4/			
17	OH+H+M=H2O+M	2.2E+22	-2.00	0.00
	Third-body chaperon efficiencies H2O/6.5/ O2/0.4/ N2/0.4/			
18	O+O+M=O2+M	2.9E+17	-1.00	0.00
	Third-body chaperon efficiencies H2O/6.5/ O2/0.4/ N2/0.4/			

* - the units for $\boldsymbol{A_r}$ are $\left[cm^3/\left(mol\times\sec\times K^{\beta_r}\right)\right]$ and $\left[cm^6/\left(mol^2\times\sec\times K^{\beta_r}\right)\right]$ for bi-molecular and tri-molecular reactions respectively.

2.3 Problem setup

2.3.1 Domain design

Development of the domain for ignition and fire modelling typically involves designing an appropriate geometry for subsequent meshing, identification and positioning of appropriate boundaries. For problems involving release of reacting gas into the ambient atmosphere (since majority of ignition and fire simulations concern phenomena occurring either in open air or in a vented enclosure), it is important to include sufficient expanse of ambient atmosphere into the domain design to prevent undesirable impact of outer boundary conditions on the numerical solution. Modelling of the fire in the enclosure typically requires addition of external domain outside of the openings in order to ensure proper boundary conditions (typically defined in terms of gauge pressure P=0). It is recommended to remove the "far field" boundary to a distance up to two characteristic sizes of the fire enclosure. While removal of the outer boundaries to a large distance from the main simulation area of interest may significantly increase computational costs in areas where no phenomena of interest take place, the experience of numerical simulations of both ignited and unignited releases performed at the University of Ulster emphasizes the advisability to remove the ambient boundary as far as practically possible from the release origin/vent location. Following is the description of problem setup and domain design of several representative problems.

2.3.1.1 Ignition problems

Numerical simulation of autoigniton utilizing DNS required implementation of a finely resolved grid, restricting the complexity and scale of domain extent. The simulation domain of Yamada and colleagues (2009) consisted of a section of the pipe extending from a high pressure tank, opening into ambient air (Figure 2.3-1). The radius of the external domain was approximately equal to 3 pipe radii and the far boundary was located at the distance 1.25 pipe lengths from the pipe end. The domain was assumed to be symmetrical in respect to the pipe centreline. Figure 2.3-2 illustrate computational domain used by Lee and Jeung (2009). In this case the entire domain consisted of a single pipe with regions initially containing hydrogen and air separated by a hemispherical membrane. The length of the upstream tube is arbitrarily

chosen to be half of the downstream length, which is sufficient for the present simulation, since an expansion wave moves only to the left-hand side and does not affect the rest of the domain. Once again only half of the pipe was simulated with symmetry conditions assumed at the pipe centreline.

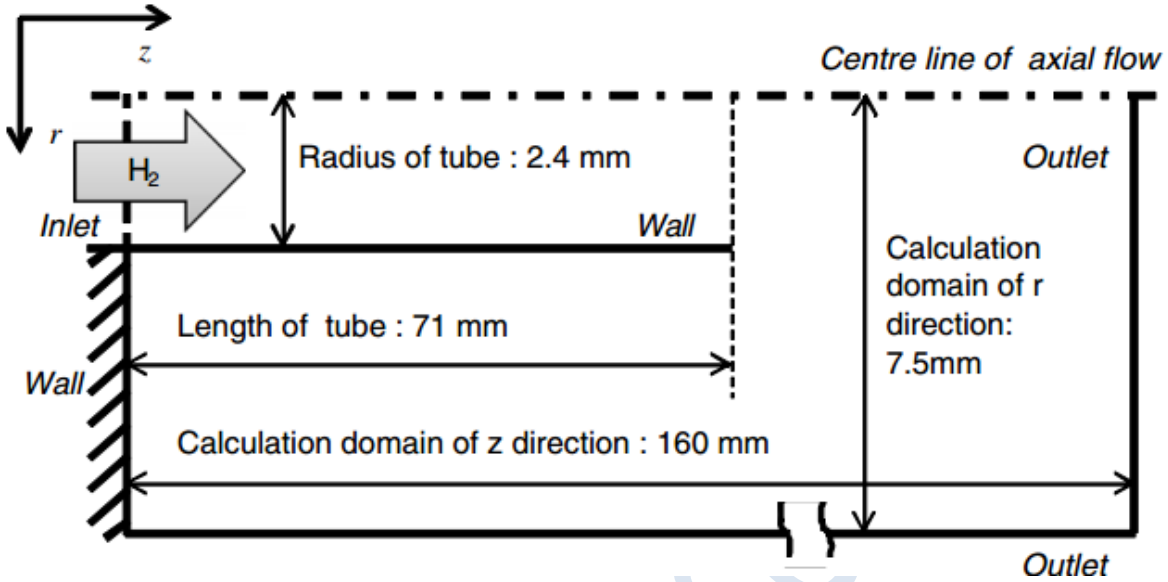

Figure 2.3-1. Scheme of computational domain used by Yamada et al. (2009).

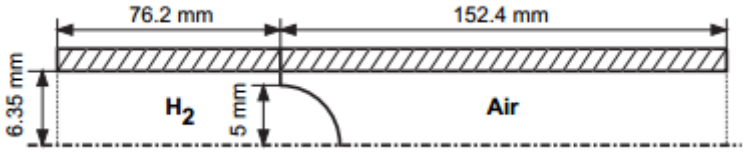

Figure 2.3-2. Scheme of computational domain employed by Lee and Jeung (2009).

The ILES model introduced in (Xu et al., 2007a) had been applied to three different types of autoignition problems. The first type (Xu et al., 2008), (Xu et al., 2009a), (Xu et al., 2009b), (Xu et al., 2011) investigate various aspects of the hydrogen release through a hole in the tank (Figure 2.3-3). It is composed of three cylindrical regions: pressurized cylinder, release hole on the cylinder wall and ambient environment. To mimic the rupturing process of the pressure boundary, a thin film covered the hole at the beginning of the simulation. As simulations start, the thin film was ruptured from the centre at controlled rates. Five rupture rates, which corresponded to a rupture time of 0.0 μs , 0.3 μs , 0.6 μs , 0.9 μs and 1.2 μs from the beginning to the complete rupture of the disk, were considered. A rupture time of 0.0 ms corresponded to the sudden release case. In all cases, the hole diameter was fixed at 3 mm. The influence of the ruptured disk was neglected. All the simulations were started from still with the computational domain filled with ambient air and pure pressurized hydrogen separated by a thin film. All the solid walls were assumed to be non-slip and adiabatic. The computational grids were clustered around the release hole and its axis in the simulated cylinder region as shown in Figure 2.3-3. Uniform grid was used in the surrounding region. Note that sufficient space was provided in both external and internal domains to eliminate the impact of boundary conditions on the ignition locations in the vicinity of the release hole. In (Xu et al., 2011) an additional obstacle in a shape of disk located in front of release hole was introduced to investigate the impact of obstacles on the autoignition process.

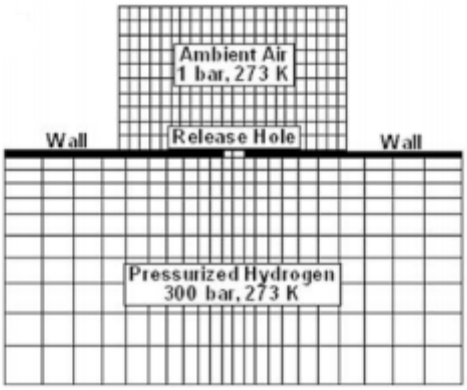

Figure 2.3-3. Scheme of computational domain used in (Xu et al., 2009a). External domain is scaled 3.3 *D* (radius) x 5 *D* (height), where *D* is hole diameter, and the internal domain inside hydrogen tank is scaled 10 *D* x 10 *D*.

The schematic plot of the computational domain shown in Figure 2.3-4 illustrates computational domain used in (Wen et al., 2009), which was primarily aimed at investigation of influence of membrane rupture dynamics on the autoignition process. The domain is composed of three cylindrical regions: pressurized cylinder, a length of release tube and ambient environment. To resolve the large scale vortices existing around the tube exit, the tube is inserted into the ambient environment 8 mm from the top. The distance of 8 mm was chosen so that the leading spherical shock would not be reflected back from the bottom wall of the ambient region to interfere with the formation of the vortices during the simulations. As discussed, the rupture process of the initial pressure boundary is essential to the spontaneous ignition. The Iris model (Goozee et al., 2006) is used to simulate the finite opening time of the pressure boundary. It assumes the pressure boundary, which is mimicked by a thin diaphragm with a thickness of 0.1 mm placed at the bottom plane of the release tube in the simulations, ruptures linearly from the centre at a finite pre-determined rate as simulations start. Formulae proposed by Spence and Woods (1964) had been used to obtain the rupture time of the diaphragm. According to this formula, the rupture time may vary from 5 to 30 μs for different release pressures and diaphragm dimensions. Therefore, three rupture times of 5 μs, 10 μs and 25 μs were considered for comparison in (Wen et al., 2009).

All the simulations were started from still conditions with the tube and ambient environment regions filled with ambient air and the pressurized cylinder region with pure pressurized hydrogen separated by a thin diaphragm. All the solid surfaces (e.g. walls) were assumed to be non-slip and adiabatic. Non-uniform grids were applied to the regions of pressurized cylinder and ambient environment and uniform grids to the tube region. Since the flame is initiated at the thin contact region, a very fine grid resolution is required there to resolve the species profiles in the ignited flame. In this case, a 15 μm mesh size is adopted to resolve the contact region inside the tube, which is also close to the grid resolution of 20 μm n. To save computing resources, a 15 μm uniform adaptive mesh was adopted to track the region between the leading shock and the contact region, while 75 μm mesh size was used for the other regions inside the tube. To accelerate simulations, the ambient environment region was only activated by adding it to the computational domain when the leading shock was 5 mm away from the tube exit end during simulations.

Once again, utilization of ILES with variable mesh cell size allowed implementation of sufficiently large domains within the hydrogen tank and in ambient atmosphere to prevent boundary impact. The final example of this problem, described by (Xu and Wen, 2012), (Xu and Wen, 2014), investigated the impact of the tube internal geometry. The computational domain is composed of a cylindrical high-pressure vessel of large diameter and a release tube with varied cross-sections as shown in Figure 2.3-5. The pressurized cylinder is set up to be sufficiently large to ensure that pressure drop during simulations does not exceed 3% of the initial pressure.

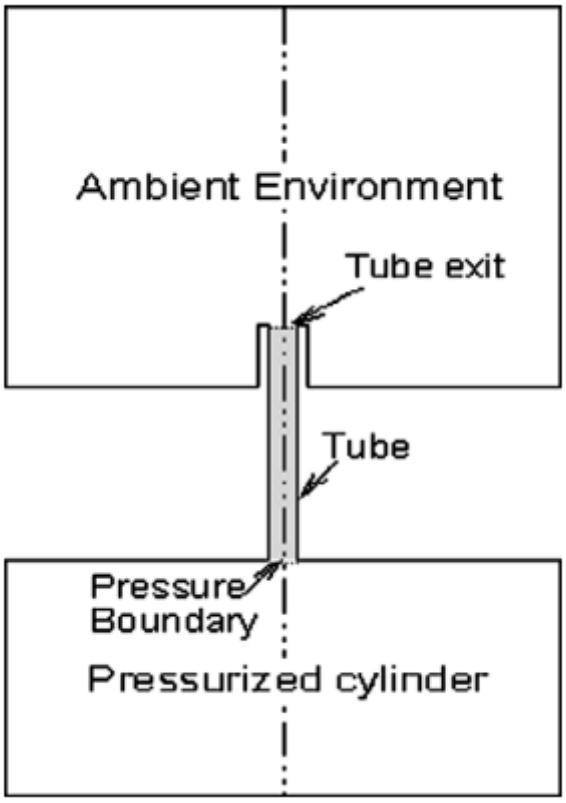

Figure 2.3-4. Scheme of computational domain used in (Wen et al., 2009).

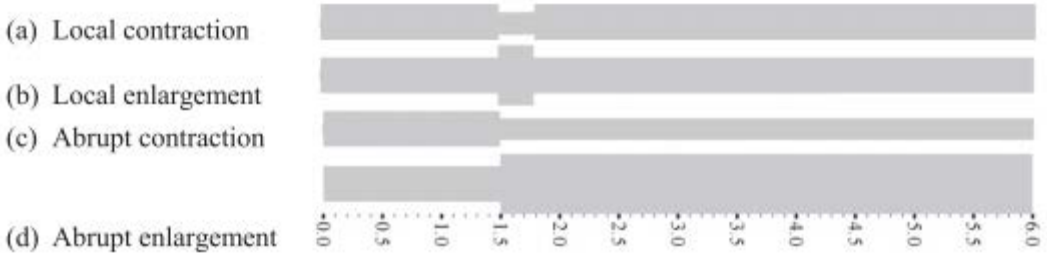

Figure 2.3-5. Scheme of computational domain with variable cross-section pipe used in (Xu and Wen, 2014).

Simulations of hydrogen autoignition in a T-shaped PRD performed at the University of Ulster (Bragin et al., 2013) used a domain consisting of a high pressure component, separated by the burst disk from a T-shaped channel, mimicking a PRD connected to the atmosphere. The problem setup was designed to mimic the conditions of experimental study of the spontaneous ignition by Golub et al. (2010). The high pressure system consisted of a 210 mm

long tube with 16 mm internal diameter (ID) followed by a 280 mm long tube with 10 mm ID, closed at the end by a flat burst disk, followed by a mock-up PRD open to atmosphere (Figure 2.3-6). The PRD had a 48 mm long axial channel of 6.5 mm ID with a flat end, and two radial channels on opposite sides of the axial channel to vent hydrogen to atmosphere. Each radial channel was 6.25 mm length and 4 mm ID (distance from the end connected to the atmosphere of one radial channel to the end of another was 19 mm). Radial channels were flush with the axial channel end wall and positioned so that the edge of each side channel touched the flat end wall of the axial channel tangentially. Note that the boundary corresponding to ambient air were far removed from the T-shaped PRD, a design made more affordable by utilization of tetrahedral mesh allowing large expansion ratio between the neighbouring cells.

The high-pressure system was modelled as closed with wall boundary condition set at the "inlet" boundary in order to exclude potential effects of inlet boundary conditions on the process. This assumption is valid because the observation time in simulation is less than a time required for a rarefaction wave to reach the far end of the high-pressure system.

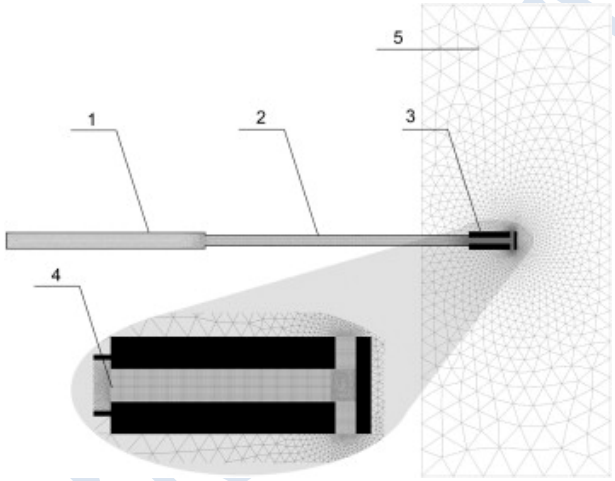

Figure 2.3-6. Computational domain and mesh used in University of Ulster simulation (Bragin et al., 2013) of spontaneous ignition in T-shaped pressure relief device (PRD): 1 and 2 – high-pressure tubes, 3 – PRD, 4 – burst disk, and 5 – external domain.

An important part of the problem was the burst disk, initially separating PRD from the high pressure system. The non-instantaneous burst disk opening is expected to play an important role in the process of ignition due to effect on mixing between hydrogen and air. Several previous works (Xu et al., 2009a) (Wen et al., 2009) investigated the impact of non-instantaneous opening of the diaphragm and concluded that it can have significant impact on the development of the flow structure. Accordingly, gradual opening of a membrane was approximated in simulations by 10 step-like process, with membrane divided into 10 concentric sections (see Figure 2.3-7) opened in sequence. Following (Spence and Woods, 1964), the following formula is applied to calculate an opening time of a diaphragm

$$t = k(\rho b d / p)^{1/2}, \quad (2.3.1)$$

where ρ is the density of the diaphragm material, b and d are thickness and diameter of the diaphragm, respectively, and the values of k are found to be in a range 0.91-0.93 (Wen et al, 2009).

The diaphragm was $5 \cdot 10^{-5}$ m thick, had diameter of $6.5 \cdot 10^{-3}$ m and was assumed to be made of annealed copper with density of 8900 kg/m^3. Opening time for each section is provided in Table 2.3-1 for four initial pressure values under investigation.

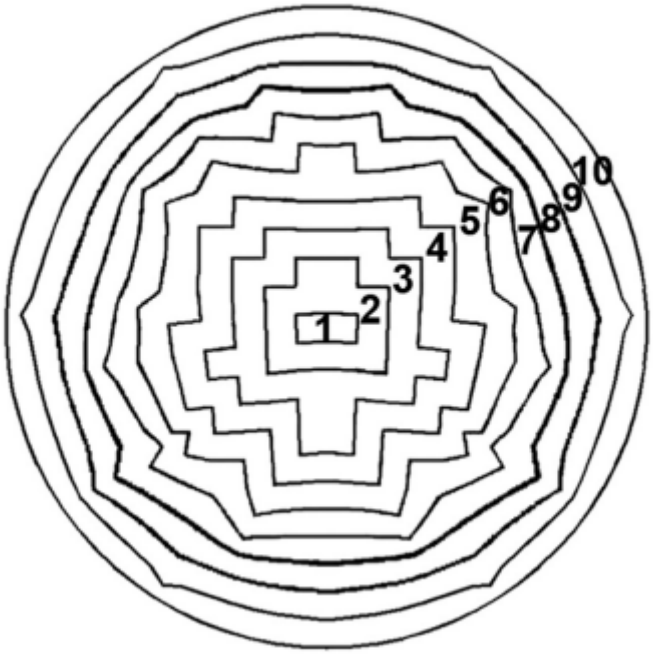

Figure 2.3-7. Step-like approximation of the membrane burst process. Sections 1-10 are opened in sequence.

Table 2.3-1. Opening time for diaphragm sections.

Initial pressure, MPa	Opening time, μs, for section									
	1	2	3	4	5	6	7	8	9	10
1.35	0	4.7	9.4	14.2	18.9	23.6	28.4	33.1	37.8	42.6
1.65	0	4.3	8.6	12.8	17.1	21.4	25.6	29.9	34.3	38.5
2.43	0	3.5	7.1	10.6	14.2	17.7	21.3	24.8	28.3	31.9
2.90	0	3.2	6.5	9.7	12.9	16.2	19.4	22.6	25.9	29.1

2.3.1.2 Jet fire problems

The problem simulated in the University of Ulster study of the plane under-expanded jet (Makarov and Molkov, 2013a) reproduced the details of the experiment performed by (Mogi and Hariguchi, 2009). Three nozzles were modelled: a round nozzle of 1.0 mm diameter and two plane nozzles having overall size 2.0 x 0.4 mm (length to width aspect ratio AR = 5.0) and 3.2 x 0.25 mm (length to width aspect ratio AR = 12.8), all three having the same cross section area.

Modelling of high pressure under-expanded reacting jets presented a considerable problem due to a large disparity of spatial and velocity scales, precluding simulations of the flow in a single computational domain from inside the nozzle down to the end and beyond the flammable envelope location or the flame tip location. On one hand, a presence of the under-

expanded jet shock structure associated with high flow velocities in a near field and a small aperture of the nozzle would dictate small time step for unsteady simulations. On the other hand, a large size of flammable envelope or jet flame and related hot current compared to the nozzle size, and slow velocities in the far from the nozzle field would require substantial computing resources and calculation times. This makes simulation of the problem in one computational domain impractical. The approach used in simulation of this problem at the University of Ulster involved separation of the computational domain into two subdomains, one describing the compressible region near the nozzle exit, while another covered the far-field region where the flow was essentially incompressible. To reduce the computational effort the problem was modelled in two stages: first the compressible flow in the near-to-nozzle field was simulated, then the results were used as boundary conditions for the far-from-nozzle field simulations where the incompressible flow approach is applied.

Figure 2.3-8 illustrates the geometry, computational domains arrangement and the types of boundary conditions for compressible flow in the near-to nozzle field and for incompressible flow in the far-from nozzle field for the round nozzle jet.

For the 1 mm diameter round nozzle, the calculation domain for the near-to-nozzle field had dimensions L (length) x D (diameter) = 0.1625 x 0.104 m. The far field domain had dimensions L x D = 7.8 x 2.0 m. The calculation domains for the plane nozzle were designed similarly, apart from the fact that the domains utilized symmetry in the vertical plane (simulations were carried out for a half of the plane nozzle jet). Near-field domains for both AR = 5.0 ratio nozzle measured L x D = 0.26 x 0.16 m and the calculation domain for the far field of both plane nozzle jets had the dimensions L x D =3.1 x 4.0 m. Calculation domains for the nozzle with AR = 12.8 ratio had the same sizes as for the nozzle with AR = 5.0, but the number of control volumes in the near-field domain was different due to the different discretization across the nozzle.

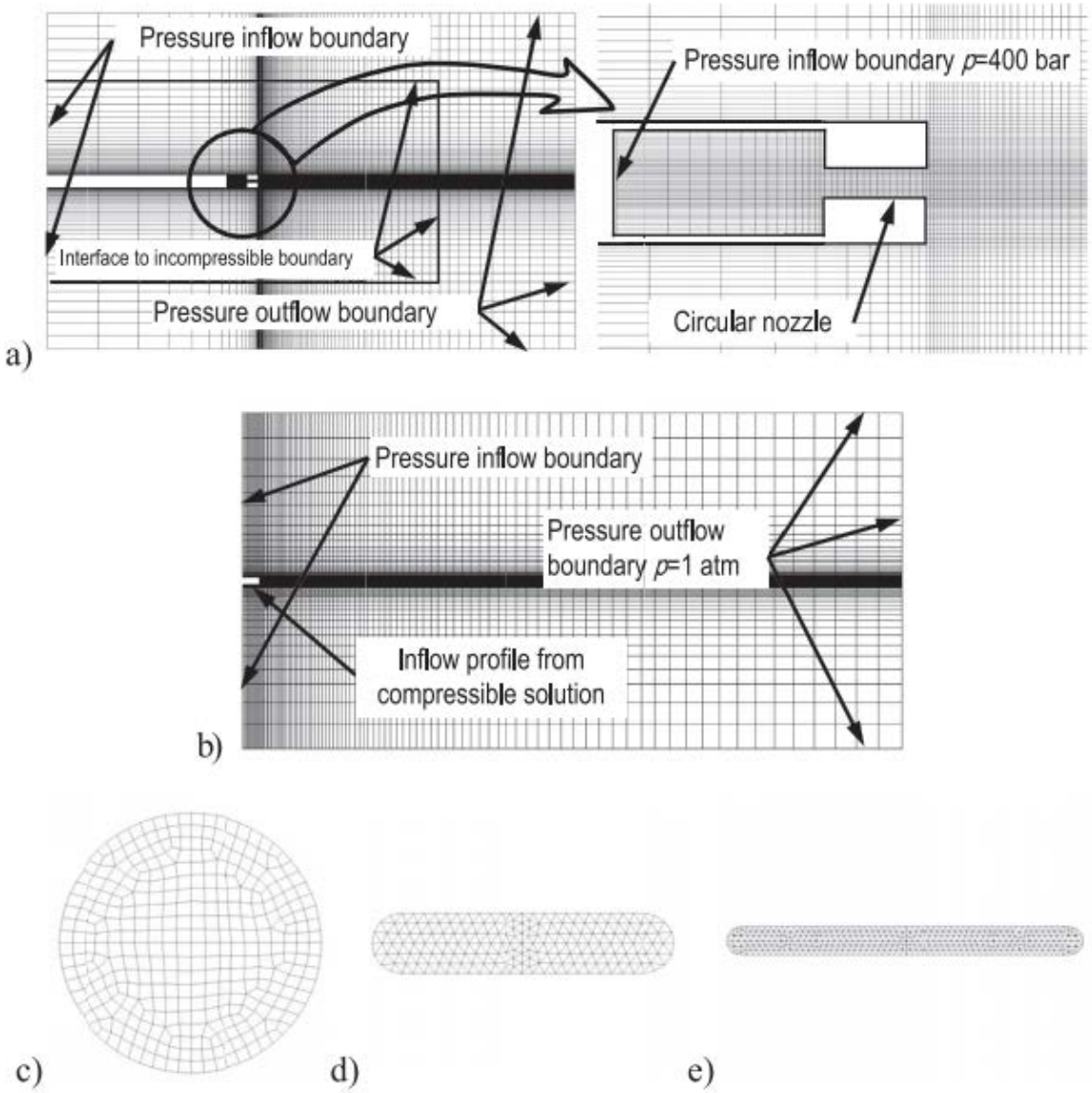

Figure 2.3-8. Computational domains: (a) domain for the near-to-nozzle field (round nozzle), (b) domain for the far-from-nozzle field (round nozzle), (c) round nozzle mesh, (d) AR=5.0 nozzle mesh, (e) AR=12.8 nozzle mesh (Makarov and Molkov, 2013a).

LES simulation of high pressure hydrogen jets (Brennan et al., 2009) was aimed at reproducing experimental data obtained by Schefer et al. (2007) at Sandia National Laboratories. The experiment involved blowdown from a high pressure tank at an initial pressure of 413 bar through a 5.08 mm diameter nozzle. The calculation domain designed to reproduce the experiment was measured approximately H×W×D = 35×8×8 m. The equivalent diameter of the notional nozzle was found to be 59.4 mm, more than ten times greater than the physical nozzle diameter. Rather than utilizing two-mesh approach used in the previously described simulation, (Brennan et al., 2009) implemented a notional nozzle approach, which allowed significant reduction of mesh maximum resolution in the vicinity of the release origin.

An RNG – based RANS simulation by Molkov et al. (2014) was aimed at identification and investigation of distinctive modes of fires resulting from hydrogen release in the vented enclosure. The enclosure was a cube with side size of 1 m characteristic for a fuel cell. There

was only one vent in each simulation either horizontal or vertical. The vent was located at the top and at the central part of a wall. The release was directed vertically upward. Hydrogen release pipe was of 10 cm length with internal diameter of 5.08 mm located in the centre of the enclosure floor 10 cm above the floor. The thickness of the enclosure aluminium walls was 2 cm (each wall was resolved by 4 control volumes).

Two calculation domains were used in numerical experiments (Molkov et al., 2014). Simulations with horizontal vent were carried out in a calculation domain in the form of a hexahedron of size L×W×H = 7×6×4 m. Simulations with vertical vents were performed in a calculation domain of size Lx Wx H = 5 x2 x4 m. Both domains included the enclosure and ambient space around enclosure.

2.3.2 Meshing

The choice of meshing requirements for ignition and jet fire modelling depends on the choice of the model utilized for the simulation. High fidelity DNS simulations would require generation of very fine mesh closely following Kolmogorov scale size ($\eta = \left(\nu^3/\varepsilon\right)^{1/4}$, where ν is the kinematic viscosity and ε is the rate of kinetic energy dissipation). Application of LES would allow significant reduction in maximum mesh resolution, as well as more significant freedom in changing mesh size outside of the regions of maximum gradients, allowing further reduction of CV number. The following is a brief description of meshes used in the numerical simulations described in the previous chapters serving as illustration of the impact of numerical model selection on grid design. Similarly to the non-reacting release modelling, RANS approach is the least sensitive to grid quality, leading to common application of highly expanded grids, aligned with jet or flow/fire axial direction, while LES and DNS require more uniform and equilateral meshes.

2.3.2.1 Spontaneous ignition modelling

Models using DNS requires ultra-fine grids, resolved down to the Kolmogorov scale. This usually results in very large grids required to cover even for 2-D model formulation and relatively small and geometrically simple computational domains. The following are several examples of the grids utilized in recent DNS studies of spontaneous ignition. Pinto and colleagues (2007) used uniform rectangular grid with a cell size of 20 x 20 μm for DNS spontaneous ignition simulation, resulting in a grid with maximum mesh size reaching 27 million cells (Pinto et al., 2007). Yamada et al., (2009) has used grid with comparable cell size measured 20-45 μm,) resulting in the total grid size of 4 million cells. Lee and Jeung (Lee and Jeung, 2009) used a Cartesian grid system with a uniform size of 19 μm close to the measured Kolmogorov scales in a shock tube. The total number of cells was about 4 million.

The ILES model of Xu and colleagues had been applied to a variety of simulation of hydrogen realise, including releases from both a hole and a tube. In either case the minimum grid size was driven by the necessity to resolve the reaction zone. Since the ignition occurs at the thin contact region, a very fine grid resolution is required there to resolve the species profiles in the ignited flame (Hilbert and Thevenin, 2002). The flame thickness depending on the local flow properties is much larger than that of the shock waves, so the thin flame can be resolved in the current two-dimensional simulations. According to Mastorakos et al. (1997) study, at least six grid points are needed across the interface between the air and the fuel to resolve the mixing layer. In previous direct simulations of non-premixed autoignition, Hilbert and Thevenin (2002) used a grid resolution of 20 μm to resolve the thin flame, while Yamada

et al. (Yamada et al., 2009) adopted a resolution of 20–45 µm. In (Wen et al., 2009) the grid resolution is limited to 15–30 µm across the contact region in order to resolve the contact region inside the tube, which is also close to the grid resolution of 20 µm (Hilbert and Thevenin, 2002).. Although the diffusion flame is directly resolved, such ‘‘direct” approach is still classified as large eddy simulation as the flow field is not fully resolved (Norris and Edwards, 1997). To save computing resources, a 15 µm uniform adaptive mesh was adopted to track the region between the leading shock and the contact region, while 75 µm mesh size was used for the other regions inside the tube. To save computational efforts, the ambient environment region was only activated by adding it to the computational domain when the leading shock was 5 mm away from the tube exit end during simulations. The non-uniform grids were clustered around the two ends of the tube and the grid sizes range from 15 µm –30 µm inside the region of ambient environment and from 15 µm –150 µm inside the region of pressurized cylinder. The total grid points are then approximately 2.3 million in the current simulations.

The simulation of Xu et al., (2009a) used similar minimal mesh resolution. To prevent false numerical diffusion to smear out the real molecular diffusion in the early stage of release, the contact surface was tracked by a number of clustered moving grids with grid spacing as small as 4 mm before the normal shock turns into a semi-spherical shock. The computational grids were clustered around the jet exit. A minimum grid spacing of 20 µm was used to resolve the reaction zone.

Xu et al., (2009a) performed grid sensitivity study for the release case of 250 bar by using a half of grid resolution of the previous simulations (800,000 cells and 40 µm maximum resolution versus 1,600,000 cells and 20 µm). Comparisons of hydrogen mass fraction, Mach number, hydroxyl (OH) mass fraction and temperature indicated that the vortices at the jet boundary have not been fully captured by the coarse mesh. The coarse mesh also incurs more false numerical diffusion which artificially increases the thicknesses of contact surface and flame. The predicted maximum temperature is shown in Figure 2.3-9. Although the flow field is less resolved and more numerical diffusion is incurred by the coarse mesh, the maximum temperature is less sensitive to the grid resolutions tested.

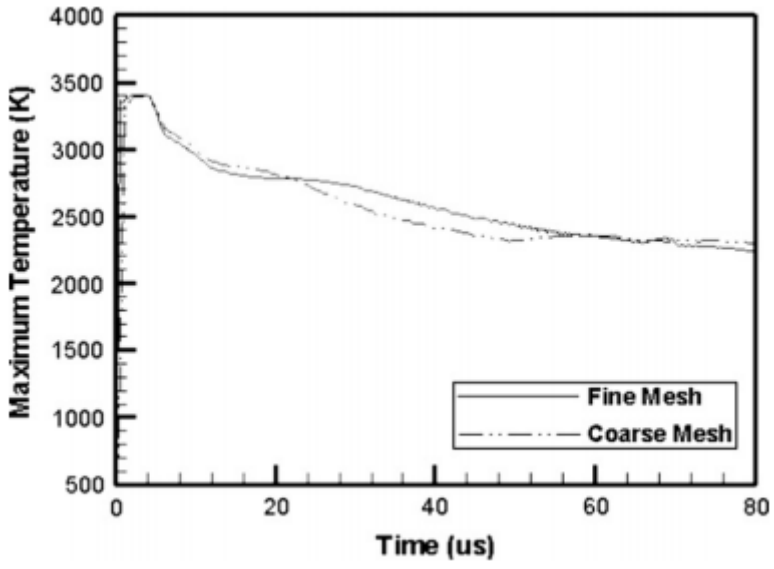

Figure 2.3-9. Maximum temperature *versus* time for fine and coarse grids (Xu et al., 2009a).

University of Ulster LES EDC simulations by (Bragin et al., 2013) employed a 3-D grid (see Figure 2.3-6) which realises a control volume based finite difference method. The axial and radial channels of the PRD were meshed with a hexahedral grid with a uniform control volume (CV) size of about 400 µm both along the axial channel and in its cross-section, excluding the intersection zone. The intersection area of the axial and the radial channels was meshed with tetrahedral CVs with size of about 200 µm, i.e. the largest CV size used in numerical simulations of the spontaneous ignition phenomenon up to date. The larger CV size was necessary in order to simulate a problem in reasonable computation time while utilizing the fully 3-D LES technique. It was "compensated" by utilizing advanced sub-grid scale (SGS) combustion modelling using the eddy dissipation concept with a detailed chemistry and the turbulence by the renormalization group (RNG) theory. The high-pressure chamber was meshed by tetrahedrons with the smallest CV size of about 250 µm clustered near the membrane of the PRD and rapidly increasing away from it reaching the maximum cell width of 10 mm at the far end. The total number of control volumes in the computational domain was equal to a moderate number of 417,685 cells.

2.3.2.2 Jet fires modelling

Simulations of plane jets using the EBU combustion model performed at University of Ulster (Makarov and Molkov, 2013a) utilized two separate grids for near and far field (see domain geometry depicted in Figure 2.3-8). For the round nozzle simulation the near field calculation domain measured 0.1625 x 0.104 m was discretised using 412,736 hexahedral control volumes (CVs). The 1 mm diameter round nozzle was discretised using 20 CVs across the nozzle diameter. This relatively fine mesh was required in order to resolve Mach disk and shock structure of this highly underexpanded jet. The far field domain measured 7.8 x 2.0 m and was discretised using 356,868 hexahedral CVs.

The calculation meshes for the plane nozzles were designed similarly, apart from the fact that the domains utilized symmetry in the vertical plane (simulations were carried out for a half of the plane nozzle jet). The domain for the near field of aspect ratio (AR) = 5.0 ratio nozzle measured 0.26 x 0.16 m and was discretised using a hybrid mesh with a mix of tetrahedral and hexahedral CVs for a total of 530,546 CVs, with 6 CVs across nozzle width and 14 CVs across its half-length. A near-field domain for the AR = 12.8 nozzle had the same dimensions, but its nozzle was discretised using 6 CVs across the width and 32 CVs across the half-length, resulting in a total CV number equal 504,040. Calculation domains for the far field of both plane nozzle jets were identical, measuring 3.1 x 4.0 m and being discretised using 868,546 hexahedral CVs. Near- and far-field meshes did not identically match at the interface due to the different cell sizes.

Two grids were employed in the LES of a high pressure hydrogen jet fire using laminar flamelet/PDF approach (Brennan et al., 2009). The finer grid consisted of 341,160 hexahedral cells with a minimum of 8 cells across the inlet boundary (i.e. a minimum cell size of approximately 7 mm in the case of 8 cells, increasing towards the boundaries). The second grid examined was coarser with 87,151 hexahedral cells and a minimum of 4 cells across the inlet boundary (i.e. a minimum cell size of 14 mm). The grids are rather moderate for proper LES, yet it can be demonstrated that they can be used to obtain a solution in a time frame reasonable for hydrogen safety engineering. Pope (2000) describes this approach as very large eddy simulation (VLES) whereby the grid and filter may be too large to resolve all the energy-containing motions. The penalty for the use of the coarse mesh is the under-resolved

flow structure and mixing close to the nozzle. To compensate for this, turbulence intensity and length scale boundary conditions should be imposed at the notional nozzle exit.

Grid resolution was shown to be more influential than turbulent boundary conditions on flame length and width. Simulations on the coarser mesh would probably require higher values of imposed turbulence intensity compared to finer grid LES to provide a similar flame length and flame width to length ratio. Mesh should be able to resolve velocity profile in the vent, where two-directional flow can appear due to buoyancy effects.

Numerical experiments on hydrogen combustion in the enclosure with one vent (Molkov et al., 2014) were performed using block-structured hexahedral grid which was concentrated toward the areas of the release pipe and the enclosure vent. Three different numerical grids were employed (one for each vent size), described in Table 2.3-2. The grids were built following generic rules for grid quality (Molkov and Shentsov, 2014).

Table 2.3-2. Three meshes used in numerical experiments (Molkov et al., 2014).

Vent size H×W	Mesh size, CVs	CVs inside enclosure	CVs in the vent, height×width×depth
3×30 cm (horizontal)	1,530,987	229,746	5×33×4 = 660
30×3 cm (vertical)	1,412,521	379,837	30×9×4 = 1080
13.9×3 cm (vertical)	1,482,475	406,555	24×9×4 = 864

2.3.3 Boundary conditions

Selection of appropriate boundary conditions is important to ensure the absence of adverse effects propagating to the area of interest from the ambient atmosphere and for proper modelling of the inflow characteristics. In fire and ignition modelling typical boundary conditions include no-slip walls, non-reflecting far-field-pressure-type outflow conditions at the atmosphere boundary and pressure or velocity-type inflow conditions for the release.

A special consideration may need to be given to the formulation of proper problem setup at the boundary. A typical example occurs in jet fire modelling, where the straightforward implementation of the inflow on the actual release nozzle would often require extremely fine mesh resulting in use of impractically large computational resources. Several alternative approaches, including utilization of several meshes with different structure and resolution requirements, utilization of effective nozzle or volumetric source approach can be used in order to resolve this problem.

The boundary conditions for the simulation of plane jets using EBU combustion model (Makarov and Molkov, 2013a) corresponded to unconstrained environment. For simulation of compressible flow the inner (near-field) domain had pressure inflow boundary condition for hydrogen inflow, corresponding to P = 400 bar pressure in the tank, no-slip condition on the nozzle walls, and pressure inflow condition on the boundary opposite to the release direction, accounting for the entrainment flow into the computational domain. Other boundaries provided interface, through which the solution from the compressible near-field domain was passed to incompressible far-field domain as its boundary condition. The interface was located far from the compressible boundary to minimize potential effect of its numerical approximation errors onto the incompressible stage boundary conditions. Far-field domain

featured pressure inflow boundary condition in the direction opposite to the release direction and the pressure outflow on all other boundaries.

Near- and far-field grids, used for compressible and incompressible simulation stages respectively, were not identical at the outflow/inflow interface. An interpolation of simulation results was required at the inflow boundary of the incompressible stage domain. This could potentially lead to deterioration of the accuracy of calculation results. Special attention therefore was paid to mesh refinement at the interface to make sure that maximum values of key flow parameters (flow velocity and hydrogen vol. fraction) at the interface between compressible and incompressible domains were matching each other. Table 2.3-3 gives relative errors for the hydrogen mass flow rate, the total impulse, the maximum hydrogen mass fraction and the maximum absolute velocity at the compressible outflow/incompressible inflow interface between the domains for all three simulated cases. The error is relatively small and a smooth, continues solution through both domains was preserved.

Table 2.3-3 shows that the total hydrogen mass flow rate through the whole nozzle geometry (keeping in mind that only half of a jet was simulated in case of AR = 5.0 and AR = 12.8 nozzles using the symmetry condition). Values are comparable and close to each other, i.e. 1.56, 1.52 and 1.36 g/s of hydrogen for the round, AR = 5.0, and AR = 12.8 nozzles respectively. The difference of 15% can be explained by the increase of losses in the flow pathway with a minimum of losses for the round nozzle and then the increase of losses for plane nozzles with the increase of the aspect ratio.

Table 2.3-3. Values of numerical parameters controlled at the outflow/inflow interface between compressible/incompressible domains, and their relative error $\Delta\varepsilon$ (non-reacting jet simulations). Note: simulations for the rectangular nozzles were performed in a half of the real geometry, and by this reason the mass flow rate shown in the table is multiplied by 2.

Nozzle type	Boundary	H_2 mass flow rate kg/s	$\Delta\varepsilon$, %	Impulse, kg m/s^2	$\Delta\varepsilon$, %	Max H_2 fraction	$\Delta\varepsilon$, %	Max velocity, m/s	$\Delta\varepsilon$, %
Round	Outflow	0.0156	1.28	31.1	2.89	0.9405	1.75	1534.5	1.83
	Inflow	0.0154		30.2		0.9246		1506.4	
AR=5.0	Outflow	0.0152	1.32	15.72	0.70	0.6240	0.05	1375.9	0.01
	Inflow	0.0150		15.61		0.6237		1375.7	
AR=12.8	Outflow	0.0136	1.47	14.46	1.80	0.5216	2.93	1248.5	2.94
	Inflow	0.0134		14.20		0.5063		1211.8	

Alternative approach used in (Brennan et al., 2009). Cumber et al., (1995) postulated that 32 to 64 control volumes (CV) per nozzle diameter are required for accurate modelling of under-exapnded flow. Since this requirement extrapolated to the entire computational domain would require prohibitively large mesh, a variety of alternative approaches was proposed to reduce mesh size, introducing the concept of effective source diameter, whereby the shock structure formed in the under-expanded jet is replaced by a notional nozzle.

Birch et al (1984) developed the concept of an effective source diameter, based on the area which would be occupied by the same mass flow rate at ambient pressure and temperature with a uniform sonic velocity. Birch et al. (1984) showed that the behaviour of under-expanded jets is similar to classical subsonic free jets provided that an appropriate scaling factor is employed to describe the effective size of the jet source. The original nozzle diameter d is substituted by an equivalent diameter d_{eq}

$$d_{eq} = d\sqrt{P / P_{atm}}(2/\gamma + 1)^{\gamma/\gamma - 1}, \quad (2.3.2)$$

where P/P_{atm} is the the ratio of reservoir to atmospheric pressure. This approach was further developed at University of Ulster (Molkov et al., 2008) from the mass and energy conservation, extending it to non-ideal gas in the reservoir at pressures up to 1000 bar which are realistic for hydrogen storage please see (SUSANA D2.1, 2016) for details.

One of parameter which needs to be modelled in LES is the turbulence at the jet release origin. In reality there will be perturbations in the velocity of the turbulent jet fire at the jet exit. If these fluctuations are not modelled by setting appropriate boundary conditions, individual instantaneous velocity components are assumed to be equal to their mean velocity counterparts. However, these fluctuations are important for mixing to occur between the fuel and oxidizer in a hydrogen jet fire. The level of mixing will dictate the combustion behaviour and thus will influence the length and shape of the jet fire. Therefore, if a reliable methodology is to be developed for modelling high pressure jet fires then appropriate fluctuations should be modelled at the boundary. (Brennan et al., 2009) uses a random flow generation technique (Smirnov et al., 2001) in order to simulate these perturbations.

The turbulence length scale, l is restricted by the size of a duct in internal flows and an approximate relationship between l and the size of the duct, D, is $l = 0.07D$ (Fluent). Thus a value of 7% of the equivalent diameter (notional nozzle diameter) was considered as an initial value for the turbulent length scale at the jet boundary.

The VLES approach, as used in the modelling of high pressure jets using a laminar flamelet/PDF combustion model (Brennan et al., 2009) uses an under-resolved grid, in which the grid and filter can be too large to resolve all the energy-containing motions. To compensate for the under-resolution of the mixing and turbulent flow structure close to the nozzle, turbulence intensity and length scale boundary conditions should be imposed at the notional nozzle exit.

Comparison of the flame length and flame width/length ratio were calculated and compared with the experimental data for different turbulent intensities imposed at the notional nozzle (see Table 2.3-4). Turbulence intensity of 5, 20, 25 and 30% at the notional nozzle had been applied with the fine and 20, 25 and 30% with the coarse grid. A turbulent length scale was specified at the jet exit as 7% of the equivalent diameter in 4 simulations with the fine grid and all three cases with coarse grid. An additional two cases with turbulence length scales equal to $d_{ef} / 2\pi$, i.e. approximately 16% of the equivalent diameter d_{ef}, and to 50% of the equivalent diameter were also run on the fine grid, with the turbulent intensity fixed at 25%. Examination of the results indicates that the simulation on a coarse grid resulted in overestimation of the flame length and underestimation of width/length ratio for all turbulent intensities. It was demonstrated that in the region 0–20% turbulence intensity had a limited effect on the flame length and width. Beyond 20% an increase in turbulence intensity led to a decrease in the flame length and the increase of the flame width across nearly the whole range of the tested turbulence intensities.

However, the simulation became less stable as the turbulence intensity approached 30% leading to stability issues. Changes in the turbulent length scale at the nozzle exit were found to have a little effect on the flame length and width. A turbulence intensity of 25% and turbulence length scale equivalent to 7% the equivalent diameter provided the closest agreement with experimental observations for a finer grid resolution with 8 CVs across the notional nozzle diameter. However, agreement shown for turbulence intensities in the range 5–25% for the finer grid was very close to experimental observations as well. It would seem that for moderate grid resolution the final length and width of the flame are relatively insensitive to values of turbulence intensity provided the value is less than 30%.

Table 2.3-4. Average flame length and width to length ratio for different turbulent intensities and length scale at the effective nozzle.

	Fine mesh						Coarse mesh			Experiment
Turbulence intensity at the inlet, (%)	5	20	25	30	25	25	25	30		
Turbulent length scale (% of d_{ef})	7	7	7	7	16	50	7	7	7	
Mean flame length (m)	11.68	12.16	10.92	9.47	11.11	10.63	16.89	16.96	15.80	10.6
Mean flame width to length ratio	0.19	0.19	0.21	0.25	0.20	0.22	0.11	0.11	0.12	0.17

Domain outlet boundary conditions were set to the same pressure and temperature as in the calculation domain. Non-slip boundary condition was applied on all surfaces.

Experience of fire simulations at University of Ulster indicated that application of exaggerated initial turbulence (25-30% - close to the value expected on the jet axis) often improved the results of simulations with under-resolved mesh in vicinity of the nozzle.

2.3.4 Initial conditions

Proper setup of initial conditions is required for transient problems to have correct prediction of results and may significantly improve stability/solution behaviour for steady-state problems. Attention must be paid to fire initialization/ignition in the simulation. EBU combustion model typically doesn't require artificial ignition due to its "mixed-burned" nature. Nevertheless, its more sophisticated implementation may require introduction of trace quantity (concentration of ~10^{-3} – 10^{-6}) of reaction products as an initial condition for reaction initialization. Flamelet and EDC models using finite rate chemistry treatment usually require a high-temperature source to be patched into the reaction zone in order to initiate combustion.

A University of Ulster simulation of spontaneous ignition in T-shaped PRD (Bragin et al., 2013), for example, demonstrated the significant influence of the diaphragm opening sequence on the resulting solution and ignition/non-ignition of released hydrogen. Similar results were obtained by Xu et al., (2008).

In a plane jet simulation using a two grid approach (Makarov and Molkov, 2013a) the conditions at a time 5 s after the start of the release have been taken to simulate a quasi-steady state of the jet fire in the experiment described in (Schefer et al., 2007). Pressure and temperature in the stagnation chamber at this time were estimated as 29.6 MPa and 275.5 K respectively using the decay curves given in (Schefer et al., 2007). The temperature at the notional nozzle was calculated as 227.5 K. For steady-state compressible problems setting high-low pressure interface and hydrogen-air interface in different locations may help to improve convergence, at least at initial stage of solution.

In (Molkov et al., 2014) the temperature of hydrogen released from the pipe was 273 K, and initial temperature of air in the domain was 293 K, i.e. 20 K higher than temperature of leaking hydrogen. The release velocity was 60, 150, 300, or 600 m/s. The pipe was initially filled in with air. The composition of air in the simulations was taken as 20.7% by volume of oxygen and 79.3% of nitrogen. The sustained release of hydrogen was simulated, i.e. the mass flow rate and the temperature of hydrogen were both kept constant. The initial pressure throughout the calculation domain was set to 101,325 Pa.

2.4 Numerical options

2.4.1 Solver type

Spontaneous ignition during hydrogen release is commonly associated with interaction of shock waves with the walls and other obstacles in the vicinity of release origin. Adequate modelling of the ignition, therefore, in terms of solver selection typically means utilization of density-based solver capable of simulating compressible flows. Furthermore, importance of shock waves for ignition modelling encourage using solvers with good shock-capturing properties and low numerical diffusion. This requirement usually implies application of solvers using high-order numerical schemes. At the same time, the numerical scheme should not be excessively oscillatory, which, as will be discussed later in the section, is the behaviour exhibited by some high order schemes.

The modelling of jet fires, on the other hand, often involves utilization of pressure-based incompressible approaches using iterative implicit solvers, e.g., SIMPLE algorithm (Patankar, 1980). It should be noted that some jet fires of practical interest originate from releases from high pressure storage/piping, which means that compressibility effects play significant role in the vicinity of release origin. One of the approaches to modelling of these cases is to separate computational domain into subdomains, with fully compressible solver utilized for the sub-domain covering the vicinity of the jet fire origin, and the incompressible solver simulating fire in the (much) larger far field sub-domain, as had been discussed in the section 2.3.1 “Domain design”.

When selecting a numerical solver for ignition and/or fire modelling, it should be remembered that the addition of species production/transport equation and chemical model equations, calculating species source terms can significantly increase computation time. Furthermore, the requirements of chemical model can drive temporal- and spatial resolution requirements far beyond those of equivalent non-ignited case. The following are illustrations of election and application of numerical solvers to the ignition and jet fire problems of practical interest.

The numerical algorithm used by Xu and colleagues (Xu et al., 2007 and subsequent works) for spontaneous ignition modelling was based on an arbitrary Lagrangian and Eulerian (ALE) method (Hirt et al., 1974) in which convective terms are solved separately from the other

terms. Each time cycle is divided into two phases: a Lagrangian phase and a rezone phase. Considering the substantial scale difference between diffusion and advection, different numerical schemes were adopted in the two phases. In the Lagrangian phase, a second-order Crank-Nicolson scheme is used for the diffusion terms and the terms associated with pressure wave propagation, a 3rd-order TVD Runge–Kutta method (Balsara and Shui, 2000) is used in the rezone phase to solve the convection terms. The coupled semi-implicit equations in the Lagrangian phase are solved by a SIMPLE type algorithm with individual equations solved by a conjugate residual method (O'Rourke and Amsden, 1986). One benefit of the ALE method is allowing moving grids. To prevent false numerical diffusion smearing out the real molecular diffusion in the early stage of release, the contact surface was tracked by a number of clustered moving grids with grid spacing as small as 4 μm before the normal shock turns into a semi-spherical shock.

A mixture-averaged multi-component approach (Kee, Rupley and Miller, 1989) was used for accurate calculation of molecular transport. For spontaneous ignition chemistry, Saxena and Williams' (2006) detailed chemistry scheme which involves 21 elementary steps among 8 reactive chemical species was used. This scheme gives due consideration to third body reactions and reaction-rate pressure dependant ''falloff'' behaviour. Since high-pressure hydrogen release undergoes strong under-expansion after discharging into an open space, a detailed chemistry allowing for the pressure dependant reaction rate is beneficial to accurately simulate the hydrogen spontaneous ignition phenomenon. All the 21 elementary steps are reversible. The forward specific reaction-rate constants are explicitly calculated in a three-parameter Arrhenius form, while the backward specific reaction-rate constants are computed through the chemical equilibrium constant and calculated according to the approach in CHEMKIN (Kee et al., 1989). For the stiff chemical kinetics equations, the implicit Gear's method was used.

The solver used in LES simulation of spontaneous hydrogen ignition (Bragin et al.,, 2013) utilized explicit linearisation of the governing equations with explicit method for solution of linear equation set. A second-order upwind scheme with AUSM flux splitting was applied for flow discretisation. The four step Runge–Kutta algorithm was employed for advancement of simulations in time. The time-step was determined from Courant–Friedrichs–Lewy (Courant et al., 1967) condition, where the CFL number was equal to 0.2 to ensure stability. The in situ adaptive tabulation ISAT algorithm (Pope, 1997), offering substantial reductions in run-times by up to three orders of magnitude, is applied.

The simulations of plane jets (Makarov and Molkov, 2013a) were carried out using the software ANSYS Fluent 13. The density-based explicit solver was applied for solving compressible part of the problem, and the pressure-based implicit solver was used for incompressible simulations. The standard $k-\varepsilon$ turbulent model is known to overestimate the spread rate of axisymmetric jet as shown by Pope (1978).To avoid this effect the model was used here in conjunction with MUSCL third order approximation scheme following the study by (Houf et al. 2007), where reasonable velocity decay was achieved in simulations of a free incompressible axisymmetric hydrogen-air jet. To improve stability and to avoid "flapping" of the simulated jets in the near-to-nozzle field, simulations were started as transient (unsteady) using explicit time marching, and switched to the steady-state simulations later on when the shock structure was established. Simulations in the far-field were run as steady-state thus neglected the transient term $\partial/\partial t$.

Simulations of an experimentally observed high pressure under-expanded hydrogen jet fire (Brennan et al., 2009) were conducted using an LES/VLES technique and a laminar flamelet approach coupled with a PDF method to account for flame–turbulence interaction.

Solving the flamelet equations at each time step would be computationally intensive. Thus, (Brennan et al., 2009) utilizes flamelet ‘‘libraries’’ which are generated in advance of the simulation. The flamelet equations are solved for a range of values of Z and χ_{st}. Similarly, the assumed shape PDF functions for Z and χ_{st} are calculated in advance for a range of values of mixture fraction, scalar dissipation and mixture fraction variance. The flamelets are then convoluted with the assumed shape PDFs and look up tables are constructed. The look up table contains information on species mass fraction and temperature for given values of mixture fraction, mixture fraction variance and scalar dissipation rate. The density of the flow is then calculated based on the mixture composition.

The high pressure under-expanded jet simulation described by Brennan et al., (2009) used a segregated solver with an implicit linearization of the governing equations with bounded central-difference second order accurate scheme for momentum terms and an upwind scheme for mixture fraction terms. The PISO algorithm was applied for pressure–velocity coupling. FLUENT software was used as a CFD engine. A time step of 0.005 s was chosen to compromise between maintaining a CFL (Courant et al., 1967) number of less than 1 and computational expense. The chosen time step gives a CFL of less than 1 in the majority of the domain except of the vicinity of the jet exit.

In order to ignite jet fire in (Molkov et al., 2014) which used EDC model, a numerical ignition of hydrogen-air mixture was realized by a patch with temperature 3000 K over the zone L x W x H = 1 x 0.25 x 1 cm that comprised 62 CVs and touched the pipe exit on one side. The zone was chosen to include a region with near stoichiometric hydrogen-air mixture to facilitate the ignition. The ignition was initiated at the same time or shortly after the beginning of the release and kept until hydroxyl (OH) mole fraction would reach at least 0.01, which is generally accepted value associated with flame at normal conditions (Gran and Magnussen, 1996). Time of ignition start and finish is given in Table 2.4-1.

Table 2.4-1. Inflow parameters and numerical ignition duration (Molkov et al., 2014).

Vent size H x W	Release velocity, m/s	Flow rate, g/s	Numerical ignition, s
3 x 30 cm (horizontal)	600 m/s	1.0857	0.2-0.5
	300 m/s	0.5486	5.0-6.5
	150 m/s	0.2714	0.5-1.5
30 x 3 cm (vertical)	600 m/s	1.0857	1.5-6.0
	60 m/s	0.1086	0.0-5.5
13.9 x 3 cm (vertical)	600 m/s	1.0857	0.0-6.0
	300 m/s	0.5486	0.0-2.2

Numerical experiments of hydrogen jet in an enclosure (Molkov et al., 2014) were performed using ANSYS Fluent pressure-based solver with SIMPLE pressure-velocity coupling algorithm and spatial discretization of the first order, the gravity forces were applied. The

model applied in this study of indoor jet fire is similar to the previously described numerical simulations of spontaneous ignition of hydrogen (Bragin et al., 2013).

2.4.2 Spatial discretization schemes

Xu and colleagues investigated the impact of the discretization scheme on the accuracy of simulations of the spontaneous ignition. Since the numerical dissipation is used to model the unresolved small scales, the accuracy order of the numerical schemes applied to the convection terms is vital in ILES approach. In the convection-dominant supersonic flows, high-order WENO schemes (e.g., Dimotaksis, 2005) are normally employed to reduce the numerical dissipation and to capture shock waves. The model of (Xu et al., 2007a) was subsequently improved by replacing a second-order TVD scheme for spatial differencing with high order WENO scheme (Xu et al., 2008), (Xu et al., 2009a). It was found that the second-order TVD schemes are overly dissipative to capture the mixing process and higher order weighted essentially non-oscillatory (WENO) shock-capturing schemes can better resolve the underlying physical process with the same grid resolution (Mosedale and Drikakis, 2007). However, it should be pointed out that it is generally difficult to achieve grid independent results in solving compressible inviscid Euler equations. Hence the specific details of the complicated structures resulting from solving the Euler equations may be totally non-physical and crucially depend on the amount of numerical dissipation (Shi et al., 2003). Due to numerical diffusion, the contact surface thickness, flame temperature and thickness were found to be over-predicted by the lower order schemes. On the other hand, it was found that the 9^{th}-order WENO scheme could trigger numerical oscillation and even predict negative numerical diffusion at the contact surface (Xu et al., 2008).. To minimize numerical diffusion it was recommended that numerical schemes higher than 5th-order with a grid-resolution less or equal to 10 μm should be used while one needs to exert caution with the use of the 9th or higher order schemes in case of negative numerical diffusion. Accordingly, subsequent works (Xu et al., 2009), (Wen et al., 2009) used 5th-order upwind WENO scheme (Balsara and Shu, 2000) for the convection terms. Furthermore, second order MacCormack method used in the rezone phase to solve the convection terms was replaced with a 3^{rd}-order TVD Runge–Kutta method (Balsara and Shu, 2000). This updated model had been used in a number of follow up works aimed at investigation of the effects of the obstacles and non-instantaneous membrane opening (Xu et al. 2011), (Xu and Wen, 2012) and (Xu and Wen 2014).

A University of Ulster LES simulation of spontaneous ignition described by (Bragin et al., 2013) utilized solver used explicit linearization of the governing equations with explicit method for solution of linear equation set. Green-Gauss cell-based method is used for gradients calculation. A second-order upwind scheme with AUSM flux splitting was applied for flow discretisation.

(Brenan et al., 2009) used a segregated solver and implicit linearization of the governing equations with bounded central-difference second order accurate scheme for momentum terms and an upwind scheme for mixture fraction terms. The PISO algorithm was applied for pressure–velocity coupling. FLUENT software was used as a CFD engine. A time step of 0.005 s was chosen to compromise between maintaining a CFL (Courant, Friedrichs and Lewy, 1967) number of less than 1 and computational expense. The chosen time step gives a CFL of less than 1 in the majority of the domain except of the vicinity of the jet exit.

2.4.3 Temporal discretization schemes

For transient simulations, the governing equations must be discretized in both space and time. The spatial discretization for the time-dependent equations is identical to the steady-state case. Temporal discretization involves the integration of every term in the differential equations over a time step.

The use of explicit time stepping is fairly restrictive. It is used primarily to capture the transient behaviour of moving waves, such as shocks, because it is more accurate and less expensive than the implicit time stepping methods in such cases. You cannot use explicit time stepping in the following cases:

- Calculations with a pressure-based solver or density-based implicit formulation: The explicit time stepping formulation is available only with the density-based explicit formulation. Multi-stage Runge-Kutta explicit time integration for the density-based solver can be used also.
- Incompressible flow: Explicit time stepping cannot be used to compute time-accurate incompressible flows.
- Full-Approximation Storage (FAS) multigrid and residual smoothing cannot be used with explicit time stepping because it destroys the time accuracy of the underlying solver.

In ignition simulation studies performed by (Bragin et al., 2013; Golub et al., 2008; Maxwell and Radulescu, 2011; Pinto et al., 2007) employed explicit linearization of the governing equations.

The explicit time stepping approach is available only for the explicit scheme described above. The time step is determined by the CFL condition. To maintain time accuracy of the solution the explicit time stepping employs the same time step in each cell of the domain (this is also known as global-time step), and with preconditioning disabled. For example Explicit four step Runge Kutta algorithm was employed in (Bragin et al., 2013) for advancement of simulations in time. The time-step was determined from Courant-Friedrichs-Lewy condition, where the CFL number was equal to 0.2 to ensure stability.

2.4.4 Convergence criteria

There are no universal metrics for judging convergence. Residual definitions that are useful for one class of problem are sometimes misleading for other classes of problems. Therefore it is a good idea to judge convergence not only by examining residual levels, but also by monitoring relevant integrated quantities.

To ensure a good level of convergence, besides checking residuals only, it is a good practice to check variables of interest and make sure that they are also converged. This can be done by setting monitor points on the variables of interest. For example by adding user defined monitor points to inlet mass flow rates, temperatures along the jet, pressures, mass balance in the domain etc. similar to what is described in Section 1.4.4.

In most situations regardless of the type of solver and of solving problem there are a number of issues that have to be satisfied to get good convergence i.e.

- Monitor residual convergence (for example the default convergence criterion in ANSYS Fluent requires):

  - For the globally scaled residuals expected decrease by 1e-3 for all equations to achieve qualitative convergence;
  - For the energy and P-1 equations the criterion is 1e-6;
  - To get specie balance the locally scaled residuals should decrease by 1e-5.
- Monitoring other appropriate physical variables is a good practice to confirm the overall heat and mass balance, specie conservation etc.

If residual monitors indicate that the solution is converged, but the mass imbalance is present, this means that the solution is not fully converged and you need to reduce the values for the convergence criterion and continue iterating until solution converges.

The pressure-based solver uses under-relaxation factors to relax equations in order to control the update of computed variables at each iteration. This means that all equations solved using the pressure-based solver, including the non-coupled equations solved by the density-based solver (turbulence and other scalars), will have under-relaxation factors associated with them.

Working with under-relaxation factors, the default under-relaxation parameters for all variables are set to values that are near optimal for the largest possible number of cases. These values are suitable for many problems, but for some particularly nonlinear problems (for example, some turbulent flows or high-Rayleigh-number natural-convection problems) it is practical to reduce the under-relaxation factors initially. It is good practice to begin a calculation using the default under-relaxation factors. If the residuals continue to increase after the first 4 or 5 iterations, you should reduce the under-relaxation factors.

The density-based solver uses under-relaxation factors for equations outside the coupled set and they are modified as in the pressure-based solver. The control of stability in the density-based explicit solver is defined by a maximum limit of the Courant number which defines the time step size. By default the value is 1 but cannot be more than 2. Reducing the value of CFL number can aid convergence. For the density-based implicit solver the value of CFL number is not restricted by stability limits and the default value is 5.

2.5 Analysis of the simulation results

2.5.1 Validation and sensitivity of the results

Validation and sensitivity analysis for simulations of ignition and fires generally follows the same strategy as those for non-reacting flows, see e.g. “AIAA guide for the verification and validation of computational fluid dynamics simulations” (AIAA Guide, 1998), where validation is defined as the process of determining the degree to which a model is an accurate representation of the real world from the perspective of the intended uses of the model. Similar definition is given by Stern et al. (1999) who describe validation as a process for assessing modelling uncertainty by using benchmark experimental data and, when conditions permit, estimating the sign and magnitude of the modelling error. Different approaches to estimating experimental uncertainties are presented and discussed by Coleman and Steele (1999).

Currently validation of existing ignition simulations is complicated by lack of detailed experimental data to compare simulation results – practically all available experimental studies on spontaneous hydrogen ignition are limited to the statement of ignition success or failure as a function of experimental setup and storage pressure. Information on ignition initiation, combustion development and flame propagation or extinction within the experimental setup is not available for various reasons (including complexity of this

experimental research). Thus, validation of spontaneous ignition simulations is often limited to qualitative comparison of ignition success or failure compared to experimental observation. At the moment of writing this report the only experimental research having documented details on location of ignition initiation and flame propagation in a pipe seems to be (Kaneko et al., 2015), which makes it potentially attractive for a more detailed validation of ignition simulations,

Other good practice techniques including analysis of grid sensitivity, model sensitivity, domain size, time-step, discretisation scheme etc. are equally applicable for validation of ignition simulation results, though they are the same difficult to implement. Spontaneous ignition simulations have very strict requirements to grid resolution, especially the models relying on the finite rate Arrhenius reaction rate (resolution of real flame front thickness on the numerical grid is required), while calculation domains have to include the real scale experimental facility. As a result numerical grids are large and simulations are typically conducted at the limit of available computational resources, making grid and time step sensitivity analysis not feasible (applicable to ignition model validations listed in (SUSANA D2.1, 2016))

Validation of ignition simulations is also often complicated by uncertainty about experimental setup – pipe geometry and characteristics of wall surface, presence of valves and restrictors, burst disk details and opening duration, etc.

Simulations of fires are easier to validate and to perform sensitivity analysis – there is no such disparity of scales like in ignition problems or they may be counteracted by effective (notional) nozzle approach e.g. by (Molkov et al., 2009a). Fires typically have long time scales and experiments with steady or quasi-steady state conditions are available from the literature. Available for data for validation studies typically include flame length and flame shape. However a modeller should be aware that a pure hydrogen flame is normally invisible and criteria for specification of hydrogen flame may not be straightforward, e.g. in (Schefer et al., 2007) hydrogen-air flame was made visible conducting experiments at night and in (Mogi et al., 2005b) – by adding aqueous Na_2CO_3 salt solution in hydrogen. Presence of dust particles (whether entrained in flame with air or remaining in hydrogen storage as a result of its manufacturing process) will also increase luminosity of flame and introduce additional experimental uncertainty affecting validation of simulations.

A modeller should be aware that a general recommendation to validate model simulations against a wide range of experiments with different test conditions, including but not limited to type of a release (turbulent, transitional or laminar), ignition and its location, vent size and shape (vertical or horizontal), obstacles, etc., is applicable for fire simulations as well.

2.5.2 Interpretation of the results

Interpretation of simulations, including those of ignition and fires, usually relies on integrated evaluation of results instead of monitoring and analysis of only one variable, e.g. monitoring mass and species integral balance over calculation domain, velocity field, overpressure, temperature and species distribution, observing their limiting values etc. It is beneficial to compare quantitative results of simulations against the physics of the involved phenomena, i.e. that the temperatures are realistic, pressures and velocities are within expected range, buoyancy driven flows are correctly directed, etc. Another common check-up is comparison against analytical solution where available, i.e. characteristic velocity of a fire plume having maximum temperature T_{fire} in a compartment of height H and with surrounding temperature

T_{air} may be obtained from integral solution of momentum conservation equation as $V_H = \sqrt{2\left(T_{fire}/T_{air} - 1\right) g \cdot H}$, so maximum velocity in a fire plume obtained in CFD simulation is expected to be of a similar value. Side-by-side comparison of data generated from multiple simulations is a useful practice helping to evaluate the model performance. The statistical analysis of results (Giannissi et al., 2015) can be of assistance for comparison of different models or for validation of a model against several experiments. The statistical measures often consist of one or more statistical parameters, and/or a graphical presentation of the models performance.

One of the important parameters for the interpretation of reacting flow simulation results is hydroxyl concentration, which is used to identify the area where combustion reaction is present (available only in models with chemistry included) (Bragin et al., 2013; Molkov et al., 2014). This allows, for example, seeing how the indoor flame length is increasing when the internal space of the enclosure becomes diluted by combustion products (Molkov et al., 2014). In the case of spontaneous ignition it is possible to identify that ignition is initiated in a wall boundary layer due to air presence (non-slip conditions) and a slightly higher temperature due to stagnation conditions (Bragin et al., 2013).

In cases when the combustion model does not include detailed chemistry there is no hydroxyl to identify the combustion reaction area. A temperature range of between approximately 1300 K and 1500 K was used to specify the visible flame length and width in (Brennan et al., 2009) to compare with experimental data (Schefer et al., 2007). In (Makarov and Molkov, 2013a) temperature 1300 K was used as a visible flame threshold to validate simulations against experimental study (Mogi and Horiguchi, 2009).

It is worth mentioning that in a paper by Makarov and Molkov (2013a) two numerical grids used for compressible and incompressible simulation stages were not identical at the outflow–inflow interface. An interpolation of simulation results was required at the inflow boundary of the incompressible stage domain. Special attention was paid that key flow parameters (i.e. hydrogen mass flow rate, the total impulse, the maximum hydrogen mass fraction and the maximum absolute velocity) at the interface between compressible and incompressible domains were matching each other.

3. Deflagrations

3.1 Introduction

The modelling of deflagrations remains a challenge. Unfortunately, there is no one modelling approach which is clearly superior to all others and applicable to all circumstances (Baraldi, et al., 2010a). The reasons are rooted in the complex interactions between the turbulent flow field and combustion chemistry, together with the very wide-range of applications for which models are required.

In the open atmosphere, combustion of an initially quiescent mixture of hydrogen and air begins as a laminar flame. A cellular flame structure soon develops, typically at a radius of just 0.14 m for stoichiometric conditions (Molkov, et al., 2007). However, this cellular structure rapidly breaks down into a self-similar regime of turbulent flame propagation when the flame front reaches a radius of about 1 m. Initial turbulence and wind can also affect flame propagation.

In confined but vented deflagrations, the physics tend to be more complex - largely due to a number of flow-combustion instabilities. Of particular relevance are the Rayleigh-Taylor instability (acceleration of hot and low density combustion products into cold and higher density fresh mixture) at the vent exit and, potentially, flame-acoustic interactions.

If the flame encounters obstacles its rate of propagation can be greatly increased; due to the acceleration of the flow between and around obstacles - with a consequent increase in turbulence and thus flame surface area. This results in a positive feedback between the rate of combustion and flow turbulence, leading to ever greater rates of flame propagation and eventually the possibility of transition from deflagration to detonation.

Lean mixtures, and inhomogeneous mixtures, add further complications.

More details on the physics of hydrogen deflagrations, and the difficulties which these physics pose for CFD models, are given by Molkov (2012).

Whilst the modelling of turbulence in non-reacting flows is a considerable challenge, this is only increased in the case of turbulent combustion. The main difficulty stems from the impracticality of modelling all of the spatial and temporal scales which govern turbulent combustion, except in very limited and idealised circumstances[1].

Models for turbulent combustion are therefore required, yet a lack of physical understanding of processes to be modelled, together with the limitations of numerical models used for the solution of mathematical models of turbulence and combustion, mean that this is still a developing field and that much research remains to be done.

However, the underlying physics is essentially common to deflagrations in other gases, for example natural gas, except for the much greater propensity for transition to detonation to occur with hydrogen. Following the Piper Alpha disaster in 1988 (Cullen, 1990) much work

[1] Direct Numerical Simulation (DNS) of turbulent combustion is possible, but not for practical applications. Its role is restricted to improving fundamental understanding of turbulent combustion and for aiding the development of turbulent combustion models.

was done on the development and validation of models for gas explosions. Therefore, knowledge gained in the wider modelling of deflagrations is relevant and has thus also been drawn upon in compiling this Best Practice Guidelines (BPG), i.e. in addition to knowledge gained within the SUSANA project.

3.2 Selection of physical models

The physical sub-models for turbulence and combustion essentially underpin the validity of CFD simulations of hydrogen deflagrations. The following Sections give guidance on selection of physical models for application to deflagration modelling.

3.2.1 Conservation equations

The governing equations are those for the conservation of mass, momentum, energy and chemical species, supplemented by an equation of state, which can readily be found in any textbook on fluid flow and combustion.

However, the approach taken to the modelling of turbulence (i.e. RANS or LES) determines the modelled form of these conservation equations, and also introduces additional equations. Furthermore, the modelling of combustion involves yet more modelled equations, but the exact form of these equations depends entirely on the modelling approach employed.

Thus, the governing conservation equations (derived from first principles) are not solved directly, but rather modelled forms of these equations are solved – and these modelled equations take many different forms. It is not possible to reproduce all of these forms here. However, one set of modelled equations for premixed combustion can be found below in the Section 3.2.3 ‘Premixed Combustion Modelling’.

3.2.2 Turbulence modelling

Turbulent flow consists of unsteady eddies with a wide range of time and length-scales. For FCH applications it is impossible to simulate directly all of these scales of motion, as this would require a vast computing resource which does not exist. Such approaches, known as Direct Numerical Simulation (see Section 3.1) are instead limited to very simple idealised flows at low turbulent Reynolds numbers. Models for turbulence are therefore required.

There are two main approaches to the modelling of turbulence, both of which involve an averaging of the fundamental governing conservation equations, followed by the addition of sub-models for unknown quantities which appear in these equations as a consequence of averaging.

RANS-approaches

The approach which has been in practical use for over four decades relies on the time-averaging of the conservation equations. This time-averaging results in the RANS class of models. There is a very wide range of RANS models, none of which has universal applicability.

By far the most commonly-used category of RANS model is that based on the solution of two additional turbulent transport equations. These equations provide a turbulent length and time-scale which are combined to give a turbulent viscosity which is assumed to act in addition to molecular viscosity. See Versteeg and Malalasekera (2007) for more details of such approaches.

The most common two-equation turbulence model is the k-ε model (Launder and Spalding, 1974). It is very widely-used in the modelling of turbulent flows, including deflagrations. However, it has a number of weaknesses, some of which are very significant. These weaknesses are outlined in the ERCOFTAC Best Practice Guidelines (Casey and Wintergeste, 2000) and are not repeated here. The key BPG which emerge from these Guidelines in respect of RANS models are as follows:

- There is no universally valid general model of turbulence that is accurate for all classes of flows. Validation with test data is necessary for all applications. That is, if the application represents a significant departure from previous validation cases, there will be significant uncertainty in the accuracy of results in the absence of further validation.
- When using a particular turbulence model check the published literature with regard to known weaknesses of the model. That is, it is essential that the limitations of the model are understood for the FCH application being modelled.
- Select an appropriate near-wall model (Versteeg and Malalasekera, 2007). Decide whether to use a wall function method, in which the near-wall region is bridged with wall functions, or a low Reynolds number model, in which the flow structure in the viscous sub-layer is resolved. This decision will be based on the available resources (low Reynolds number models require a very fine mesh near to the wall, which can be computationally costly) and the requirements for resolution of the boundary layer. The validity of the wall function approach or the use of a low Reynolds number model should be examined for the flow configuration under study. Wall functions are not (strictly) valid in the presence of separated regions and/or strong three dimensional flows.

Whilst wall functions are a more attractive proposition for the modelling of the near-wall region – as they are far less costly than low Reynolds number models – they may be strictly invalid in some deflagration applications, e.g. flows in vented enclosures, and around obstacles. This remains an area of uncertainty for the modelling of hydrogen deflagrations.

LES-approaches

The other main approach to the modelling of turbulence relies on the averaging of the conservation equations over a small spatial filter – and which in effect is often determined by the mesh size. The aim is to simulate the large turbulent eddies directly with the use of an appropriate mesh resolution, thereby leaving only the small-scale turbulence (which cannot be resolved on the mesh) to be modelled. This is the LES approach.

LES is based on the premise that the small scales of turbulent motion are more universal, and so more amenable to modelling, than the large scales (which are simulated directly). Therefore, the effects of the small-scale eddies are modelled using a ‘sub-grid’ model. See Versteeg and Malalasekera (2007) for an introduction to LES.

In principle, LES models of turbulence should have a more universal applicability that RANS approaches. However, in the same way that there is no universally valid RANS turbulence model, neither does there appear to be a universally valid LES model. As with RANS, there is a proliferation of LES sub-grid models.

In addition, LES needs much greater computer resource than RANS methods, as it requires not only a far finer mesh resolution but also very short computational time-steps. Furthermore, LES is much more demanding of the accuracy of numerical schemes.

This has led to the adoption of a less rigorous form of LES, in which a relatively coarse mesh is used, known as VLES – Very Large Eddy Simulation. Whereas the mesh in a LES would allow for, say, 80% of the turbulent kinetic energy of the flowfield to be resolved directly, in a VLES the mesh is too coarse to resolve many of the turbulent eddies – such that only 20% of the turbulent kinetic energy would be resolved directly, the remainder must be accounted for by the sub-grid model (Pope, 2000).

Many of the applications of LES to the modelling of hydrogen deflagrations fall into the category of VLES.

The advantage of VLES over LES in deflagration modelling is a reduction in the number of mesh cells by many orders of magnitude, typically of the order of 10^6 cells for practical applications (Makarov, et al., 2010). The drawback is that far greater reliance is then placed on the performance of the sub-grid model.

This leads to the following BPG, which follow similar lines to those for RANS models:

- As there is no universally valid general model of turbulence that is accurate for all classes of flows, validation with test data is necessary for all applications. That is, if the application represents a significant departure from previous validation cases, there will be significant uncertainty in the accuracy of results in the absence of further validation.
- VLES sub-grid models for turbulent combustion modelling need to be robust, as the majority of the turbulent kinetic energy cannot be resolved by the mesh. Therefore, it is essential that the capabilities, limitations, and range of applicability of the sub-grid model are understood for the FCH application being modelled. An RNG-based (ReNormalization Group) model (Yakhot and Orszag, 1986) has been found effective for the VLES modelling of deflagrations in the open atmosphere (Molkov, et al., 2007) and in vented enclosures (Keenan, et al., 2013).
- As with RANS approaches, an appropriate near-wall model needs to be used. See above for guidance. This is an area of uncertainty in the VLES modelling of hydrogen deflagrations.

3.2.3 Premixed combustion modelling

3.2.3.1 Background

Modelling of premixed combustion in the context of hydrogen studies typically means deflagration modelling (the other potential application are microflames and lifted off flames, where partially premixed combustion can occur). Deflagration modelling uses an equation system similar to the one used for fire modelling. The important difference however, is that deflagration modelling uses compressible approach. Species transport is commonly modelled using progress variable method. Furthermore, the approach to modelling of burning velocity (i.e., combustion rate) has strong effect on the deflagration process development.

3.2.3.2 Open-air deflagration

Introduction

The most common RANS-based approach to the modelling of hydrogen deflagrations appears to be the two-part methodology in which a turbulent burning velocity is calculated in

conjunction with the solution of a transport equation for a reaction progress variable. For instance, see (Yanez, et al., 2010), (Wen, et al., 2010) and (Wooley, et al., 2013).

VLES approaches to the modelling of hydrogen deflagrations retain many of the attractive features of a full LES approach to combustion modelling, whilst overcoming the practical limitations of LES regarding the need for a very fine mesh resolution and thus very large meshes. This is essentially because it is the large turbulent length scales which are characteristic of deflagrations (Molkov, 2012), and VLES offers the prospect that these large length scales can be captured using relatively coarse meshes. Of course, the chemical reactions occurring in combustion take place at very fine molecular-scales, and these processes must be modelled rather than captured directly.

UU LES model

An important feature of large-scale open atmosphere (without obstacles) deflagrations, which a CFD model desirably should reproduce, is the self-similar flame acceleration even in quiescent (no flow turbulence) mixture. The LES model developed at the University of Ulster (Molkov et al., 2007) had been applied to simulate an open-air flame front propagation in the largest documented open atmosphere hydrogen-air deflagration experiment GHT 34 (Schneider and Pförtner., 1983).The model (Molkov et al., 2007) comprised of filtered three-dimensional mass, momentum and energy conservation equations in the fully compressible form with the flame front propagation modelled using the filtered progress variable equation:

$$\frac{\partial}{\partial t}(\overline{\rho}\widetilde{c}) + \frac{\partial}{\partial x_j}(\overline{\rho}\widetilde{u}_j\widetilde{c}) = \frac{\partial}{\partial x_j}\left(\frac{\mu_{eff}}{Sc_{eff}}\frac{\partial \widetilde{c}}{\partial x_j}\right) + \overline{S}_c, \quad (3.2.1)$$

where c is the combustion progress variable, S_c is a progress variable source term and Sc_{eff} is the effective Schmitt number. The dilution of an initial hydrogen-air cloud by atmospheric air is addressed by additional conservation equation

$$\frac{\partial}{\partial t}(\rho Y_a) + \frac{\partial}{\partial x_j}(\rho u_j Y_a) = \frac{\partial}{\partial x_j}\left(\frac{\mu_{eff}}{Sc_{eff}}\frac{\partial Y_a}{\partial x_j}\right) + \frac{Y_a}{Y_f + Y_a}\overline{S}_c, \quad (3.2.2)$$

where Y_a and Y_f are mass fractions of air and fuel, respectively. The source term in the progress variable equation can be written using the gradient method (Prudnikov, 1967), (Laskey et al., 1988) as:

$$\overline{S}_c = \rho_u S_t \left|grad\,\widetilde{c}\right|, \quad (3.2.3)$$

where $\left|grad\,\widetilde{c}\right|$ is the gradient of the progress variable and S_t is the turbulent burning velocity. The use of the turbulent burning velocity concept and the gradient method provides a convenient way to ensure that the prescribed physical mass burning rate per unit area $\rho_u S_t$ is simulated in an artificial numerical flame front, which occupies 3–5 control volumes independent of a mesh size. The gradient method enables decoupling of the physical mass burning rate from the numerical requirement of having 3–5 cells through the simulated flame front thickness.

In the flamelet combustion regime the turbulence–combustion interaction is purely kinematic and chemistry enters the combustion model only through a value of the laminar burning velocity S_u. The model therefore has no adjustable parameters. An increase of the turbulent burning velocity occurs due to unresolved sub-grid scale (SGS) effects of the hydrodynamic

instability of premixed turbulent combustion. It is modelled using transcendental equation derived from the renormalization group (RNG) theory (Yakhot, 1988):

$$S_t = S_u \cdot \exp\left(\frac{u'}{S_t}\right)^2, \tag{3.2.4}$$

where S_u is the burning velocity of sub-grid flamelets and u' is the SGS unresolved fluctuation velocity.

The "small-scale" turbulence, generated by the flame front itself at scale comparable with a thickness of real laminar flame, changes the burning velocity of "sub-grid scale" flamelets due to flame wrinkling, i.e. increase of flame surface area. This phenomenon cannot be resolved by LES, when a large-scale problem is simulated, and has to be modelled. To account for an increase in the flame propagation velocity caused by this phenomenon the burning velocity of SGS "flamelets" was modified from laminar to:

$$S_u = S_{u0} \cdot \Xi, \tag{3.2.5}$$

where S_{u0} is the laminar burning velocity, and Ξ is the flame front wrinkling factor reflecting effect of the small-scale turbulence, generated by flame front itself, on the value of SGS burning velocity. As the onset of instabilities occurs soon after the ignition, it seems that the "initial" burning velocity value, measured and reported by the authors of the experiment, i.e. S_{u0}=2.39 m/s, already accounts for some velocity augmentation. The value of laminar burning velocity of stoichiometric hydrogen–air mixture S_{u0} =1.91 m/s (Lamoureux et al., 2002), obtained by the Schlieren method for a premixed flame, propagating outward from a point ignition source, was used in simulations. In this study, the same value of burning velocity was used in the whole range of flammable hydrogen concentrations in diluted by air mixture down to the lower flammability limit of 4% by volume. Below the lower flammability limit the source term in the progress variable equation was equal to zero.

The combustion product expansion coefficient for stoichiometric hydrogen–air mixture at conditions of experiment GHT 34 (Schneider and Pförtner., 1983), calculated using the CHEMKIN code, is E_i =7.2. The maximum value of the flame front wrinkling factor due to selfinduced flame front turbulence, according to formula

$$\Xi_{\max} = \frac{E_i - 1}{\sqrt{3}}, \tag{3.2.6}$$

$\Xi_{\max}$ = 3.6. In the model (Molkov et al., 2004) the self-similar acceleration of flame front was simulated vie the gradual increase of this wrinkling factor Ξ with a flame front radius from its initial value Ξ = 1, immediately after ignition, to the maximum theoretical value $\Xi_{\max}$, when the self-similar regime of turbulent flame propagation is established, was calculated by the equation:

$$\Xi = 1 + (\Xi_{\max} - 1)(1 - \exp(-R / R^*)), \tag{3.2.7}$$

where the characteristic radius of the onset of self-similar flame propagation regime was accepted in (Molkov et al., 2004) according to the analysis of Gostintsev et al. (1988), R^* = 1.0 m.

In (Molkov et al., 2006) the self-similar acceleration of the flame front was accounted using the fractals mechanism for the flame surface development:

$$S_t = S_u \cdot f\left(Y_{H_2}\right) \cdot \left(R/R_0\right)^{D-2}, \tag{3.2.8}$$

where S_u - burning velocity at the radius R_0 of the fractal propagation regime onset and D=2.33 – accepted in this study the fractal dimension value. In this model the dependence of burning velocity on fuel concentration was accounted for by using a linear function $f\left(Y_{H_2}\right)$, which was equal $f\left(Y_{H_2}\right)=1$ in stoichiometric mixture and $f\left(Y_{H_2}\right)=0$ at lower flammability limit (4% by volume of hydrogen).

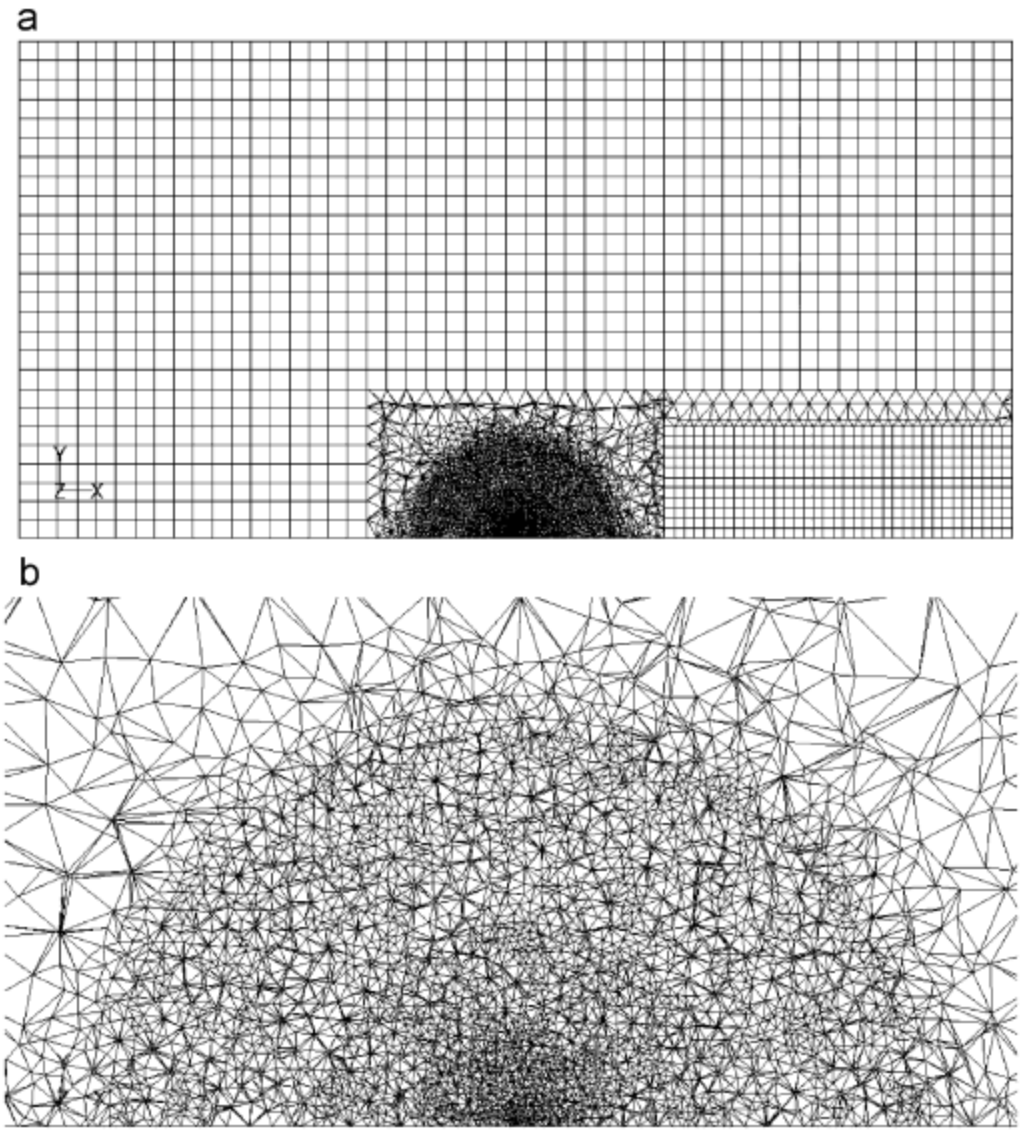

Figure 3.2-1. Cross section of the calculation domain: (a) whole domain, (b) enlargement of the area $R \le 22$ m.

The simulations used FLUENT (2006) realization of LES based on the control-volume discretisation method as numerical solver. The discretised governing equations were solved using the explicit method. Convection terms were linearised using the second order accurate upwind scheme, diffusion terms—using the central-difference second-order accurate scheme.

The Runge–Kutta algorithm was employed for advancement of the solution in time. The time step was determined from CFL = 0.8 condition.

Simulation pressure dynamics was compared against experimental records at distances up to 80 m. The calculation domain included not only the space for flame propagation and location from where simulated pressure dynamics was recorded, but the whole area of hemispherical pressure wave propagation and measured 200 × 200 × 100 m (L × W × H). The tetrahedral unstructured mesh was used in the area of combustion with an average control volume (CV) size from about 0.4 m close to the ignition source to obtain better resolution in the flame propagation area and up to 1.0–1.2 m beyond flame propagation at $10 < R \leq 22$ m. Then tetrahedral CV size increased gradually with distance up to 4 m closer to the domain boundaries. To decrease the total number of CVs and simulation time, the area beyond 30 m from the ignition source was meshed using structured hexahedral grid with CV size 4 m. However, the area designated for recording pressure dynamics had a finer mesh resolution with CV size just 2 m to minimize impact of numerical diffusion on the recorded overpressure dynamics. All above allowed to keep the total number of CV at a relatively modest 309 494 (Molkov et al., 2007). The calculation domain cross section and the enlargement of its area inside a radius $R \leq 22$ m are shown in Figure 3.2-1.

Non-slip adiabatic boundary conditions were applied on the ground. Non-reflecting boundary conditions were used on the boundaries in atmosphere. The initial pressure in the calculation domain was equal to p = 98.9 kPa, and the initial temperature T = 283 K. The initial value of the progress variable and air concentration at $R \leq 10$ m, were c = 0, Y_a = 0.9713; and at $R >$ 10 m: c = 0, Y_a = 1.0. Ignition was modelled by an increase in the progress variable in one control volume during 15 ms, calculated as a time of laminar flame propagation through this control volume.

Simulation of large scale deflagrations in open air may require account for fractal nature of the flame shape, leading to flame acceleration. For example, inter-comparison model exercise described in Garcia et al., (2010), demonstrated that introduction of fractal model in the expression for burning velocity allowed capture of experimentally observed flame acceleration. As can be seen in Figure 3.2-2 (simulation “UU(a)” and “UU(b)”), account for fractal flame front shape reproduces flame acceleration in a large-scale open atmosphere deflagration, closely following experimental curve of flame radius dependence on time.

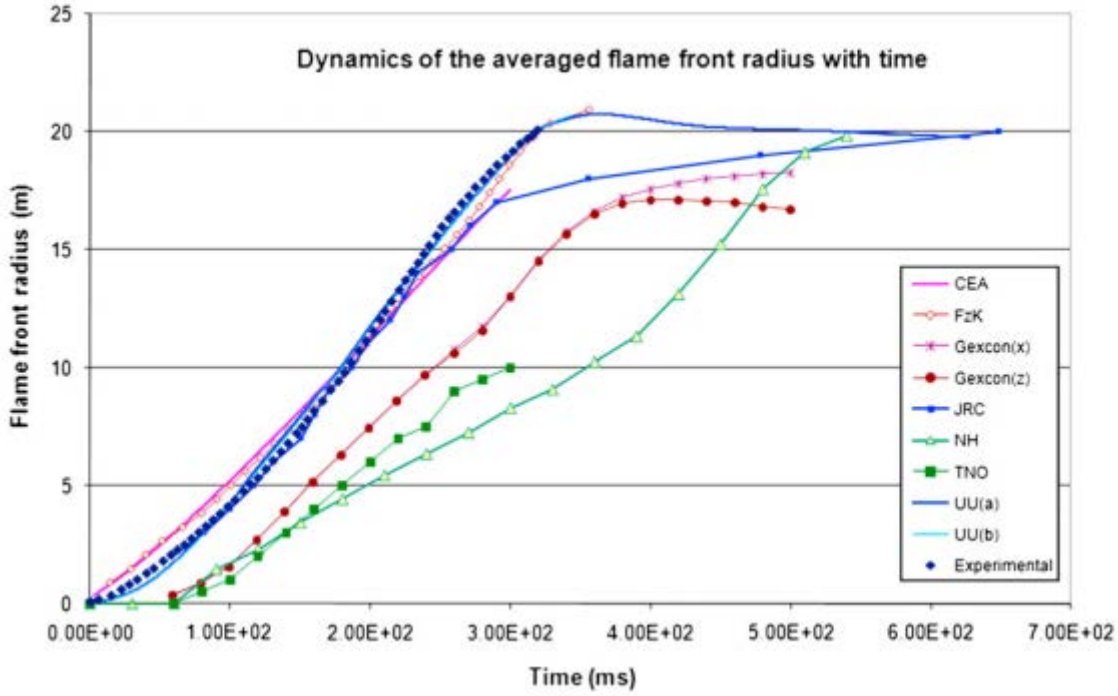

Figure 3.2-2. Average flame front radius versus time – comparison of experimental data versus simulations. Simulations UU(a) and UU(b) incorporate the term modelling fractal shape of the flame front (Garcia et al., 2010).

Based on the above, the BPG for modelling of open air deflagrations are:

- The self-similar flame acceleration, observed for large-scale (i.e. order 1 m and larger) open-air deflagrations, should be addressed in the model.
- Calculation domains should be large enough to include not only the flame propagation area and area of particular pressure sensor, but extend equally in all axes directions from the ignition source to catch spherical pressure wave propagation. Ideally some further space beyond the point, where pressure is of interest, should be included in the computational domain to avoid influence of boundary conditions on the simulation results.
- Use of uniform mesh in the area of flame propagation is advisable.

3.2.3.3 Vented deflagration

Introduction

This section addresses modelling and simulations of deflagrations in vented enclosures including modelling of the Rayleigh-Taylor (RT) instability at the vent exit, which is believed to be an important for reproduction in simulations of so called external explosion (or sometimes called "coherent deflagration") phenomenon and has been examined by several research groups. The section also touches modelling of deflagrations in closed vessels, i.e. the vent area is zero.

Keenan, et al. (2013) investigated the Rayleigh-Taylor instability in the context of a confined vented hydrogen deflagrations in a 63.7 m^3 chamber. They concluded: "…..*when considering the modelling of large scale vented deflagration scenarios, the Rayleigh Taylor instability must be included as a sub-grid scale premixed combustion sub-model*." In the absence of a

sub-model for the RT instability, they found that the intensity of the external explosion, and in turn the magnitude of the internal explosion overpressure, could not be accurately captured.

This leads to the following BPG, applicable to both RANS and VLES approaches:

> A sub-model for the Rayleigh-Taylor instability should be included for accurate prediction of the intensity of both the external explosion and, in turn, the intensity of the internal explosion. For example, see Yanez, et al. (2010) for a RANS-based methodology and Keenan, et al. (2013) for a VLES methodology.

Rayleigh-Taylor (RT) instability impact

Keenan at al., (2014) performed numerical simulation of vented deflagration under conditions similar to the conditions used in the experiments described by Bauwens et al. (2011). These experiments were performed using the FM Global 63.7 m^3 large scale test chamber, with a single square vent of 2.7 m^2 or 5.4 m^2. Ignition occurred at either the centre of the back wall or at the centre of the chamber, at a height of 1.5 m. Hydrogen concentration in air was 18% by volume inside the chamber.
Numerical simulation was based on the equation system described in (Molkov et al., 2006). The transport equation for the progress variable, which is defined as the mass fraction of the products of combustion, is applied for flame propagation tracking:

$$\frac{\partial}{\partial t}(\overline{\rho}\widetilde{c}) + \frac{\partial}{\partial x_j}(\overline{\rho}\widetilde{u}_j\widetilde{c}) = \frac{\partial}{\partial x_j}\left(\frac{\mu_{eff}}{S_{c\,eff}}\frac{\partial \widetilde{c}}{\partial x_j}\right) + \overline{S}_c, \qquad (3.2.9)$$

where c is the combustion progress variable, S_c is is a progress variable source term and $S_{c\,eff}$ is the effective Schmitt number. The source term in the progress variable equation can be written using the gradient method (Prudnikov, 1967), (Laskey et al., 1988) as:

$$\overline{S}_c = \rho_u S_t \left|grad\,\widetilde{c}\right|, \qquad (3.2.10)$$

where $\left|grad\,\widetilde{c}\right|$ is the gradient of the progress variable and S_t is the turbulent burning velocity.
The effective viscosity, effective Prandtl number and Schmidt number are calculated according to the renormalization group (RNG) theory (Yakhot and Orszag, 1986). Simulation used the latest version of the multi-phenomena turbulent burning velocity deflagration model as described in (Molkov, 2012) based on a modified Yakhot (1986) equation and takes into account various phenomena affecting the turbulent burning velocity.

The simulation results shown in Figure 3.2-3. They are shown compared against experimental data on internal pressure dynamics (Bauwens et al., 2011). When considering the central ignition cases, the original model failed to satisfactorily reproduce the experimental pressure dynamics (Bauwens et al., 2011). However the model did show general agreement with the maximum pressures and general shape of the experimental results, when considering the back wall ignition case. It is clear from these results that the first distinct pressure peak has not been reproduced.
Rayleigh-Taylor instability was first described by Lord Rayleigh (1883) and by Sir G. Taylor (1950). It occurs at the interface between two fluids of different densities, subjected to acceleration in the direction from the lighter to the heavier. Accelerations in the flow, as described by Zeldovich et al.(1985), may vary periodically in magnitude and sign and as such can have a stabilizing and destabilizing effect on the flame front.
The growth of this instability has been found to occur most prominently as the flame accelerates through the vent (Tsuruda and Hirano, 1987) and also close to the vent following

the expulsion of the hot combustion gases (Solberg et al, 1981). Additionally, according to previous research at the University of Ulster work (Makarov et al., 2010), the flow conditions required for the growth of RT instability were identified following the application of the former model to analysis of the experiments described in (Shirvill et al., 2007). This result provided the basis for the inclusion of RT instability during the simulation of the present vented deflagration scenarios.

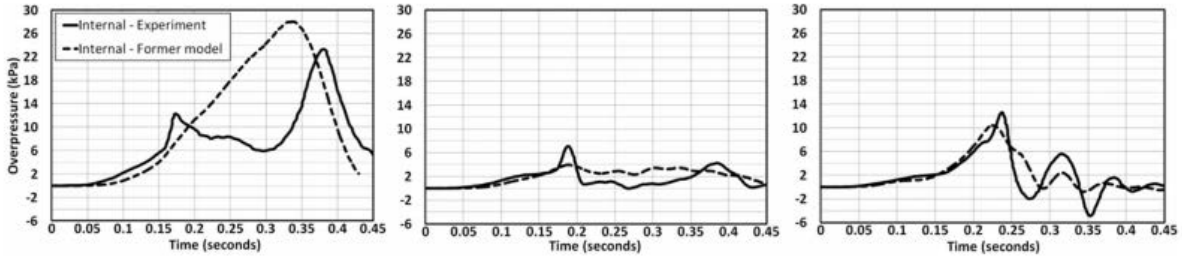

Figure 3.2-3. Comparison between experiment and original model simulations, central ignition case, 2.7 m^2 vent (left); central ignition case, 5.4 m^2 vent (centre); and back wall ignition case, 5.4 m^2 vent (right).

Rayleigh-Taylor instability was identified as playing a major role in pressure build-up during the external deflagration encountered within large scale scenarios. A model representing this instability has been developed (Keenan et al, 2014) and added to the multi-phenomena turbulent burning velocity deflagration model. The model has been implemented in the form of a separate transport equation for the Ξ_{RT} wrinkling factor, containing source and sink terms developed based on phenomenological considerations of RT instability. Detailed description of the RT model implementation is provided in (Keenan et al., 2014).

The influence of this mechanism was limited to the external deflagration only. This updated model was then tested against the pressure-time history data obtained from large scale experiments undertaken by FM Global (Bauwens et al., 2011). Following the addition of this mechanism the intensity of the external deflagration was substantially increased. This had a significant influence on the internal pressure dynamics. The increased intensity of the external deflagration caused a decrease in the efficiency of the venting process, leading to an increase in the internal pressure. Following the fast dissipation of the external premixed combustion, the high pressure inside the chamber could be more efficiently vented. This process, now more closely captured, recreated the experimentally observed first pressure peak recorded during each experiment analyzed.

Figure 3.2-4 demonstrates that, following the introduction of the RT instability mechanism to the model, the simulation results have improved. In the 5.4 m^2 vent cases the magnitude of the internal pressure peak associated with the external deflagration has been more closely replicated. The general shape of the pressure-time curves produced from both central and back ignition for the case with 5.4 m^2 vent agree quite closely with the experimental results. The sharp pressure increase in these cases, associated with the external deflagration has now been reproduced. Furthermore, for the case of the central ignition in the simulation with 5.4 m^2 vent, the decrease in pressure to near atmospheric levels following this peak, has been replicated.

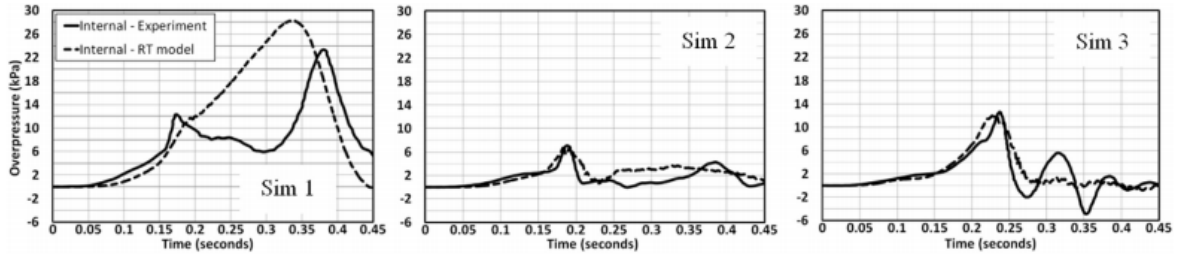

Figure 3.2-4. Comparison between experiment and RT model simulations, central ignition case, 2.7 m^2 vent (left); central ignition case, 5.4 m^2 vent (centre); and back wall ignition case, 5.4 m^2 vent (right).

The introduction of RT instability into the multiphenomena turbulent burning velocity deflagration model led to closer agreement between the simulated and experimental results. The addition of this mechanism was required in order to capture the main features and pressure transients associated with the external explosions ("coherent deflagrations") that occurred. Therefore:

when planning to model large scale vented deflagration scenarios (especially with large openings), RT instability should be considered for inclusion in SGS premixed combustion sub-model.

3.2.3.4 Congestion

Obstacles in the path of the flame front can have a very large influence on rates of combustion, flame propagation and therefore peak overpressure. They also pose a considerable challenge in their modelling, as they can be too numerous and/or at too small a scale to be able to resolve directly with the mesh. However, their effects cannot be ignored.

The approach which is usually taken is to include sub-models to account for their influence, often referred to as PDR – Porosity Distributed Resistance. The PDR approach has been most commonly-used within the context of RANS modelling of deflagrations.

For example Puttock et al. (2014), report the application of a PDR-approach to the modelling of hydrogen deflagrations based on the OpenFoam code, in which the dependent variable is the flame wrinkle factor; defined as the ratio of the average flame surface area per unit volume to the average flame area projected in the direction of the mean flame propagation. In this method the sub-grid flame area generation rate is included as a source term for flame wrinkle factor. It is reported that this leads to a flame thickness which is not dependent on mesh cell size, and thus good mesh independence.

FLACS-Hydrogen (Hansen et al., 2005) also uses a PDR-based approach. However, PDR approaches can rely heavily on calibration against test data, so there is uncertainty when they are applied outside the range of known validation cases.

- Follow code-vendor guidelines when applying PDR-based methods.
- Often, the partitioning of the geometry between mesh-resolved and sub-grid obstacles is carried out automatically. The user must understand how this is undertaken to avoid the modelled geometry being unexpectedly modified.
- When using PDR-based models outside their range of validation there will be significant uncertainty in the accuracy of results.

3.2.3.5 General comments

There appears to be a large difference in complexity between experiments used to validate and guide the development of hydrogen deflagration models, and FCH applications. For instance, the former are usually undertaken with homogenous hydrogen-air mixtures, often at stoichiometric conditions and often with quiescent initial conditions. However, in FCH applications, releases of hydrogen are often from high pressure sources, leading to high initial turbulence and a markedly non-uniform distribution of hydrogen – in which concentrations can range from 100% to 0%. In other circumstances, stratified flows and layering can occur. Therefore, in practice, releases of hydrogen often do not result in fully pre-mixed conditions.

The experience from modelling of deflagrations of realistic releases of natural gas (Hansen et al., 2001) is that models perform significantly less well when compared to validation cases for the idealised quiescent and uniform stoichiometric conditions which have been used to guide their development. There is no reason to suspect that this will not also be the case with hydrogen deflagrations.

Indeed it appears that the modelling of lean hydrogen-air deflagrations poses particular difficulties, not least because of uncertainty in the laminar burning velocity at low concentrations.

These difficulties are described by Makarov and Molkov (2013b) in the modelling of a deflagration in a 120 m^3 experimental facility with a small vent area, using a 10% by volume mixture of hydrogen in air. In this pilot study the authors found it necessary to introduce an ad-hoc flame wrinkling factor which took different values depending on the ignition location. They concluded that this factor was needed to compensate for effects not explicitly included in the overall model, such as the Rayleigh Taylor instability at the vent exit and flame-acoustic interactions. This leads to the following BPG:

- It should not be assumed that models which have been demonstrated to be valid for uniform and / or stoichiometric conditions are also valid in general for non-uniform / lean mixtures.

Usually, the approach taken in the modelling of natural gas deflagrations is to convert the non-uniform cloud resulting from a realistic release, to an equivalent volume of stoichiometric gas-air mixture. There are a number of means by which this conversion can be undertaken (Hansen et al., 2013), leading to greater or lesser conservatism in the size of the equivalent stoichiometric cloud.

It is not clear whether this issue has been fully addressed in the hydrogen deflagration modelling community, although Middha and Hansen (2009) do compare peak overpressures obtained from modelling combustion in a non-uniform hydrogen cloud to that of its stoichiometric equivalent; they concluded that the two sets of values “agree reasonably well”.

However, if models are to be used in risk assessments, rather than just compared against validation cases, account will regularly need to be taken of highly non-uniform initial conditions. This leads to the following tentative BPG:

- The highly non-uniform concentration field resulting from a realistic release of hydrogen should be post-processed to an equivalent uniform stoichiometric volume before deflagration modelling is undertaken - unless the deflagration model has been specifically validated for such non-uniform conditions.

- The method used to undertake this conversion to an equivalent uniform stoichiometric volume should be conservative, i.e. err on the side of caution.

There are a very wide range of approaches which have been applied to the modelling of deflagrations (Baraldi et al., 2010a). For RANS-based models these include: the Eddy Break-up Model, the Eddy Dissipation Model, turbulent flame speed approaches in conjunction with a reaction progress variable, the G-equation approach, PDF approaches, Flame Surface Density Models, and Fractals models. Within each of these approaches there can be many alternative methods employed – for example, Flame Surface Density models can be based on a transport equation and several models exist to close that equation, such as the Coherent Flame Model, amongst others. For LES, there is also a wide range of combustion models which have been employed, often similar in approach to RANS-based models.

It is impractical to provide BPG for each of these approaches. Instead, BPG are formulated for those combustion models which have been applied specifically to the modelling of hydrogen deflagrations and which show the most promise of wide applicability.

However, it is stressed that, at this stage, no one model appears to be decisively superior. For instance, the outcome of an inter-comparison exercise on the performance of CFD models in simulating hydrogen deflagrations in a tunnel (Baraldi et al., 2009) concluded that a wide range of combustion modelling approaches, both RANS and VLES-based, were able to successfully capture peak overpressures – and to within 20% of measurements.

Broadly similar conclusions were reached during an inter-comparison exercise on the modelling of hydrogen deflagrations in open atmosphere (Garcia et al., 2010), and vented hydrogen deflagrations (Baraldi et al., 2010b), although in both cases overall levels of agreement were often less satisfactory.

The difficulties of reaching a conclusion on model superiority have been highlighted by Makarov et al. (2009a) in an inter-comparison of a wide range of deflagration models (seven different models, used by seven partners) applied to a hydrogen explosion in a vehicle refuelling station. The authors stated that although a great deal of work had been done in this inter-comparison, it was still relatively limited: "*single experimental test, only two simulations out of nine are really 'blind', only one partner provided a grid sensitivity analysis*" and concluded: "*It is also worth noting that the authors do not intend to claim, based on this single comparison with experiments, that some particular models are good and some are bad*".

On a different matter, although VLES approaches to the modelling of hydrogen deflagrations appear to have fewer free parameters than some RANS methods, there still appears to be some uncertainty in the best values of parameters. For instance, in the approach used by the University of Ulster (Makarov and Molkov, 2013b) and NCSR Demokritos (Tolias et al., 2014) a model constant ψ appears ($0 < \psi < 1$). A value of unity is in use for lean hydrogen-air mixtures and a value of 0.5 for near-stoichiometric mixtures. Tolias et al. (2014) examined the effect of a small reduction in the value of ψ, from 0.5 to 0.45, in the modelling of hydrogen deflagrations in an empty tunnel. They found that the maximum overpressure was also reduced, by 7 % to 8 %, and that it was brought into somewhat better agreement with measurements. This leads to the following BPG:

- The values of model constants recommended by code developers should be used, unless otherwise indicated by research which is directly relevant to the FCH application being modelled.

Finally, the following BPG applies to all hydrogen deflagration modelling applications of CFD:

- Guidance provided by code vendors and developers must be followed. For instance, see (Hansen et al., 2005).

3.3 Problem setup

3.3.1 Domain design

The extent of the domain has the potential to greatly affect the results of computations. If the domain is too small the propagation of the pressure wave will not be correctly captured.

- Generally, the domain should be much larger than the expected flammable volume.

For example, in the VLES modelling of hydrogen deflagrations in a 4.6 m x 4.6 m x 3.0 m vented enclosure, Keenan et al. (2013) report that: "*The calculation domain comprises a large hemispherical area of radius 25 m. At its centre is a representation of the deflagration facility. This large area was created in order to avoid the effects of boundary conditions on the external deflagration and also to accommodate the diverging pressure wave generated.*"

In addition, Makarov and Molkov (2013b) describe the VLES modelling of lean hydrogen deflagrations in an enclosure of dimensions 10 m x 4 m x 3 m, with a vent size of 0.74 m x 0.74 m. In these simulations the enclosure was located centrally within a hemispherical domain of radius 50 m.

Tolias et al. (2014) report simulations of hydrogen deflagrations in a tunnel of length 78.5 m and 2.4 m diameter. Results compared favourably to experimental measurements of pressure-time histories. However, the computational domain was much larger than the tunnel, being 200 m long, 60 m wide and 31 m high. The authors also explored the effect of a larger domain, but found this to have negligible effect.

In the modelling of hydrogen deflagrations in the open, equally large domain sizes are required. Thus, Molkov et al. (2007) use a hemispherical domain of radius 200 m surrounding a hydrogen-air cloud of radius 10 m.

These two examples illustrate the extent of the domain which could typically be required. However, there is a trade-off between the overall extent of the computational domain and the required computing resource; as the former is increased, so does the latter.

- Check the open literature for applications of CFD modelling to FCH technologies. Choose a computational domain which has been shown to be sufficiently-large for applications which most closely mirror that to be modelled.
- Sensitivity tests to the extent of the computational domain should be undertaken unless there is supporting information from the open literature.

There is also interplay between the location of far-field boundaries and the boundary conditions specified at these locations. This issue is further addressed in Section 3.3.3.

3.3.1.1 Geometry

Geometry, and its representation, is a key aspect of CFD modelling, especially for practical applications of CFD. It is particularly relevant in the case of hydrogen deflagrations, when

obstacles can have a major impact on rates of flame propagation, and in the venting of confined deflagrations in which vent area strongly influences peak overpressures.

Often, PDR-based explosion models will automatically partition the geometry into mesh-resolved and sub-grid elements; the BPG in 3.2.3.4 should be followed.

At the stage in a project when a risk assessment is undertaken, the geometry may not yet be finalised. This uncertainty is addressed in more detail in the ERCOFTAC BPG (Casey and Wintergeste, 2000), and leads to the following guidance:

- Check that the modelled geometry reflects the actual 'as-built' geometry.

Lea (2010) provides general advice on how to ensure that CFD simulations meet project objectives, and highlights the importance of ensuring that the user does not become drawn into representing geometrical elements which have negligible influence on flow and combustion. Otherwise, there is a danger that the user will waste time and computational resource which should have been more properly expended on, for example, refining the mesh in key areas of the domain.

If it is unclear whether a loss of geometrical detail will be significant, scoping simulations should be undertaken comparing results with and without such detail included.

3.3.2 Meshing

The mesh resolution has a very important influence on the magnitude of numerical error. In extreme cases mesh-related numerical error can contaminate all aspects of the computation such that little credence can be placed on the results.

As a less extreme example, Makarov, et al (2009b) report that mesh resolution appeared to be the determining factor in an assessment of the performance of a wide range of approaches to the modelling of lean uniform and non-uniform mixtures of hydrogen and air in a 10.7 m^3 closed vessel. The physical models ranged from a sophisticated VLES-based approach to the modelling of turbulence and combustion – to a simple inviscid flow model with a flame front tracking algorithm. They concluded: "……*the sophisticated model is not the only solution and in many cases cannot substitute for the simple model and better grid resolution*".

- The sensitivity of the model results to the mesh resolution should be examined.

There is no single best mesh type, i.e. structured, unstructured, tetrahedral/polyhedral cells, etc. For instance, good results for pressure time histories in hydrogen deflagrations have been obtained for a structured Cartesian mesh with area porosities to represent curved solid surfaces (Tolias et al., 2014), and with a fully unstructured tetrahedral mesh (Keenan et al., 2013). In addition, Wooley et al. (2013) successfully use an adaptive mesh – which is automatically refined in response to regions of high flow gradients – to track the flame front in confined deflagrations in methane-hydrogen and air mixtures.

PDR-based RANS models for hydrogen deflagrations in spaces congested by obstacles may have been calibrated against test data using a particular mesh cell size, or a limited range of cell sizes. The code vendor may offer advice on the mesh resolution to employ:

- When applying PDR-based RANS models, follow code-vendor guidelines on mesh resolution.

3.3.3 Boundary conditions

The boundary conditions define the computational problem. Therefore, they are of great importance.

In the modelling of hydrogen deflagrations, two types of boundary usually need to be considered; solid walls and outer far field boundaries in the atmosphere.

- A successful strategy appears to be the application of adiabatic, no-slip conditions at solid boundaries, and a non-reflecting pressure condition at far field boundaries (Molkov et al., 2007), (Keenan et al., 2013).

The application of adiabatic wall boundary conditions is a simple approach, but it should be noted that this will almost always tend to lead to the prediction of higher over-pressures than would otherwise have occurred - as there is no heat loss to solid surfaces. Exceptions to this general rule could possibly occur if significant buoyancy-induced natural ventilation flows, which may increase initial turbulence, would otherwise be present prior to ignition.

For instance, Tolias et al. (2014) suggest that after peak pressure has been reached in the modelling of hydrogen deflagrations in a tunnel, the use of adiabatic wall boundary conditions are likely to have been responsible for the pressure drop being too slow in comparison to measurements. A similar conclusion was also reached by Baraldi et al. (2009)

As outlined in Section 3.3.1, there is also interplay between the type of boundary condition and the location of far-field boundaries. For instance, Gallego et al. (2005) conclude that the modelling of minimum pressures (in the expansion wave) from hydrogen deflagrations in the open atmosphere were not well captured during a code inter-comparison exercise as a consequence of a combination of too small a computational domain and the specification of simple outflow conditions at the far-field boundary. They conclude that this could have been avoided by the use of a larger domain. This conclusion was also drawn by Garcia et al. (2010).

In-flow to the computational domain - for example, wind in FCH applications in the open atmosphere - can lead to uncertainty in the specification of boundary conditions, especially for turbulence quantities.

- When modelling hydrogen deflagrations in the open atmosphere, follow best practice guidance from the atmospheric flow modelling community for the specification of in-flow boundary conditions, e.g. Franke et al. (2007) and take note of Section 1.3.3 of these BPG. Note that different specifications apply to RANS and LES approaches.

3.3.4 Initial conditions

As expected, for vented hydrogen-air explosions an increase in the initial turbulence increases the flame propagation speed and this translates into higher peak overpressures.

Bauwens and Dorofeev (2014) state that initial turbulence acts primarily by generating higher initial flame wrinkling while having a minimal effect on the growth rate of wrinkles. They propose that this can be accommodated in CFD simulations by application of a factor to increase the effective burning velocity (presumably in the initial stages only), but conclude that further research is required.

Earlier, (Wen et al., 2010) reported that use of a turbulent burning velocity approach (in conjunction with a transport equation for reaction progress variable) – as commonly used in the RANS-modelling of deflagrations – led to a strong dependence on initial turbulence

parameters. To achieve best agreement with experimental data for hydrogen-air explosions in a model storage room the authors "…..*fine-tuned (turbulence parameters) to…..bring the predictions close to experimental data at 30% hydrogen concentration case"*. Following tuning, the model was applied to a wider range of concentrations; 15% and 50%. However, in FCH applications initial turbulence parameters are likely to be unknown.

It is also noted that many validation cases will be for quiescent initial conditions. As a consequence, there is likely to be more uncertainty in the outcomes of simulations when initial turbulence is a factor.

This leads to the following BPG:

- The effects of initial turbulence should be included in turbulent combustion sub-models for vented explosions - as its omission would lead to under-prediction in peak overpressure.
- If there is uncertainty in the level of initial turbulence, this should be explored by means of sensitivity tests.

3.4 Numerical options

Unless numerical errors are controlled - by the selection of appropriate discretization schemes, convergence criteria, and mesh resolution - the use of even the most sophisticated sub-models for turbulence and combustion can still produce poor results which can be far removed from reality.

Therefore, understanding and control of numerical error is very important, and perhaps especially so in the modelling of hydrogen deflagrations - in which large spatial and temporal gradients of flow variables need to be resolved if peak overpressures are to be captured.

3.4.1 Solver type

Finite volume solvers are the dominant type within the CFD modelling of hydrogen deflagrations. However, KIT's COM3D model (Breitung et al, 1999) is a finite difference code.

A wide range of solution algorithms have been employed, in which explicit or implicit schemes are used. Within the implicit schemes, examples of the use of SIMPLE (e.g. Hansen et al, 2005), SIMPLER (e.g. Tolias et al, 2014) and PISO (e.g. Bauwens et al, 2011) can all be found.

It appears that there is no one solver type which appears to be decisively superior.

However, regardless of solver type, modellers of hydrogen deflagrations have ensured that the Courant Friedrichs Lewy (CFL) number is always kept below unity for reasons of stability and/or accuracy. Specific codes tend to each have a recommended maximum CFL number. This leads to the following BPG:

- CFL numbers should be less than unity.
- Code developer's guidance on maximum CFL number should be followed by users.

3.4.2 Spatial discretization schemes

It is well known that the order of accuracy of spatial discretization schemes is an important factor in CFD simulations. Schemes which are first-order-accurate (such as the upwind scheme) introduce artificial diffusion into the solution, leading to artificial mixing and a reduction in the spatial gradients of flow variables. The numerical error associated with spatial discretization can be reduced by the use of higher-order schemes. More details can be found in Versteeg and Malalasekera (2007).

This is especially relevant to deflagration modelling, as high spatial gradients are an inherent feature of these flows.

Keenan et al. (2013) explored the consequences of using a first-order scheme in the modelling of hydrogen deflagrations in a large vented enclosure. They report: "*Following authors experience the reduction of discretization scheme from 2nd order to 1st order resulted in a significant decrease of combustion rate and an underestimation of pressure peaks*."

This leads to the following BPG:

- First-order-accurate spatial discretization schemes must not be used in the modelling of hydrogen deflagrations.
- Higher-order-accurate discretization schemes should be 'bounded' to avoid non-physical overshoots or undershoots in the values of flow variables. See Versteeg and Malalasekera (2007).

3.4.3 Temporal discretization schemes

It is also well known that the order of accuracy of temporal discretization schemes is an important factor in CFD simulations. Schemes which are first-order-accurate can introduce artificial dispersion (phase error) and dissipation (amplitude error) into the solution. The numerical error associated with temporal discretization can be reduced by the use of higher-order schemes. More details can be found in Versteeg and Malalasekera (2007).

This is especially relevant to deflagration modelling, as high temporal gradients are an inherent feature of these flows.

In general, schemes which are at least second-order-accurate tend to be employed in the CFD modelling of hydrogen deflagrations. For instance, Backward Euler (e.g. Wen et al, 2010) and Crank Nicholson (e.g. Tolias et al, 2014) second-order schemes have been used. However, first-order Euler schemes are also used within the framework of explicit (e.g. COM3D code) or implicit (e.g. FLACS code) schemes.

However, temporal discretisation error is not just governed by the time discretisation scheme, as it also depends on the size of the computational time-step. The latter is also governed by the CFL number. This leads to the following BPG:

- Code developer's guidance on time-step size should be followed, consistent with recommendations on maximum CFL number.

In the case of LES or VLES-based deflagration models, the required time-step will very likely be smaller than is the case for RANS-based approaches, due to the requirement to resolve at least some of the turbulent eddy motion. For instance, Keenan et al (2013) use a VLES approach requiring a time-step of just 10^{-6} seconds.

3.4.4 Convergence

The importance of ensuring that numerical solutions are well-converged is illustrated by Molkov et al. (2007). This 2007 paper provides results of updated simulations which were first reported by Gallego et al. (2005); the pressure-time history at monitor locations during a large hydrogen deflagration in the open atmosphere is much improved. Molkov et al. (2007) attribute this improvement – at least in part – to a more precise solution of aspects of turbulence combustion model. In addition, the more general guidance on monitoring of convergence set out in Section 1.4.4 should be followed.

Convergence control may include control over mass conservation of particular specie, e.g. hydrogen, over time in its pure form (H_2) and in chemical compounds (H_2O, H_2O_2, HO etc.), as well as energy balance. For computational domains with boundaries permitting inflow and outflow the conservation control should include inflow and outflow of the controlled quantities. When using implicit iterative solvers those may be controlled both for each time step and over time. Specie or energy conservation imbalance indicate poor convergence and poor simulation results should be expected.

3.5 Analysis of the simulation results

3.5.1 Validation and sensitivity of the results

Jallais (2013) highlights that larger experiments provide a more challenging test for models, probably as a result of the increasing influence of various combustion instabilities, leading to the following BPG:

- Models must be validated against a range of scales of experiments, including large-scale experiments where the data exists.

Bauwens et al. (2011) also demonstrate that even within the same experiment there can be considerable variation in the performance of a model. For instance, in the modelling of a vented hydrogen-air explosion from a 64 m^3 chamber, using OpenFOAM, at lean conditions of 18.5% hydrogen in air by volume, there was a very large difference in the performance of the model for ignition at the back wall and ignition at the front of the chamber; in the former case pressure vs. time histories were well-predicted, whereas in the latter case the peak pressures were very significantly under-predicted. The authors attributed this behaviour to a number of factors, which are not discussed here. The wider significance of this particular example is that it highlights the need for models to be validated against an extensive range of test conditions.

- Models should be validated against data from a wide range of test conditions, including: mixture composition, ignition location, vent area, presence/absence of obstacles, initial turbulence, layering/stratification. Ideally, the effect of acoustic damping material on vessel walls would also be included in the dataset.

The results of CFD simulations depend on the initial and boundary conditions applied by a user, together with the numerical and physical sub-models embedded in a code. This leads directly to the following BPG:

- Ideally, the sensitivity of simulations to uncertainty in model input parameters should be examined in a structured fashion

3.5.2 Interpretation of results

There are several parameters which are of particular interest in the results of CFD modelling of hydrogen deflagrations. Where possible, a full analysis of results should include examination of the following parameters and ideally a comparison of these parameters to measurements (if these exist).

- Maximum overpressure.
- Pressure vs. time history at key locations.
- Rate of pressure rise at key locations, defined for example as: $\frac{\partial P}{\partial t} = \frac{P_{\max} - 0.1P_{\max}}{t_{p\max} - t_{0.1P_{\max}}}$

  where P_{max} is the maximum overpressure, t_{Pmax} is the time when the maximum overpressure is reached, and $t_{0.1Pmax}$ is the time when 10% of the maximum overpressure is reached (e.g. Baraldi et al, 2009).
- Flame arrival time at key locations.
- Flame speed at a key location, e.g. at exit from a vessel.
- Flame speed vs. time history.
- Flame radius vs. time (more relevant to deflagrations in the open, or the initial stages of a confined deflagration).

A statistical analysis of results in comparison to measurements can be very useful for obtaining an overview of the performance of a model. If such an approach is possible, the following BPG applies:

- Statistical performance measures should be chosen so as to illustrate both the bias and spread of results.

For example, see Baraldi et al (2009), who select the Geometric Mean Bias and Geometric Mean Variance as appropriate measures.

LES results for overpressure vs. time histories may need to be filtered so as to remove high frequency components from pressure signals, so as to enable comparisons to measurements made using the same filtering approach.

4. Detonations

4.1 Introduction

Among different accident scenarios detonation is considered often as ‘worst case’ scenario, and therefore, in safety analysis detonation modelling should be considered as ‘must have’ model.

For steady state detonation a set of conservation equations in Euler formulation and a model of chemical interaction are necessary and sufficient in most cases. Often the right selection of the chemical interaction model plays a key role in the successful implementation and utilization of the detonation model.

In more complex cases such as, e.g., transient regimes of detonation, deflagration-to-detonation transition, interaction with obstacles, shock reflections, flames, etc. utilization of the Navier-Stokes equations, as well as modelling of turbulence, could be required for adequate reproduction of the relative phenomena.

4.2 Selection of physical models

4.2.1 Conservation equations

The governing equations for detonation are the conservation equations for mass, momentum and energy. Since the molecular transport can be neglected in detonation, the governing equations concern only the convective transfer. The conservation equations are given in following expressions (4.2.1)-(4.2.4):

- mass

$$\frac{\partial \rho}{\partial t} + \nabla \cdot (\rho \vec{\mathrm{u}}) = 0 \tag{4.2.1}$$

- momentum

$$\frac{\partial \rho \vec{\mathrm{u}}}{\partial t} + \nabla \cdot (\vec{\mathrm{u}} \otimes (\rho \vec{\mathrm{u}})) + = -\nabla \mathrm{p} + \rho g \tag{4.2.2}$$

- species mass fraction

$$\frac{\partial \rho Y_k}{\partial t} + \nabla \cdot (\rho Y_k \vec{\mathrm{u}}) = \omega_k \tag{4.2.3}$$

- energy

$$\frac{\partial \rho e}{\partial t} + \nabla \cdot (\vec{\mathrm{u}}(\rho \mathrm{e} + \mathrm{p})) = \sum_{k=1}^{N} h_k \omega_k + \rho \vec{\mathrm{u}} \cdot g \tag{4.2.4}$$

here ρ is the mass density; $\vec{\mathrm{u}}$ is the velocity vector; p is the pressure; g is the gravitational acceleration; Y_k is the mass fraction of the k-th species of the gas; ω_k is the k-th species ration rate; e is the total energy, which means the sum of kinetic energy and internal energy; h_k is the energy released by k-th species in the reaction.

In addition, to close the system of the equations, auxiliary equations such as the equation of state and the equation for the chemical reaction term, ω_k, should also be specified. These

equations have been already given in the previous Sections of the current document (in the ignition part and deflagration part), so no detailed information is presented here.

4.2.2 Turbulence modelling

Taking into account the high speeds that are developed in detonation, it can be considered that the effect of the heat losses as well as the effect of the dissipation, turbulence, etc., is negligible.

Thus, in most practical cases the modeller can limit himself by using the Euler set of equations (without modelling thermal losses, turbulence and radiation) instead of the Navier-Stokes. This simplification will significantly speed up the calculations.

4.2.3 Detonation modelling

4.2.3.1 Detonation theory

The simplest theory to predict the behaviour of detonations of gases is known as Chapman-Jouguet (CJ) theory, developed around the turn of the 20th century. This theory, described by a relatively simple set of algebraic equations, models the detonation as a propagating shock wave accompanied by exothermic heat release. Such a theory confines the chemistry and diffusive transport processes to an infinitely thin zone.

A more complex theory was advanced during World War II independently by Zel'dovich, von Neumann, and W. Doering. This theory, now known as ZND theory, admits finite-rate chemical reactions and thus describes a detonation as an infinitely thin shock wave followed by a zone of exothermic chemical reaction. With a reference frame of a stationary shock, the following flow is subsonic, so that an acoustic reaction zone follows immediately behind the lead front (the Chapman-Jouguet condition).

Both theories describe one-dimensional and steady wave fronts. However, in the 1960s, experiments revealed that gas-phase detonations were most often characterised by unsteady, three-dimensional structures, which can be predicted by one-dimensional steady theories only in an averaged sense.

Note here, that even though for the detailed description of the detonation process a high-resolution simulation is necessary, which permits reproducing the complex 3D structure of shocks and combustions, in many practical cases, the averaged values are very well predicted by 1D theory, as CJ-theory and ZND-theory.

The main detonation parameters are defined as following:

$$\begin{aligned} D_{CJ} &= \sqrt{0.5(\gamma_p - 1)((\gamma_p + 1)\,\mathrm{Q}_{chem} + (\gamma_p + \gamma_r)\,\mathrm{T}_0 \mathrm{C}_v^r\,\mu_r)} \\ &\quad + \sqrt{0.5(\gamma_p + 1)((\gamma_p - 1)\,\mathrm{Q}_{chem} + (\gamma_p - \gamma_r)\,\mathrm{T}_0 \mathrm{C}_v^r\,\mu_r)} \\ &\approx \sqrt{2(\gamma_p^2 - 1)\,\mathrm{Q}_{chem}} \end{aligned} \tag{4.2.5}$$

$$P_{CJ} = P_0 \frac{(\mathrm{D}^2 + (\gamma_r - 1)\,\mathrm{T}_0 \mathrm{C}_v^r\,\mu_r)}{(\gamma_p + 1)(\gamma_r - 1)\,\mathrm{T}_0 \mathrm{C}_v^r\,\mu_r} \tag{4.2.6}$$

$$P_{vN} = P_0\left(\frac{4\left(\gamma_p\gamma_r - 1\right)Q_{chem}}{\left(\gamma_p\gamma_r - 1\right)T_0 C_v^r \mu_r} - \frac{\gamma_r - 1}{\gamma_p - 1}\right) \tag{4.2.7}$$

$$\rho_{vN} = \rho_0 \frac{\left(\gamma_r - 1\right)p_0 + \left(\gamma_r + 1\right)P_{vN}}{\left(\gamma_r + 1\right)p_0 + \left(\gamma_r - 1\right)P_{vN}} \tag{4.2.8}$$

here CJ subscript means Chapman-Jouguet condition, vN subscript refers to ZND theory conditions, subscript r refers to reactants, and subscript p refers to products. The rest variables have their usual meaning, D is detonation speed, γ is specific heat ratio, Q is heat of combustion, T is temperature, C_v is heat capacity, P is pressure, ρ is density.

The above formulas show that the main averaged parameters of steady state detonations are completely independent of the specifics of the chemical kinetics, and this fact is exploited in several numerical detonation models.

4.2.3.2 Detailed chemistry modelling

Detailed chemistry model represents the realistic chemistry of H_2, O_2, and will involve large number of species and reactions. For example the Li mechanism (Li et al. 2004) consists of the following equations.

Formula	Activation Energy	Temperature exponent	Pre-Exponential factor
H+O2=O+OH	3,55E+015	-0,406	1,66E+004
O+H2=H+OH	5,08E+004	2,67	6,29E+003
H2+OH=H2O+H	2,16E+008	1,51	3,43E+003
O+H2O=OH+OH	2,97E+006	2,02	1,34E+004
H2+M=H+H+M	4,58E+019	-1,4	1,04E+005
O+O+M=O2+M	6,17E+015	-0,5	0,00E+000
O+H+M=OH+M	4,71E+018	-1	0,00E+000
H+OH+M=H2O+M	3,80E+022	-2	0,00E+000
H+O2(+M)=HO2(+M)	1,48E+012	0,6	0,00E+000
HO2+H=H2+O2	1,66E+013	0	8,23E+002
HO2+H=OH+OH	7,08E+013	0	2,95E+002
HO2+O=O2+OH	3,25E+013	0	0,00E+000
HO2+OH=H2O+O2	2,89E+013	0	-4,97E+002
HO2+HO2=H2O2+O2	4,20E+014	0	1,20E+004
HO2+HO2=H2O2+O2	1,30E+011	0	-1,63E+003
H2O2(+M)=OH+OH(+M)	2,95E+014	0	4,84E+004
H2O2+H=H2O+OH	2,41E+013	0	3,97E+003
H2O2+H=HO2+H2	4,82E+013	0	7,95E+003
H2O2+O=OH+HO2	9,55E+006	2	3,97E+003
H2O2+OH=HO2+H2O	1,00E+012	0	0,00E+000
H2O2+OH=HO2+H2O	5,80E+014	0	9,56E+003

Using the detailed chemistry in the simulation means that accounting for distributions of the species OH, H, O, H_2O_2 and HO_2 is necessary. In practice, solving the transport equations for all species on a high resolution mesh which could be necessary for the short living components (e.g. H_2O_2 , HO_2) may result in large computational cost.

4.2.3.3 One step Arrhenius law

In many cases utilization of a simplified (reduced) chemical interaction description is sufficient to obtain simulated explosion process with correct major detonation parameters, such as peak pressure in detonation wave, density and temperature in detonation wave, and detonation speed (see Section 4.2.3.1). There is a variety of such models differing mostly in the number of remaining reactions in the reduced mechanism. The most popular reduced chemical models are two-step and one-step reactions. For the simplification we limit ourselves by consideration one-step reaction. The Arrhenius detonation model (Arrhenius et al. 1889) is based on the formulation

$$k = K_{ch} e^{-\frac{E_{ch}}{T}} \tag{4.2.9}$$

in which k is the rate of chemical reaction, K_{ch} is the pre-exponential factor, E_{ch} is the activation energy divided by universal gas constant R; the units thus [K] for E_{ch} and temperature.
With this assumption, the consumption of the fuel could be specified as,

$$\Delta y_{H_2} = \Delta t \cdot y_{H_2} K_{ch} \cdot e^{-\frac{E_{ch}}{T}} \tag{4.2.10}$$

Note that, the reaction zone must be resolved. That means that large number of cells must be placed in this reaction zone.

This is a limitation of the Arrhenius formula for the numerical simulation of detonation, because, if the cell size of the domain is not small enough, the reaction zone may not be well resolved and the results may become inaccurate.

4.2.3.4 Heaviside detonation

As a specific model designed for under-resolved simulations, in which space resolution requirements cannot be satisfied, as it happens in most engineering and safety simulations, a new universal model (Heaviside detonation model) was developed in KIT, which does not require high resolution and is able to predict major detonation parameters.

The Heaviside detonation model is based on the fact that the Chapman-Jouguet parameters are independent of the chemical kinetics (this model assumes an infinitively fast chemical reaction).

The Heaviside function, is generally defined as:

$$\theta : \Re \to \Re$$

$$\theta(x) = \begin{cases} 0 & x < x_0 \\ 1 & x > x_0 \end{cases} \tag{4.2.11}$$

This function allows defining the consumption of fuel

$$\Delta y_{H_2} = 100 \cdot C_f \frac{\Delta t}{\Delta x} y_{H_2} \cdot R_r \tag{4.2.12}$$

This consumption formula has no real physical interpretation, it is just a mechanism to provide enough variation of the species and heat release to generate and maintain the detonation.

Here C_f is the constant of the model of the order of 6. The model shows almost no influence of the C_f constant as the R_r factor works as a shocking capturing algorithm. The "Heaviside" factor R_r is defined with

$$R_r = \begin{cases} 0 & T < T_0 \\ \dfrac{T - T_1}{T_1 - T_0} & T_0 < T < T_1 \\ 1 & T > T_1 \end{cases} \quad (4.2.13)$$

The values of the temperatures, for this model, are:

$T_0 = 800K$

$T_1 = 1700K$

T_0 is supposed to simulate the auto-ignition temperature and it is set to a constant value, almost independent for all concentrations. Following the references (Li et al. 2004), (International Electrotechnical Commission 2000) and (Zabetakis, 1965) this temperature is almost independent of the chemical composition of the unburned gas for given pressure and temperature.

4.2.3.5 LES model

Zbikowski and colleagues (Zbikowski et al., 2008) developed LES model of a large scale hydrogen-air detonations which doesn't require Arrhenius chemistry. The equations of the LES model were obtained by filtering three-dimensional instantaneous conservation equations for a compressible Newtonian fluid. The renormalization group (RNG) model is applied for subgrid scale (SGS) modelling of turbulence.

The extent of reaction in the detonation wave can be measured in terms of the progress variable, which has zero value of progress variable c = 0 immediately behind the shock and c = 1 at the Chapman-Jouguet (CJ) plane at which reaction is complete (Nettleton, 1987). Chemical kinetics are account for in the combustion model only through its influence on the detonation velocity and modelling of detailed chemistry can be omitted in this approach. This creates conditions for grid independency of the numerical methodology when the gradient method is applied. The combustion model is based on the progress variable equation,

$$\frac{\partial}{\partial t}(\overline{\rho}\widetilde{c}) + \frac{\partial}{\partial x_j}(\overline{\rho}\widetilde{u}_j\widetilde{c}) = \frac{\partial}{\partial x_j}\left(\frac{\mu_{eff}}{S_{c\,eff}}\frac{\partial \widetilde{c}}{\partial x_j}\right) + \overline{S}_c, \quad (4.2.14)$$

similar to the deflagration model described in (Molkov et al., 2006), which was applied for the first time to simulate propagation of a reaction front following and coupled with a leading shock. Gradient method (Lasket et al., 1988) based on the product of pre-shock mixture density and detonation velocity is used for the source term modelling,

$$S_c = \rho_u \cdot D \cdot \left|\nabla \widetilde{c}\right|, \quad (4.2.15)$$

where D is detonation velocity. The only difference between deflagration and detonation mathematical models is the substitution of turbulent burning velocity by detonation velocity. Detonation velocity D was pre-calculated for each mixture composition, e.g. with the help of the Shock and Detonation Toolbox (CANTERA Toolbox). It enables computation of the gas phase explosion parameters using realistic thermo-chemistry and detailed chemical kinetics

and exploits Goodwin's Cantera (Goodwin, 2005) software. Calculation of the detonation wave propagation is based on Reynolds's algorithm (Reynolds, 1986), where location of the sonic plane is the criterion for finding *D*.

The source term in the energy conservation equation is $S_e = \Delta H_c \cdot S_c$, where ΔH_c is the standard heat of combustion. Integration of this source term through the thickness of the numerical reaction zone reproduces correct value of energy released during combustion of mixture passing unit area of reaction front in unit of time. CANTERA (Godwin, 2005) was used to thermodynamically calculate the lower heat of combustion of hydrogen-air mixture.

The gradient method does not define the exact location of the reaction front as an interface in a computational cell or between cells, but represents it as a monotonous change of the progress variable through a number of control volumes (CV) (Oran and Boris, 2001). The numerical requirement for a flame front thickness simulated by the gradient method is about 4–5 CVs (Hawkes and Cant, 2001). Bearing in mind that real reacting zone thickness in detonation wave is a few millimeters, we understand that simulated reaction zone for large scale problems could occupy up to a few meters (4–5 CV of 1 meter each) and simulation of a fine structure of the detonation wave is not possible. This requirement of 4-5 cells is valid for the shock resolution too. It is worth noting that simulated shock is essentially thickened compared to real shock of a few free path distances. This numerical requirement to simulated ''fronts'' should be correctly addressed in the numerical realisation of the model to keep reaction front behind the shock without their nonphysical overlap. This numerical peculiarity could lead to ''loss'' of a part of released combustion energy out of feeding the leading shock and as a result to ''not resolving'' von Neumann spike and other non-physical simulated parameters.

The LES model was verified against solutions of the Zel'dovich–von Neumann–Doring (ZND) theory (Zeldovich, 1940), (Neumann, 1942), (Doring, 1943). Simulated detonation velocity, von Neumann spike pressure, Chapman–Jouguet pressure and Taylor wave parameters were found to be in good agreement with theoretical values. The model is practically grid independent in the range of cell sizes 0.1–1.0 m, possess no adjustable parameters and doesn't require any ''calibration'' of the heat of combustion and the ratio of specific heats.

4.3 Problem setup

4.3.1 Domain design

The design of the computational domain in detonation simulations requires an appropriate geometry for subsequent meshing, identification and positioning of proper boundaries. According to the ZND detonation model, detonation wave is composed by the supersonic wave front, the chemical reaction zone which end at the point traveling in sonic speed (the CJ point) and the burnt gas behind the sonic point, influence behind the sonic point can hardly affect the detonation, so simulation of detonation are mostly focused on the simulation of the shock front and reaction zone. In the following Sections, two domain settings are introduced in details, the computational domain with Adaptive Local Mesh Refinement (ALMR) and the dynamic computational domain for detonation simulation.

In most cases, no specific requirements are necessary for domain setting. Simple equidistant grid is a good choice for most cases if required resolution can be achieved with such mesh. Simple reflecting or mirroring boundary conditions should be applied at solid boundaries. In

case of detonation in open space, non-reflecting boundary conditions at the domain margins should be applied.

Compression effect is the dominate factor in the propagation of detonation wave, so high pressure reproduced by high resolution is quite important for the simulation of detonation. In order to reach the necessary resolution required by simulation of detonation and control the total computational cost, the technique of local mesh refinement can be used. Especially in simulation of detonation cellular structure, the local mesh refinement can largely reduce the total computational cost. In the case of using the local mesh refinement adaptively the total computational cost can be reduced to quite low level. In the following Sections, some practical guidelines about how the refined region should be generated in the computational domain are introduced.

4.3.1.1 Computational domain with ALMR

The 1D model for detonation structure is credited to Zeldovich, von Neumann and Doering, which is also called ZND model. In the model, there are mainly three zones after the detonation shock front: the induction zone, where the gas are compressed and heated to the ignition temperature; the reaction zone, where the chemical happens and the energy is released; the products, where the reactions are completed. The ZND model is illustrated in the following figure.

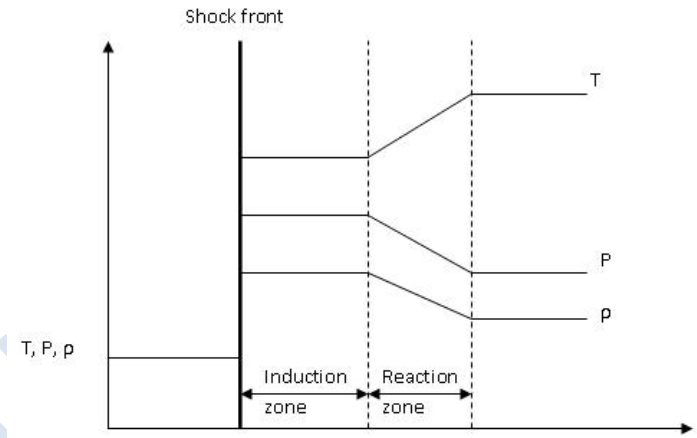

Figure 4.3-1. ZND model.

Supported by the numerical analysis based on the ZND model, it is found that the reaction finished at the CJ point which is the sonic point after the shock front (Lee, 2008). Therefore, the oscillation behind the CJ point will not influence the chemical reaction of detonation, and the propagation of detonation should mainly depends on the shock and the reaction zone. The following figure shows the pressure curve of the 1D detonation wave. Point F in the figure represents the CJ point.

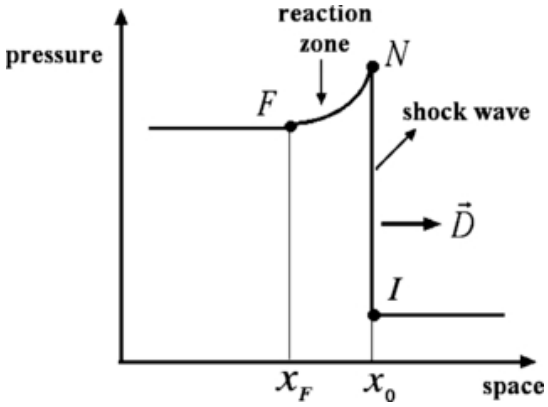

Figure 4.3-2. CJ point of the 1D detonation wave.

Theoretically, fine resolution should cover the induction zone and the reaction zone to maintain the propagation of detonation numerically. In actual calculations, under the consideration of saving working efforts in grid regeneration and minimizing the numerical diffusion, areas of the region covered by fine resolution should be larger than the theoretical requirement. Cellular structure is the characteristic of detonation wave, and thus the size of the cellular structure can be used to define the size of the refined region. Normally, one cell length region covered by fine resolution behind the shock is enough for covering the reaction zone behind the detonation shock. The space left in front of the shock wave should depend on the competition between the calculation efforts and the grid regeneration efforts. Figure 4.3-3 shows the necessary refinement region in 2D detonation simulation.

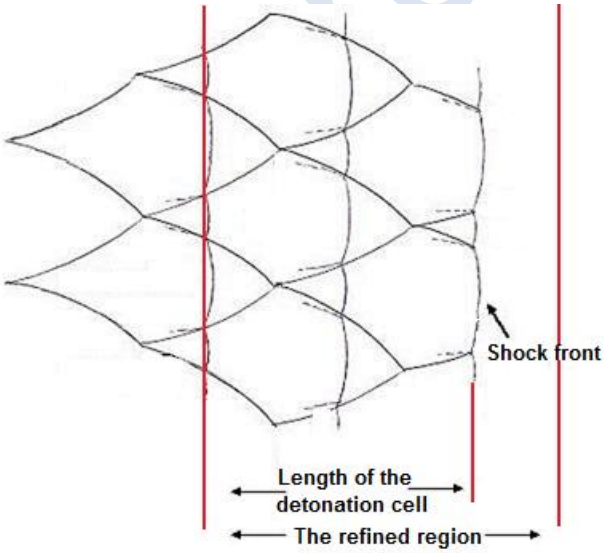

Figure 4.3-3. Necessary refinement region in 2D detonation simulation.

Sometimes, in case of appearance of irregular size cellular structures or in presence of obstacles in the computational domain that influence the process, the refinement region behind the shock wave can be larger. In the following paragraphs, the detonation simulation in the domain with ALMR is shown.

The simulation of 2D detonation in the channel with size of 30x600 mm is presented. In order to reproduce the cellular structure of the detonation wave, resolution around 0.2 mm should be used and very large computational resources are required. With the help of the ALMR,

80% computational efforts can be saved. In this simulation, base level (the domain with coarsest resolution) is covered by resolution of 1 mm and the refinement region is covered with resolution 0.25 mm, the refinement region behind the shock wave is enlarged for dealing with the appearance of irregular cellular structures. The following three sets of figures show the computational domain in three different stage of the detonation: the driven detonation, detonation without the cellular structures and the detonation with cellular structures.

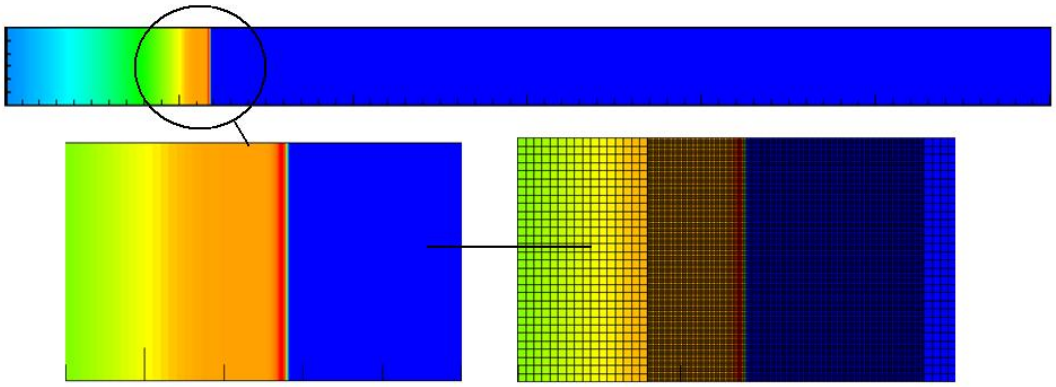

Figure 4.3-4. Domain setting of the driven detonation phase.

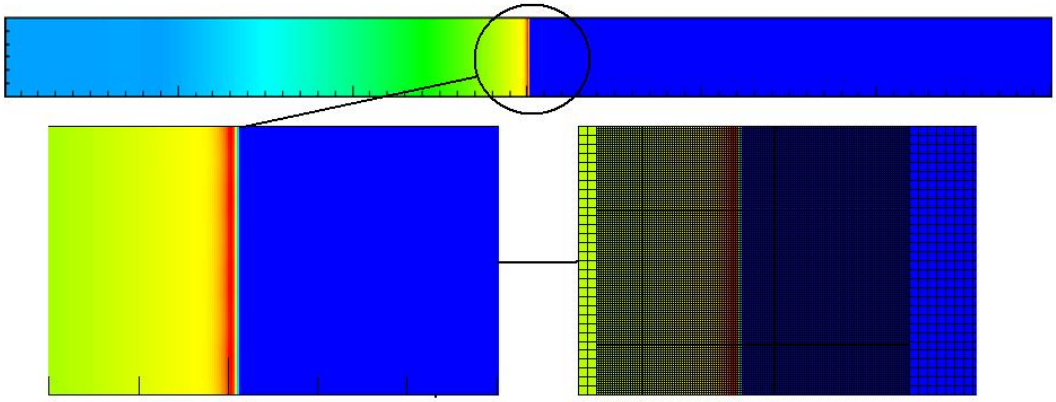

Figure 4.3-5. Domain setting of the phase without cellular structures.

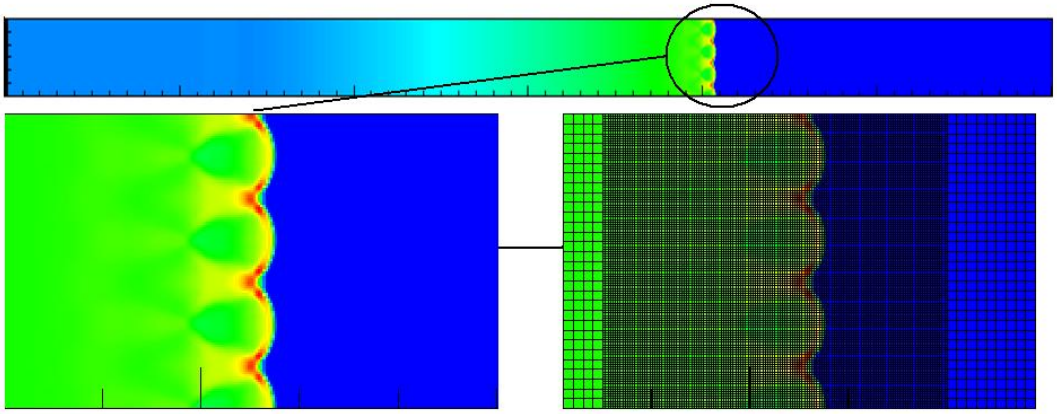

Figure 4.3-6. Domain setting of the phase where cellular structures appear.

As the above figures show, the refinement region should always include the induction zone and the reaction zone. The local mesh refinement in the example is given simply as a block-structured sub-domain, but the fine resolution can be given as a series of block-structured no overlapping sub-domains in the calculation to save more computational efforts. In addition, setting of the regions with high resolution can be more complicated in the expansion detonation wave such as the detonation in open environment or detonation propagation from small volume part to open volume part. However, the key factor for deciding which regions demand high resolution will never change; the high resolution should include at least the induction zone and the reaction zone.

4.3.1.2 Dynamic computational domain (KIT)

As mentioned in Section 4.3.1.1, perturbation behind the CJ point can hardly influence the propagation of detonation wave and the gas in front of the shock wave will keep its own motion (in most cases they have zero velocity in any directions). Such property of detonation wave brings lots of conveniences to the implementation of ALMR. Indeed, such property of detonation wave also makes it is possible to use the dynamic computational domain.

In simulation with ALMR, refined region changes according to the movement of detonation wave but the computational domain remains unchangeable. In the simulation with dynamic computational domain, the domain itself should change as the detonation wave propagates.

Difficulties of using the dynamic computational domain focus on the setting of boundaries, especially the boundary behind the shock wave. However, if the boundary behind is located also behind the CJ point, the way the boundary condition is set will never affect the induction zone and the reaction zone of detonation. So, in detonation simulations, if the direction of detonation propagation is constant and attention is paid only on the shock wave, induction zone and the reaction zone the dynamic computational domain can be used. Comparing to the ALMR, such method even save the computational efforts for the calculation on base level.

Similar to the setting of the refinement regions, the boundary behind the shock wave in the dynamic computational domain should also be placed behind the CJ point. The details and rules of the domain setting do not differ from the setting of the ALMR, and thus the detailed description is not repeated here.

4.3.2 Meshing

The choice of the meshing usually depends on what chemical model is used in the simulation of detonation and what physical phenomena the simulation seeks to model. In contrast, the solution of Euler equations does not depend on the meshing strongly. In the following sections, meshing requirements for different chemical mechanisms are presented.

4.3.2.1 Detailed chemistry model

The detailed chemistry model gives the full chain reaction in the detonation and it can best represent the reality of the chemistry part during detonation. However, such chemical model also requires the highest resolution in the simulation and typically lead to spatial resolution of the order of 1 to 10 µm.

4.3.2.2 One step Arrhenius model

The one step Arrhenius chemical model is the simplified model of the chemical reaction in detonation. It only concerns the distribution of hydrogen, oxygen and water, so the resolution

required by the Arrhenius model may be not strict as the detailed chemistry. However, the resolution in the simulation with step Arrhenius model should still be fine enough to reproduce the high pressure in induction zone, otherwise the detonation may decay or have some unphysical stair-like structure in front of the pressure peak (typical behaviour for TVD schemes). Figure 4.3-7 shows the importance of resolution in one-step Arrhenius detonation simulation. It is clear that under coarse resolution the pressure of detonation wave cannot be predicted accurately.

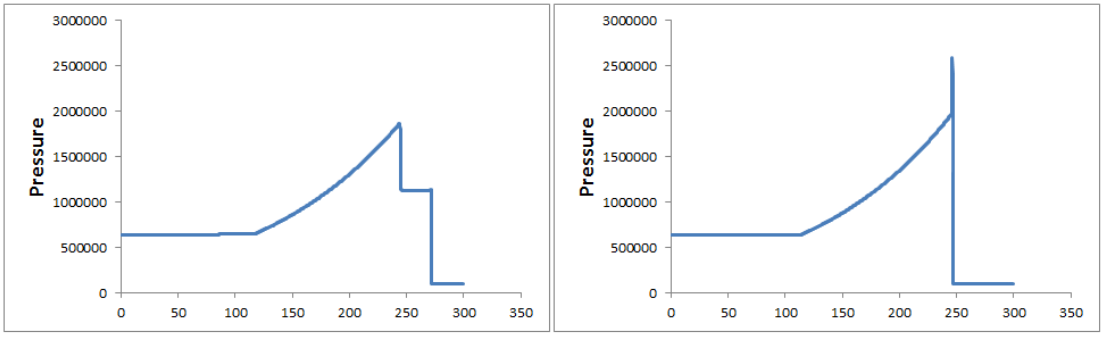

Figure 4.3-7. 1D detonation simulation with resolution 0.1 m (a) showing unphysical step structure and finer resolution 0.001 m (b) showing proper physical behaviour.

As shown in the figure, the resolution is quite important in production of reliable 1D detonation. Resolution plays a dominate role also in reproduction of other characteristics of the detonation wave. One of the most important characteristics of the detonation in 2- or 3-dimensional space is the cellular structures. The reproduction of the cellular structures depends strongly on the resolution used in the induction zone and the reaction zone.

Resolution required by the detonation modelled with one step Arrhenius depends on the pre-exponential factor K_{ch} which relates to the intensity of the chemical reaction and E_{ch} which is the activation energy. The two parameters control the width of detonation cellular structure, and normally around 40 computational cells in the area of detonation cell are required to obtain correct cellular structure.

In the stoichiometric hydrogen-air mixture, the width of the cellular structure is about 1.2 cm, so the resolution should be around 0.3 mm to simulate the cellular structure correctly. Some examples where detonations are simulated with different resolution are presented next.

The first example is the 2D detonation simulation in a closed tube with size of 30x600 mm. In this case, there will be appeared around 3 cellular structures in the simulation and the proper resolution used in the simulation should be 0.3 mm. If the resolution is not high enough, the cellular structure cannot be reproduced in the simulation. The Figure 4.3-8 below shows the case with resolution 1 mm. It can be observed that the cellular structure as the numerical smoke-foil record (the maximum pressure record in each cell) did not appear even till the detonation wave reaches the right end of the channel.

Figure 4.3-8. Numerical smoke-foil record for 2D detonation with resolution 1 mm.

In contrast, the cellular structure can be reproduced in the simulation with the resolution 0.25 mm. Figure 4.3-9 is the numerical smoke-foil record for 2D detonation under finer resolution. As shown in the figure, some cellular structure can be observed at the 2/3 length of the channel.

Figure 4.3-9. Numerical smoke-foil record of simulation with resolution 0.25 mm.

The second example shown is the 3D detonation simulation. Comparing to the 2D simulation the 3D case may cost much more computational efforts to reproduce the cellular structures. However, the rule that approximately 40 cells are required to simulate one cellular structure should still be followed. The simulation involves detonation in a square cross section tube with the size 40X40X800 mm. The following figures (Figure 4.3-10, 4.3-11 and 4.3-12) are the comparisons of the simulation with resolution 4 mm and the simulation with local mesh refinement (which reach the resolution 0.25 mm at the induction zone and the reaction zone) at different stages .

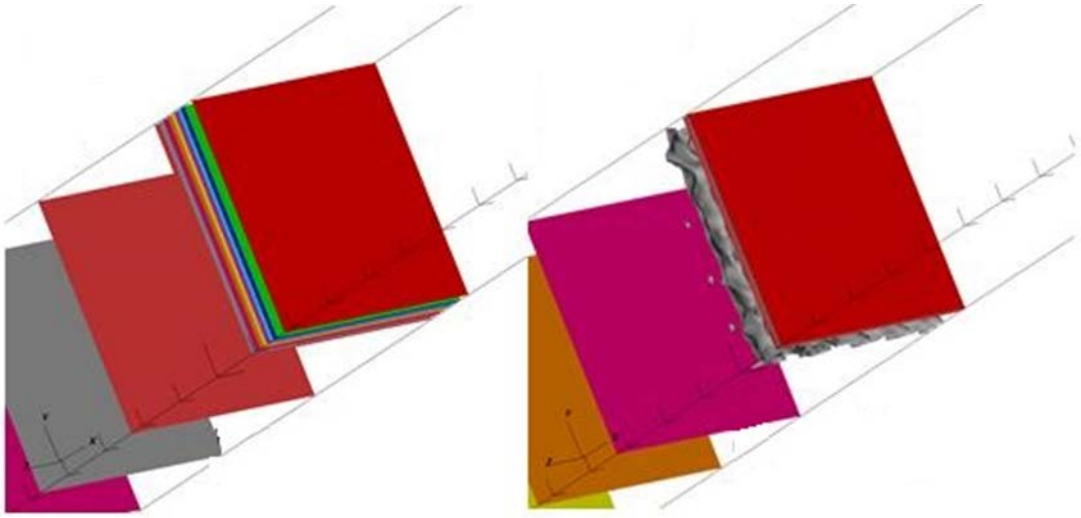

Figure 4.3-10. Contour figure of V_x in coarse grid (a) and ALMR (b) simulation at initial state.

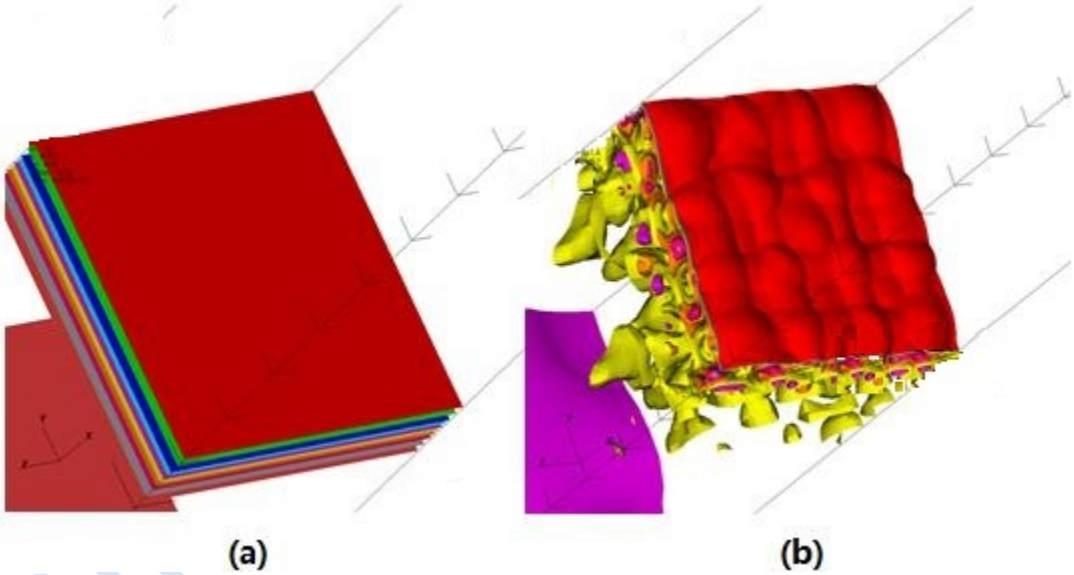

Figure 4.3-11. Contour figure of V_x in coarse grid (a) and ALMR (b) simulation when detonation wave travels to the middle of the channel.

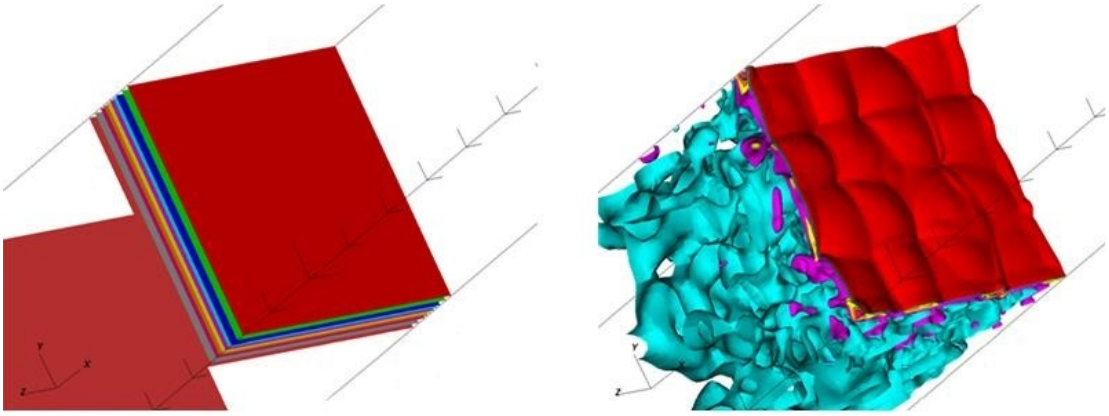

(a) (b)

Figure 4.3-12. Contour figure of V_x in coarse grid (a) and ALMR (b) simulation when detonation wave reach the end of the channel.

In the figures above, the comparison between coarse grid simulation and simulation with ALMR are given in three different time steps. In the coarse grid calculation, the resolution is not fine enough to simulate the triple points and no detonation cellular structure has been generated. In contrast, the simulation with ALMR can reach the resolution 0.25 mm locally and some perturbation has been generated since the step 400. In the longer time simulation, about 16 detonation cells have been generated.

To sum up, although the resolution required by the one-step Arrhenius model can be much coarser than the detailed chemistry (about 1-2 order of magnitude), usage of the resolution should still be done with care. It is better to check the size of the detonation cellular structure from some published experiment data prior performing the simulation, otherwise the simulation can be quite costly in time and computational resources (too fine resolution may results in quite huge amount of computational efforts and too coarse resolution may cost too much human resources in domain setting).

4.3.2.3 Heaviside model

As mentioned in the detonation modelling, Heaviside detonation model is a simplified model, specially designed for problems in which geometrical or computational constraints force the use of coarse grids. So, the resolution required by the model can be quite coarse (2-3 order of magnitude bigger than the one step model).

Figure 4.3-13 shows the results of Heaviside detonation simulation under the resolution of 100 m. The figure shows that the simulation is stable and will not produce some unphysical results. Thus, very coarse resolutions can be used in the detonation simulation with the Heaviside model.

In addition, very fine resolution should be avoided in the Heaviside detonation simulation. Figure 4.3-14 shows the restart calculation of the detonation simulation with the Heaviside model. At the beginning the detonation is simulated with the one step model and the cellular structures can be achieved by a proper resolution. However, in the restart calculation using Heaviside model with the same resolution, those cellular structures disappear. So in the simulations, which the cellular structures are wanted, Heaviside model should be avoided in the chemical modelling.

Figure 4.3-13. Results of Heaviside detonation simulation.

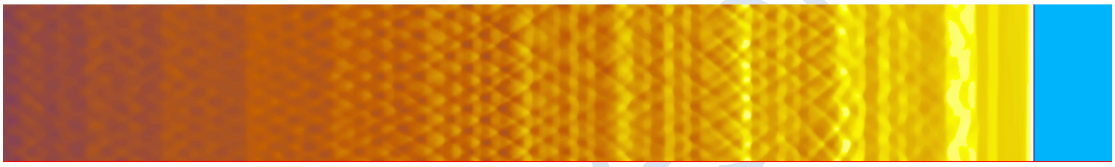

Figure 4.3-14. Restart calculation with the Heaviside model.

4.3.3 Boundary conditions

Mentioned in the section of governing equations, heat conductivity, diffusion and viscosity are quite small to propagation of detonation and can be neglected in numerical simulation of detonation. Therefore, the Euler equations which concern the effect of convection only are used to simulate the flow motion of detonation wave. Similarly, since heat conductivity, diffusion and viscosity can be neglected in numerical simulation, heat losses and friction at the boundaries can also be ignored in numerical simulation. Therefore, in numerical simulation of detonation wave the most commonly used boundary condition is mirror boundary condition which is also called slipping boundary condition. Formulas of mirror boundary condition are shown in the following equations (the slipping boundary is assumed in i direction).

$$u_j^{mirror} = \begin{cases} u_j^{gas} & i \neq j \\ -u_j^{gas} & i = j \end{cases}$$
$$\rho^{mirror} = \rho^{gas} \qquad (4.3.1)$$
$$e^{mirror} = e^{gas}$$

In addition, besides the most commonly used mirror boundary condition, the non-reflecting boundary condition (open boundary condition) is also used in some cases in which the computational domain has open boundaries. Firstly, the auxiliary wave amplitude L is given.

$$L_1 = \frac{\partial v_x}{\partial x} - \frac{1}{\rho c}\frac{\partial p}{\partial x}, \quad L_2 = v_x(\frac{\partial p}{\partial x} - \frac{1}{c^2}\frac{\partial p}{\partial x}), \quad L_3 = \frac{\partial v_y}{\partial x}$$
$$L_4 = \frac{\partial v_z}{\partial x}, \quad L_5 = \frac{\partial v_x}{\partial x} + \frac{1}{\rho c}\frac{\partial p}{\partial x}, \quad L_{5+i} = \frac{\partial Y_i}{\partial x} \tag{4.3.2}$$

For convenience, the Neumann style of non-reflecting boundary conditions is given based on the upper auxiliary variables L.

$$\frac{\partial \rho}{\partial x} = \frac{L_2}{v_x} + \frac{\rho}{2c}(L_5 - L_1), \quad \frac{\partial v_x}{\partial x} = \frac{1}{2}(L_5 + L_1)$$
$$\frac{\partial v_y}{\partial x} = L_3, \quad \frac{\partial v_z}{\partial x} = L_4, \quad \frac{\partial Y_i}{\partial x} = L_{5+i} \tag{4.3.3}$$
$$\frac{\partial p}{\partial x} = \frac{\rho c}{2}(L_5 - L_1)$$

Totally speaking, the most commonly used boundary conditions in detonation simulation are slipping boundary condition and non-reflecting boundary condition. However, in some scientific researches in which the viscosity terms are used in the governing equations, the no-slip boundary condition and several of wall functions might be used. The no-slip boundary condition and wall functions have been introduced in details in the previous turbulent flow sections, and thus they are not repeated here.

4.3.4 Initial conditions

Setting of the initial condition of detonation simulation mainly focuses on how to initialize detonation directly. Typical approach is in definition of high-pressure and high temperature region to initiate the detonation wave directly.

It is called the initiator and mimics the initiation of detonation by means of the use of high explosives. Good practice implies that the size and characteristics of this area may be so that the detonation regime is reached but the obtained detonation is not overdriven at longer distances. Some proposed values for the pressure and temperature for the most usual case of stoichiometric H2-Air mixture are:

T=3000k
P=200bar

Normally, in 1D detonation the length of 1 cm high pressure and temperature region is enough to initiate the detonation. Under the consideration of the expansion of the shock wave, the volume of region should be larger in higher dimension problems.

Setting of the initiator with different structure can also influence the production of the cellular structures. Figure 4.3-15 shows that three different shapes of initiator can have different influences to the production of cellular.

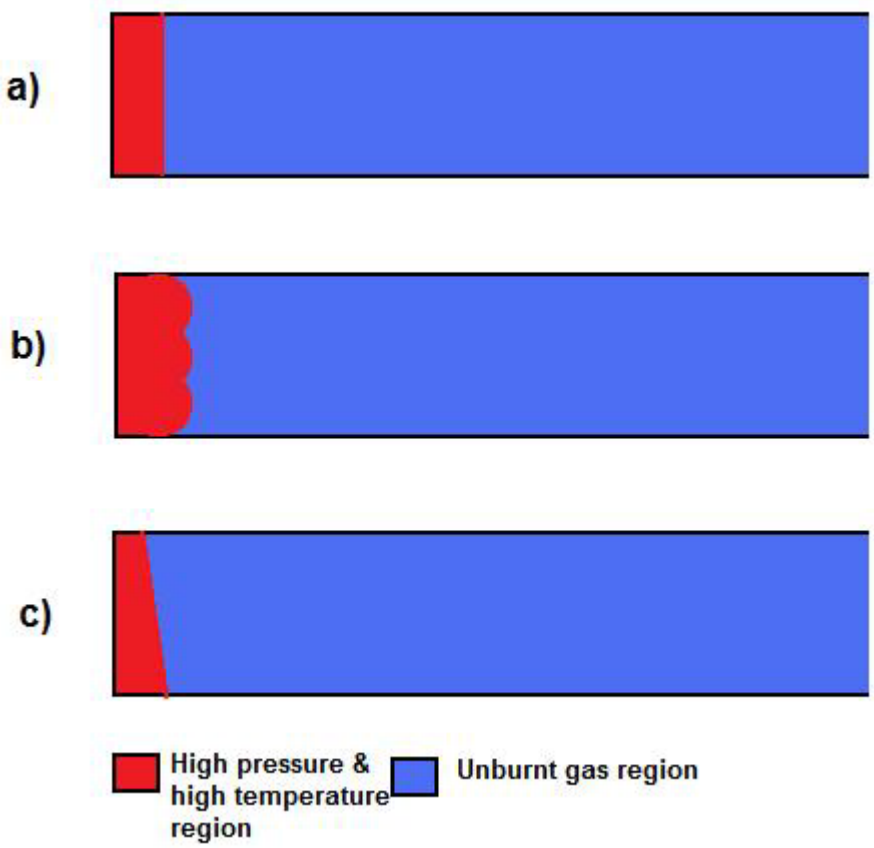

Figure 4.3-15. Common shapes of initiator.

Case a) in Figure 4.3-15 is the flat initiator. Such initiator requires initial perturbation in the computational domain or some unsymmetrical perturbation terms in the conservation equation. Construction of the cellular structures in detonation simulation is due to the instability of the flame, so some perturbations are quite necessary in numerical simulation. Normally the initial perturbation can be given to the pressure or velocity field. The gravity force can be the unsymmetrical perturbation terms in the conservation equations to helping the generation of cellular structures. Disadvantage of such initiator is the generation of the cellular structure may take some time.

Case b) in Figure 4.3-15 is the sphere initiator. Cellular structures can be generated immediately by such initiator, but the size of those cellular structures may be different from the experiment data. Initially, the size of the structures depends on the number of the sphere structures in the initiator. Later, as the influence of the initiator becomes less and less, the size of the cellular structures will approach the experiment data. So, although the cellular structures can be achieved immediately, the appearance of the correct cellular structure may take a while.

Case c) in Figure 4.3-15 is the slope initiator. The slope size of the high pressure and high temperature region is also a kind of initial perturbation. Comparing to the flat initiator, such initiator does not require special perturbation treatment to the variables and does not require additional perturbation terms in the conservation equations. Comparing to the sphere initiator, the slope structure does not influence of the size of initial cellular structure strongly.

4.4 Numerical options

4.4.1 Solver type

Detonation wave transports in supersonic regime and the recommended solver type for the solution of the conservation equations is the explicit solver. Although the implicit solver or semi-implicit solver can also be used in the calculation of convection of the fluid, the time step should still be restricted by the stability of the solution of chemical part. The solvers which are intentionally designed for the low-Mach number conditions should not be used for simulations of strong shocks, i.e. for detonations. Therefore, the explicit solvers should be used in the simulation of detonation wave.

4.4.2 Spatial discretization schemes

Since the resolutions required by detonation simulation are usually very high, up to second order schemes are enough to get good results (this does not mean that higher order schemes are not possible, indeed higher order schemes are also quite recommended in scientific simulations). In the following Sections, some common first order and second order schemes are introduced.

4.4.2.1 1st order solver

If we have a grid $\left\{u_i^n = u\left(i\Delta x, n\Delta t\right)\right\}$ than one can easily see that,

$$u_i^{n+1} = u\left(\left(i - \frac{a\Delta x}{\Delta x}\right)\Delta x, n\Delta t\right) =$$

$$= \begin{cases} u_{i-1}^n \frac{a\Delta x}{\Delta x} + u_i^n\left(1 - \frac{a\Delta x}{\Delta x}\right) + O(\Delta x^2) & a \geq 0 \\ -u_{i+1}^n \frac{a\Delta x}{\Delta x} + u_i^n\left(1 + \frac{a\Delta x}{\Delta x}\right) + O(\Delta x^2) & a \leq 0 \end{cases} \tag{4.4.1}$$

The value at next time step is calculated by linear interpolation between nearest points. Another way to write the same thing is,

$$\frac{u_i^{n+1} - u_i^n}{\Delta t} + a\begin{cases} \frac{u_i^n - u_{i-1}^n}{\Delta x} & a \geq 0 \\ \frac{u_{i+1}^n - u_i^n}{\Delta x} & a \geq 0 \end{cases} = O(\Delta x) \tag{4.4.2}$$

That is: to approximate spatial derivatives we use *upstream* difference. One can easily see that an attempt to replace spatial derivative here by downstream or by central difference produce unstable scheme. There is one more way to write same expression,

$$\frac{u_i^{n+1} - u_i^n}{\Delta t} + a\frac{u_{i+1}^n - u_{i-1}^n}{2\Delta x} + \frac{|a|\Delta x}{2}\frac{u_{i-1}^n - 2u_i^n + u_{i+1}^n}{\Delta x^2} \approx 0 \tag{4.4.3}$$

To make scheme with central difference stable, one can add a term that looks like a diffusion with the coefficient $\frac{|a|\Delta x}{2}$. This effect is well-known as numerical diffusion of numerical viscosity.

Now we can return to Euler equations. Described solver use upstream differences for all spatial derivatives in Euler equations with one except. As we know derivatives of pressure in this equations are responsible for propagation of sound waves. Sound waves propagate in all directions so there is no preferred direction for these terms. Instead a diffusion-like term with coefficient $\frac{c\Delta x}{2}$ is added to momentum equation.

Resulting scheme is very simple and computationally efficient. It is stable if CFL < 1.0. It shows no oscillations near discontinuities. The main disadvantage of this method is the high numerical diffusion that is introduced. The results of this diffusion usually look like smoothing of gradients of transported quantities.

However this method will not significantly smear shock wave fronts. That is because shock wave is self-maintained flow pattern. So, this method can be used for simulation of some cases where most important effect is propagation and reflection of shock waves.

4.4.2.2 Second order TVD solver

This solver is based on article of Ami Harten (Harten, 1983). TVD here means *Total Variation Diminishing*. Author also uses notion *Total Variation Non-Increasing*.

Normally, Total Variation is

$$\mathrm{TV}^n = \sum_i \left| u_{i+1}^n - u_i^n \right| \tag{4.4.4}$$

TVD means that $\mathrm{TV}^{n+1} \le \mathrm{TV}^n$. TVD is almost equivalent to *Monotonicity*.

If we return to general hyperbolic problem we generalize definition of total variation,

$$TV = \sum_i \sum \left| L_{i+\frac{1}{2}} \cdot \left(\bar{Q}_{i+1} - \bar{Q}_i \right) \right| \tag{4.4.5}$$

Here $L_{i+\frac{1}{2}}$ is the matrix of left eigenvectors of some approximation of the Jacobian matrix at an intermediate point. Internal sum is the addition of the absolute values of the elements of the vector.

To build a second order TVD solver for hyperbolic equations, we start with some TVD variant of first order solver with upstream differences. This solver, of course, has a numerical diffusion that can be estimated.

Then, we try to remove this diffusion from our method. To do that, we try to modify the set of eigenvalues of our system. The modified system is equivalent to the original with negative numeric diffusion. However, these changes should be limited to ensure that resulting numerical method remains TVD.

Resulting method should be second order everywhere except on points of discontinuity or local extrema. For a linear hyperbolic system, this method is proven to be TVD. For non-

linear case, the proof is not known. However this method is considered to be quite reliable. As author (Harten) says:

'...At this time we do not have estimates of the possible increase in total variation in solutions of scheme ... , and therefore cannot prove convergence in the nonlinear system case.'

In the implemented method, the user can switch off the second order correction. In this case, the user gets a first order method which is certainly TVD. In some (rare) cases switching off 2^{nd} order can be necessary. Sometimes, it is sufficient to switch off second order correction term only on one characteristic. This characteristic corresponds to propagation of entropy.

It is well known that nonlinear hyperbolic equations can produce discontinuous solutions even from smooth initial conditions. A physically admissible one, among all possible discontinuous, is one that is close to the solution of original equation with an infinitely small diffusion term added.

The numerical method already has some intrinsic numerical diffusion. However, this diffusion term, which coefficient depends on the dimensionless characteristic velocity $|\frac{u\Delta t}{\Delta x}|$, can vanish at some points. To ensure that this term would never be zero, it is suggested to use, instead of absolute value, the function

$$Q(x) = \begin{cases} \frac{1}{2}\left(\frac{x^2}{\varepsilon} + \varepsilon\right) & |x| < \varepsilon \\ |x| & |x| \geq \varepsilon \end{cases} \tag{4.4.6}$$

The dimensionless parameter ε should have small value such as 10^{-4}. Its effect is limited to points where the condition CFL<ε is fulfilled. The increase of this parameter raises the numerical diffusion thus increasing its stability.

4.4.2.3 AUSM+up

AUSM+up is a hydrodynamic solver created by Liou and published in the ref (Liuo, 2006). Let consider the inviscid fluid equations. We study 1D flux with the multi-dimensions directions splitting. Then the equations are written as,

$$\partial_t Q + \nabla \cdot F = 0 \tag{4.4.7}$$

Q, and F are the conservative variables and inviscid flux is defined by,

$$Q = \begin{pmatrix} \rho \\ \rho u \\ \rho v \\ \rho w \\ \rho e \\ \rho \phi \end{pmatrix} \tag{4.4.8}$$

$$F = \begin{pmatrix} \rho u \\ \rho u^2 + p \\ \rho uv \\ \rho uw \\ \rho u\left(\frac{\rho e + p}{\rho}\right) \\ \rho u\phi \end{pmatrix} \tag{4.4.9}$$

where ϕ represent any passive scalar. For the next equations, in order to simplify the notation, the variable H is introduced. This variable is defined as,

$$H = \frac{\rho e + p}{\rho} \tag{4.4.10}$$

The flux is then divided in two vectors, one containing the convective and other containing the pressure fluxes,

$$F = \rho u \begin{pmatrix} 1 \\ u \\ v \\ w \\ H \\ \phi \end{pmatrix} + \begin{pmatrix} 0 \\ p \\ 0 \\ 0 \\ 0 \\ 0 \end{pmatrix} = \dot{m}\vec{\psi} + P \tag{4.4.11}$$

That is, in function of common mass flux,

$$f_{1/2} = \dot{m}_{1/2}\vec{\psi}_{L/R} + p_{1/2} \tag{4.4.12}$$

Where the simple up-winding is defined,

$$\vec{\psi}_{L/R} = \begin{cases} \vec{\psi}_L & \dot{m}_{1/2} > 0 \\ \vec{\psi}_R & \dot{m}_{1/2} \le 0 \end{cases} \tag{4.4.13}$$

The mass flux rate at the interface has the form,

$$\dot{m}_{1/2} = a_{1/2} M_{1/2} \rho_{L/R} = a_{1/2} M_{1/2} \begin{cases} \rho_L & M_{1/2} > 0 \\ \rho_R & M_{1/2} \le 0 \end{cases} \tag{4.4.14}$$

The interface Mach number could be given in terms of L and R Mach values (Mach number can here be negative) as,

$$M_{L/R} = M_4^+(M_L) + M_4^-(M_R) + M_p \tag{4.4.15}$$

In this formula $M^{+}{}_{4}^{-}$ are polynomial functions of degree 6 given by,

$$M_4^{\pm}(M) = \begin{cases} M_1^{\pm}(M) & M \ge 1 \\ M_2^{\pm}(M)\left[1 \mp 16\beta M_2^{\mp}(M)\right] & M < 1 \end{cases} \tag{4.4.16}$$

and,

$$M_1^{\pm}(M) = \frac{1}{2}\left(M \pm |M|\right)$$
$$M_2^{\pm}(M) = \pm\frac{1}{4}\left(M \pm 1\right)^2 \quad (4.4.17)$$

The diffusion term M_p was introduced to enhance calculations of low Mach number and is defined as,

$$M_p = -\frac{K_p}{f_a}\max\left(1-\sigma\overline{M}^2, 0\right)\frac{p_R - p_L}{\rho_{1/2} a_{1/2}^2} \quad (4.4.18)$$

where,

$\sigma \le 1$,

$$\rho_{1/2} = \frac{\rho_R + \rho_L}{2}, \quad (4.4.19)$$

$$a_{1/2} = \frac{a_L + a_R}{2} \quad (4.4.20)$$

The M variable could be defined,

$$\overline{M}^2 = \frac{u_L^2 + u_R^2}{2a_{1/2}^2} \quad (4.4.21)$$

And the f function,

$$f_0 = M_o\left(2 - M_o\right) \quad (4.4.22)$$

$$M_0^2 = \min\left(1, \max\left(\overline{M}^2, M_\infty^2\right)\right) \quad (4.4.23)$$

For the general interface pressure formula we have,

$$p_{1/2} = p_L P_5^+\left(M_L\right) + p_R P_5^-\left(M_R\right) - p_u \quad (4.4.24)$$

The fifth degree polynomials P, are defined in an analogous way,

$$P_5^{\pm}(M) = \begin{cases} \frac{1}{M} M_1^{\pm}(M) & |M| \ge 1 \\ M_2^{\pm}(M)\left[\left(\pm 2 - M\right) \mp 16\alpha M M_2^{\mp}(M)\right] & |M| < 1 \end{cases} \quad (4.4.25)$$

The pressure diffusion term is defined as,

$$p_u = -K_u P_5^+\left(M_L\right) P_5^-\left(M_R\right)\left(\rho_L + \rho_R\right) f_a\, a_{1/2}\left(u_R - u_L\right) \quad (4.4.26)$$

The parameters chosen are,

$$\alpha = \frac{3}{16}\left(-4 + 5 f_a^2\right) \quad (4.4.27)$$

$$\beta = \frac{1}{8}$$
$$K_p = 0.25,$$
$$K_u = 0.75,$$
$$\sigma = 1. \qquad (4.4.28)$$

4.4.3 Temporal discretization schemes

In numerical simulations, spatial discretization scheme provide proper accuracy in space, meantime a proper order of temporal discretization scheme should be used to keep the accuracy. High order spatial discretization scheme combined with low accuracy temporal discretization scheme can only provide a low accuracy solution. In following parts, several common used temporal discretization schemes are introduced.

4.4.3.1 1st order scheme

The 1st order temporal discretization scheme is also called the forward Euler scheme, it has the format,

$$\frac{\partial u}{\partial t} = f(u)$$
$$u^{n+1} = u^n + f(u^n) \qquad (4.4.29)$$

Such scheme can provide first order temporal accuracy and costs the least computational effort. In some industrial simulations this scheme is used commonly, in order to save computational resources. The disadvantage of such scheme is that it can reduce the total accuracy of the solution to 1st order even if high order spatial discretization scheme is used.

4.4.3.2 Alternating direction (AD) scheme

The solver TVD is a second order 1D method, and the alternating direction (AD) scheme is used to keep its accuracy in high dimension problems. The process of the AD based solution is shown as,

$$\begin{array}{ll} U^A = U^n + \frac{1}{2}\Delta t \times F_X^n & U^{n+1} = U^D + \frac{1}{2}\Delta t \times F_X^D \\ \downarrow & \uparrow \\ U^B = U^A + \frac{1}{2}\Delta t \times F_Y^A & U^D = U^C + \frac{1}{2}\Delta t \times F_Y^C \\ \downarrow & \uparrow \\ U^{n+\frac{1}{2}} = U^B + \frac{1}{2}\Delta t \times F_Z^B \quad \rightarrow & U^C = U^{n+\frac{1}{2}} + \frac{1}{2}\Delta t \times F_Z^{n+\frac{1}{2}} \end{array} \qquad (4.4.30)$$

In the formulas, the symbol F_i^k means the derivative term in the direction i by using the data on step k. As shown by equation (4.4.30), calculation in AD based solution is given direction by direction. The X direction's convection terms are calculated firstly by using half time step $0.5\Delta t$, and the intermediate phase A is reached. Then, based on the results in phase A, calculation is made with the same time step in Y direction to get the data in phase B. After

that, the convection terms in direction Z are calculated to achieve the half time intermediate step n+0.5Δt. In order to keep the second order accuracy in time (detailed truncation error analysis for the alternating direction scheme is given in Appendix A), calculations with the opposite order are made in the rest half step of calculation. Finally, after all the six steps' calculations, the result in time step n+1 can be achieved.

For all the second order spatial discretization schemes, calculation with the AD scheme can achieve second order accuracy in both temporal and spatial discretization.

4.4.3.3 2nd order Runge-Kutta (RK) scheme

The 2nd order RK scheme is another possible achievement to get second order temporal accuracy. The format of such scheme is as following,

$$\begin{aligned} &\frac{\partial x}{\partial t} = f(x) \\ &k_1 = f(x_n) \\ &k_2 = f(x_n + \Delta t \times k_1) \\ &x_{n+1} = x_n + \frac{1}{2}\Delta t(k_1 + k_2) \end{aligned} \tag{4.4.31}$$

Such scheme is the combination of 2 forward Euler schemes, so it is quite easy for implementation. The disadvantage of such scheme is the consuming of memory which should be more than the AD scheme. In the calculation with AD scheme, the intermediate phases such as the phase a, phase b, phase n+1/2, phase c, phase d are not necessary to be stored extra. However, the two intermediate phase k_1 and k_2 must be stored in the memory.

4.4.3.4 4th order Runge-Kutta (RK) scheme

For some scientific researches, high order spatial discretization scheme should be used in the simulations. In order to keep the high accuracy brought by the spatial discretization schemes, high order temporal schemes should be used as well. The 4th order RK scheme is one of the most commonly used high order schemes. The scheme has the formula,

$$\begin{aligned} &\frac{\partial x}{\partial t} = f(x) \\ &k_1 = f(x_n) \\ &k_2 = f(x_n + 0.5 \times \Delta t \times k_1) \\ &k_3 = f(x_n + 0.5 \times \Delta t \times k_2) \\ &k_4 = f(x_n + \Delta t \times k_3) \\ &x_{n+1} = x_n + \frac{1}{6}\Delta t(k_1 + 2k_2 + 2k_3 + k_4) \end{aligned} \tag{4.4.32}$$

Comparing to the 2nd order scheme, the 4th order scheme has 4 intermediate phases which require more computational efforts and memory. The High order temporal scheme must be used accompanied with high order spatial schemes, otherwise the ideal accuracy cannot be achieved.

4.4.4 Convergence criteria

Explicit solver is the solver type recommended for the simulation of detonation. Explicit solvers do not have convergence stage, which are typical for the iterative schemes, such SIMPLE, etc. The stability of the calculations is preserved by the choice a time step small enough. On one hand it should not be too large to consume all fuel in one time step in the numerical cell where chemical reactions occur, and on the other hand the hydrodynamic part of calculations should be also stable.

The single parameter preserving the stability of the hydrodynamic part is named after Richard Courant, Kurt Friedrichs, and Hans Lewy who described it in their 1928 paper (Courant et al. 1928). Normally the CFL number in simulation is,

$$CFL = \frac{(c + |u|)_{max} \cdot \Delta t}{\Delta x} \tag{4.4.33}$$

c is the local sound speed, u is the local velocity, Δt is the time span for the temporal discretization and the Δx is the size of the mesh.

Depending on the numerical algorithm used, CFL condition can be as high as 0.9. For instance, for TVD scheme it can be 0.9. Greater value than 0.94 may produce non-convergent solution. For many schemes, a 'safe' value for the CFL number is 0.3. These values are selected for conditions when small time steps are necessary. Setting the parameters to the generally recommended values will result in better performance.

4.5 Analysis of the simulation results

In the former Sections governing equations, chemical models, setting of computational domain and initiation of detonation were introduced. In the following Sections, the methodology of analysis of the simulation when it is compared with the real world experiment is introduced.

4.5.1 Validation and sensitivity of the results

Detonation is the most violent combustion mode. Through analysis of the 1D conservation law of detonation, it was identified that the chemical reaction is the key to the propagation of the detonation wave. During the analysis of a detonation wave using the 1D model, the propagation speed of the shock front can be derived in a simple form. Following such analysis the speed of detonation wave depends on the chemical energy released by the reactants:

$$\begin{aligned} D_{CJ} = &\sqrt{0.5(\gamma_p - 1)\left((\gamma_p + 1)Q_{chem} + (\gamma_p + \gamma_r)T_0 C_v^r \mu_r\right)} \\ &+ \sqrt{0.5(\gamma_p + 1)\left((\gamma_p - 1)Q_{chem} + (\gamma_p - \gamma_r)T_0 C_v^r \mu_r\right)} \\ &\approx \sqrt{2(\gamma_p^2 - 1)Q_{chem}} \end{aligned} \tag{4.5.1}$$

In upper equation, γ_p and γ_r are the specific heat ratio of the products and the reactants, Q_{chem} is the energy released per mass through reactants, T_0 is the temperature of the reactants, C_v^r is the heat capacity of the reactants and the μ_r is the mass per mole of reactants. Based on the speed of the detonation wave important parameters such as the von Neumann

pressure, CJ pressure and von Neumann density can be estimated (Zeldovich, Barenblatt, Librovich and Makhviladze, 1985).

$$P_{CJ} = P_0 \frac{(D^2 + (\gamma_r - 1)T_0 C_v^r \mu_r)}{(\gamma_p + 1)(\gamma_r - 1)T_0 C_v^r \mu_r}$$

$$P_{vN} = P_0 \left(\frac{4(\gamma_p \gamma_r - 1)Q_{chem}}{(\gamma_p \gamma_r - 1)T_0 C_v^r \mu_r} - \frac{\gamma_r - 1}{\gamma_p - 1}\right) \quad (4.5.2)$$

$$\rho_{vN} = \rho_0 \frac{(\gamma_r - 1)p_0 + (\gamma_r + 1)P_{vN}}{(\gamma_r + 1)p_0 + (\gamma_r - 1)P_{vN}}$$

In code validation, if the key parameters from the numerical simulation are in very good agreement with the real experiment the validation is considered successful. However, during comparison of those parameters some uncertainty analysis are necessary, otherwise the uncertainties in experiments or simulations can destroy the validation. Propagation velocity and pressure records of detonation wave are quite common physical variables obtained from the experiments; therefore the following discussion will be focused on the comparison of propagation speed and of pressure.

4.5.1.1 Comparison of detonation propagation in validation

In the comparison of detonation propagation speed, synchronization between numerical simulation and experimental results at the sensors is critical. Directly initiated detonations in experiments are usually achieved by some violent explosions, whose processes are quite complicated. In contrast, initiations of detonation in simulation are mostly simplified as a region with high pressure and high temperature. Such simple initiation can hardly reproduce the initiation of detonation in experiment numerically. Therefore, there should be error in the propagation of detonation between simulation and experiment. Thus, synchronization of the detonation wave at some sensors and comparison of the results at the rest sensors are necessary. The choice of sensors used for synchronization is commonly focused on the sensors which are at the upstream of the detonation propagation path. In this way enough sensors are left for comparison. However, it is worth noticing that the sensor selected for the synchronization should not be too closed to the initiation point; otherwise the driven detonation detected by this sensor may result in much faster propagation speed in short time and it might destroy the comparison at the rest sensors.

In the Appendix, selecting the correct synchronization point will be shown in case 5 of the Appendix.

4.5.1.2 Comparison of pressure of detonation

As mentioned in the beginning of Section 4.5.1, correctly representation of pressure peak can also indicate a successful validation. However, in some cases the comparison of the pressure peak can be quite disappointing. Indeed, some big difference in pressure peak is still acceptable in the code validation. Compared to the thickness of reaction zone of detonation the resolution used in simulation for large scaling problem is much larger. The value obtained by the simulation is an averaged result instead of the real peak value. So, the pressure peak in the numerical simulation should be smaller than the experimental. Another reason why the difference in pressure peak is so large is the physical property of detonation wave. Detonation is a kind of violent supersonic combustion mode and one of its most important characteristics is its cellular structure. The cellular structure in the detonation can result in the overlap of the

pressure wave and the 3 dimensional overlapping can easily result in a very high pressure value. However, the Heaviside detonation model is a simplified chemical model and the previous Section has already shown that such model cannot reproduce the cellular structure numerically. As a result, when the sensors are influenced by the triple overlapping pressure wave, but the model is failed in simulating such overlapping, big differences between the computational and experimental pressure peak are expected. To sum up, although the compatibility of pressure peak might be poor at some sensors, the validation results can still be accepted if the reproduction of propagation speed is successful.

In addition, experimental errors of measurement may result in large differences between experimental and computational pressure peak. Sometimes the pressure transducers used in detonation experiments may overreact when the strong shock wave heats their surface, so it is quite possible that the pressure records are overestimated. To sum up, the comparison of the pressure peak is not as important as the comparison of detonation propagation speed. Furthermore, if the trends of computational pressure curve are similar with the experimental pressure records at a certain sensor, then the validation can still be considered successful.

4.5.1.3 Comparison of cell size

One of the most important characteristic of detonation wave is its cellular structure. Through experiments it has been found that the size of detonation cellular structure depends mainly on the concentration of hydrogen (shown by the Figure 4.5-1), which means that the size of the cellular structure can express the energy released by the chemical reaction. As a result, if the cellular structure can be reproduced numerically, the code will get a lot of confidence in simulation of detonation too.

However, the detonation cell size detected from the experiments is also an averaged value, and thus the comparison between simulation and experiment should not be focused on the exact value. For example, in experiments the cell size in 29% hydrogen-air mixture is 12 mm, however, a cell size ranged from 9 mm to 15 mm is acceptable in simulation.

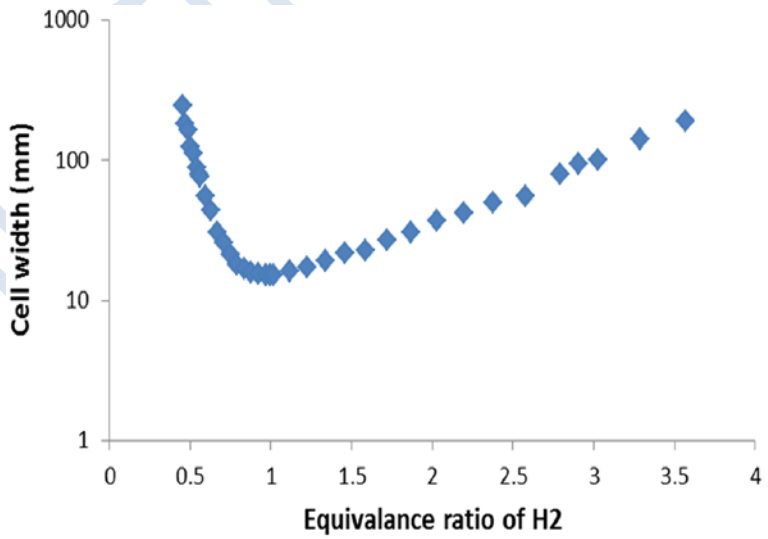

Figure 4.5-1. Detonation cell size.

4.5.1.4 Sensitivity study in detonation simulation

Sensitivity study is quite important in numerical simulation. In detonation simulation the sensitivity study should be focused on the resolution used in the computational domain. As already mentioned in previous Section, resolution used in the computational domain has a quite important role in detonation. Sometimes the results achieved by the wrong resolution may even have incorrect physical meaning. So in detonation simulation, several simulations with different resolutions are necessary, until the results converge.

Especially in simulation of detonation cellular structures, sensitivity study regarding different resolutions is quite necessary. Figure 4.5-1 shows the decay and re-initiation of detonation in obstacle environment. The resolution used in the simulation is 1 mm and the chemical model used in the simulation is one step Arrhenius model. As shown in the figure, cellular structure can be achieved under such resolution and cell size is about 25 mm.

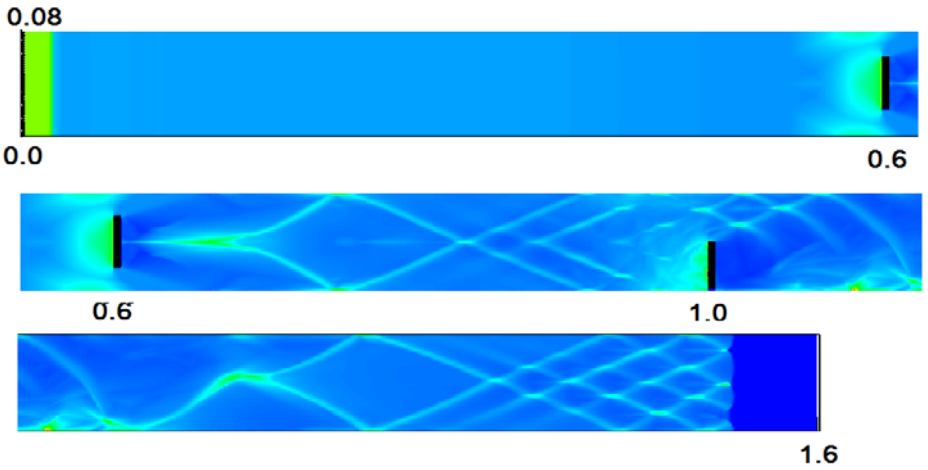

Figure 4.5-1. Smoke-foil record of detonation at resolution 1 mm.

However, the cells achieved by the 1 mm resolution seem too regular and a little too large compared to the experimental result. So, it is necessary to examine finer resolutions. Figure 4.5-2 shows the numerical simulation with resolution 0.25 mm. It is shown that the stable cell sizes varied from 9 mm to 15 mm, which is acceptable when compared to the experiment. This cell size maintains in simulations with finer resolution, which means that the result is converged and the resolution 0.25 mm is the independent one.

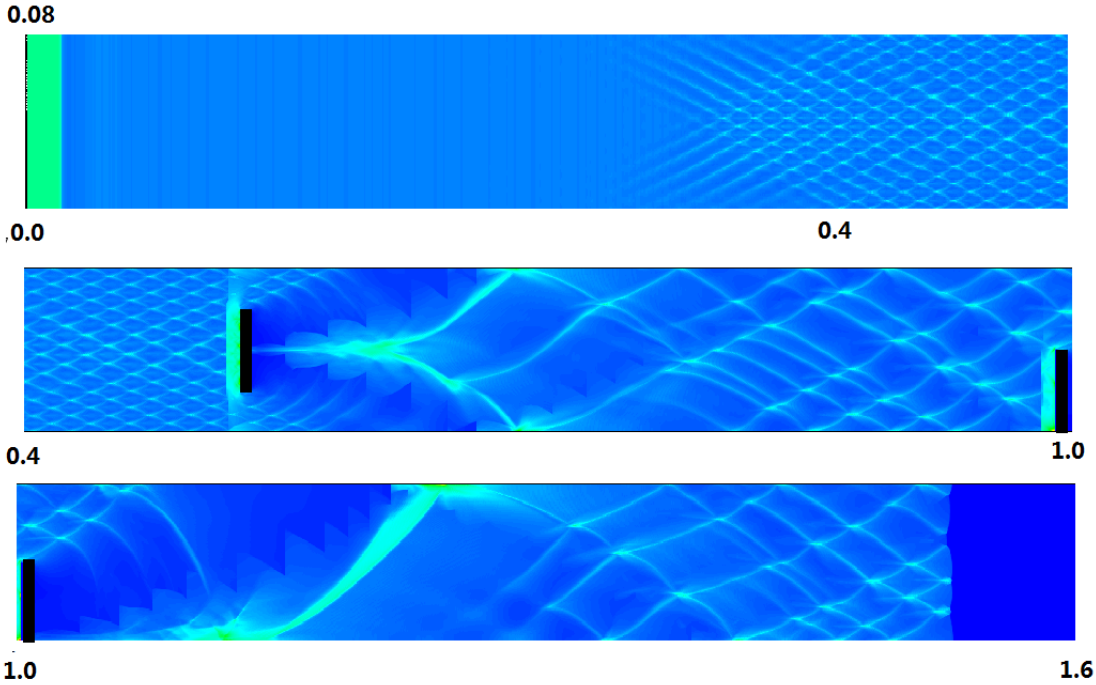

Figure 4.5-2. Smoke-foil record of detonation at resolution 0.00025m.

4.5.2 Interpretation of the results

In the analysis of detonation simulation, R-t diagram and smoke-foil records are used commonly. The R-t diagram is a general comparison between the simulation and the experiment to assure that propagation speed and pressure curve trends have been reproduced correctly by the simulation. The smoke-foil records is a more detailed comparison between simulation and experiment and such comparison shows whether the details of detonation wave can be expressed by the simulation.

4.5.2.1 R-t diagram

In the R-t diagram the horizontal axis is time and the vertical axis is distance of the sensor to a reference point. In detonation simulation the most commonly used physical variable is pressure, so in the diagram the pressure records of experiment and simulation are presented in the position of the sensor. The comparison between experimental and computational pressure records can be performed at each sensor to verify if the simulation can reproduce the experimental pressure trend.

The more important information shown in the R-t diagram is the propagation speed of the detonation wave. Slope of the line connected with the shock front of detonation is the propagation speed of detonation wave. If slopes of the lines connected by the shock detected by two neighbouring sensors are kept constant, the detonation in experiment or simulation is stable self-sustained detonation wave. If the slopes of experiment and simulation are equal, the simulation shows its capability in reproducing the correct physics. In addition, if the end of the detonation propagation path is closed, transport of the reflecting shock wave can be also analysed in the R-t diagram. Lines connected by the reflecting shock front show the propagation of reflecting shock wave. If the simulation can also reproduce the reflecting shock in experiment the validation of the code against this experiment is quite successful.

To conclude, R-t diagram is a very important method for the analysis of simulation, especially in the coarse grid simulations in which the details of detonation wave can hardly be expressed numerically and comparison of propagation speed becomes the only choice in validation.

4.5.2.2 Smoke-foil records

Smoke-foil is an important method to detect parts being highly compressed in experiments, detonation cellular structures can also be present by such important measurement (Figure 4.5-3 (left) shows the smoke-foil records in experiment). In detonation simulations, the focusing of pressure can also be record numerically to produce a numerical smoke-foil record (right of Figure 4.5-3 shows the numerical smoke-foil records).

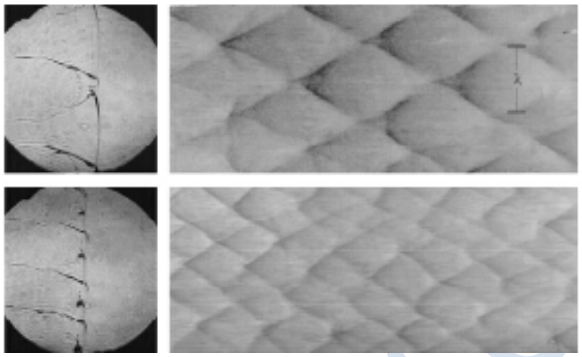

Figure 4.5-3. Smoke-foil records in experiment (left) and simulation (right).

In simulation the smoke-foil records is the records of the maximum pressure value in each control volume. After each step of calculation the code should go through the whole computational domain to check the new pressure values. If the pressure value in each control volume at each time is larger than the local maximum pressure record, the record will be replaced by the new value. At the end of the simulation, the maximum pressure record will show the maximum pressure value, which each control volume ever had during the simulation. If the model that is used and if the setting of the computational domain are capable of simulating cellular structures, the cellular structures will appear in the maximum pressure records (which can also be called numerical smoke-foil records).

It is worth noting that the cell sizes in simulation sometimes may be influenced by the initiation of the detonation. Firstly, if the region used for the initiation of detonation has curved surface, the cell size may be influenced a lot in the initial stage. As Figure 4.5-4 illustrates, initiation region of the detonation has curved surface, so the cellular structure in the initial stage is very big in size. Fortunately, the resolution used in the simulation is fine enough and the big cell structures collapse quite soon. However, in some cases when the resolution is not very high, the collapsing of the big cell structure may delay.

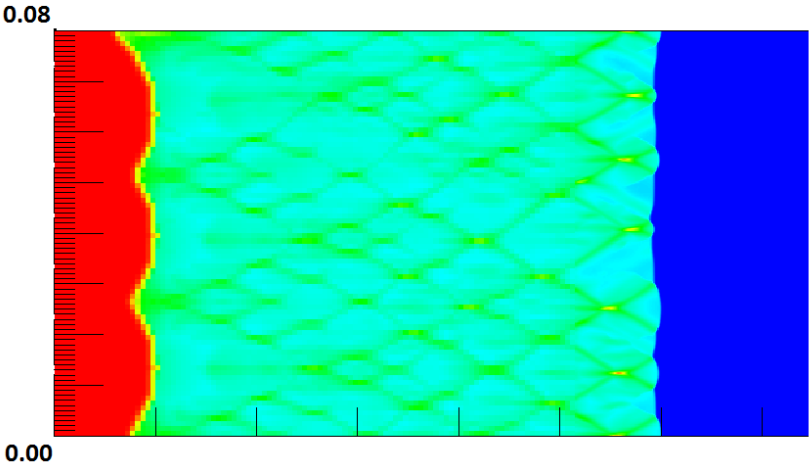

Figure 4.5-4. Initiation of detonation with curved surface.

Moreover, in the cases that the areas of the initiation regions are too big, the cell size at the initial stage can also be influenced significantly. Normally, large initiation region usually results in a longer period of driven detonation, detonation cell size at this period of time usually are much smaller than the self-sustained case. Figure 4.5-5 shows a 2D detonation simulation. The left part is the cellular structure at the initial stage and the right part is the cellular structure at the end of simulation.

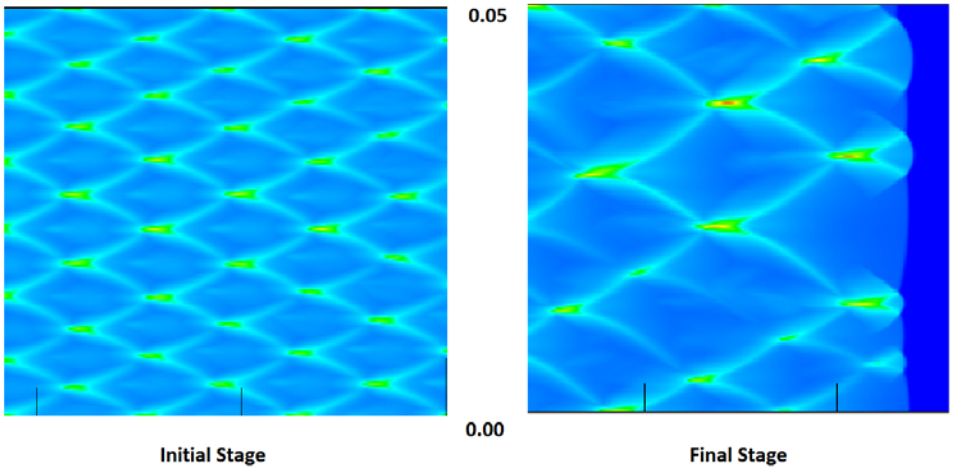

Figure 4.5-5. Cellular structure at different stages.

The cell size at the initial stage is smaller than the cell size at the end of the simulation, because it influenced by the high energy released by the initiation region, Comparing to the experiment, the cell size at the end of the simulation, which is around 12 mm, is more compatible. So, the cell size of the self-sustained detonation is more important and is recommended to be compared with the experiment.

5. CFD User Education and Training

5.1 Introduction

CFD tools are currently being offered and sold by software vendors on the basis that the software can be used to generate detailed and realistic information about fluid flows. However, it must be considered that any informed CFD practitioner will be able to describe numerous examples where results, which may seem plausible and in agreement with experiment, can be obtained from simulations containing numerous modelling and/or numerical problems. This means that the modelling approach undertaken should not be used as a robust predictive tool. Therefore, to recognise such deficiencies, it is essential that users of CFD software understand the modelling and numerical aspects underlying the code that they use, so that they can correctly evaluate the results obtained (Badcock and Richards, 1999). This is particularly essential as the field of parallel computing and computational fluid dynamics (CFD) continues to rapidly develop. This improving capability to generate large volumes of data, related to the analysis of often complex flow problems, has however outpaced the growth of the education and training services which are required in order to make effective use of these ever improving simulation tools (Badcock and Richards, 1999). As CFD gains wider and wider range of applications in the research and engineering community, the number of cases where it is being misapplied is, unfortunately, growing. This misuse is often caused by a lack of understanding of areas of applicability of specific numerical methods or software packages (Chernyavsky, 2012). Additionally, this lack of understanding can be compounded by increasingly more powerful tools that are now available and incorporate an ever widening variety of advanced numerical solvers. This growth in both capability and complexity, often unavoidably results in non-transparent interface options and compatibility issues between component solvers and underlying solver mechanics, with the prevailing perception of such commercial software packages as mysterious black boxes (Guessous et al., 2004). As a result, the proper utilisation of such advanced modelling software, or the development of problem specific numerical simulation code, requires detailed knowledge of the numerical methods employed, along with its strengths and limitations (Chernyavsky, 2012).

It is therefore clear that, appropriate education and training services must be utilised in order for users to properly understand the requirements associated with undertaking numerical simulations. These requirements include the principles and reasoning behind the process of the selection of the numerical method, the generation of the grid and the choice of the optimal computational parameters for the specific physical problem under consideration. However the utilisation of such services is currently lacking. This lack of penetration of CFD into the educational and training services on offer is undoubtedly attributable to a deficiency of CFD training within educational establishments, a lack of knowledge regarding what educational CFD tools are available and also the perceived substantial start-up time associated with developing appropriate educational CFD materials. Teaching of the principles outlined above should constitute an integral part of CFD (or other numerically-based simulated-related practice) courses. Such education and training services would particularly benefit from a hands-on approach, where for example students would be encouraged to apply various methods to obtain a solution to a standard problem and then discuss the results, thereby exploring areas of applicability, as well as the limitations, of the specific methods implemented (Chernyavsky, 2012).

5.2 Recommendations for user training

The use of CFD has gained broad acceptance within engineering education. It has been adopted in both undergraduate and graduate level courses in many universities. Traditionally, CFD education has been focused on the training of specialised analysts, putting an emphasis on algorithms and code development. In the past this was appropriate for training such CFD specialists, prior to the development and widespread use of commercial codes. However, over the last twenty years, with the rapid development of commercial CFD packages, this approach is no longer appropriate. According to a survey by NAFEMS, 80% of CFD analysts (users) now use commercial CFD packages (Morris, 2005). These analysts are using commercial CFD packages to simulate a widespread spectrum of flow problems, incorporating advanced physics, complex geometries and mesh generation tools. Therefore users require not only a strong mathematical background in order to understand the requirements associated with undertaking numerical simulations, but also require further training to effectively use such modern commercial software and successfully apply it to real world and industrial applications. For example developments to the "CFD curriculum" have included the addition of commercial packages such as Fluent, Star-CD and CFX as an integral part of taught classes (Henderson et al., 1998), (Guessous et al., 2004), (Aung 2003), (Pines 2004) and (Bhaskaran and Collins, 2003). Additionally, as the learning curve associated with the use of commercial packages can be steep, many educational courses also introduce simplified CFD software into, for example their Fluid Mechanics class (LaRoche et al., 2002), (Appanaboyina and Aung, 2004), (Jia et al., 2006), (Stern et al., 2004) and (Stern et al., 2006). The early introduction of such teaching software packages is found to help students understand fluid flow and the internal structure of CFD (Hu et al., 2008), prior to being exposed to the complexities of a full commercial CFD software package.

As education and training must be tailored to meet the needs of all students, with various academic and industrial backgrounds (i.e. it cannot be assumed that all students have a solid background in mathematics and/or physics), courses should be designed to include not only lectures, but also labs, hands-on sessions and project work, in order to effectively teach CFD.

Industrial practitioners will benefit from on-line learning options tailored specifically to the needs of industry and relative newcomers to fluid mechanics and its modelling. For example, this includes a series of on-line courses developed by NAFEMS, covering:

- Fluid dynamics review for CFD
- Practical CFD
- Elements of Turbulence Modelling
- CFD for structural designers and analysts

5.2.1 Theoretical study

The first step in education and training must be a theoretical study of CFD techniques, in conjunction with the underlying mathematical theories. As CFD is essentially the process of transforming the corresponding partial differential equations into their discretised form, the mathematical techniques employed must be properly taught and understood. For example there are many ways in which equations can be discretised; these include the Finite Differences Method, the Finite Volumes Method and the Finite Elements Method. For the majority of cases the Finite Differences Method is preferred (Anderson, 1995). By using such techniques to create algebraic equations out of differential equations, the 'student' can thereby

use implicit or explicit methods to subsequently solve the algebraic equations created (Hirsch, 2007). The solution of such equation sets are best solved using programming languages such as FORTRAN and C++. This will provide students with experience in the use of these computational techniques as they will be required to enter these equations and use appropriate sub-routines to programme the required task.

In addition to the finite differences method, students must also be exposed to the finite volumes method and the finite elements method. The finite elements method is mostly preferred for the analysis of structures through computational techniques. The solution of all these techniques requires the use of computers to obtain a solution. Therefore theoretical CFD education is necessary in order to prepare students in discretisation methods, using computational techniques to solve equations by programming and also in the use of readymade post solver computational software (Hirsch, 2007).

The selection of appropriate boundary and initial conditions is also important and determines whether a successful solution can be achieved (Tu et al., 2012). At this theoretical stage in their CFD education and training, concepts such as error control, stability analysis, convergence criteria and solution reliability should be introduced and discussed so that students are prepared for and understand their importance during the hands-on and practical sessions to come.
The educational and taught content of the course could be organised as follows (Aung, 2003):

- **General overview of CFD (with case study):**
  - Definition of CFD.
    - The philosophy of CFD: What is CFD, why and where it is used, CFD processes, CFD commercial codes, and how CFD works together with analytical fluid dynamics and experimental fluid dynamics to study fluid mechanics.
  - Its application in many areas of engineering.
  - The components and functions of typical CFD software:
    - i.e. pre-processor, solver and post-processor.
  - Demonstration of CFD using a case study (real world, practical example).
  - Possible reference material:
    - Books: (Anderson, 1995), (Pakankar, 1980), (Versteeg and Malalasekera, 2007)
    - Online materials:
    - NAFEMS online courses: http://www.nafems.org/e-learning/ (accessed February 2016)
      - Intermediate Mechanics of Fluids: http://user.engineering.uiowa.edu/~me_160/ (accessed February 2016)
      - CFD online: http://www.cfd-online.com/Wiki/Main_Page (accessed February 2016)
      - User guide, Theory guide and programmer's guide to most commercial CFD software packages are available online

- **Governing equations of fluid dynamics:**
  - Partial differential equations (PDE) for the conservation of mass, momentum, and energy.

- Physical meaning of each term in the PDE equations, the effects of these terms on the solution procedure of the PDEs and possible neglecting of terms dependent on the case under consideration for simplification without loosing accuracy.
- Both the differential and finite volume forms of the governing equations and their applications.
- The governing equations classified for different types of flows such as viscid, inviscid, Newtonian, Non-Newtonian, compressible, incompressible, transient, and steady flows.
- Differences between diffusive, convective, and source terms in the governing PDEs, as well as the effects of these terms on the solution procedure.
- General behaviour of the PDEs and their solution methods, based on the mathematical classifications of the governing equations as elliptic, parabolic or hyperbolic.
- Importance of boundary and initial conditions in solving each type of the PDE equations.
- Possible reference material:
  - Books: (Anderson, 1995), (Pakankar, 1980), (Versteeg and Malalasekera, 2007)

- **Discretisation:**
  - Different types of discretisation methods:
    - Finite difference, finite volume and polynomial methods.
    - Finite difference (typically the most easily understood by students)
    - One-dimensional unsteady diffusion equation can be used as an example to illustrate truncation error, explicit and implicit schemes, and stability.
    - Steady state diffusion equation could be used as an example to introduce the finite volume method
  - Problems associated with the convective term when using central difference, forward, difference and backward difference.
    - One-dimensional steady state convection-diffusion problem could be used as an example to introduce the different discretisation schemes (e.g. central differences, upwind scheme) of convection term.
  - The accuracy and errors associated with each method:
    - Convergence, stability, conservativeness and boundedness issues.
  - Main advantages of the finite volume method in comparison with other methods:
    - Finite volume method being the most prevalent method used in commercial CFD software.
  - Basic essentials of discretisation methods (Zamora et al., 2010):
    - General considerations – capabilities and limitations
    - Basic concept of numerical solution algorithms
      - Convergence, consistency and stability (Pakankar, 1980)
    - Properties of numerical schemes
      - Conservativeness, boundedness, transportiveness (Versteeg and Malalasekera, 2007)
    - Basic concepts of the finite-difference method (Anderson, 1995), (Pakankar, 1980)

- Basic concepts of the finite-volume method and interpolation practices – upwind, central-differencing and other schemes (Pakankar, 1980), (Versteeg and Malalasekera, 2007)
- The philosophy of the weighted residual method, as a generalised discretisation technique, including the finite-element methods.

- **Grid generation:**
  - Different types of grid and grid generation methods:
    - Structured grid methods, unstructured grid methods, and hybrid grid methods.
    - Including the body-fitted coordinate method and the adaptive grid method.
  - Opportunity to undertake short project work on the generation of different types and sizes of mesh.
  - Solution algorithms and numerical methods used for solving the discretised equations.
  - Common solutions algorithms for Pressure-Velocity coupling:
    - For example SIMPLE and PISO.
  - Different solution algorithms compared and contrasted, to facilitate student understanding.
  - Numerical solution methods covering both direct and iterative solution methods:
    - Advantages and disadvantages of both, using for example (Chapra and Canale, 2001).
  - Explicit and implicit solution algorithms.
  - Possible reference material:
    - Books: (Versteeg and Malalasekera, 2007)

- **Turbulent flow and turbulent models:**
  - Turbulent flow and turbulent boundary layers.
  - Turbulence models including: RANS, LES models and DNS
  - Application of models, wall treatment and wall functions.
  - To include errors and uncertainty in CFD modelling.
  - Possible reference material:
    - Using Versteeg and Malalasekera (Versteeg and Malalasekera, 2007)
      - Solutions from Versteeg and Malalasekera (Versteeg and Malalasekera, 2007) compared to solutions obtained from commercial CFD software.
    - Verification and validation of CFD simulations
      - WP4 of SUSANA project – Verification and Validation Procedures, (SUSANA D4.2, 2016).
      - WP6 of SUSANA project – The CFD Model Evaluation Protocol, (SUSANA D6.2, 2016).
    - Guidelines for best practice in CFD
      - WP3 of SUSANA project – Guide to Best Practice in Numerical Simulations, (SUSANA D3.2, 2016).

- **Combustion and its modelling:**
  - Combustion chemistry
  - Combustion regimes
  - Non-premixed
  - Premixed
  - Models for non-premixed combustion (fires)
  - Models for premixed combustion (deflagrations)
  - Applications

Possible reference material using Versteeg and Malalasekera, (2007), Cant and Mastorakos, (2008), Warnatz, Maas and Dibble, (2006)

5.2.2 Numerical Programming

The next part of CFD education and training should be centred on the development of numerical programming skills. As the equations already introduced are difficult, and more importantly impractical, to solve by hand, numerically suited programming languages such as FORTRAN and C++ should be selected and used to implement these equation sets which have been discretised.

Historically, FORTRAN is initially used to introduce the students to the task of programming the required complex structures and numerical algorithms. Then as the students become more comfortable and confident with FORTRAN, other programming languages such as PASCAL or C++ can also be introduced. It may also be appropriate to introduce MATLAB and its derivatives, VISUAL Basic (for example the OpenFOAM CFD toolbox, produced by OpenCFD Ltd at ESI group) or Mathematica (Gunal and Ozcan, 2008) at this stage, in order to allow the students to use the ready-made algorithms contained within these packages (Gottlieb and Orszag, 1977). As the parallel computation becomes more and more popular it might necessary to mention parallel programing, including Message Passing Interface (MPI) parallel (Gropp et al., 1996), Open Multi-Processing (OpenMP) parallel (Ayguadé et al., 2008), hybrid parallel and General-purpose computing on graphics processing units (GPU) parallel (Fung et al., 2002), (Fung and Mann, 2004). However it should be noted that students should have a fundamental grasp of the required programming techniques prior to their introduction to these visual programming languages.

5.2.3 Computational Simulation Software Usage

The final stage of education and training involves the use of computational simulation software to post process and visualise the results. A project-based learning approach can be undertaken to complete this work. Each exercise/project should be designed in order to give the students an understanding of a particular topic already covered within the fluid dynamics courses that they have likely already undertaken. This work should thereby practically demonstrate the advantages and limitations of CFD, using this hands-on approach.

This hands-on part of the course could likely start with a series of demonstrations, providing the students with the required facilities to follow along as the demonstration proceeds. For example, simple three-dimensional flows could be used as exemplars to provide an overview of the CFD process. These hands-on sessions should contain free time to allow the students to go back to or repeat particular stages within the process of numerically simulating the experiment and/or allow the time for the demonstrators to assist students and answer

questions. Gradually, as these sessions proceed students will be able to move at their own pace, progressing from requiring detailed instructions, to semi-detailed instructions, to finally only requiring the specification of the problem to be solved (Chen, 2015).

Typical steps in using CFD computational and Visualisation software (Guven and Velidi, 2011):

1. Create the proper geometry to analyse the system in detail.
    - Programming techniques can be used to calculate the necessary vertices and using appropriate modelling software the required calculations and creation of vertices can be generated automatically.
2. Implement proper meshing techniques.
    - Proper meshing of the system must be completed, so that the flow phenomena can be appropriately solved
    - Students should experiment with the various meshing techniques available, for example hexahedral and tetrahedral (in 3D), in order to understand where to use each element (Roache, 1997).
3. Use post-processing software to analyse and visualise the results (Visser et al., 1999).
    - Correct usage of boundary conditions
    - Initialisation of the system
    - At this stage proper guidance is very important, as setting the correct boundary, and initial, conditions can be considered both an art and a science.

The main outcomes of this project-based learning approach can be summarised as follows (Zamora et al., 2010):

- Familiarity with the industrial applications of thermal and fluid mechanics.
- Capability to define new problems, which can be outlined by the students using the CFD facilities at hand.
- Accumulation of knowledge, as different types of problems will be numerically simulated and compared with experimental results
- Understanding of the key phenomena and main parameters of interest by graphically visualising the problem.
- Demonstrate the capability to interpret and explain the obtained solution to the problem, involving critical analysis and validation of the obtained simulation results.
- The project topics proposed to students should be tailored to their particular area of interest, i.e. release and dispersion, fires, ignition, deflagration, DDT and detonation.
    - Examples of project work can be found in (Hu et al., 2008) and (Zamora et al., 2010)

Evaluation of students (Zamora et al., 2010):

- Written examination on the basic aspects of the syllabus
- Homework exercises (individual and group orientated)
- Completion of written project report(s) (in groups)
- Presentation of project work, including Questions and Answers and project defence (in groups)

5.3 Conclusions

As highlighted above it is essential for CFD to be implemented both with theory as well as through practice. This approach is essential in order for students to get a full understanding of the system under analysis. To enhance successful education and training; theory, programming and visualisation needs to be taught and demonstrated through a combination of classes, hands-on laboratories and tutorials. The application of such an approach will create a more successful group of students who can then quickly apply their knowledge and become productive in their chosen area of research, or within industrial applications.

However, it should be noted that a number of issues were highlighted following the application of educational and training courses by various institutions (Hu et al., 2008), (Zamora et al., 2010), (Chen, 2015), (Aung, 2003) and (Guven and Velidi, 2011). It was found that, on the whole, students were able to generate geometries and meshes, set up physical models, solve the numerical problems and visualise and analyse the flow field with appropriate post-processing tools. However, they found it very difficult to model new flow phenomenon without instruction. Additionally, students also reported that they had more difficultly with the lectures, than with the project work. As traditional CFD courses were commonly designed for CFD developers, such lectures are difficult for beginners in CFD to follow and understand. This was especially apparent for students without a background in mathematics, fluid dynamics and heat transfer. As reported by Aung (Aung, 2003) one of the main difficulties with students was the topic of turbulent flows. This was due to a lack of theoretical background. If students were able to take an additional course in fluid dynamics, dealing with viscous and turbulent flows, it was felt that their understanding would be much improved. It is clear therefore that lecture material must be tailored to the background of the students being taught. During the development of lectures emphasis must be given on including material which bridges the gap between theory and the practice of CFD. Students must have a clear appreciation of why it is essential to understand the theoretical background, and how it can be applied to solve the real world problems that they will likely encounter during their future CFD work. Students reported that they were happy with the applied method of combining theory, experimental work and CFD together to help them gain an understanding of the fundamentals of CFD and to improve their theoretical and technical abilities. Students liked the hands-on and self-discovery approach implemented. Once a demonstration was given, students were then felt learn for themselves, but supported when required by advice from the instructor. This approach also resulted in students showing enthusiasm towards learning more about CFD.

From the perspective of instructors there was a desire to ensure students were provided with proper under-pinning knowledge of the mathematical aspects of CFD. The development of proper course material must follow a systematic approach, without assuming student prior knowledge. It is clear that such material should be delivered with high levels of student interaction and feed-back. Special allowances should also be made to allow students to work at their own pace outside of the set timeframe of the course; therefore online resources or multi-media should be included within course material. This will increase student confidence and willingness to experiment, as students themselves will be able to recognise their need to work in their own time to increase their exposure and experience with the software being utilised. Aung (Aung, 2003) reported that appropriate lab sessions are an essential component of education and training, to remove deficiency and allow a set time for students to concentrate on gaining hands-on experience and seek the advice of instructing staff.

Commercial CFD software packages have undoubtedly improved in terms of being user-friendly, as well as ease-of-use; however the learning curve for students is still steep. Therefore much practice and experimentation is required in order to gain greater confidence and reduce frustration. Following the implementation of appropriate education and training courses, students can gain an understanding of CFD, as well as the internal structure and operation of CFD solvers. They can also build up their knowledge of fluid mechanics and heat transfer, interpret and validate CFD results and become aware of the pitfalls of CFD simulations. This should therefore bring the gradient of the learning curve associated with CFD to a more acceptable level.

6. Appendix

6.1 Sample Case 1 - H_2 outdoor release

As sample case for hydrogen release outdoors is chosen an experiment with LH2 release in open unobstructed environment. Details for the experiment and the modelling approach are presented in the following paragraphs.

6.1.1 Experimental description

Several tests were performed by Health and Safety Laboratory (HSL), in order to study the LH2 dispersion. Test 7 is selected as sample case and involves horizontal spill of LH2 0.86 m above the ground. The mass flow rate is 60 l/min, the spill duration is 305 sec and the spill diameter is 26.6 mm. The average wind direction was in line with the release and the average wind speed at 2.5 m was about 3 m/s. More details for the experiment can be found in (Hooker et al., 2011). The HSL experimental site is shown in Figure 6.1-1.

Figure 6.1-1. The HSL experimental site.

30 sensors were deployed to measure temperature at 1.5, 3.0, 4.5, 6.0 and 7.5 m downwind the spill point and 0.25, 0.75, 1.25, 1.75, 2.25 and 2.75 m above the ground. All sensors were in line with the release.

6.1.2 Simulation set-up

For the simulation the ADREA-HF CFD code was used, which solves the transient, fully compressible conservation equations for the mass, momentum and static enthalpy. The conservation equation for hydrogen mass fraction is also solved. For the turbulence the k-ε model is used with extra buoyancy terms (Venetsanos et al., 2010).

The source was modelled as a two-phase jet. The flashed vapour fraction at source is estimated assuming isenthalpic expansion from the storage conditions to the ambient conditions, as is recommended in Section 1.2.5 “Release modelling”.

The boundary conditions that were applied in open boundaries were symmetry conditions. The domain was extended to ensure that the symmetry boundary condition is applicable. A no-slip boundary condition was imposed on the ground. Velocity and temperature wall functions are used with roughness length equal to 1 mm. For hydrogen mass fraction zero gradient condition is applied on the ground. One-dimensional temperature equation is solved

inside the ground, in order to provide the temperature at the ground interface. The solid substrate is concrete; however, no experimental data for its properties are available. For the simulation the properties that were used are density $\rho = 2371 kg/m^3$, heat capacity $c_p = 880 J/kg \cdot K$ and thermal conductivity $\lambda = 1.13 W/m \cdot K$ .The concrete thickness was set equal to 20 cm, which is deep enough to be able to assume that the temperature on the bottom of the simulated ground domain is constant over time, and equal to the initial concrete temperature.

6.1.3 Sensitivity studies

According to Section 1.3.1 “Domain design”, several sensitivity studies should be performed, in order to ensure that the prediction is unaffected by numerical errors. Therefore, for the sample case grid independency study, a domain extension sensitivity study and time step sensitivity study was performed.

For the grid sensitivity study 5 different grid sizes were tested. Symmetry was assumed along the y-axis. Table 6.1-1 shows the grid characteristics. The first grid (Grid 1) is a coarse grid. However, the basic instructions for the grid construction are followed, i.e. refinement is imposed in regions where high gradients are expected, which in this case these regions are near the source and on the ground. In a small region downwind the spill point equidistant cells along x-direction are set and then the grid expands. The expansion ratios are kept small near the spill point (1.05), while higher expansion ratios are used further downwind the spill, but not higher than 1.12 in any case.

In Grid 2 the minimum cell size is half of the respective one in Grid 1. In Grid 3 the minimum cell size is equal to the source area, in order to check the effect on the results. The source discretization was not studied more here. However, the refinement near the source (using equidistant cells) can reduce the numerical error which might be introduced by insufficient source discretization. Grid 4 was the same as Grid 1 in all directions except from the x-direction, along which the grid is the same as Grid 2. Finally, Grid 5 is the same as Grid 4, however, through in the x-direction an even finer grid is used.

The results from the grid independency study are presented in Figure 6.1-2. As the figure indicates the refinement along the x-direction is very significant. This was expected, since the flow direction is mainly along x-direction (horizontal release). The largest discrepancies are observed with the coarse grid (Grid 1), especially at the lower sensors. The results with the other grids are similar at most of the sensors with small differences. Therefore, a good compromise between accuracy and computational time is Grid 4, and thus Grid 4 is considered as the independent one.

Table 6.1-1: The grid characteristics.

Name	Total cell number	Cell number in (x,y,z)	Minimum dx	Minimum dy	Minimum dz	Expansion ratios
Grid 1	144,936	(61,44,54)	0.05	0.025	0.05	1.05-1.12
Grid 2	301,305	(82,49,75)	0.025	0.014	0.0266	1.05-1.12
Grid 3	434,026	(82,67,79)	0.025	0.0117	0.0237	1.05-1.12
Grid 4	194,832	(82,44,54)	0.025	0.025	0.05	1.05-1.12
Grid 5	258,984	(109,44,54)	0.025	0.025	0.05	1.05-1.12

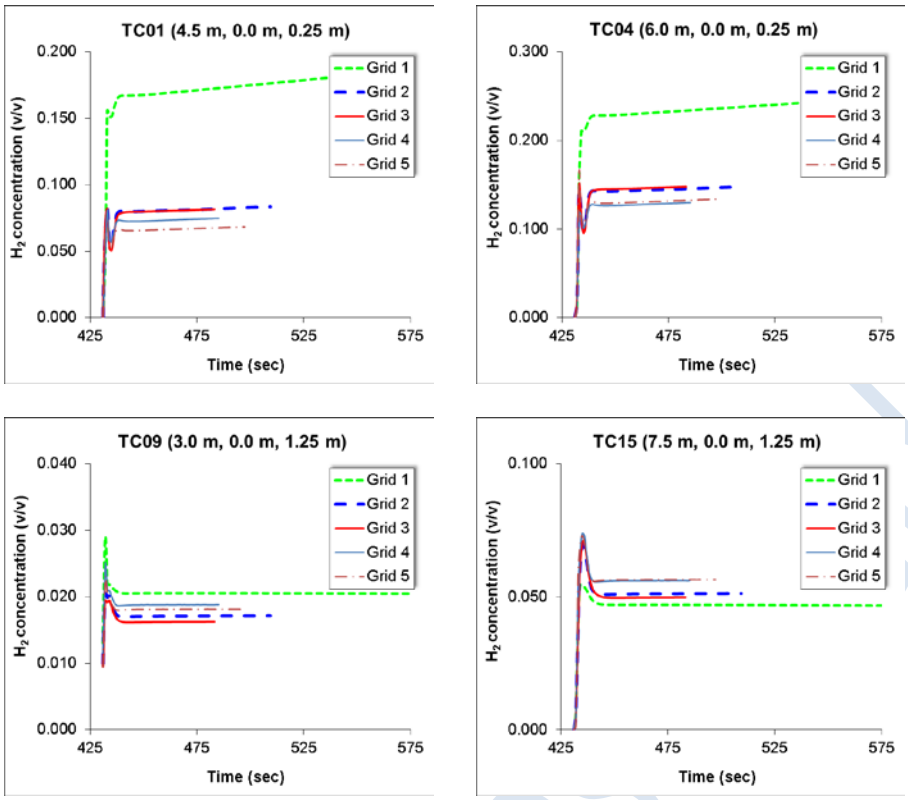

Figure 6.1-2. The results from the grid independency study.

For the independent grid (Grid 4) a domain sensitivity study is performed. Three different domains are examined. The first domain (Domain 1) is extended 5 m and 10 m upwind and downwind the release respectively along x-direction. In y-direction the domain is extended 10 m and in z-direction is extended 10 m. Domain 2 is extended 10 m more than Domain 1 in x-direction, while Domain 3 is extended 5 m less than Domain 1 in y-direction. Based on Figure 6.1-3, the results are identical for the three domains. Therefore, Domain 3 is considered the independent one and is used for the rest of the analysis.

Table 6.1-2: Dimensions of the computational domains used for the domain sensitivity study.

Name	Dimensions of origin and end of the domain (m)	Expansion along x-direction (upwind and downwind the release (m)	Expansion along y-direction (m)	Expansion along z-direction (m)	Total number of cells	Cells in (x,y,z)
Domain 1	(-5,0,0) - (10,10,10)	5 and 10	10	10	194,832	(82,44,54)
Domain 2	(-5,0,0) - (20,10,10)	5 and 20	10	10	209,088	(88,44,54)
Domain 3	(-5,0,0) - (10,5,10)	5 and 10	5	10	168,264	(82,38,54)

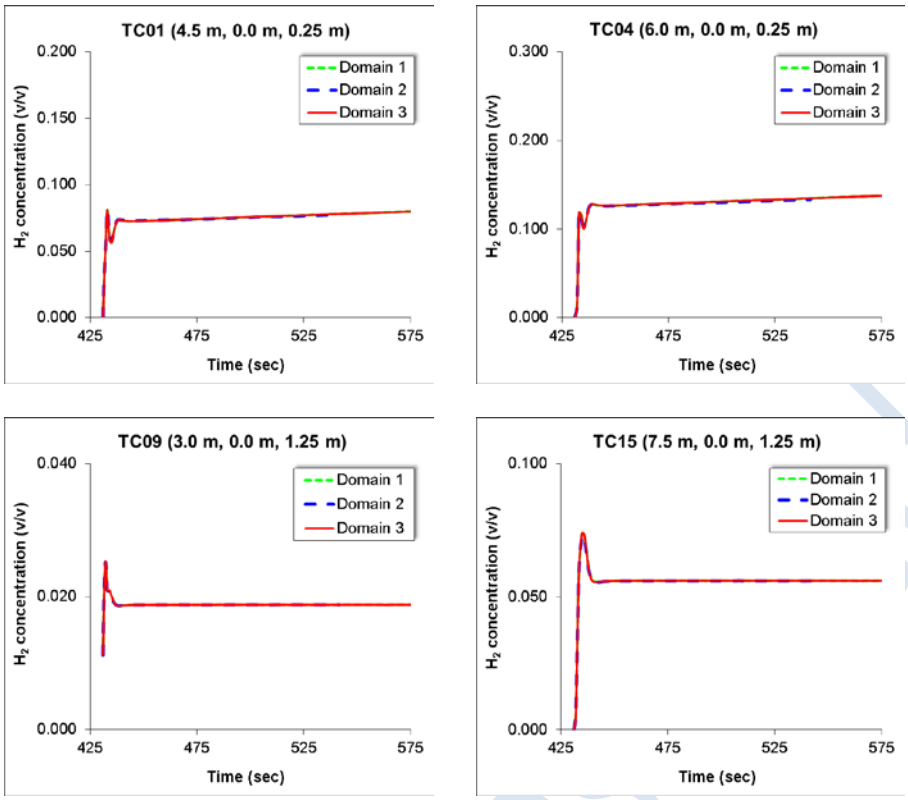

Figure 6.1-3. The results from the domain sensitivity study.

A CFL sensitivity study, and consequently a time step sensitivity study were also performed. A CFL restriction equal to 2.5, 5 (dt=$1.2 \cdot 10^{-2}$ s) and 10 was imposed. The results with CFL equal to 2.5 and 5 are presented in Figure 6.1-4. The results are very similar, thus CFL=5 is the independent one. The results with CFL=10 are not shown, because there were small convergence problems during the simulation and the time step was decreased and fluctuated between the value that corresponds to CFL=10 and the value that correspond approximately to CFL=5.

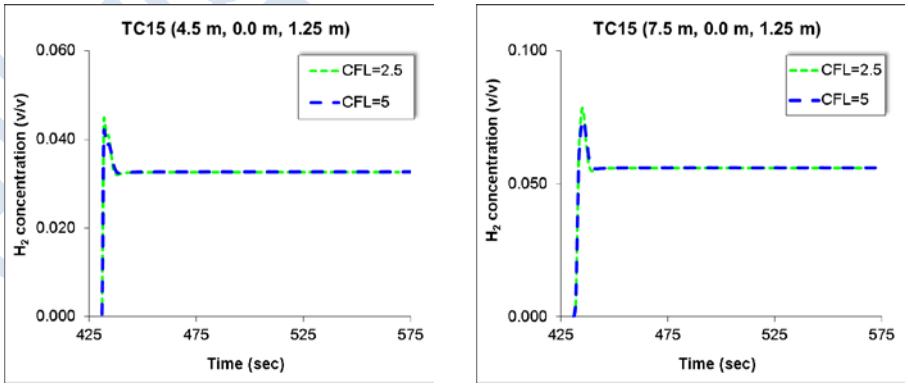

Figure 6.1-4. The results from the time sensitivity study.

6.1.4 Results and Discussion

Figure 6.1-5 shows the time series of the temperature at several distances downwind the release for both experiment and prediction. The measured temperature exhibits high

oscillations due to the fluctuations of wind direction and due to wind turbulence. The transient wind direction is not modelled here, however it has been modelled in (Giannissi et al., 2014) and it was shown that it significantly influences the predictions. The predictions tend to overestimate the peaks that experimental temperature exhibits at the high sensors (1.25 m), while it under-estimate them at the lower sensors (0.25 m) at the early stage of the release.

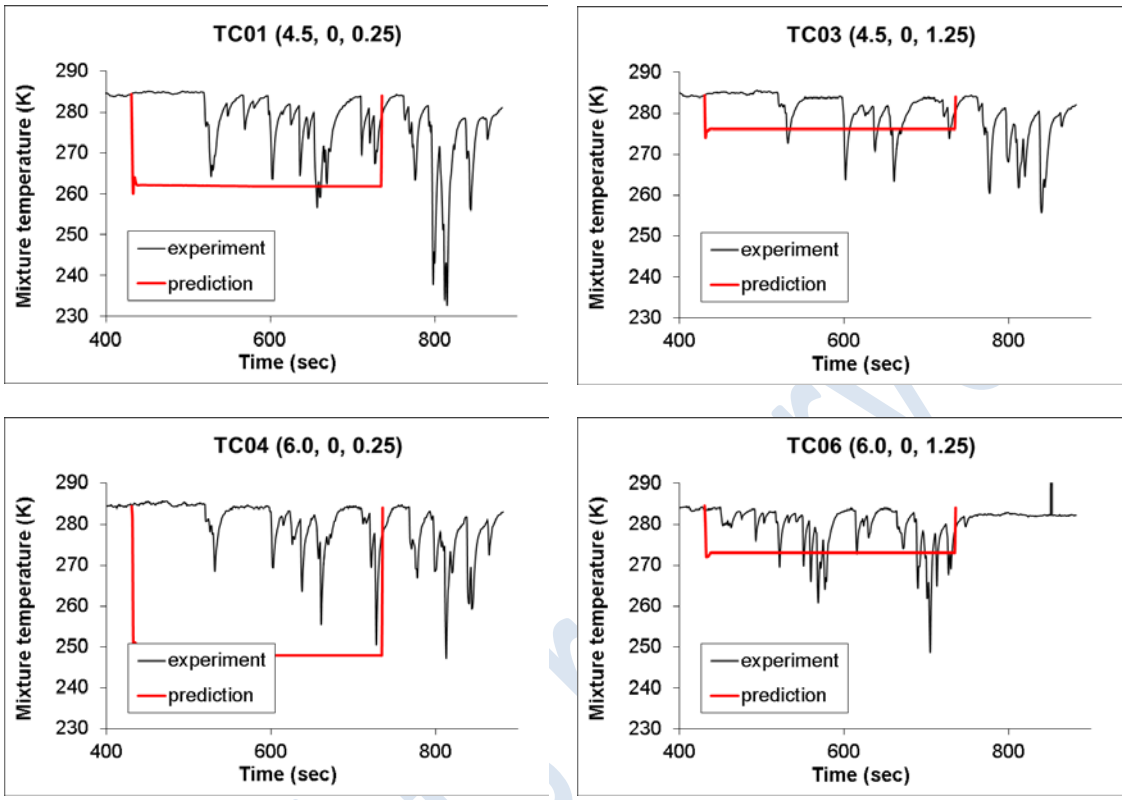

Figure 6.1-5. The predicted and the experimental temperature time series at several positions downwind the spill point.

Figure 6.1-6 shows the experimental minimum temperature compared to the predicted temperature at steady state. The results show that at height (0.75 m) approximately equal to the spill point's position the temperature is under-predicted at all sensors downwind the release. At the lower sensors (0.25 m) the predictions over-predict the minimum temperature at all distances up to 4.5 m. At 6 m the prediction is in good agreement with the experiment as far as the minimum temperature is concerned. At the remaining sensors the minimum temperature is under-predicted.

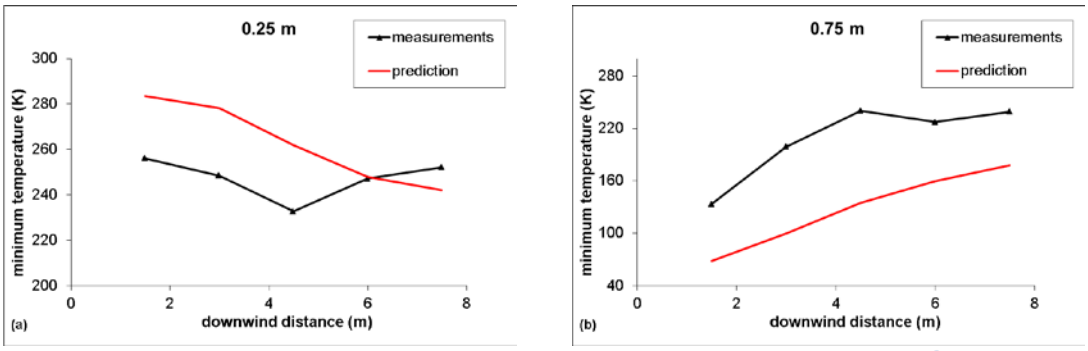

Figure 6.1-6. Minimum temperature as a function of distance at steady state conditions 0.25 m (left) and 0.75 m (right) above the ground.

6.1.5 Conclusions

The HSL test 7 was chosen as sample case for hydrogen release outdoors. During this experiment LH2 is released horizontally 860 mm above the ground with spill rate 60 l/min.

The ADREA-HF CFD code is used to simulate this experiment. Grid, domain and time step sensitivity studies were performed according to Best Practice. The measured and predicted temperatures are compared with each other at several sensors. The simulation tends to over-predict the temperature, and consequently to under-predict the concentration at most of the sensors except for the sensors at the height approximately equal to the spill's height, where prediction underestimate the temperature. In order to improve the prediction other factors that might influence hydrogen dispersion can be taken under consideration, such as ambient humidity (Giannissi et al., 2014).

6.2 Sample Case 2 - H_2 indoor release

6.2.1 Introduction

In order to demonstrate an example of application of best practice in CFD simulations of light gas release in indoor configurations, one of the experiments that was carried out in the GARAGE facility has been selected.

Before starting numerical simulations, the CFD user has to make several decisions as explained in the main document e.g. the choice of the type of mesh, the mesh resolution, the time-step, the turbulence model, etc. According to the best practice, the effect of the choices on the simulations results should be verified by means of additional simulations. The main aim of the additional simulations is to demonstrate that the selected choices do not affect the numerical results (e.g. grid independency, time-step independency) and that the selected choices were made according to the most suitable strategy for the specific case. In this specific case, the availability of experimental data facilitates the demonstration of the suitability of some of the choices. In the case that experimental data are not available, many of the stages that are shown in this section can be carried out even without the comparison between simulation results and the experimental measurements e.g. grid independency, time step independency, mesh type independency. In the following paragraphs, the results of sensitivity studies on the following key-parameters are described:

- Grid resolution
- Time-step
- Mesh type
- Distance of boundary conditions
- Turbulence model

6.2.2 Experimental description

The GARAGE facility has a rectangular shape with the size of 5.76 m (length) x 2.96 m (width) x 2.42 m (height). The release source is located at a height of 22 cm from the floor in the middle of the GARAGE. The flow at the pipe exit is fully developed. All the relevant information is summarised in Table 6.2-1.

Helium was used as a hydrogen surrogate for safety reasons. 64 sensors for the measurements of gas concentration were located inside the facility as shown in Figure 6.2-1 and in Table 6.2-2. The selected experiment has a total duration of about 20000 s and helium was released for the first 3740 seconds trough a pipe with a 29.7 mm diameter. The pressure balance with the external environment occurs by means of a small vent/opening.

Table 6.2-1. Test parameters

Garage x-dimension (mm)	5760
Garage y-dimension (mm)	2960
Garage z-dimension (mm)	2420
x release (mm)	2880
y release (mm)	1480
z release (mm)	220

Exit diameter (mm)	29,7
Volumetric flow rate - STP (NL/min)	18
He mass flow rate (g/s)	0,0536
Garage Temperature T (°C)	24,1
Exit velocity (m/s)	0,47
Release Direction	Upwards
Release Type	Continuous
Release duration (s)	3740
Released volume - STP (NL)	1122
He released mass (g)	200,28
Target concentration (%)	2,94%
Total measurement time (s)	90440
Re at exit (24.1°C)	115

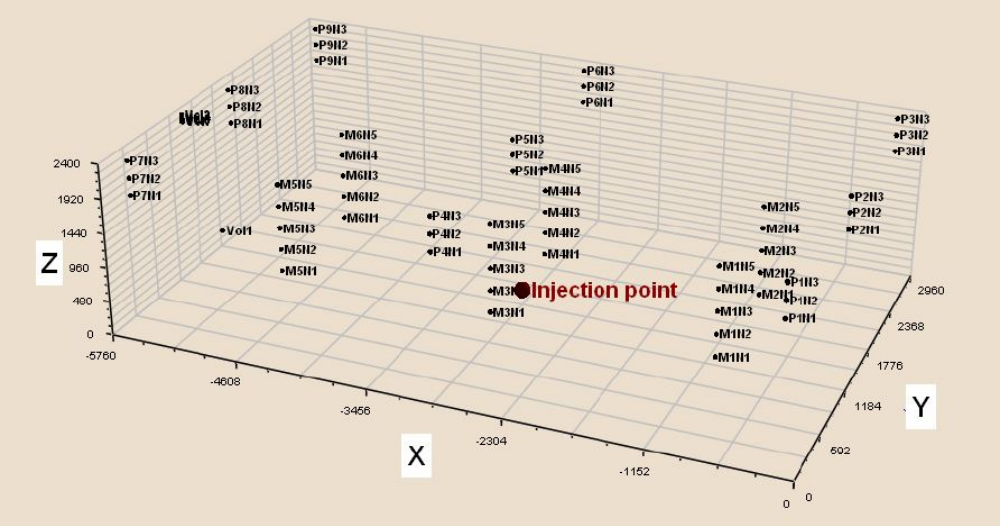

Figure 6.2-1. Sensor positions.

Table 6.2-2. Sensor coordinates.

Sensor name	x (mm)	y (mm)	z (mm)
M1N1	-1000	1001	315
M1N2	-1000	1001	630
M1N3	-1000	1002	945
M1N4	-1000	1000	1260
M1N5	-1000	995	1575
M2N1	-1000	1957	315
M2N2	-1000	1959	630
M2N3	-1000	1960	945
M2N4	-1000	1958	1260
M2N5	-1000	1955	1575
M3N1	-2920	1002	315
M3N2	-2920	1003	630

M3N3	-2920	1004	945
M3N4	-2920	1000	1260
M3N5	-2920	1001	1575
M4N1	-2915	1960	315
M4N2	-2915	1961	630
M4N3	-2915	1958	945
M4N4	-2915	1959	1260
M4N5	-2915	1960	1575
M5N1	-4840	1010	315
M5N2	-4840	1009	630
M5N3	-4840	1005	945
M5N4	-4840	1003	1260
M5N5	-4840	1002	1575
M6N1	-4835	1960	315
M6N2	-4835	1959	630
M6N3	-4835	1959	945
M6N4	-4835	1958	1260
M6N5	-4835	1957	1575
P1N1	-190	155	1900
P1N2	-190	151	2135
P1N3	-190	150	2370
P2N1	-151	1480	1900
P2N2	-151	1480	2135
P2N3	-150	1480	2350
P3N1	-190	2817	1900
P3N2	-190	2815	2135
P3N3	-192	2813	2370
P4N1	-2965	152	1900
P4N2	-2968	152	2135
P4N3	-2970	158	2370
P5N1	-2971	1485	1900
P5N2	-2972	1480	2135
P5N3	-2974	1480	2350
P6N1	-2981	2810	1900
P6N2	-2979	2810	2135
P6N3	-2976	2810	2370
P7N1	-5602	150	1900
P7N2	-5603	150	2135
P7N3	-5608	150	2370
P8N1	-5593	1483	1900
P8N2	-5596	1481	2135
P8N3	-5604	1483	2370
P9N1	-5606	2810	1900
P9N2	-5609	2811	2135
P9N3	-5606	2810	2370
Vol1	-5740	1480	235
Vol2	-5745	1030	2315
Vol3	-5745	1030	2295
Vol4	-5745	1030	2275

Vol5	-5745	1030	2255
Vol6	-5745	1030	2235
Vol7	-5745	1030	2215

6.2.3 Modelling strategy

The main parameters of the CFD simulations are:

- CFD code: ANSYS CFX 15.5
- Isothermal simulation. (garage T = 24.1° C).
- Source modelled as a 3D pipe.
- Inlet mass flow rate = 0.05355 g/s
- Multicomponent flow model: the code assumes that the various components of a fluid are mixed at the molecular level and that they share the same mean velocity, pressure and temperature fields, and that mass transfer takes place by convection and diffusion.
- The computational domain outside the box is extended in all the three directions to avoid boundary conditions at the small opening in the facility.
- Advection scheme: High resolution.
- Transient scheme: Second order backward Euler.

The flow is laminar inside the pipe since the Reynolds number is very low (~115) and well below the critical Reynolds number (2300). Nevertheless because of buoyancy the flow accelerates in the jet inside the facility. At some distance from the nozzle the jet can become unstable and break down into eddies. Therefore it seems reasonable to select a turbulence model which is capable of describing both laminar and turbulent flow like the SST transitional model. The k-ω based Shear-Stress-Transport (SST) model was originally designed to give highly accurate predictions of the onset and the amount of flow separation under adverse pressure gradients by the inclusion of transport effects into the formulation of the eddy-viscosity (Menter, 1994). This results in a major improvement in terms of flow separation predictions but not only. The full transition model is based on two transport equations, one for the intermittency and one for the transition onset criteria in terms of momentum thickness Reynolds number. It is called 'Gamma Theta Model' and it is the recommended transition model for general-purpose applications. It uses a new empirical correlation (Langtry and Menter, 2009) which has been developed to cover standard bypass transition as well as flows in low free-stream turbulence environments. This built-in correlation has been extensively validated together with the SST turbulence model for a wide range of transitional flows.

In order to evaluate the effect of a different modelling strategy regarding the flow regime, also results with the laminar approach and the Detached Eddy Simulation (DES) approach are shown in the turbulence model paragraph.

The idea behind the Detached Eddy Simulation model of Strelets (2001) is to switch from the SST-RANS model to an LES model in regions where the turbulent length predicted by the RANS model is larger than the local grid spacing. In this case, the length scale used in the computation of the dissipation rate in the equation for the turbulent kinetic energy is replaced by the local grid spacing.

6.2.4 Computational mesh

Several computational meshes were generated as described in Table 6.2-3. The geometry is composed of the garage room, a small vent/opening and an external room. In Table 6.2-3 one can find the number of computational nodes inside the garage room, the type of mesh (H for hexahedra mesh, T for tetrahedral mesh), the number of nodes in the external room, and the total number of nodes.

The details of the meshes (i.e. mesh #1, mesh #2, mesh #2.b, mesh #3, mesh #4, mesh #5 and mesh #6) on the symmetry plane are reported in Figure 6.2-2 to Figure 6.2-8. A hybrid mesh was initially generated. Tetrahedral cells were used in 3 regions where larger gradients can be expected: the jet region, the ceiling where the jet impinges and separates in several directions, and the vent. In those regions a higher mesh resolution is required and that can be achieved thanks to the flexibility of the tetrahedral grid. In the remaining part of the garage room, hexahedral cells were applied since they can provide a smaller numerical diffusivity especially during the stage when the gas release is stopped. After the initial computational grid (mesh 1), other meshes were generated to perform some sensitivity studies on the effect of the mesh on the simulation results. The results of the sensitivity studies are presented in the next paragraphs.

Special attention was also dedicated to the modelling of the release source, the inlet pipe. The details of the inlet boundary meshes are reported in Figure 6.2-9.

Table 6.2-3. List of computational meshes.

	n. of nodes			
# Mesh	**Garage**		**Out**	**TOT**
1	0.10 M	H+T	5700	0.11 M
2	0.46 M	H+T	5700	0.47 M
2.b	0.46 M	H+T	8700	0.47 M
3	2.85 M	H+T	5700	2.86 M
4	0.54 M	H*	5700	0.55 M
5	0.69 M	H	5700	0.70 M
6	0.14 M	T	5700	0.15 M

* = tetra mesh in the release zone

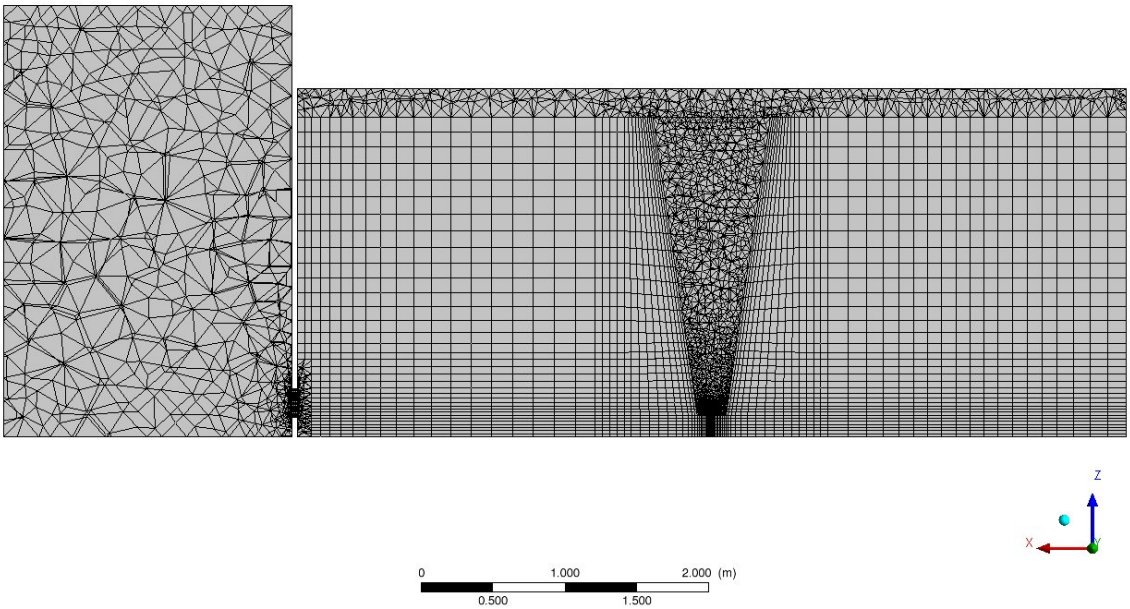

Figure 6.2-2. Mesh at symmetry plane for mesh #1.

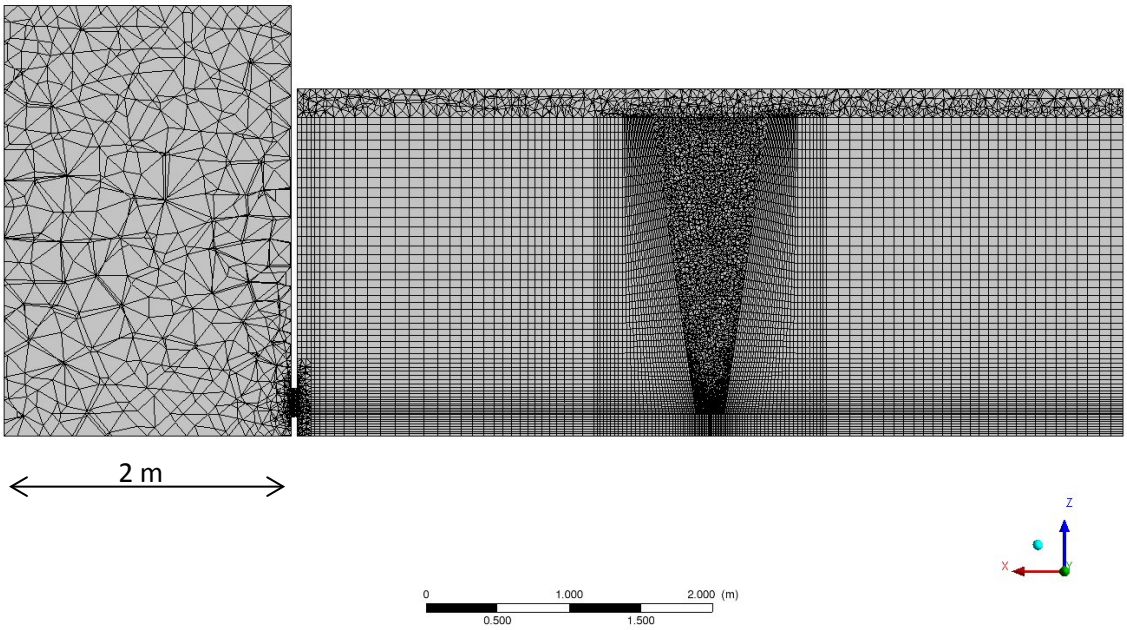

Figure 6.2-3. Mesh at symmetry plane for mesh #2.

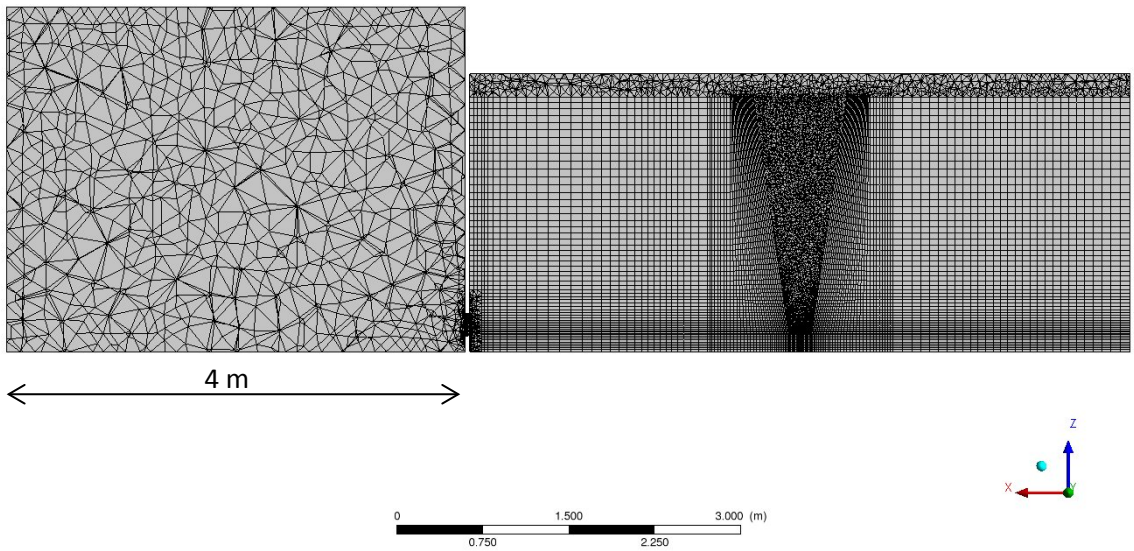

Figure 6.2-4. Mesh at symmetry plane for mesh #2.b.

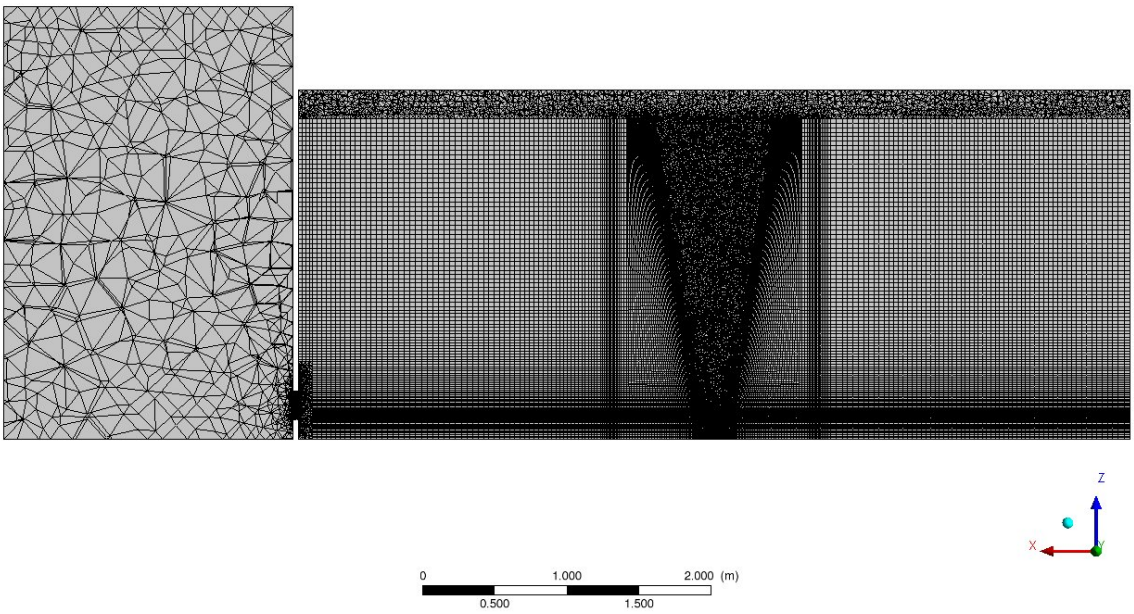

Figure 6.2-5. Mesh at symmetry plane for mesh #3.

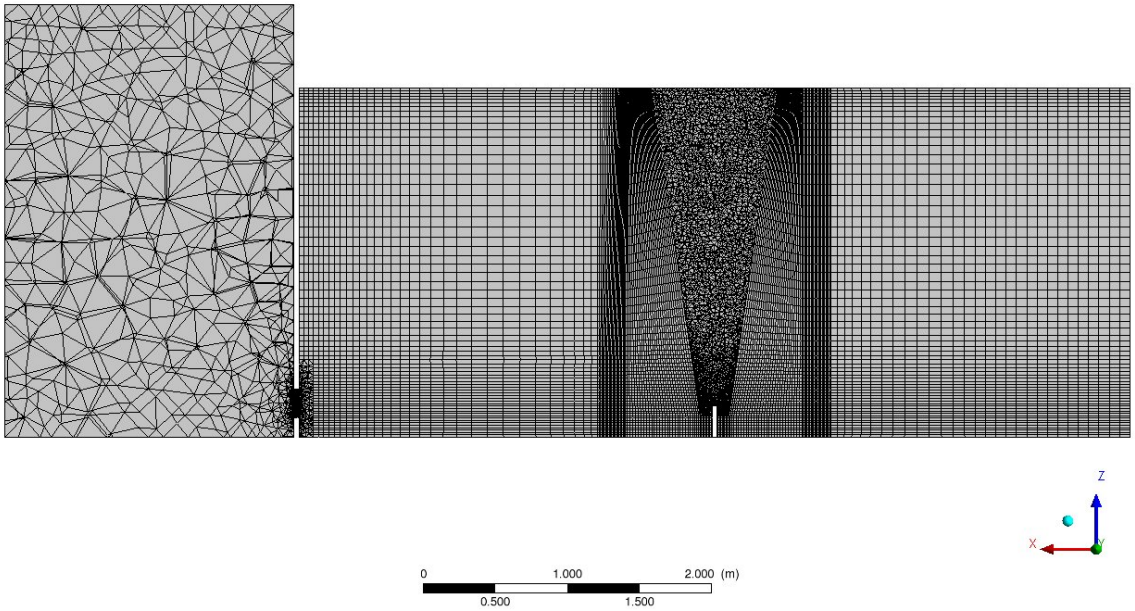

Figure 6.2-6. Mesh at symmetry plane for mesh #4.

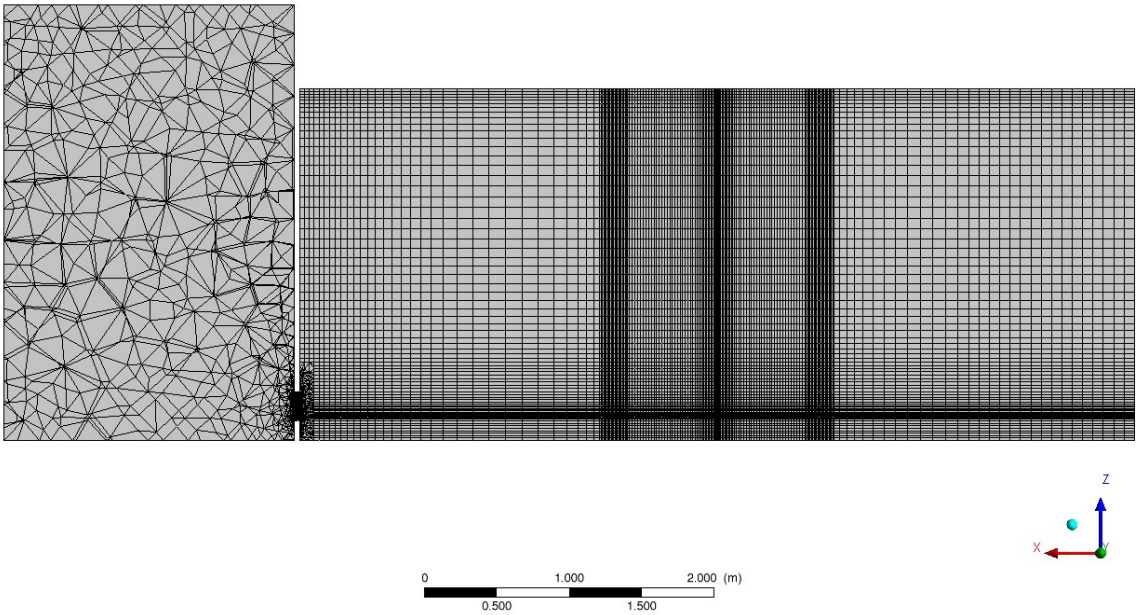

Figure 6.2-7. Mesh at symmetry plane for mesh #5.

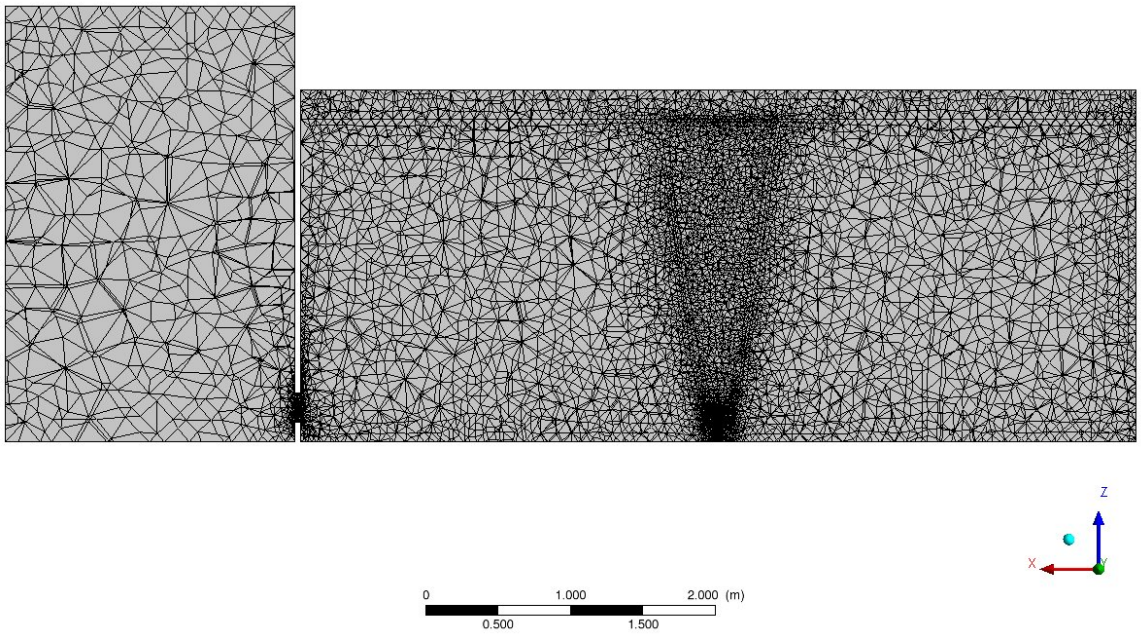

Figure 6.2-8. Mesh at symmetry plane for mesh #6.

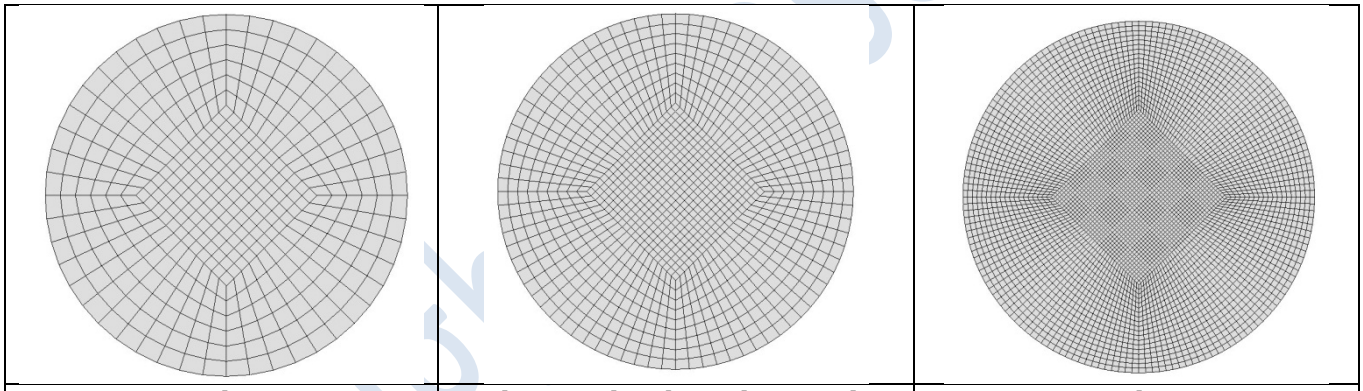

Mesh #1	**Mesh #2, Mesh #2.b, Mesh #4, Mesh #5**	**Mesh #3**
n. of nodes on the circumference: 56	n. of nodes on the circumference: 80	n. of nodes on the circumference: 160

Figure 6.2-9. Computational mesh on the boundary inlet surface in the pipe.

6.2.5 Sensitivity studies

A list of the performed simulations is reported in Table 6.2-4.

Table 6.2-4. Matrix of performed simulations.

	Case	# Mesh	Comp. time	Sim. time	n. of CPUs	TS	T.Model	notes
Sensitivity cases	a	1	0d 19h 15m	7500 s	15	1 s	SST trans	
	b	2	10d 23h 31m	7500 s	45	0.1 s	SST trans	
	c	3	6d 46h 52m	7500s	45	1 s	SST trans	
	d	2		7500 s	15	1 s	SST trans	
	e	2	1d 07h 51m	7500 s	15	5 s	SST trans	
	f	2.b	1d 17h 10m	7500 s	30	1 s	SST trans	
	g	4	2d 06h 50m	7500 s	30	1 s	SST trans	

h	5	2d 21h 43m	7500 s	30	1 s	SST trans	
l	6	0d 14h 47m	7500 s	45	1 s	SST trans	
m	5	1d 03h 16m	7500 s	45	1 s	LAM	
o	1	0d 09h 13m	7500 s	45	1 s	LAM	
p	2	0d 22h 59m	7500 s	45	1 s	LAM	
q	3	6d 21h 36m	7500s	45	1 s	LAM	
r	1	0d 10h 59m	7500 s	45	1 s	DES	
s	3	9d 07h 43m	7500s	45	1 s	DES	
i	2	2d 07h 44m	20000 s	45	1 s	SST trans	Ref. case
j	2	1d 21h 24m	20000 s	45	1 s	Laminar	
k	2	2d 06h 34m	20000 s	45	1 s	DES	

6.2.5.1 Mesh resolution sensitivity

In the following figures, the comparison of the simulation results, using SST, laminar and DES model respectively, for the mesh #1 (0.11 million node), #2 (0.47 million node), and #3 (2.86 million node) is shown with the experimental measurements for 2 lines of sensors.

A relevant parameter to compare computational results from different grid is the relative error, as it is mentioned in Section 1.3.2.3:

$$relative\ error = \frac{C_{coarse} - C_{fine}}{C_{fine}} \tag{6.2.1}$$

Zero relative error indicates that grid independency has been achieved. However, zero values are usually very difficult to be achieved. Therefore, small values, e.g. <10% are assumed to provide sufficient grid independency.

Since we have to present the results in a compact form in this annex, we do not show the relative error for all the sensors and all the time-steps and we only describe the relative error for the maximum concentration for a selected number of sensors. Nevertheless it must be emphasised that the relative error should be calculated in all sensors and in all time steps.

SST model

In Figure 6.2-10 and Figure 6.2-11, the comparison of the simulation results for the mesh #1 (0.11 million node), #2 (0.47 million node), and #3 (2.86 million node) is shown along with the experimental measurements for 2 lines of sensors, using the SST model.

As shown in Figure 6.2-12, the maximum relative error for mesh #1 with respect to mesh #2 is about 6%. As illustrated in Figure 6.2-13, since in at least one sensor, the maximum relative error is about 10% for mesh #1 with respect to mesh #3 while for mesh #2 (still with respect to mesh #3), the maximum relative error is about 4%, we have selected mesh #2 as the preferential mesh for the continuation of this analysis.

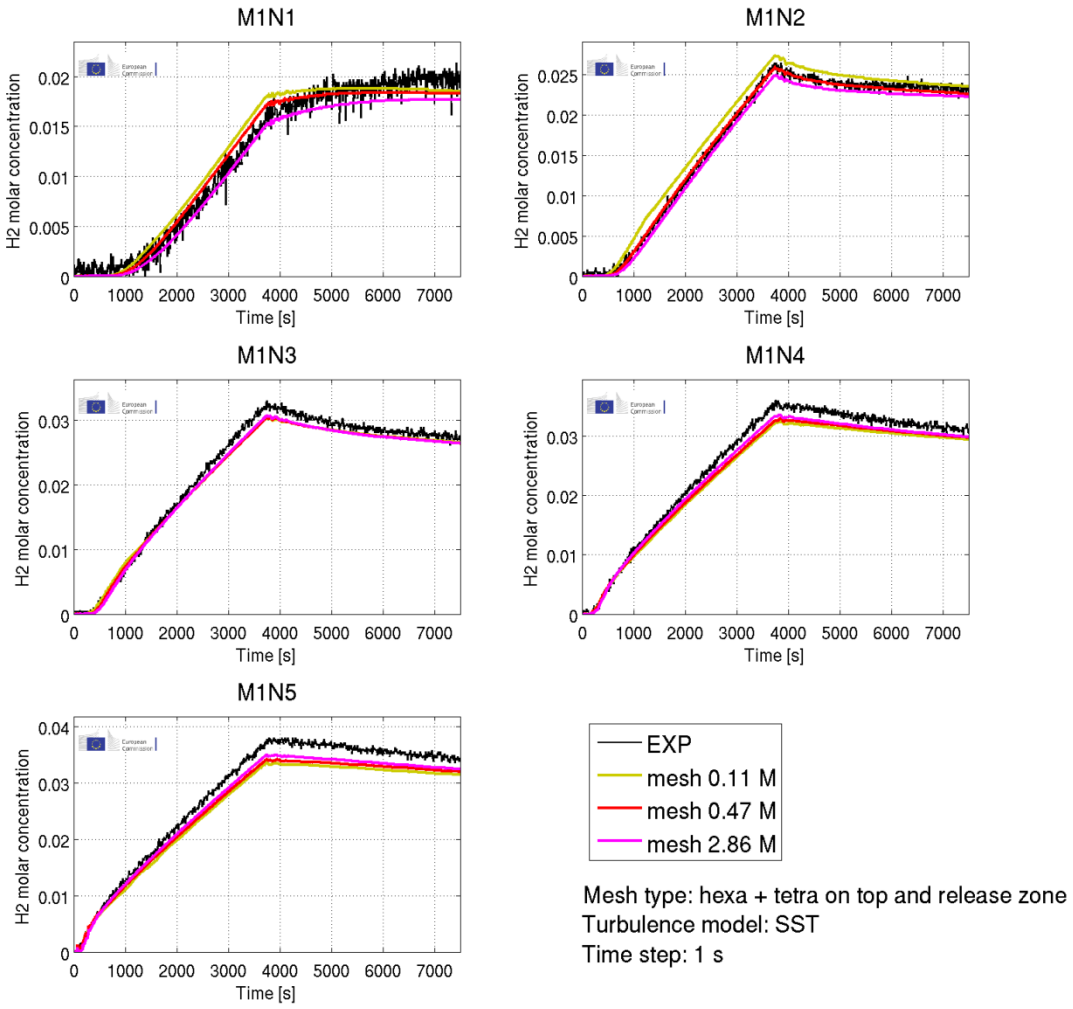

Figure 6.2-10. Helium molar concentration in M1N sensors. Mesh #1 (0.11 M; simulation a), #2 (0.47 M; simulation c), and #3 (2.86 M; simulation d).

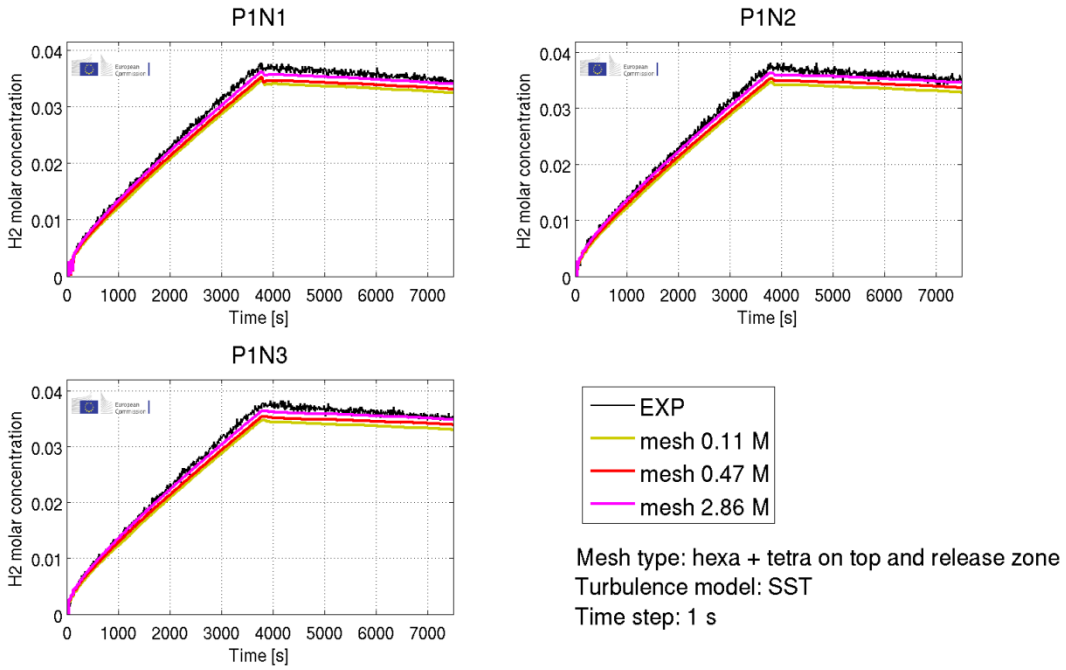

Figure 6.2-11. Helium molar concentration in P1N sensors. Mesh #1 (0.11 M; simulation a), #2 (0.47 M; simulation c), and #3 (2.86M; simulation d).

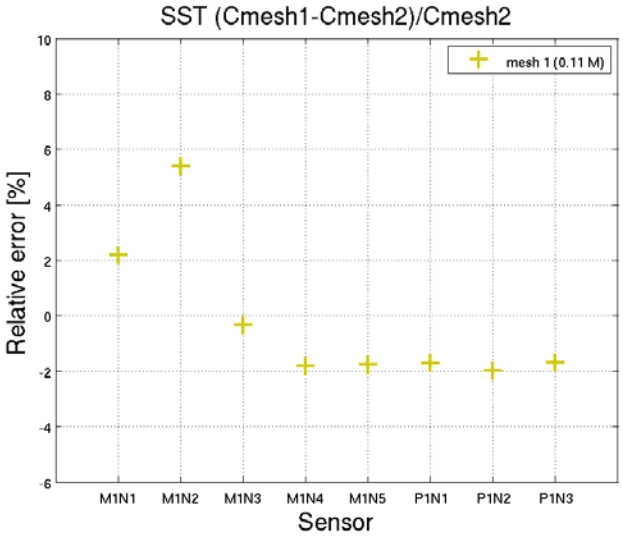

Figure 6.2-12. Relative error of the maximum concentration for mesh #1 relative to mesh #2. SST model.

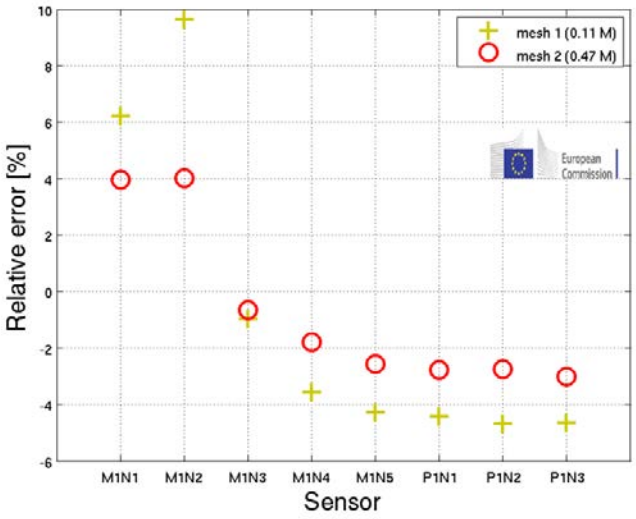

Figure 6.2-13. Relative error of the maximum concentration for mesh #1 and #2 relative to mesh #3. SST model.

Laminar model

In Figure 6.2-14 and in Figure 6.2-15, the comparison of the simulation results for the mesh #1 (0.11 million node), #2 (0.47 million node), and #3 (2.86 million node) is shown along with the experimental measurements for 2 lines of sensors, using the laminar model.

As illustrated in Figure 6.2-16, the maximum relative error of mesh #1 with respect to mesh #2, is just above 10% and that could lead to think that some level of grid independency has been achieved. Nevertheless that is not confirmed if mesh #3 is considered in the analysis. As shown in Figure 6.2-17, since in at least one sensor, the maximum relative error with respect to mesh #3 (the mesh with the finest resolution) is about 35% for mesh #1 while for mesh #2, the maximum relative error is larger than 20%, mesh independent results were not achieved with the laminar model. That is a clear indication that at least 3 meshes should be considered in grid sensitivity investigations.

It must be emphasised that the accuracy of the laminar model seems to decrease with finer mesh resolution for some of the M1N sensors. That is a clear indication that the laminar model is not capable of describing the experiment with a good level of accuracy for all sensors. The better results with the coarser grid were caused by the wrong reason that is a numerical effect. With the finer mesh resolution, the diffusion error decreases and the model shows its real accuracy capability for this experiment.

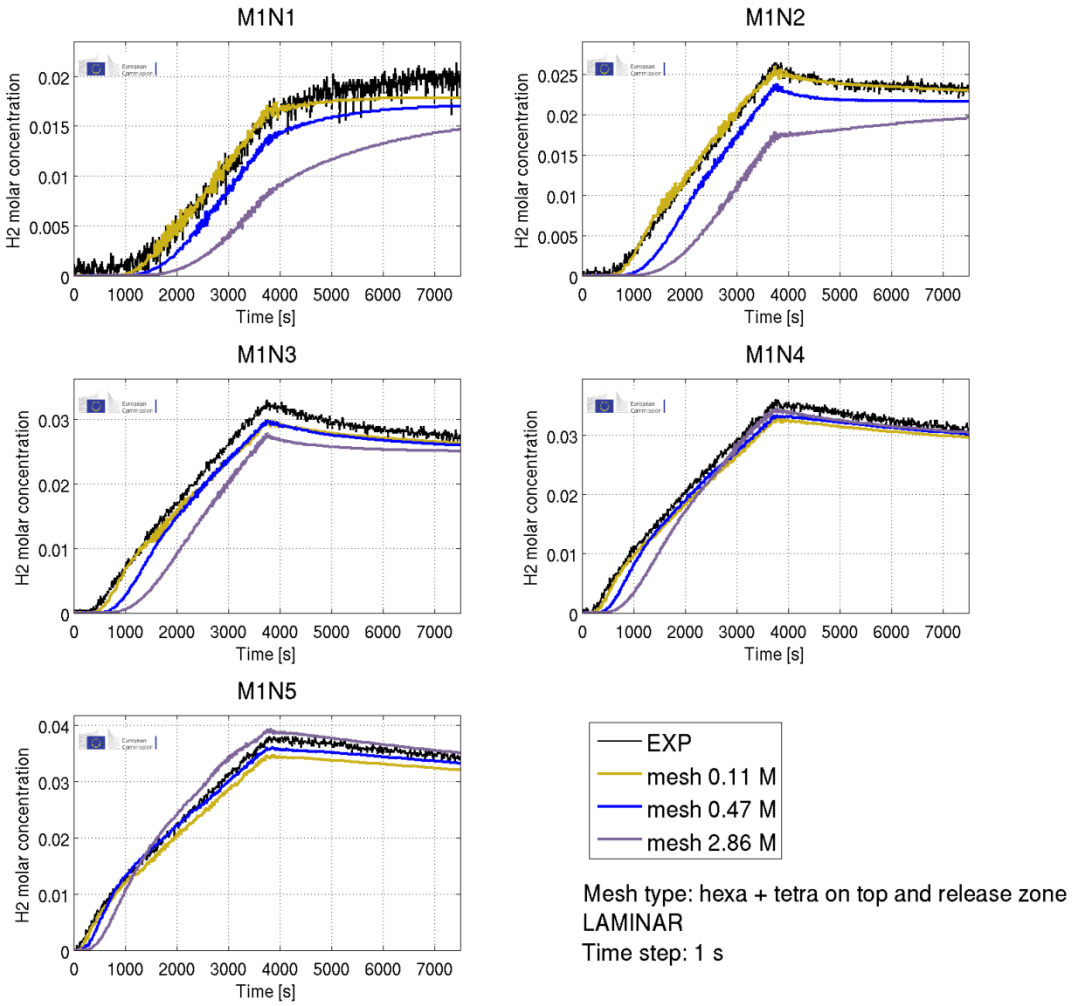

Figure 6.2-14. Helium molar concentration in M1N sensors. Mesh #1 (0.11 M; simulation o), #2 (0.47 M; simulation p), and #3 (2.86 M; simulation q); Laminar model.

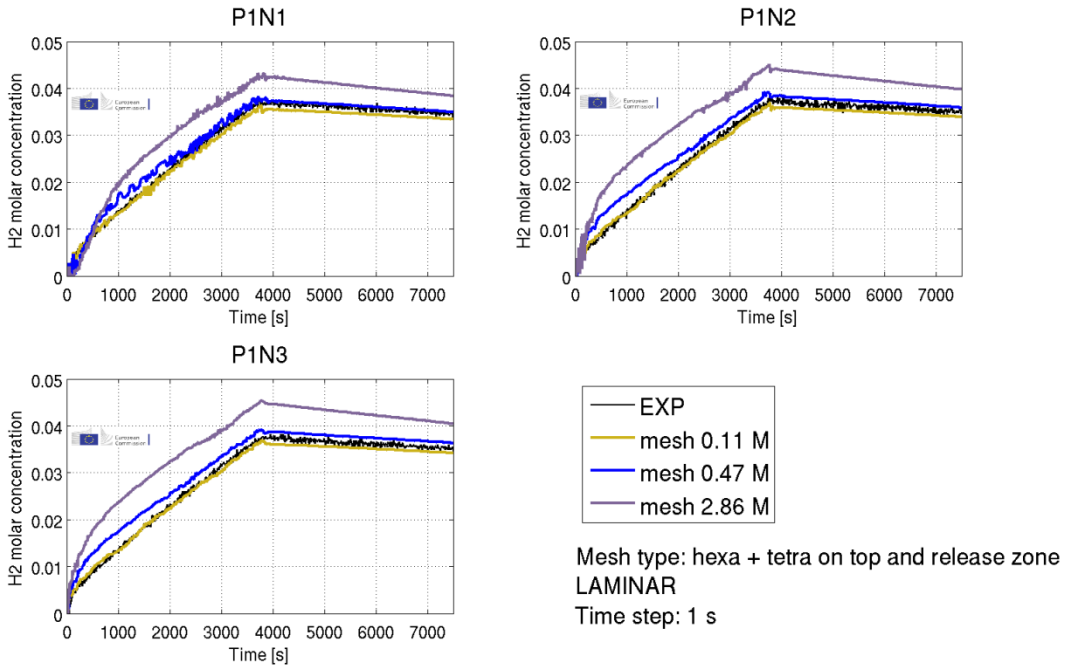

Figure 6.2-15. Helium molar concentration in M1N sensors. Mesh #1 (0.11 M; simulation o), #2 (0.47 M; simulation p), and #3 (2.86 M; simulation q); Laminar model.

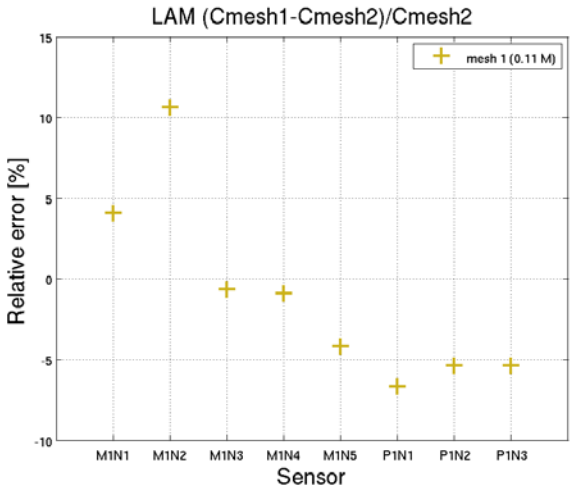

Figure 6.2-16. Relative error of the maximum concentration for mesh #1 relative to mesh #2; laminar model.

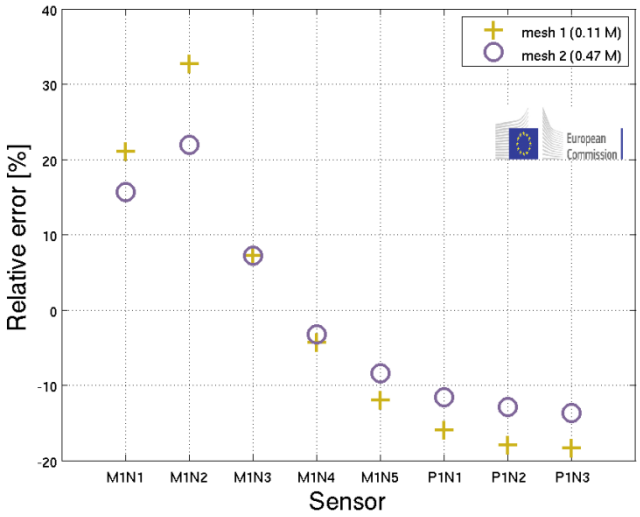

Figure 6.2-17. Relative error of the maximum concentration for mesh #1 and #2 relative to mesh #3; laminar model.

DES model

In Figure 6.2-18 and in Figure 6.2-19, the comparison of the simulation results for the mesh #1 (0.11 million node), #2 (0.47 million node), and #3 (2.86 million node) is shown along with the experimental measurements for 2 lines of sensors, using the DES model.

As depicted in Figure 6.2-20, the maximum relative error of mesh #1 with respect to mesh #2 is about 10%. Also in this case, like for the laminar case, one could think that some level of grid independency has been achieved. However that is not confirmed by the following analysis. As shown in Figure 6.2-21, since in at least one sensor, the maximum relative error is about 30% for mesh #1 while for mesh #2, the maximum relative error is about 20%, mesh independent results were not achieved with the DES model.

It should be highlighted that LES grid independency analysis requires special attention. As explained by (Gullbrand, 2002), when explicit filtering is used, the explicit filter width has to be kept constant while the computational grid is refined to obtain a grid-independent solution. With implicit filtering, since the filter is directly connected to the mesh resolution, the solution converges towards a direct numerical simulation (DNS) as the grid is refined, and not towards the filtered Navier-Stokes equations (Gullbrand, 2002). Moreover in the DES model, there is a further complication that is the switch between the RANS-SST model and the LES model that can also be affected by the mesh resolution. The overall results of the above mechanisms is that in the exact same location, according to the selected mesh resolution (coarse, finer, finest), different models could be applied by the code e.g. RANS or LES and sub-grid modelling or no sub-grid modelling.

As far as the DES performance with respect to the measurements is concerned, the grid independency analysis showed that a finer mesh resolution causes a worsening of the model accuracy in several sensors. The same behaviour for the DES model was shown also by (Gant, 2010) and was partly explained by (Geurts, 2006), at least for the LES model. The total error is the sum of the modelling error and the discretization error. The two errors have opposite effects and tend to compensate each other. In the coarse grid the modelling error is cancelled out by the discretization error and the total error is small. The discretization error

decreases with increasing resolution and the total error approaches the modelling error which is by itself larger than the total error in coarser grids.

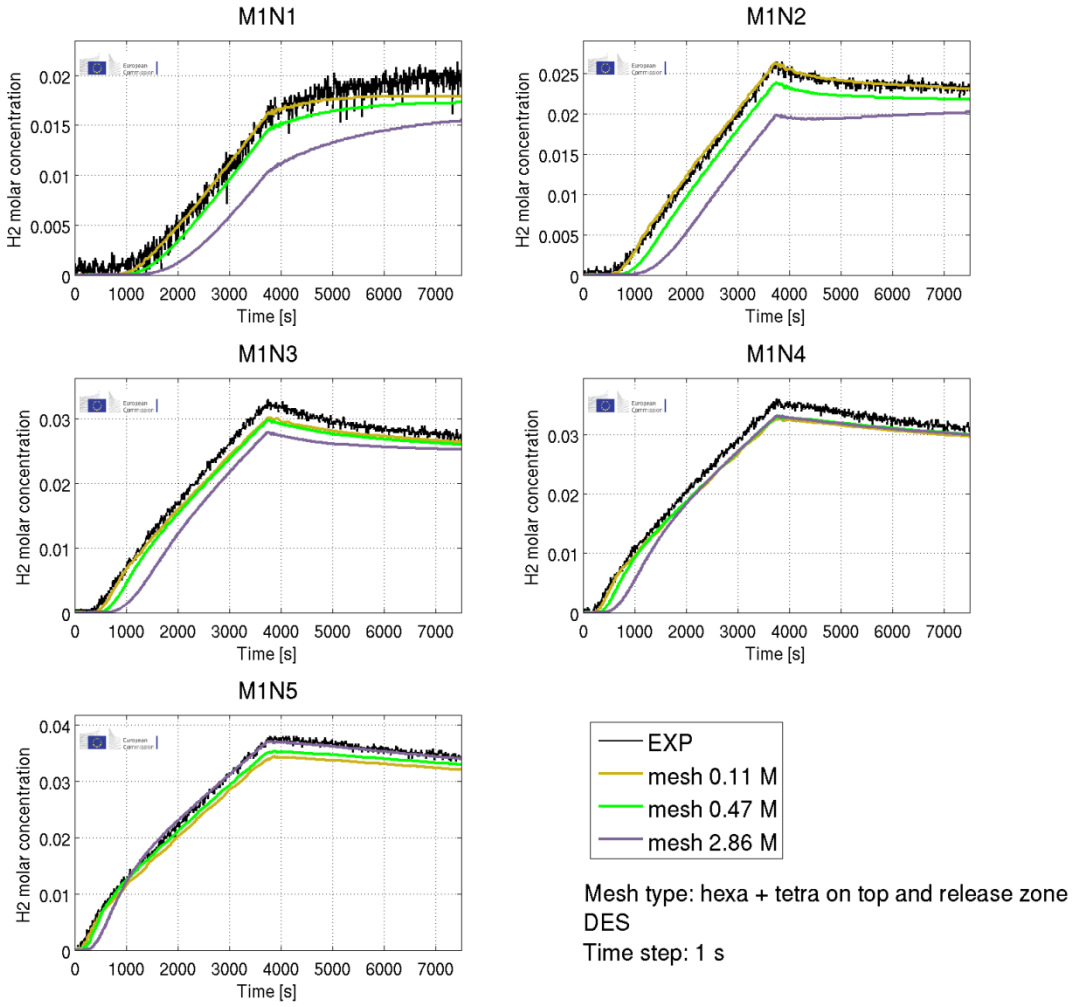

Figure 6.2-18. Helium molar concentration in M1N sensors. Mesh #1 (0.11 M; simulation r), #2 (0.47 M; simulation k), and #3 (2.86 M; simulation s); DES model.

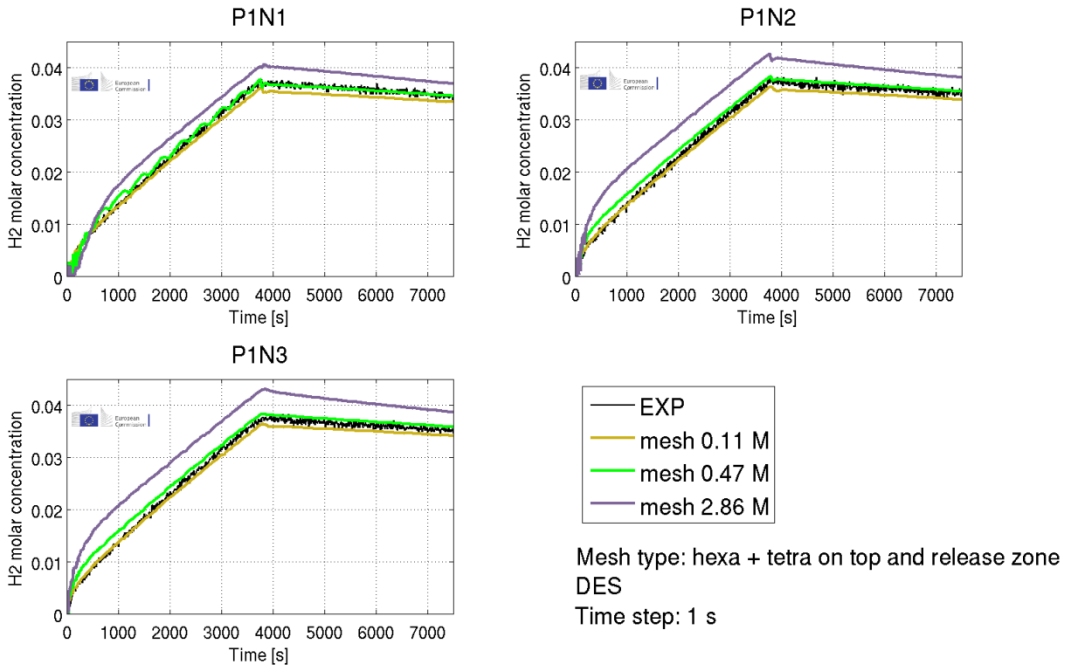

Figure 6.2-19. Helium molar concentration in M1N sensors. Mesh #1 (0.11 M; simulation r), #2 (0.47 M; simulation k), and #3 (2.86 M; simulation s); DES model.

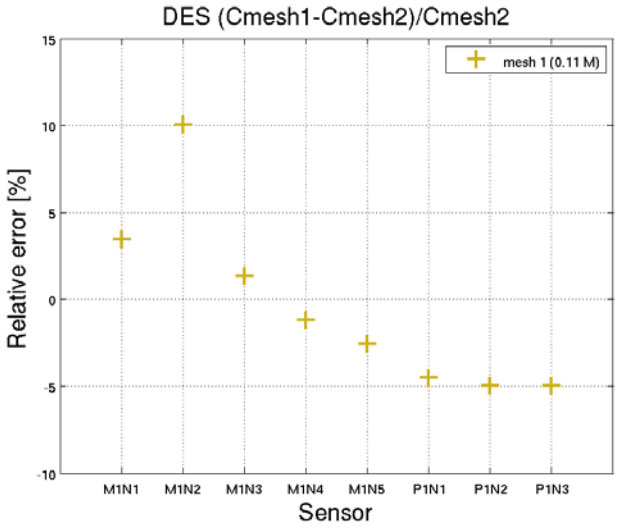

Figure 6.2-20. Relative error of the maximum concentration for mesh #1 relative to mesh #2; DES model.

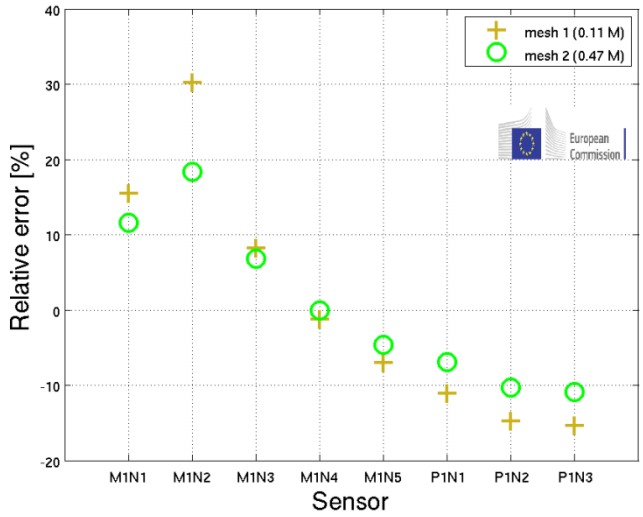

Figure 6.2-21. Relative error of the maximum concentration for mesh #1 and #2 relative to mesh #3; DES model.

6.2.5.2 Time-step sensitivity

In Figure 6.2-22 and Figure 6.2-23, the comparison of the simulation results for 3 time-steps (0.1 s, 1 s and 5 s) with the experimental measurements is shown for 2 lines of sensors. In Figure 6.2-24, the relative error of the simulation results for the maximum concentration with 5s and 1s time-step relative to 0.1 s time-step is shown. Also in this sensitivity study like for the grid independency study, only some partial results are shown for demonstration purposes (maximum concentration on selected sensors) while it must be emphasised that the relative error should be calculated for all sensors and for the whole duration of the simulation. A 5 s time-step produces a large relative error (up to 20%) while the difference between the results with 1s and 0.1 s is negligible. Therefore, a 1 s time-step will be applied in the rest of this study.

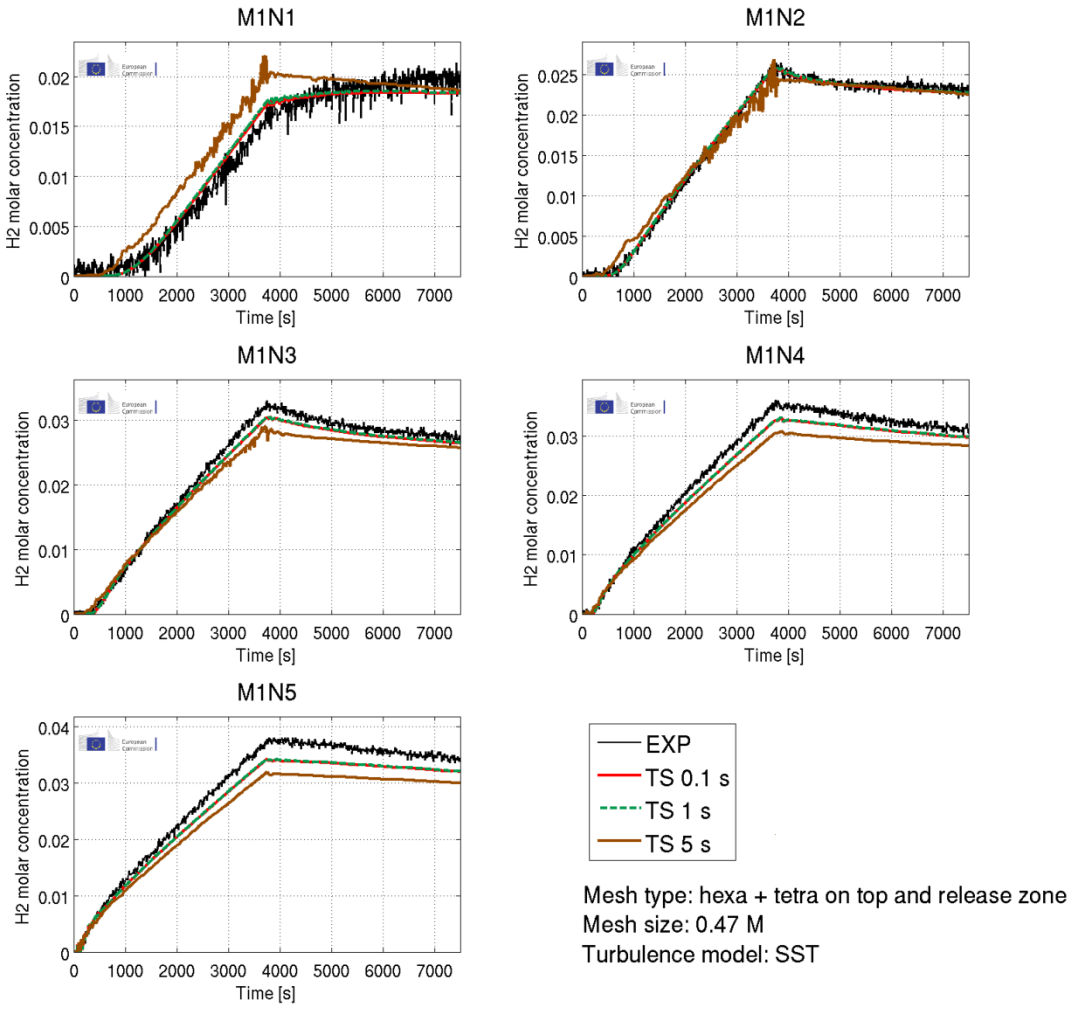

Figure 6.2-22. Helium molar concentration in M1N sensors. Mesh #2. Simulation b (0.1 s), d (1 s), and e (5 s).

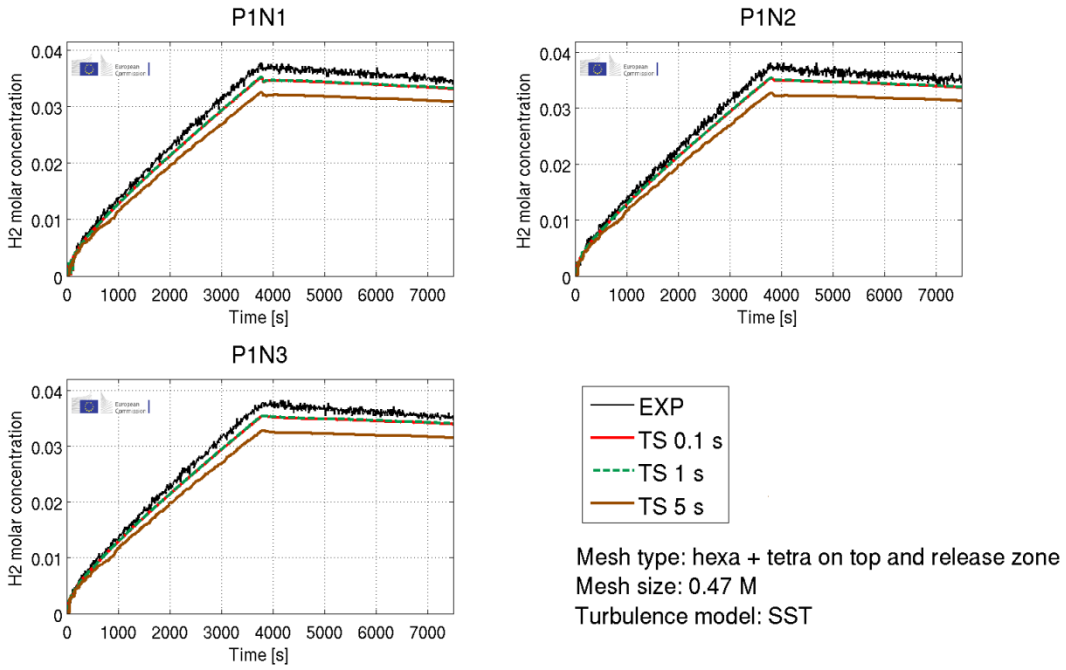

Figure 6.2-23. Helium molar concentration in P1N sensors. Mesh #2. Simulation b (0.1 s), d (1 s), and e (5 s).

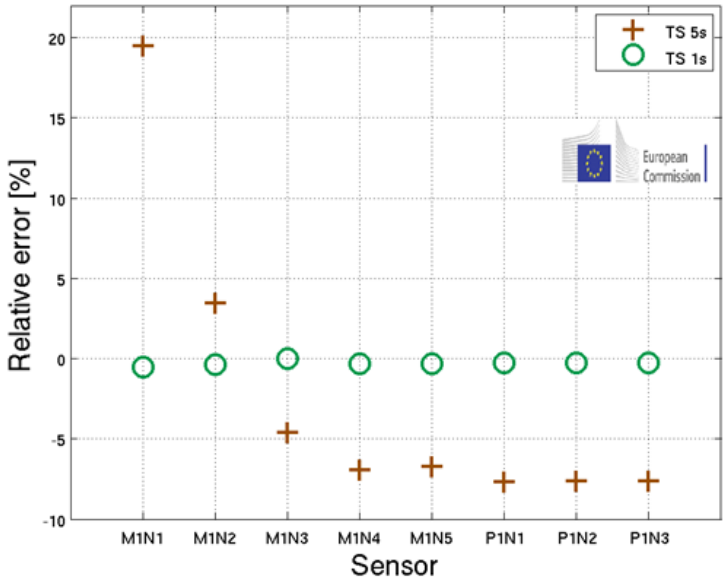

Figure 6.2-24. Relative error for the maximum concentration for the simulation results with 5s and 1 s time-step relative to 0.1 s time-step; mesh #2.

6.2.5.3 Mesh type sensitivity

In Figure 6.2-25 and Figure 6.2-26, the comparison of the simulation results for different meshes with the experimental measurements is shown for 2 lines of sensors. In all simulations the SST turbulence model was employed. 4 grids are considered:

- the reference case (mesh #2 - Figure 6.2-3; tetra mesh in the jet region, in the ceiling region, and in the vent region and the external box; hexa mesh in the remaining regions of the garage),
- a mesh similar to mesh #2 but without any mesh refinement in the ceiling region (mesh #4 - Figure 6.2-6),
- a fully hexa mesh (mesh #5 - Figure 6.2-7),
- a fully tetra mesh (mesh #6 - Figure 6.2-8).

With the fully hexa mesh (mesh #5), a much larger concentration gradient is captured in the simulation compared to the experiment. In the upper part (closer to the ceiling), the concentration is over-estimated by the simulation while in the bottom part (closer to the floor), the concentration is under-estimated. In the fully tetra mesh, the results are not as accurate as with mesh #2, especially in the bottom part of the facility and especially during the diffusion period (after the gas release has been stopped) where the flow is dominated by molecular diffusion.

The difference in the simulation results between mesh #2 and mesh #4 is negligible therefore the mesh refinement in the region close to the ceiling does not seem to be necessary. On the contrary the initial assumptions for using a hybrid mesh (mesh #2, hexa + tetra in specific regions like the jet region) has been shown to be valid since in a full hexa (mesh #5) and in a full tetra mesh (mesh #6) the simulation results are not as accurate as in the hybrid mesh, especially in the sensors that are located in the bottom part of the facility (e.g. sensor M1N1).

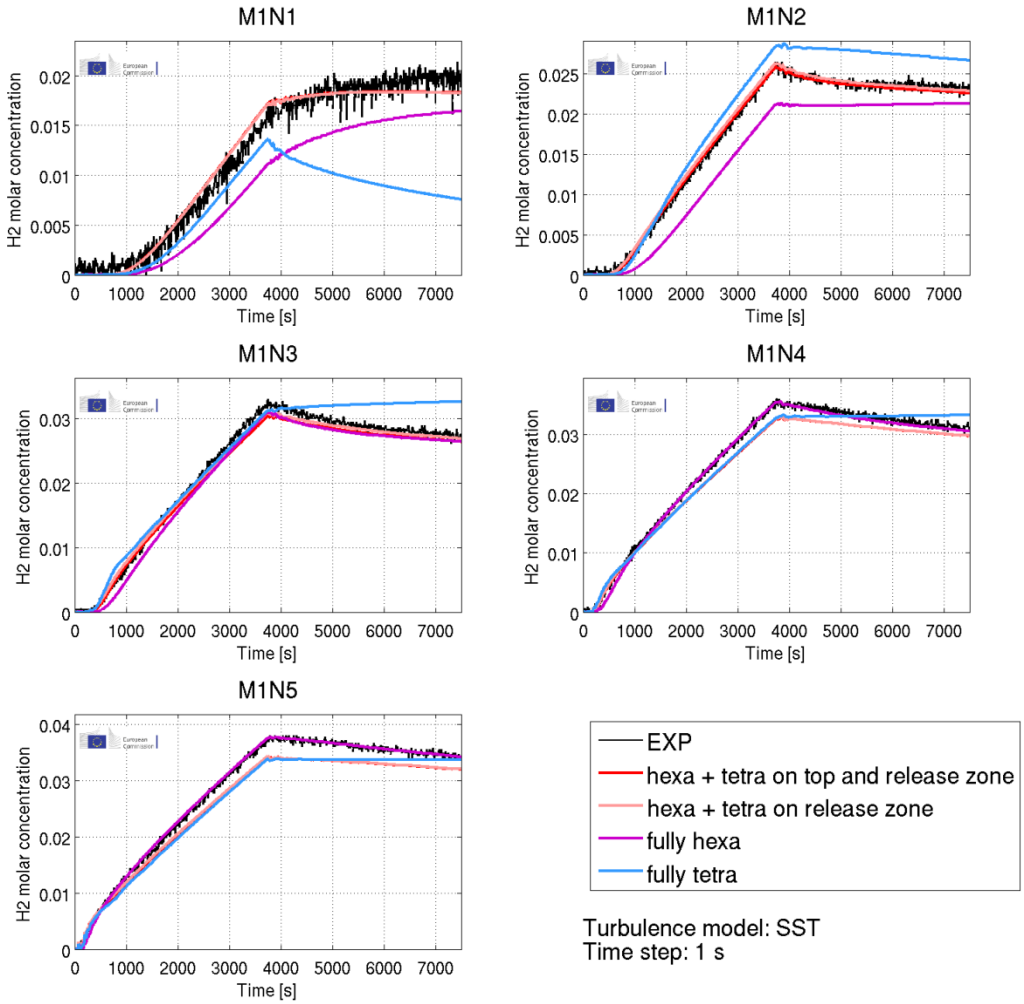

Figure 6.2-25. Helium molar concentration for M1N sensors. Mesh #2 (Hexa + tetra on the ceiling and release zone; simulation b), #4 (hexa + tetra on the release zone; simulation g), #5 (fully hexa; simulation h), and #6 (fully tetra; simulation l).

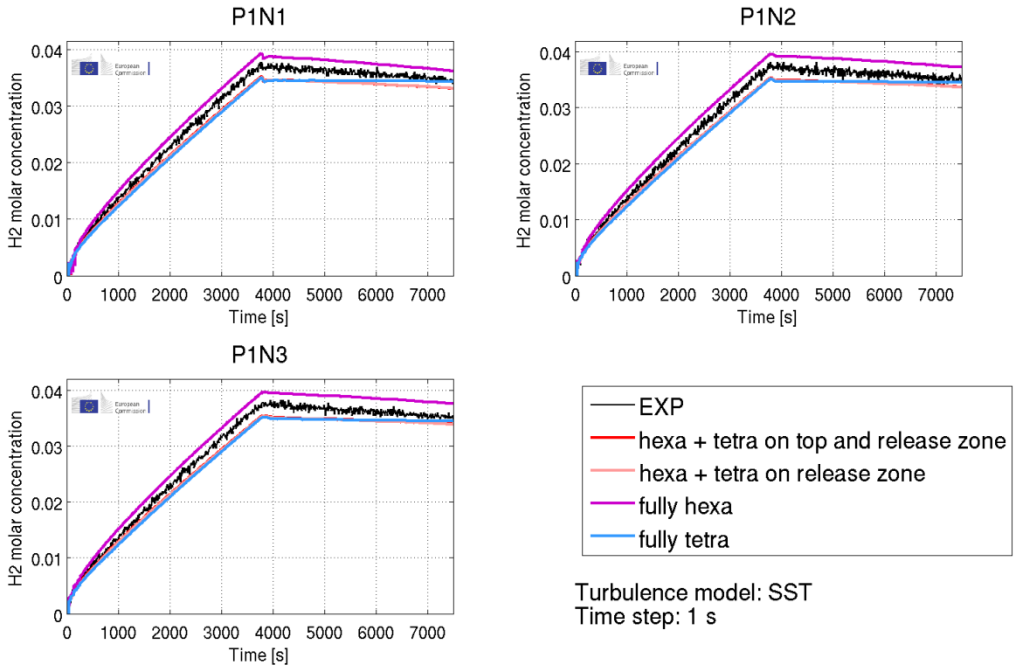

Figure 6.2-26. Helium molar concentration for P1N sensors. Mesh #2 (Hexa + tetra on the ceiling and release zone; simulation b), #4 (hexa + tetra on the release zone; simulation g), #5 (fully hexa; simulation h), and #6 (fully tetra; simulation l).

6.2.5.4 Domain size sensitivity

The size of the external room can affect the simulation results as shown in Papanikolaou et al (2010) for a similar configuration, since the distance between the boundary conditions and the regions where the main phenomena occur can play a role in the result accuracy. Therefore an additional simulation was performed with an increase size of the external room to verify that potential effect.

In Figure 6.2-27 and Figure 6.2-28, the comparison of the simulation results for 2 sizes of the external room is shown for 2 lines of sensors. In this specific case, doubling the length of the external room does not affect the results.

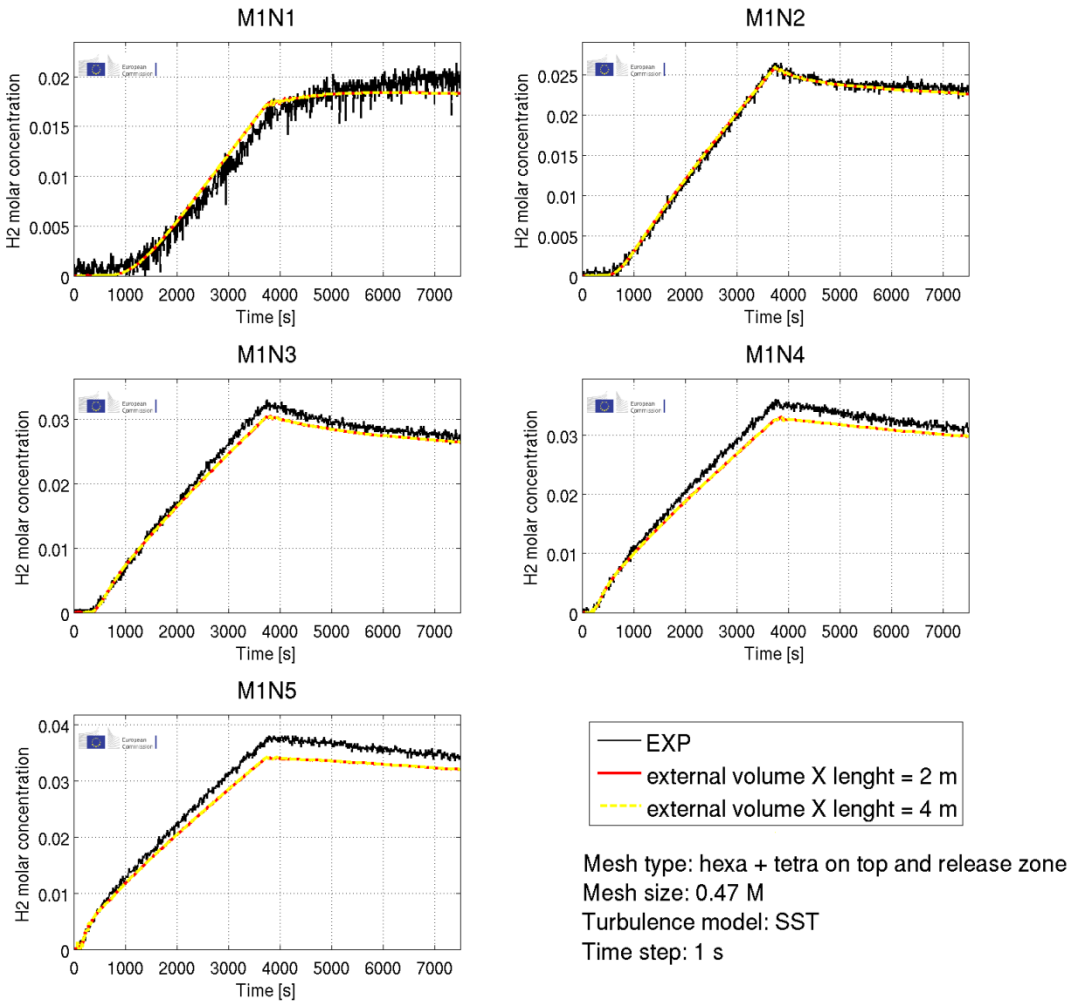

Figure 6.2-27. Helium molar concentration for M1N sensors. Mesh #2 (smaller external volume; simulation a) and mesh 2b (larger external volume; simulation f).

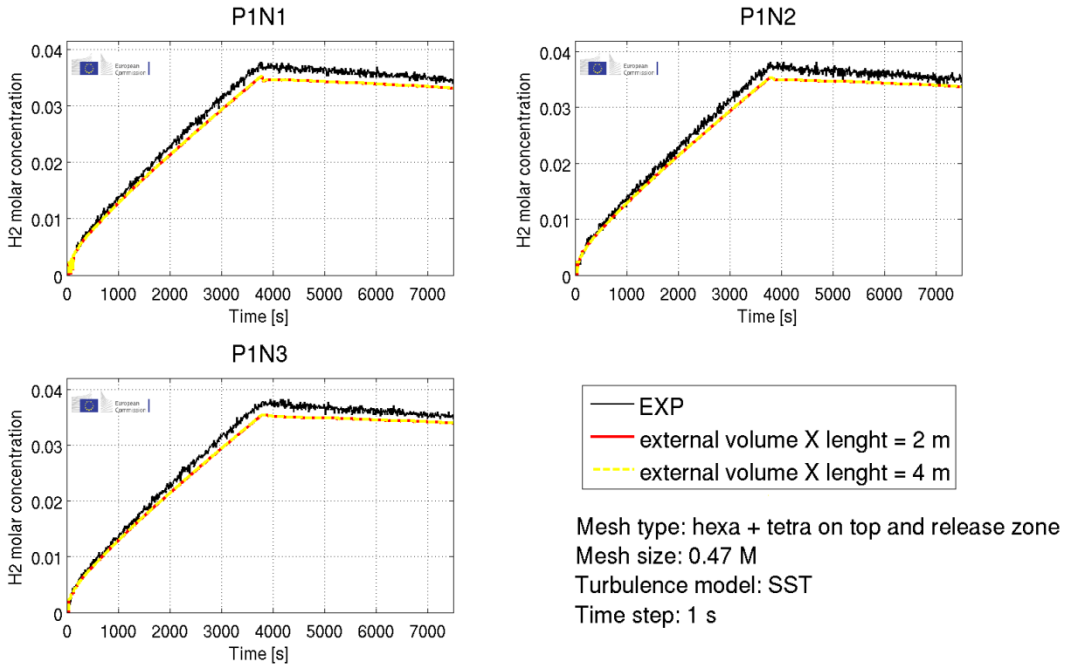

Figure 6.2-28. Helium molar concentration for P1N sensors. Mesh #2 (smaller external volume; simulation a) and mesh 2b (larger external volume; simulation f).

6.2.5.5 Turbulence model sensitivity

Since it is expected that the flow could be partly laminar and partly turbulent, the SST transitional model was initially selected. After several calculations, it was confirmed that the SST model is suitable for the simulation of this experiment.

Simulations with the laminar model and the DES model were also performed but it was not possible to show grid independence for the 2 models. By comparing the grid independent SST results with the laminar and DES mode on the finest mesh, it was shown in the previous Sections that the SST model is the more accurate and therefore the more suitable for this experiment.

6.2.5.6 Final results for the reference case

The reference case was run with the SST transitional model, mesh #2, and a time step of 1 s. The position of the sensors in the facility is illustrated in Figure 6.2-1, Figure 6.2-29, and Figure 6.2-30. Sensors are placed in vertical lines. The letter p identifies the lines of 3 sensors that are located in the top region of the room, just under the ceiling while the letter m identifies the lines of 5 sensors that are located at medium and low heights in the facility. In Figure 6.2-31, the results in the 6 m lines are shown for the top and bottom sensors in each m line while in Figure 6.2-32, the data for one representative sensor in the p lines are presented.

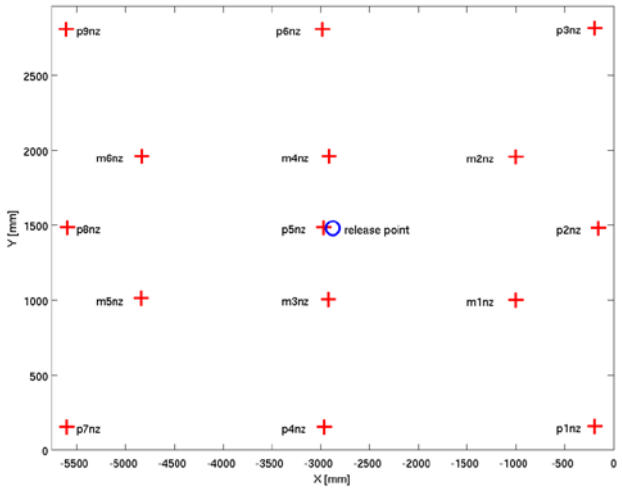

Figure 6.2-29. Top view of the experimental facilities with sensors and inlet pipe position.

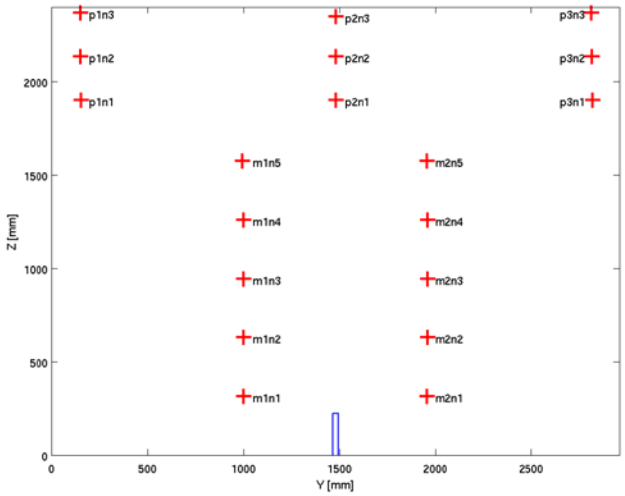

Figure 6.2-30. Side view of the experimental facilities with sensors and inlet pipe position.

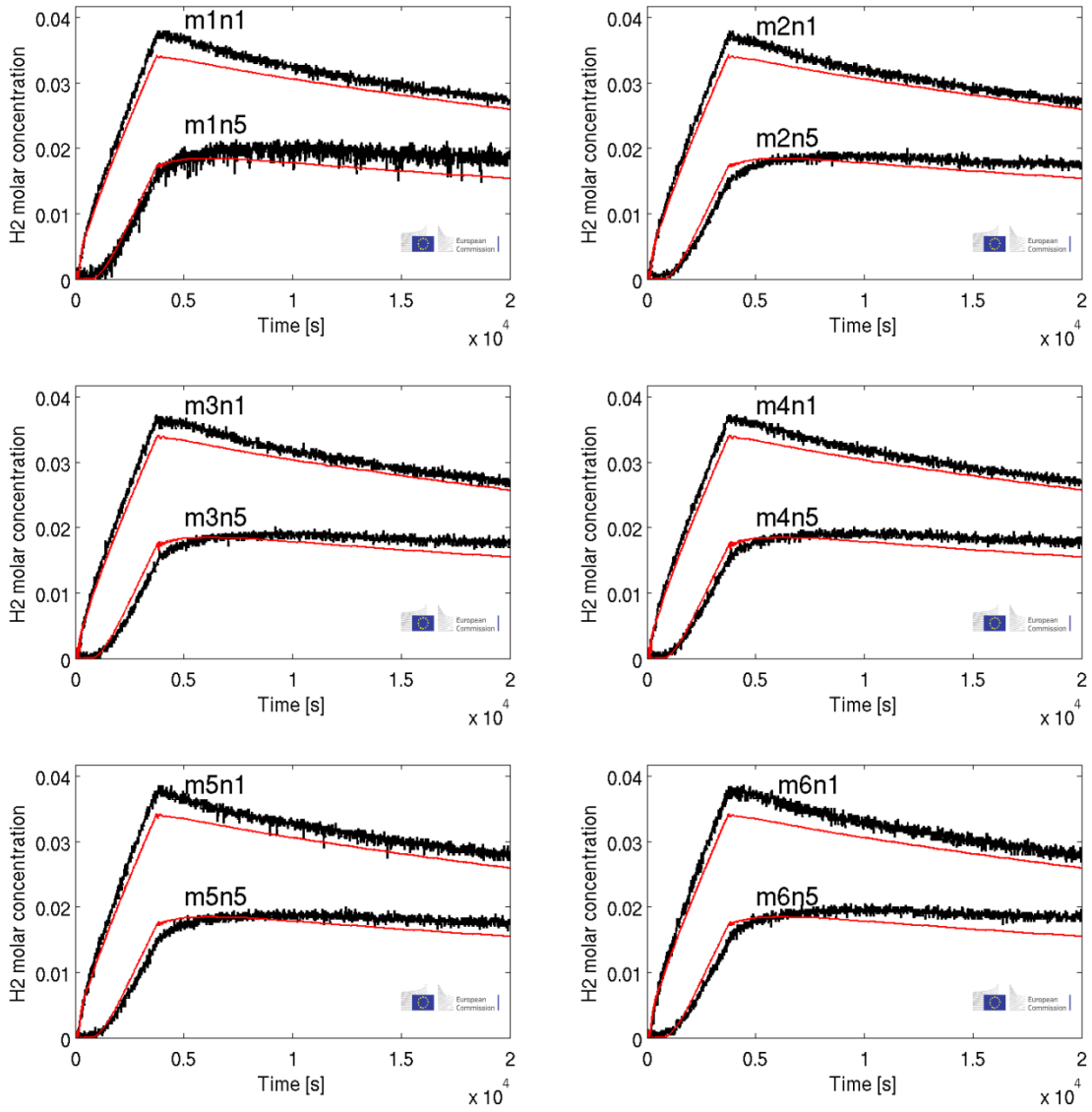

Figure 6.2-31. Helium molar concentration – Reference case (SST, TS = 0.1 s, mesh #2).

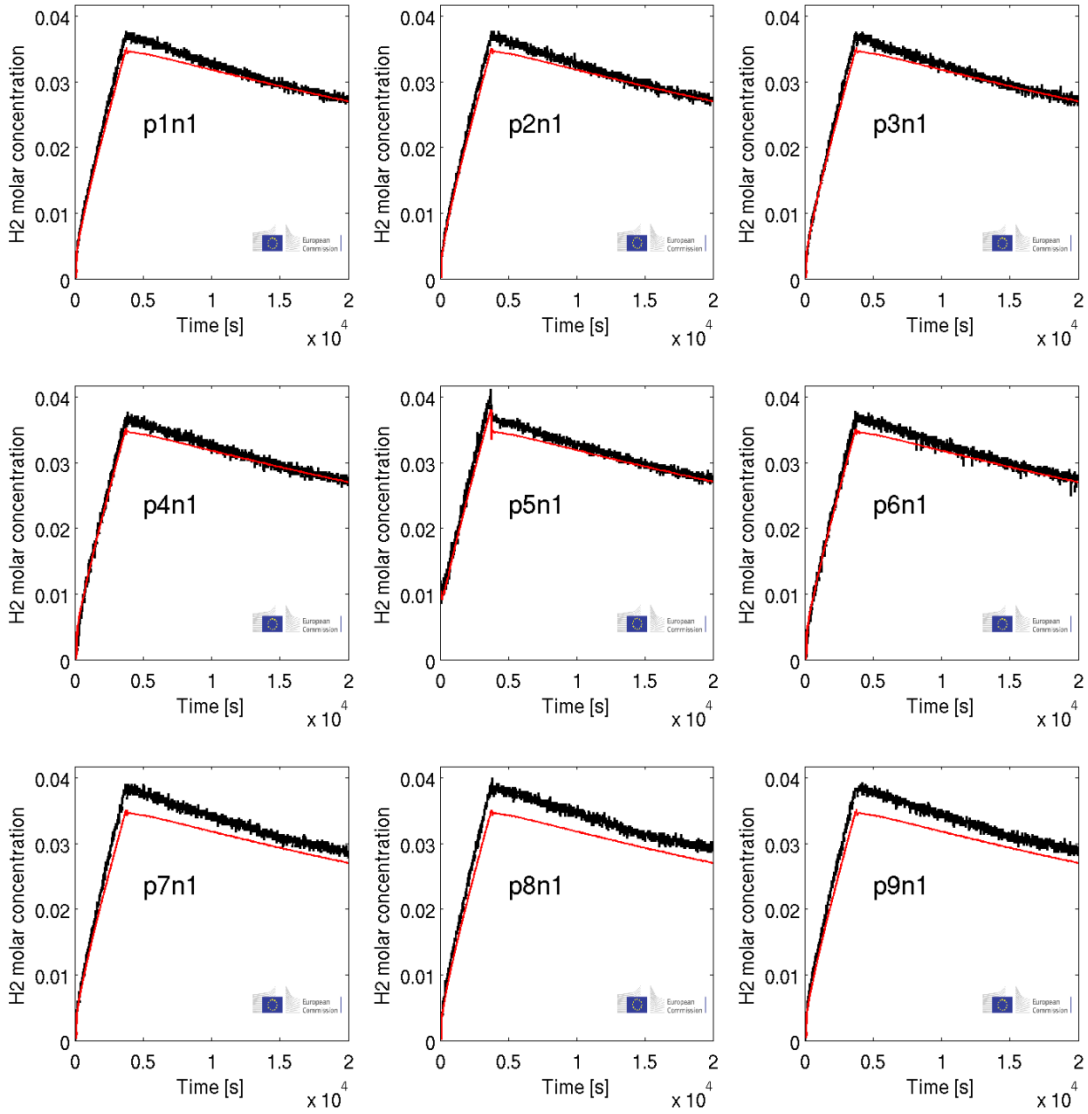

Figure 6.2-32. Helium molar concentration – Reference case (SST, TS = 0.1 s, mesh #2).

The agreement between the simulation results and the experimental data is satisfactory. It must be emphasised that it was shown that the calculation results are grid-independent, and time-step independent. Different types of computational mesh were also considered. Moreover, it was demonstrated that the size of the computational domain for the external environment was large enough and it did not affect the results.

6.3 Sample Case 3 - Ignition & Fire

Most simulations of hydrogen spontaneous ignition by the diffusion mechanism were carried out in 2D formulations, with validation only for relatively simple axisymmetric geometries and fine mesh to directly resolve the diffusion ignition phenomenon. One dimensional modelling of ignition is limited by the applicability of ignition models because ignition could occur somewhere aside of centre-line. In spite of a measure of success achieved by 2D models, capturing the physics of turbulent mixing requires implementation of a fully 3D model. Furthermore, utilization of 3D models is required in order to be able to perform simulations and reproduction of experimental results obtained in complex realistic geometries, where 2D simulations cannot be applied. The use of two dimensional models is justified by the fact that the flame front has to be well resolved, and utilisation of three dimensional grids with micron resolution is not feasible from the computational point of view. Therefore, the use of combustion models with sub-grid-scale modelling such as eddy dissipation concept (EDC) with chemistry allows to model combustion at fine scales using coarser grid resolution.

Similar approach was recently used for simulation of hydrogen jet fires indoors (Molkov et al., 2014), lift-off and blow-off (Shentsov et al., 2016b) and hydrogen high pressure tank rapture with a blast wave and a fireball (Kim et al., 2015; Shentsov et al., 2016a).

As sample case an experiment and validation for a spontaneous ignition in a T-shape device was chosen. Details for the experiment and the modelling approach are presented in the following paragraphs.

6.3.1 Experimental description

Experimental research on spontaneous ignition has been conducted by (Golub et al., 2010). The hydrogen was released from a high pressure system into a channel ending in a T-shaped nozzle mimicking Pressure Relief Device (PRD). The geometry of a high-pressure system and T-shaped channel were taken (Golub et al., 2010).

The high-pressure system consisted of a 210 mm long tube with 16 mm internal diameter (ID) followed by a 280 mm long tube with 10 mm ID at the end of which was a flat burst disk, made of a soft metal with cuts to facilitate failure. On the other side of the burst disk was a simulated PRD open to atmosphere (Figure 6.3-1). The PRD had a 48 mm long axial channel of 6.5 mm ID with a flat end, and two radial channels on opposite sides of the axial channel to vent hydrogen to atmosphere. Each radial channel was 6.25 mm length and 4 mm ID (distance from the end connected to the atmosphere of one radial channel to the end of another is 19 mm). Radial channels were flush with the axial channel end wall and positioned so that the edge of each side channel touches tangentially the flat end wall of the axial channel. The burst disk opening time was estimated as about 10 μs ((Golub et al., 2010). To register spontaneous ignition a light sensor was installed along the axis of radial channels of the PRD.

(Golub et al., 2010) stated that the light sensor did not record any signal when the initial pressure in high-pressure chamber was below 1.2 MPa, and record positive signal when the pressure was 2.9 MPa. Private communication (Golub, 2010) indicated that the ignition was also observed at pressure 2.43 MPa.

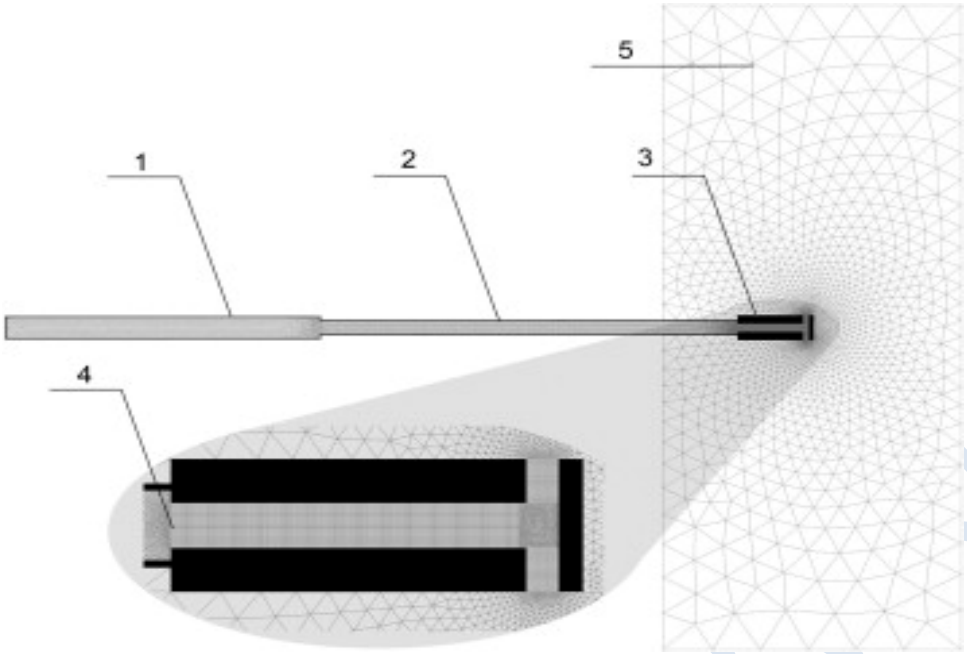

Figure 6.3-1. The geometry and computational domain: 1 and 2 – high-pressure tubes, 3 – PRD, 4 – burst disk, and 5 – external domain (Bragin et al., 2013).

6.3.2 Mathematical methodology

6.3.2.1 Governing equations

The simulation employed LES with a set of filtered three-dimensional compressible equations for conservation of mass, momentum (Navier-Stokes), energy and species serving as governing equations. The renormalization group (RNG) theory (Yakhot and Orszag, 1986) is used as a sub-grid-scale (SGS) model to calculate the effective viscosity. Full model description and details can be found in (Bragin et al., 2013).

6.3.2.2 Combustion model

The hydrogen spontaneous ignition simulation used an EDC model (Magnussen, 1981) with updates incorporating detailed Arrhenius chemical kinetics in turbulent flames as the combustion sub-model. EDC model expression for a combustion rate is based on an assumption that chemical reactions occur in the small scale structures on the Kolmogorov's scale where the dissipation of turbulence energy takes place.

6.3.2.3 Chemical reaction model

The simulation utilized the detailed 21-step chemical reaction mechanism of hydrogen combustion in air employing 37 elementary reactions by (Gutheil et al., 1993). The specific forward reaction rate constants are given in (Bragin et al., 2013) and backward rates for reversible reactions are calculated through the equilibrium constants.

6.3.3 Simulation approach

6.3.3.1Calculation domain

The axial and radial channels of the PRD were meshed with a hexahedral grid with a uniform control volume (CV) size of about 400 μm both along the axial channel and in its cross-section, excluding the intersection zone see Figure 6.3-1. The intersection area of the axial and the radial channels was meshed with tetrahedral CVs with size of about 200 μm, i.e. the largest CV size used in numerical simulations of the spontaneous ignition phenomenon up to date. This is due to the application of the LES technique requiring 3D domain and thus larger CV size to simulate a problem within reasonable computation time. The high-pressure chamber was meshed by tetrahedrons with the smallest CV size of about 250 μm clustered near the membrane of the PRD and rapidly increasing away from it reaching the maximum cell width of 10 mm at the far end. The total number of control volumes in the computational domain amounted to a moderate number of 417,685 cells.

6.3.3.2 Initial and Boundary Conditions

No-slip impermeable adiabatic boundary conditions were used on walls. Non-reflecting open "pressure-far-field" boundaries were implemented outside of the PRD. The high-pressure system was modelled as closed to exclude potential effects of inlet boundary conditions on the process. This assumption is justified because the observation time in simulation is less than a time required for rarefaction wave to reach the far end of the high-pressure system. Hydrogen initial pressure in the high-pressure system p0 = 1.35, 1.5, 1.65, 2.4 and 2.9 MPa. Initial temperature T0 = 300 K and the mole fraction of hydrogen equal to 1 were assumed in the high-pressure system before the burst disk rupture in all cases. Space within PRD and external area were filled with air (0.23 mass fraction of oxygen and 0.77 of nitrogen) at atmospheric conditions (p0 = 0.101 MPa and T0 = 300 K).

6.3.3.3 Burst disk opening

The importance of membrane opening and internal tube geometry in predicting ignition phenomena was demonstrated by a number of publications and reviewed in (SUSANA D2.2, 2016). The non-instantaneous burst disk opening plays an important role in the process of ignition due to effect on mixing between hydrogen and air. The opening of a membrane was therefore approximated in simulations by a step-like process consecutive opening of 10 concentric sections (see Figure 6.3-2).

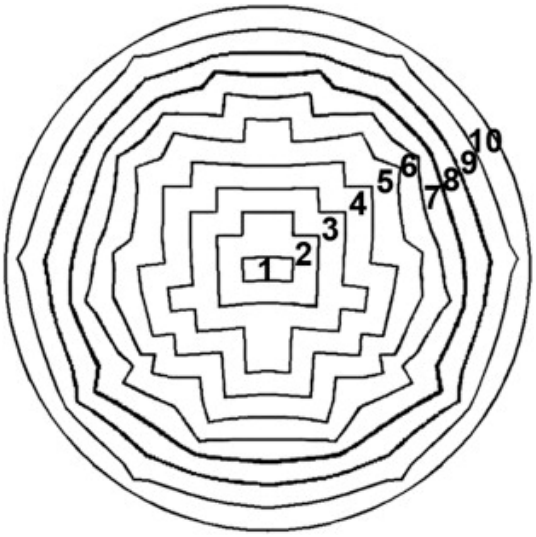

Figure 6.3-2. Step-like approximation of a burst disk rupture process: 1–10 are sections that open in series (Bragin et al., 2013).

Opening time of a diaphragm sections was calculated using Spence and Woods (1964) approach

$$t = k(\rho bd / p)^{1/2}$$

where ρ is the density of the diaphragm material, b and d are thickness and diameter of the diaphragm, respectively, and the values of k are found to be in a range 0.91–0.93 (Wen et al., 2009). Density of annealed copper was taken to be equal 8900 kg/m^3. Diaphragm sections opening times for various initial pressures are listed in Table 6.3-1.

Table 6.3-1. Opening time for diaphragm sections.

Initial pressure, MPa	Opening time, μs, for section									
	1	2	3	4	5	6	7	8	9	10
1.35	0	4.7	9.4	14.2	18.9	23.6	28.4	33.1	37.8	42.6
1.5	0	4.5	9	13.5	18	22.5	27	31.5	36	40.4
1.65	0	4.3	8.6	12.8	17.1	21.4	25.6	29.9	34.3	38.5
2.43	0	3.5	7.1	10.6	14.2	17.7	21.3	24.8	28.3	31.9
2.90	0	3.2	6.5	9.7	12.9	16.2	19.4	22.6	25.9	29.1

6.3.4 Numerical details

- Code: Numerical simulation was performed using ANSYS Fluent 6.3 CFD software
- Discretisation: finite volume
- Solver type: coupled, density based solver
- Numerical scheme for convective terms: second order upwind AUSM flux splitting
- Transient numerical scheme: explicit time stepping
- In-Situ Adaptive Tabulation (ISAT) method (Pope, 1997) is used to reduce chemical reaction calculation time

- CFL number: 0.2

6.3.5 Results and Discussion

Numerical simulations were performed for initial hydrogen pressure 1.35, 1.5, 1.65, 2.43 and 2.9 MPa. For the cases with 1.35 and 1.5 MPa initial pressure no auto-ignition was observed and hydrogen-air mixture temperature remained well below the combustion temperature (Figure 6.3-3, top). The absence of ignition is further confirmed by the absence of noticeable quantities of reaction products, such as hydroxyl OH (Figure 6.3-3, bottom).

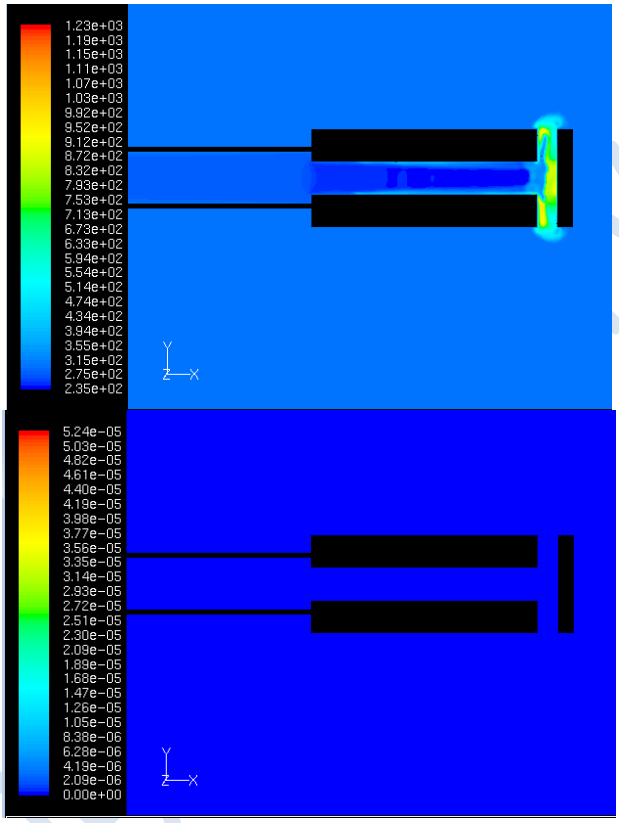

Figure 6.3-3. Temperature (top) and OH concentration (bottom) contours at the axis of the T-shaped PRD at t=7.46e-5 s for the case with 1.5 MPa initial pressure.

There is an ignition followed by a self-extinction of reaction at storage pressures 1.65 and 2.43 MPa. The minimum pressure at which the ignition has been observed numerically is 1.65 MPa. However, the initial spot of combustion is quickly self-extinguished. The simulation indicated a tentative ignition in a significantly smaller region (detailed simulations reported in Bragin et al., 2013 indicate that it is self-extinguished within approximately 1e-5 s). More details on the simulation results are provided in Bragin et al., (2013).

For the case with initial pressure 2.9 MPa, the ignition was observed at approximately 6.2e-5 second, after the secondary reflection of shock wave from the radial channels of T-shaped PRD. Observation of flow evolution in a simulation video indicated that ignition occurs at the location of the leading shock wave secondary reflection. The first reflection occurs when the shock traveling along the axis of the channel reaches the closed off end of the PRD. At this time the ignition is not possible as the area still lacks hydrogen. Once the hydrogen flows

around the edge from the axial into radial channels, it starts mixing with air heated by shocks, providing the necessary conditions for ignition of the mixture. It can be seen that for both initial pressures combustion is initiated in the radial channel in a location which is closer to the upstream wall. The fact of ignition and its location can be confirmed by sudden appearance of large quantities of hydroxyl OH at the same locations (Figure 6.3-4, bottom). These observations are in agreement with the experiment (Golub et al., 2010).

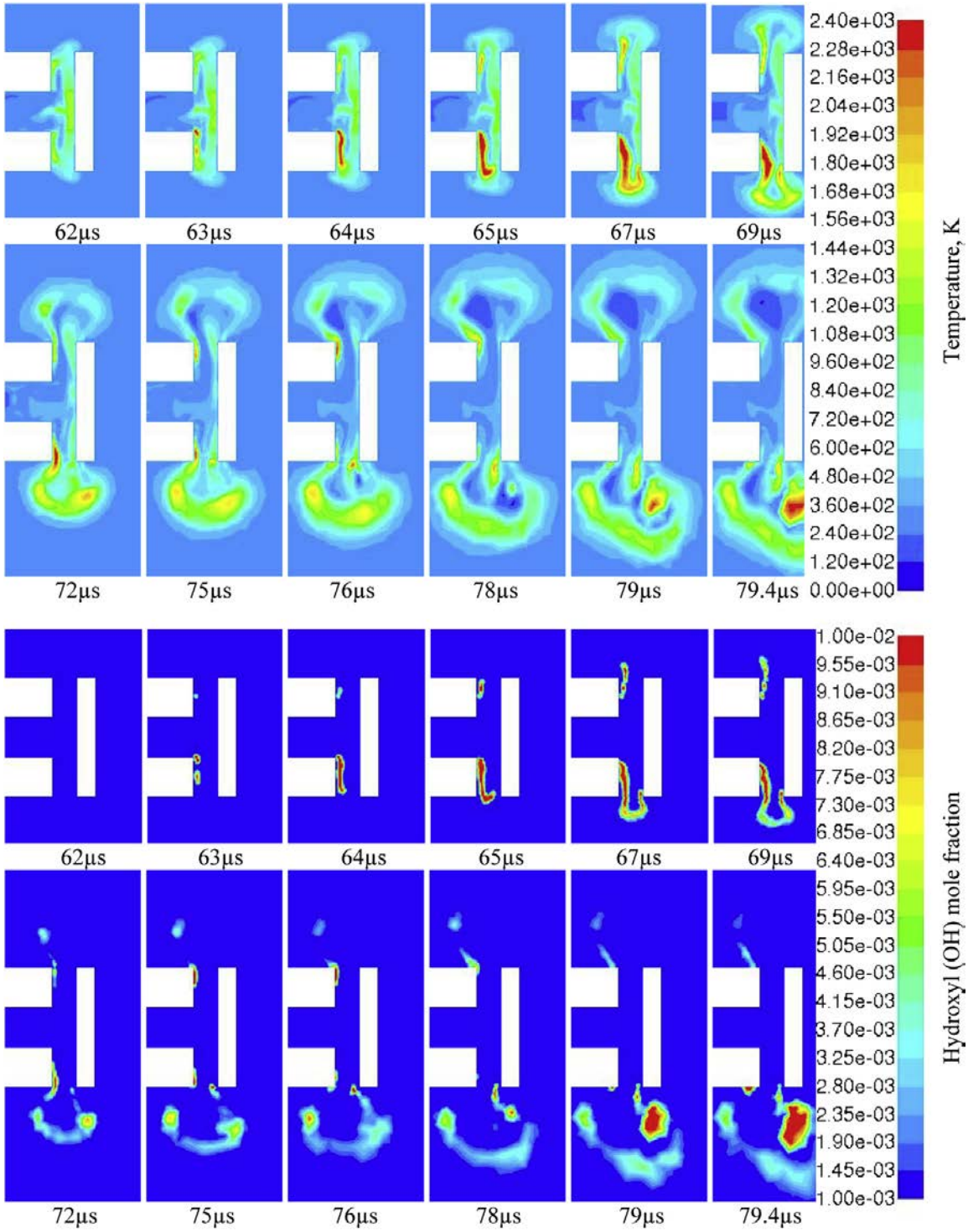

Figure 6.3-4. Temperature (top) and OH concentration (bottom) contours at the axis of the T-shaped PRD at t=6.65e-5 s for the case with 2.9 MPa initial pressure.

In the case of initial storage pressure 1.65 MPa an ignition spot is not located in the symmetry plane. Temperature and hydroxyl mole fraction dynamics are shown in Figure 6.3-5 in 3D. The combustion is located within the axial channel and propagated upstream of the flow rather than with the main flow. When oxygen in the boundary layer is consumed the chemical reaction is self-extinguished. These simulations explain why "ignition" was not reported in the experimental paper for this pressure. Indeed, the light sensor can register only the ignition in the radial channel and cannot see the process within the axial channel unless special arrangements are done, e.g. the axial channel has transparent walls. This is the one of advantages of use 3D modelling when phenomena can be spotted in the place which does not exist in 2D or 1D modelling approaches.

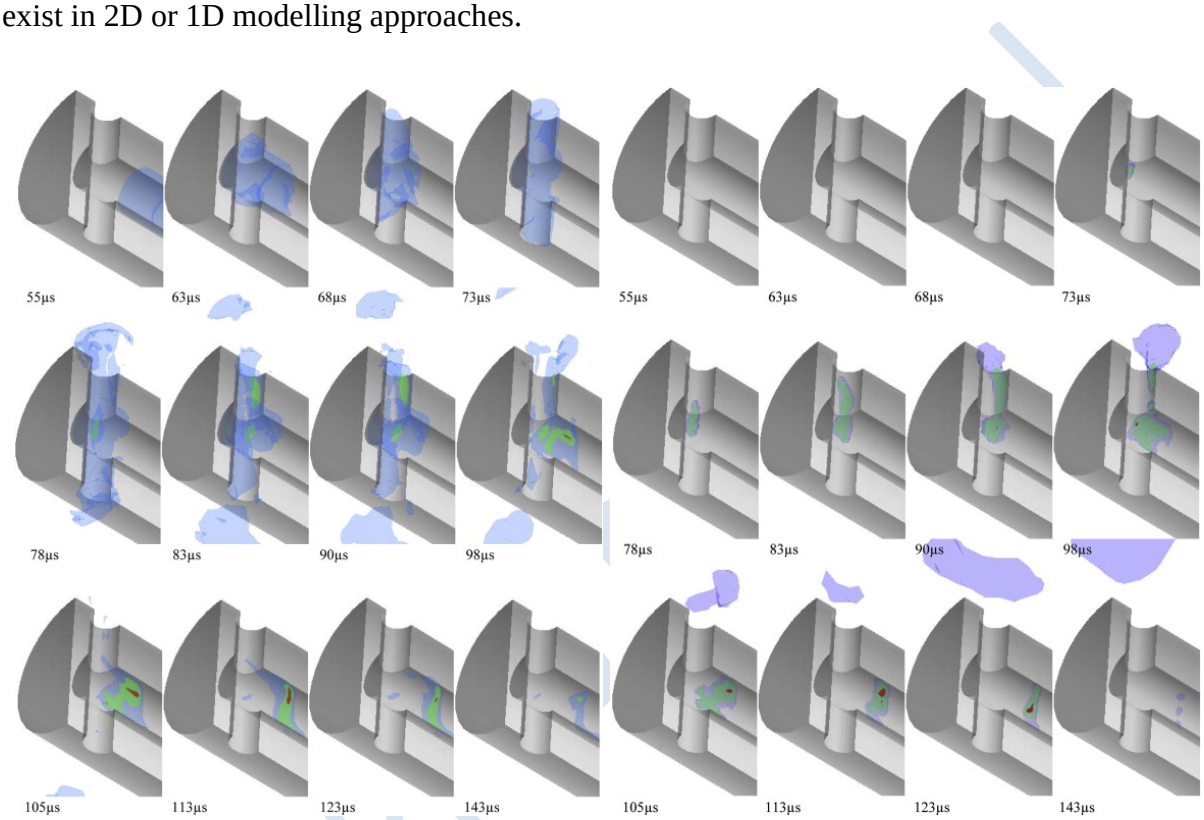

Figure 6.3-5. Temperature iso-surfaces during ignition for the initial hydrogen storage pressure 1.65 MPa. Blue – 550 K, Green – 1500 K, and Red – 2400 K (left). Hydroxyl mole fraction iso-surfaces during ignition for the initial hydrogen storage pressure 1.65 MPa. Blue – 0.0002, Green – 0.002, and Red – 0.02 (right).

6.3.6 Conclusions

The LES model based on the eddy dissipation concept with detailed Arrhenius kinetics for modelling of SGS combustion, and renormalization group theory for modelling of SGS turbulence was applied to modelling of the hydrogen spontaneous ignition during release into the T-shaped channel. Gradual rupture of the flat burst disk was implemented to simulate realistic process of PRD burst which affects the mixing process between heated by shock air and expanding hydrogen.

Numerical simulations predicted hydrogen autoignition at the release pressure of 2.9 MPa, while no ignition was observed for the release at 1.35 and 1.5 MPa, which matches the results of experiments. An ignition followed by a self-extinction of reaction at 1.65 and 2.43 MPa was observed.

6.4 Sample Case 4 - Deflagration

6.4.1 Introduction

This Section seeks to illustrate the role of Best Practice Guidelines (BPGs) in helping to ensure the quality and reliability of Computational Fluid Dynamics (CFD) modelling of hydrogen deflagrations. In particular, this Section considers the potential usefulness of the SUSANA BPGs using, as a case study, vented hydrogen deflagration modelling carried out by HSL for a 'Round Robin' benchmark activity performed for the EC H2FC project (note that the modelling had been carried out prior to the SUSANA BPGs being finalised).

6.4.2 FM Global Experiment

The H_2FC Round Robin activity involved carrying out simulations of a vented hydrogen deflagration experiment performed by FM Global (Bauwens et al., 2011). The experiment was carried out using a 64 m^3 enclosure with a floor area of 4.6 m x 4.6 m and a height of 3.0 m, as shown in Figure 6.4-1. The enclosure has a 5.4 m^2 square vent located in the centre of one of the walls, flush with a concrete slab outside the enclosure. Outside the vent is a porch-like structure consisting of the concrete slab with five vertical pillars along either side connected by a series of horizontal 'roof' beams. The vertical pillars are located at distances of 0 m, 0.8 m, 2.1 m, 3.4 m and 4.7 m from the vent.

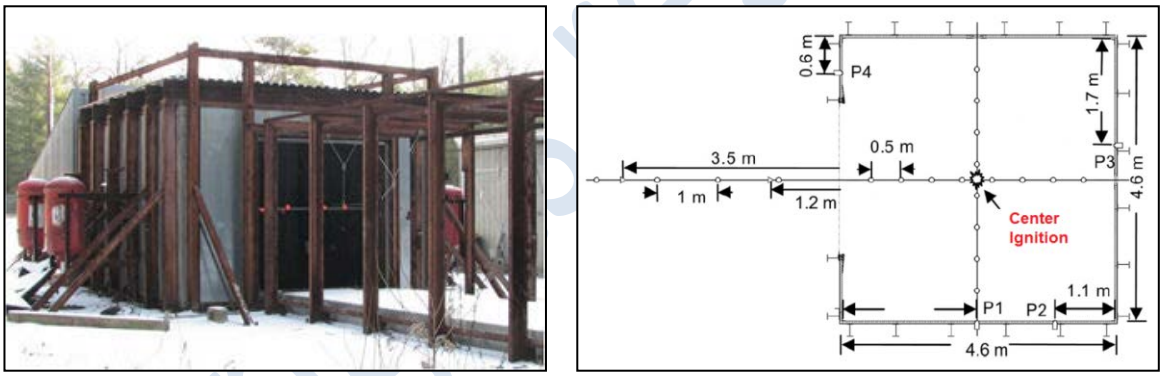

Figure 6.4-1. Photo (left) of the experimental set-up and plan view (right) of the enclosure with pressure transducers (marked P1 to P4) and flame time-of-arrival thermocouples (circles).

The experiment involved filling the enclosure with a homogeneous hydrogen-air mixture with a hydrogen concentration of 18% by volume. The mixture was ignited at the centre of the enclosure and the characteristics of the resulting deflagration were measured using four pressure transducers (P1, P2, P3 and P4) installed inside the enclosure (as shown in Figure 6.4-1) and twenty flame time-of-arrival thermocouples. The thermocouples were located 1.4 m above the enclosure floor at 0.5 m intervals inside the enclosure and 1 m intervals outside the enclosure. An initial velocity fluctuation of 0.1 m s^{-1} was measured inside the enclosure immediately prior to ignition.

6.4.3 H_2FC Modelling

HSL participated in the H_2FC Round Robin benchmark by carrying out simulations using ANSYS CFX v16.0 (ANSYS, 2015) and GexCon FLACS v10.2 (GexCon, 2015).

ANSYS CFX, henceforth referred to as CFX, is a general purpose CFD code that is capable of modelling a wide range of fluid flows. Several authors have already demonstrated its ability to simulate hydrogen deflagrations including Bender and Menter (2002), Hoyes et al. (2013), Sathiah et al. *(*2014) and Wen et al. (2010).

Figure 6.4-2 shows the geometry used for the CFX simulations. It consists of an enclosure with a vent and a porch. The dimensions of the enclosure, vent and porch were chosen to match the experimental set-up.

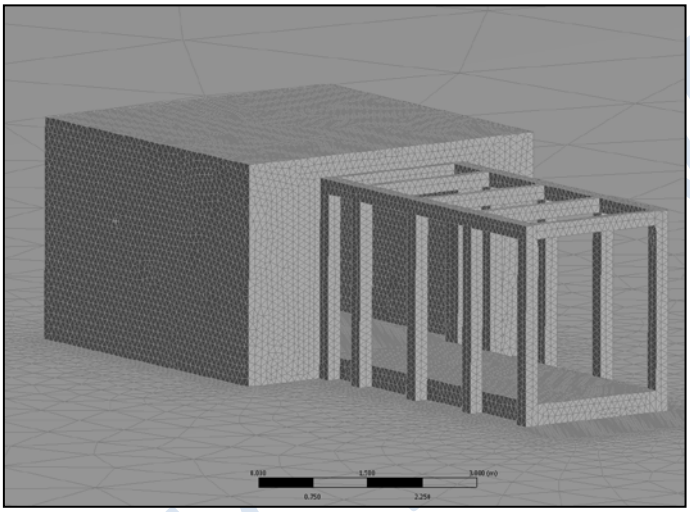

Figure 6.4-2. Model geometry used for the ANSYS CFX simulations.

The CFX simulations were carried out using tetrahedral meshes with mesh refinement near the ignition location, inside the enclosure and inside the porch. Turbulence was modelled using the k-ε turbulence model with buoyancy production and dissipation, heat transfer was modelled using the total energy model and combustion was modelled using the Burning Velocity Model (BVM) with the Zimont turbulent flame speed correlation and laminar flamelets (ANSYS, 2015).

GexCon FLACS, henceforth referred to as FLACS, is also capable of simulating a wide range of fluid flows. However, in contrast to CFX, FLACS has a relatively limited range of sub-models and meshing options. Moreover, FLACS has a number of explosion-specific user guidelines such as guidelines for the mesh resolution in regions where combustion is expected to occur.

Figure 6.4-3 shows the geometry used for the FLACS simulations. The dimensions of the enclosure, vent and porch were (as for the CFX geometry) chosen to match the experimental set-up. Simulations were carried out using single-block Cartesian meshes (FLACS does not support unstructured meshes) with mesh refinement in the enclosure and porch.

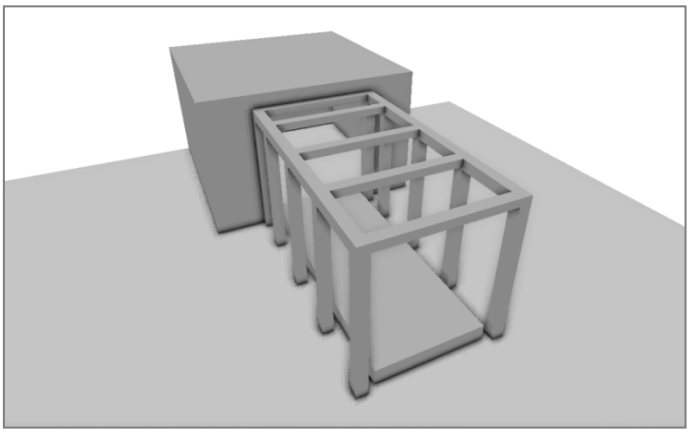

Figure 6.4-3. Model geometry used for the GexCon FLACS simulations.

The FLACS simulations were carried out using the k-ε turbulence model, while combustion was modelled using the FLACS "beta-flame" model (GexCon, 2015).

6.4.4 The Role of BPGs

This Section seeks to highlight the potential value in following the SUSANA BPGs using examples from HSL's vented hydrogen deflagration modelling. The examples cover the choice of computational domain size, mesh resolution and initial turbulence conditions. Note that the SUSANA BPGs include advice on a much wider range of issues, including the design of the computational geometry, choice of turbulence and combustion models, and the selection of appropriate numerical solution procedures. Moreover, HSL's modelling for H_2FC covered a wider range of sensitivity analyses than described here.

6.4.4.1 Computational Domain Size

The computational domain consists of the volume or volumes that are included in the computational model. In the case of the vented hydrogen deflagration simulations the computational domain consists of the volume inside the enclosure and an external volume.

The purpose of the external volume is to enable the prediction of flame propagation and over-pressures outside the enclosure. The actual external volume is bounded by the ground but is otherwise unbounded (i.e. the experiment is open to the atmosphere). The ground was included in both the CFX and the FLACS models while the unbounded external region was constrained using 'external' computational domain boundaries.

It is important that these external boundaries are placed sufficiently far from the region of interest (i.e. well away from the enclosure) so as not to influence the computational predictions. In the SUSANA BPGs it is noted that the computational domain should be much larger than the flammable volume. Moreover, it is suggested that tests should be performed to assess the sensitivity of the model predictions to the size of the computational domain (unless evidence for a suitable domain size already exists in the literature).

FLACS Domain Size Sensitivity

The use of single-block Cartesian meshing in FLACS restricts the extent to which the mesh resolution can be reduced with increasing distance from the enclosure. Consequently, large computational domains can lead to a large number of mesh cells that can make the simulations computationally expensive.

Simulations were carried out to assess the sensitivity of the peak over-pressure to the computational domain size. The objective was to determine the computational domain size required to provide computational domain size independent results. Simulations were also carried out to assess the sensitivity of the predictions to the condition applied on the external boundaries (Euler versus Plane Wave, GexCon, 2015).

Figure 6.4-4 shows peak over-pressure predictions for a range of computational domain sizes and external boundary conditions. The peak over-pressure increases with increasing domain size for domain sizes less than 10.5 m, while for domain sizes larger than 10.5 m the peak over-pressure is insensitive to the domain size. The peak over-pressure is sensitive to the choice of external boundary condition, with the Plane Wave condition giving the highest predictions.

The results shown in Figure 6.4-4 are from simulations that were carried out to assess the sensitivity of the peak over-pressure to the computational domain size in the z direction, as the vertical extent of the domain was considered an important factor. Similar analyses were carried out for the x and y directions. Following the sensitivity analyses, all subsequent simulations were carried out using a domain size of 20 m x 14.4 m x 12 m, as this was found to provide domain size independent results. The Euler boundary condition was used as this is recommended in the FLACS user guidelines.

CFX Domain Size Sensitivity

The use of tetrahedral meshing in CFX means the mesh resolution can be continually reduced with increasing distance from the enclosure. Consequently, large computational domains can be used with relatively modest increases in the number of mesh cells.

The different meshing strategy in CFX motivated a different approach to specifying the computational domain size. Rather than carry out a detailed computational domain size sensitivity study, the CFX simulations were carried out using a very large computational domain size of 100 m x 100 m x 100 m, together with a less-rigorous computational domain size sensitivity study.

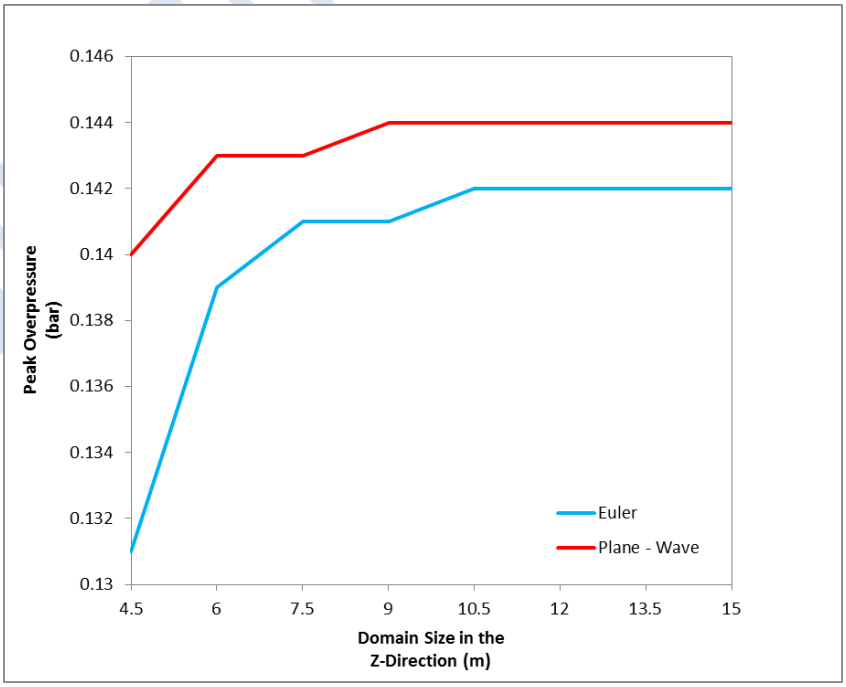

Figure 6.4-4. Sensitivity of FLACS peak over-pressure predictions to the computational domain size and external boundary condition.

The CFX computational domain size sensitivity study indicated that a domain size of 100 m x 100 m x 100 m would be more than sufficient to provide domain size independent results. This finding is supported by the FLACS results, which indicate that a domain size of 20 m x 14.4 m x 12 m is sufficient to provide domain size independence results (although it is recognised that different codes may require different domain sizes to achieve domain size independent results). Subsequent CFX simulations were carried out using a domain size of 100 m x 100 m x 100 m.

6.4.4.2 Computational Mesh Resolution

The computational mesh is the collection of computational cells in which the conservation equations that form the basis of CFD are solved. Various mesh types are possible including unstructured tetrahedral meshes (as used in the CFX simulations) and structured Cartesian meshes (as used in the FLACS simulations). The SUSANA BPGs advise that there is no preferred mesh type for modelling hydrogen deflagrations.

Whilst there is no preferred mesh type, the mesh resolution is widely acknowledged as being important. The SUSANA BPGs note that mesh resolution can have a significant influence on the magnitude of numerical errors. Using more mesh cells can provide greater accuracy but tends to make simulations more computationally expensive. Typically, the mesh resolution is varied throughout the computational domain with higher mesh resolution being used in areas of interest (e.g. inside the enclosure) and lower mesh resolution being used elsewhere (e.g. away from the enclosure).

BPGs typically advise modellers to assess the sensitivity of their predictions to the mesh resolution. For example, the Nuclear Energy Agency (NEA) BPGs recommend a mesh sensitivity analysis be carried out using at least two meshes with significantly different resolutions (NEA, 2015). The SUSANA BPGs state that the sensitivity of model results to the mesh resolution should be examined.

FLACS Mesh Sensitivity

Recognising the potential importance of mesh resolution, HSL carried out a mesh sensitivity study using meshes with cell sizes in the enclosure of 30 cm, 20 cm, 10 cm, 5 cm and 2.5 cm. A 30 cm mesh resolution results in the gas cloud being resolved by 10 cells across its smallest dimension; this is the minimum resolution recommended by GexCon. A 20 cm mesh resolution follows guidelines stating that a finer mesh should be used if a highly reactive fuel is being modelled. The 10 cm mesh resolution enables the walls of the enclosure to be resolved exactly without the cells in and around the enclosure walls being assigned a porosity (note that in the 30 cm and 20 cm simulations the cells in and around the enclosure walls are assigned a porosity but a no-flow condition is enforced on the boundaries between cells adjacent to the enclosure walls such that they remain non-porous). A 5 cm mesh resolution enables all aspects of the simulated geometry to be resolved exactly, while a 2.5 cm mesh resolution is the finest resolution suggested by GexCon for use in explosion modelling.

Figure 6.4-5 compares peak over-pressure predictions with the peak over-pressure measured during the FM Global experiment. From Figure 6.4-5 it can be seen that FLACS v10.2 over-predicts the peak over-pressure for all the mesh resolutions investigated. Furthermore, it can be seen that each of the mesh refinements: from 30 cm to 20 cm, 20 cm to 10 cm and 10 cm to 5 cm, give improvements in the peak over-pressure prediction. However, the final

refinement from a 5 cm to 2.5 cm resolution gives a peak over-pressure prediction which lies slightly further from the experimental value for the finer of the two meshes. Because strictly mesh independent results were not achieved and because of limited computational resources, the grid which provided the closest results to the experimental was chosen.

In addition to assessing the sensitivity of the peak over-pressure predictions to the mesh resolution, HSL also assessed the sensitivity of the flame speed predictions to the mesh resolution. HSL found that a mesh resolution of 5 cm was sufficient to provide reasonably mesh independent results (for both the peak over-pressure and the flame speed) and therefore chose to use this resolution for all subsequent simulations.

CFX Mesh Sensitivity

A similar approach was followed in CFX whereby a mesh sensitivity study was carried out using meshes with cell sizes in the enclosure of approximately 15 cm (coarse), 12.5 cm (medium), 10 cm (fine), 7.5 cm (very fine)and 5 cm (ultra fine). Figure 6.4-6 compares over-pressure predictions with the peak over-pressure measured during the FM Global experiment. The simulation on the coarse mesh gave a peak over-pressure of about 5 kPa, while the simulations on the medium, fine and very fine meshes gave values between 6.3 kPa and 6.7 kPa, and the simulation on the ultra-fine mesh gave a prediction of 7.7 kPa.

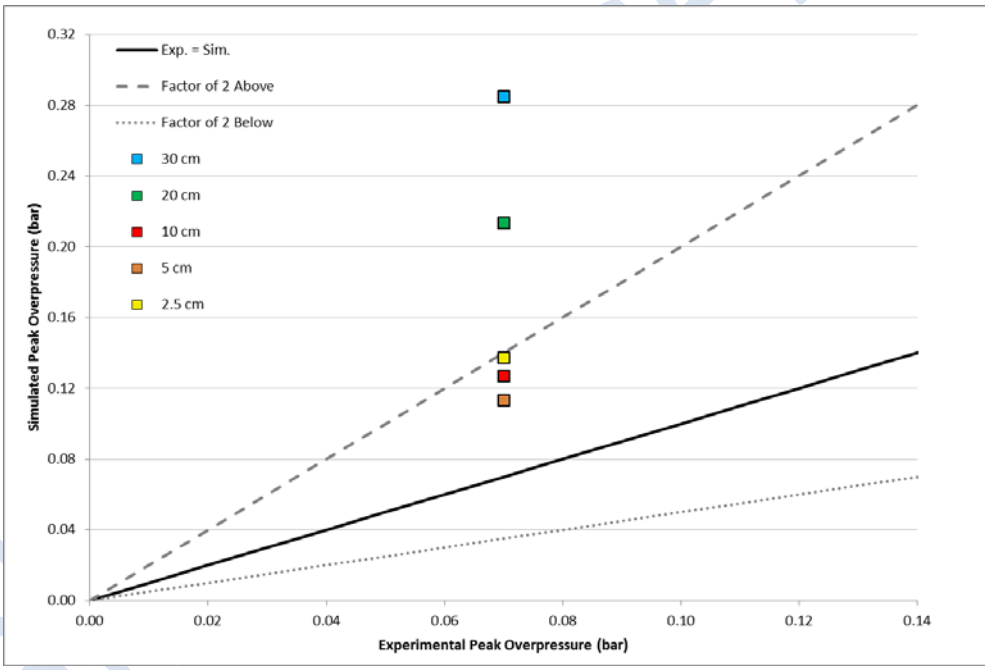

Figure 6.4-5. Comparison of predicted and measured peak over-pressures for a range of mesh sizes for the FLACS v10.2.

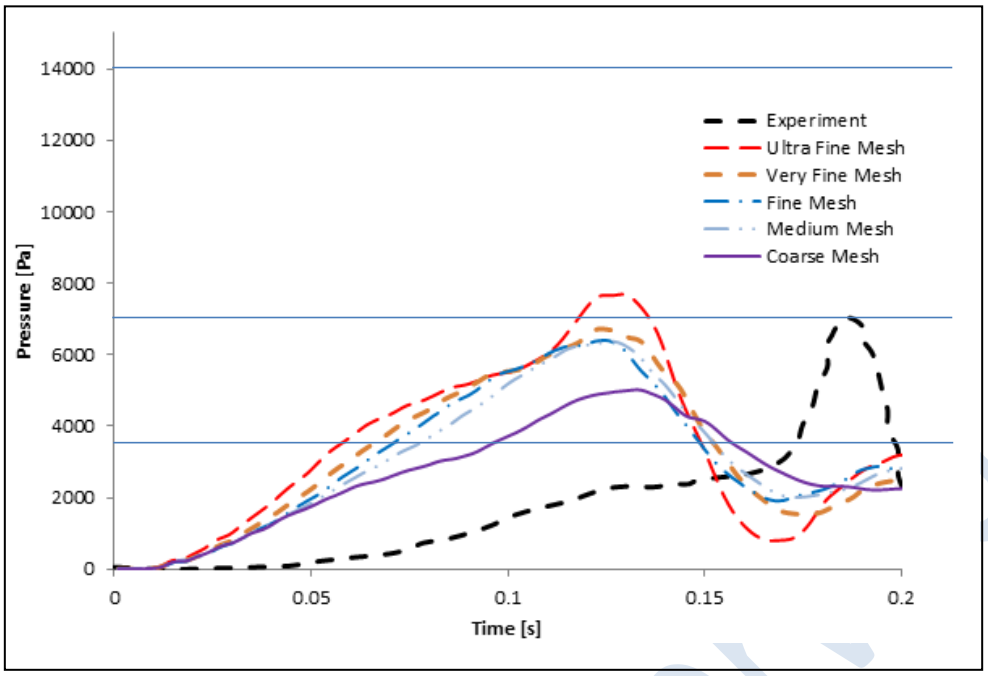

Figure 6.4-6. Over-pressure predictions from simulations carried out using CFX and peak over-pressure measured during the FM Global test.

The CFX mesh sensitivity study also examined flame speed predictions. Figure 6.4-7 compares flame speed predictions with the measurements from the FM Global test. Overall, the flame speed predictions show a lower level of mesh dependence than the over-pressure predictions. Whilst the simulation on the coarse mesh gave a maximum flame speed of 72 m s^{-1}, all four simulations on the finer resolution meshes gave a maximum flame speed of about 86 m s^{-1}.

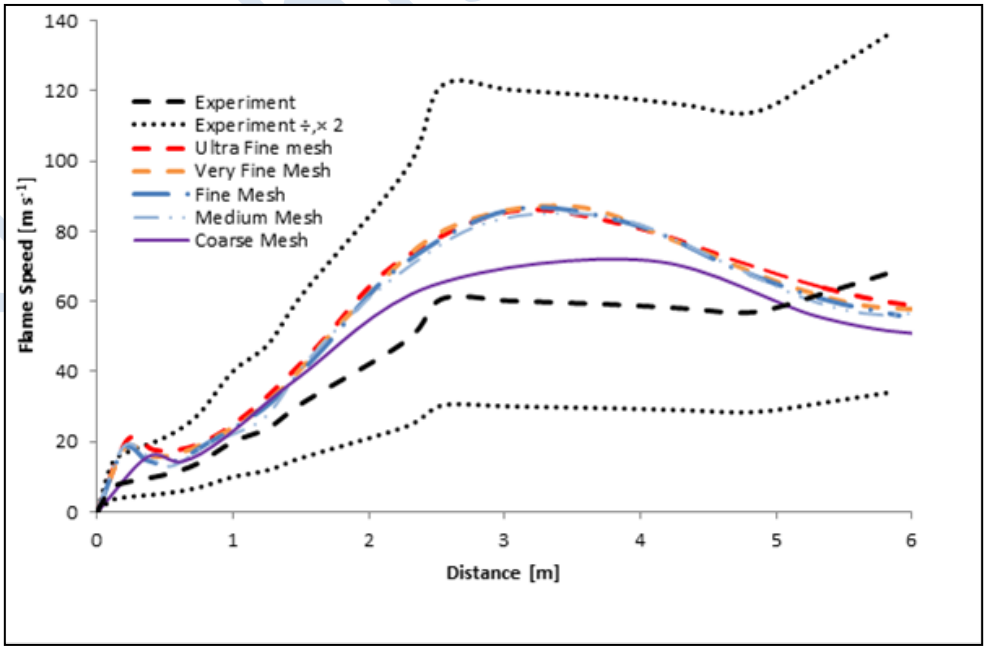

Figure 6.4-7. Flame speed predictions from simulations carried out using CFX and flame speed measurements from the FM Global test.

Comparison of the simulation results with the experimental measurements indicates that the predictions are converging (as the mesh resolution is increased) to a maximum flame speed and peak over-pressure that are slightly larger than the experimental values. HSL chose to carry out their final simulations using the ultra-fine resolution mesh.

6.4.4.3 Initial Turbulence Conditions

CFD simulations require a full-set of initial conditions including initial velocities, gas concentrations and turbulence conditions. Where simulations are carried out using Reynolds Averaged Navier Stokes (RANS) turbulence models, as is the case here, the initial turbulence conditions are typically specified in terms of an initial turbulence kinetic energy or initial turbulence velocity fluctuation, and an initial turbulence eddy dissipation or initial turbulence length scale.

It is widely recognised that initial turbulence conditions can have a significant effect on the behaviour of hydrogen deflagrations (e.g. Hooker et al., 2015). If the initial turbulence kinetic energy is under-prescribed the explosion generated over-pressures can be under-predicted. The SUSANA BPGs recommend specifying the initial turbulence conditions according to experimentally measured values where available and, where there is uncertainty, the BPGs recommend undertaking a sensitivity study.

FLACS Sensitivity to Initial Turbulence Conditions

In FLACS, the initial turbulence conditions are specified in terms of an initial velocity fluctuation and an initial turbulence length scale. GexCon recommend setting the initial turbulence fluctuation equal to an experimentally measured value and they recommend setting the initial turbulence length scale equal to 10% to 20% of the smallest mesh cell size.

HSL followed GexCon's recommendation for the initial turbulence fluctuation and used a value of 0.1 m s^{-1}, as measured in the FM Global test. For the initial turbulence length scale, HSL carried out simulations to assess its effect on the peak over-pressure prediction. HSL considered initial turbulence length scales between 0.05 cm and 1 cm, recognising that values less than 0.5 cm are outside of the range of values recommended by GexCon (10% to 20% of the smallest mesh cell size, for a smallest mesh cell size of 5 cm, corresponds to an initial turbulence length scale between 0.5 cm and 1 cm).

Results from the initial turbulence length scale sensitivity study are shown in Table 6.4-1. The results show that the predicted peak over-pressure increases from around 6 kPa to 16 kPa as the initial turbulence length scale is increased from 0.05 cm up to 1 cm. HSL carried out their final simulations using an initial length scale of 0.5 cm, which was found to provide the best agreement with the measurements, whilst still satisfying GexCon's recommendation.

Table 6.4-1. Peak over-pressure predictions from FLACS simulations with an initial turbulence fluctuation of 0.1 m s^{-1} and different initial turbulence length scales (*note that length scales of 0.05 cm and 0.25 cm are outside of the range recommended by GexCon).

Initial turbulence length scale (cm)	Peak over-pressure prediction (kPa)
0.05*	6.2
0.25*	9.0
0.5	11.3
0.75	13.1
1.0	16.0

CFX Sensitivity to Initial Turbulence Conditions

Advice was sought from ANSYS regarding the choice of initial turbulence conditions. ANSYS recommended using an artificially high initial turbulence kinetic energy of 1 m^2 s^{-2} (corresponding to an initial velocity fluctuation of 0.8 m s^{-1}) and an initial turbulence eddy dissipation of 10 m^2 s^{-3} (corresponding to an initial turbulence length scale of 1.6 cm). These values were used by Bender and Menter (2002) to model lean hydrogen deflagrations.

HSL also carried out simulations with an initial turbulence kinetic energy of 0.5 m^2 s^{-2} and initial turbulence eddy dissipations of 5 m^2 s^{-3} and 20 m^2 s^{-3}. Peak over-pressure predictions from HSL's simulations are shown in Table 6.4-2. The predictions vary between 1 kPa and 12 kPa, depending on the choice of initial turbulence conditions. HSL carried out their final simulations using an initial turbulence kinetic energy of 1 m^2 s^{-2} and an initial turbulence eddy dissipation of 10 m^2 s^{-3}, as recommended by ANSYS.

Table 6.4-2. Peak over-pressure predictions from CFX simulations with different initial turbulence conditions (*note that ANSYS recommended using an initial turbulence kinetic energy of 1 m^2 s^{-2} and an initial turbulence eddy dissipation of 10 m^2 s^{-3}).

Initial turbulence kinetic energy (m^2 s^{-2})	Initial turbulence eddy dissipation (m^2 s^{-3})	Peak over-pressure prediction (kPa)
0.5	20	1
1*	10*	2
1	10	7
1	5	12

6.4.5 Final Results

6.4.5.1FLACS

The final FLACS simulation was carried out using a domain size of 20 m x 14.4 m x 12 m, a mesh resolution in the enclosure of 5 cm, an initial turbulence fluctuation of 0.1 m s^{-1} and an initial turbulence length scale of 0.5 cm. Figure 6.4-8 compares flame speed and over-pressure predictions from the final simulation with the experimental measurements. Lines indicating a factor of 2 variation about the experimental data are also included.

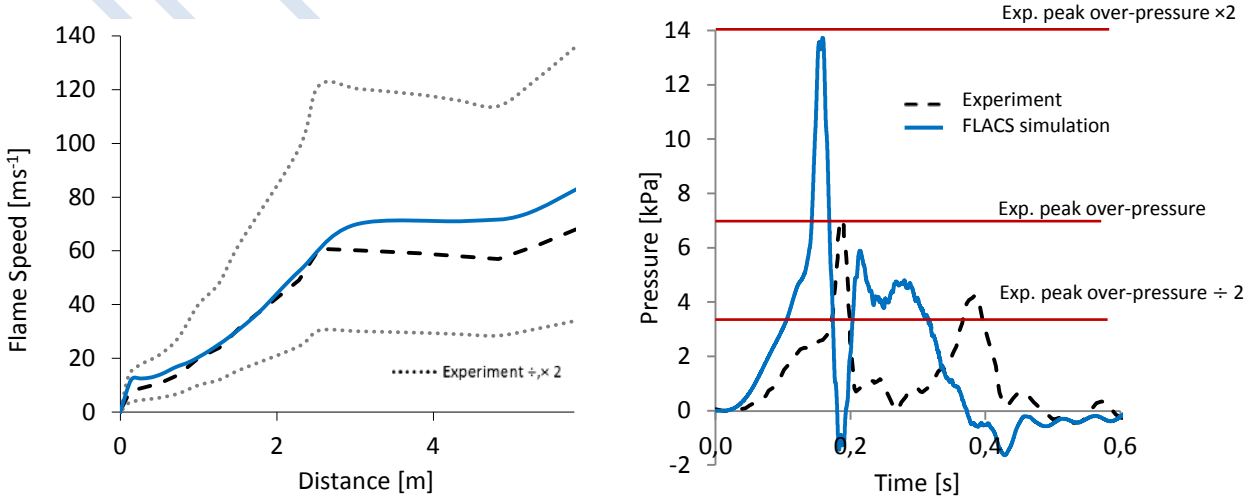

Figure 6.4-8. Flame speed (left) and over-pressure (right) predictions from the final FLACS simulation. Blue lines show the CFD predictions, dashes black lines show the experimental measurements and dotted black lines indicate a factor of 2 variation about the flame speed measurements.

The predicted flame speed shows excellent agreement with the experimental measurements. The initial acceleration phase is accurately predicted, while the flame speed plateaus at a value around 10% higher than the experimental value. The pressure predictions also follow a similar pattern to the experimental measurements, although the predicted peak over-pressure is nearly twice the measured value. The subsequent pressure-oscillations are not well predicted. A second pressure peak is present in both the simulation and the experiment, although the second peak occurs much earlier in the simulation.

6.4.5.2 CFX

The final CFX simulation was carried out using a domain size of 100 m x 100 m x 100 m, a mesh resolution in the enclosure of 5 cm, an initial turbulence kinetic energy 1 m^2 s^{-2} (corresponding to an initial velocity fluctuation of 0.8 m s^{-1}) and an initial turbulence eddy dissipation of 10 m^2 s^{-3} (corresponding to an initial turbulence length scale of 1.6 cm). Figure 6.4-9 shows both the flame speed and over-pressure predictions. The experimental data are shown along with lines indicating a factor of two variation about the experimental data.

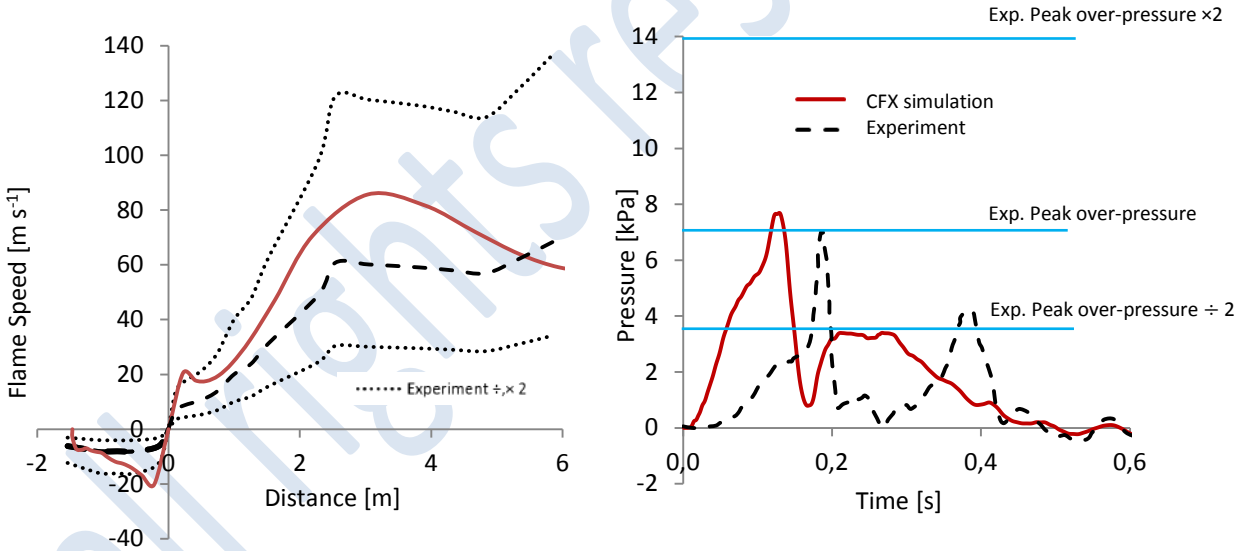

Figure 6.4-9. Flame speed (left) and over-pressure (right) predictions from the final CFX simulation. Red lines show the CFD predictions, dashes black lines show the experimental measurements and dotted black lines indicate a factor of two variation about the flame speed measurements.

Overall, the flame speed predictions are qualitatively similar to the experimental measurements. They show an initial acceleration phase over the first 2 m to 3 m followed by a relatively steady period between 3 m and 5 m. The flame speed is over-predicted during the acceleration phase and the maximum flame speed is about 40% higher than the experimental value (taken to be the value at the end of the acceleration phase).

The peak over-pressure is in good agreement with the experimental value, although there are some differences in the transient behaviour. The experimental measurements exhibit two

strong pressure peaks at 0.2 s and 0.4 s of 7 kPa and 4 kPa, separated by a trough to 0 kPa at around 0.27 s. The simulation is also characterised by a large peak followed by a trough and a weaker secondary peak. The height of the main pressure peak is about 7.7 kPa (10% higher than the experimental value) whilst the trough drops to about 0.8 kPa rather than 0 kPa and the height of the second over-pressure peak is 3.4 kPa in comparison to the experimental value of 4 kPa.

6.4.6 Discussion

Examples from HSL's vented hydrogen deflagration modelling, which was carried out for the H_2FC Round Robin benchmark activity, have been presented to illustrate the potential usefulness of the SUSANA BPGs. Three issues addressed by the BPGs have been considered, namely the choice of computational domain size, mesh resolution and initial turbulence conditions.

For each of the issues considered, HSL carried out sensitivity analyses, which is consistent with advice in the SUSANA BPGs. FLACS predictions were seen to be sensitive to the choice of domain size while both the FLACS and CFX predictions were sensitive to the mesh resolution and initial turbulence conditions. The fact that these sensitivities exist highlights the value in following BPGs and carrying out sensitivity analyses. By carrying out sensitivity analyses it is possible to build confidence and trust in CFD predictions.

For both FLACS and CFX, it was possible to use a sufficiently large computational domain to obtain computational size independent results. Similarly, it was possible to use a sufficiently high mesh resolution to obtain reasonably mesh independent results. Although full mesh independence was not achieved for both the over-pressure and the flame speed predictions, the level of mesh sensitivity at the higher resolution meshes was relatively small.

While it was possible to achieve computational domain size independent results and a reasonable level of mesh independence, it was not possible to obtain results that were independent of the initial turbulence conditions. The initial turbulence conditions were seen to have a significant effect on both the FLACS and CFX predictions. There was a significant level of uncertainty, even though experimental data on the initial turbulence velocity fluctuation were available. For example, FLACS simulations with an initial turbulence velocity fluctuation equal to the measured value and an initial turbulence length scale within the range suggested by GexCon (10% to 20% of the smallest mesh cell size) gave peak over-pressures that varied between 11.3 kPa and 16.0 kPa. A greater level of uncertainty can be expected in situations where no experimental data are available.

The approach taken in CFX, whereby the initial turbulence kinetic energy and turbulence eddy dissipation are set to artificially high values (as used by Bender and Menter, 2002) is also subject to some uncertainty. In particular, it is unclear how applicable this approach is to other hydrogen deflagration scenarios that could involve different geometries or different initial turbulence conditions.

HSL's final set of simulations were carried out with initial turbulence conditions specified according to advice from the code vendors (GexCon and ANSYS). Both the FLACS and CFX final simulations gave predictions that were in reasonable or good agreement with the FM Global measurements. However, more work is required to confirm the wider applicability of these modelling approaches.

6.5 Sample Case 5 - Detonation

In simulation of detonation, selecting proper numerical models, setting the computational domain and the analysis of the uncertainty are all very important. In this section the simulations of the industrial scaling detonation problems and numerical reproduction of detonation cells are shown as examples for “best practice”.

6.5.1 Industrial scaling detonation simulations

In the project SUSANA, KI-RUT-HYD05 and KI-RUT-HYD09 are selected as the benchmarking in detonation simulation.

6.5.1.1 Experiment facility

The two experiments were conducted in the 60m long RUT facility. In the two experiments, different premixed hydrogen-air mixtures and ignition points were selected. Basic geometry of the RUT facility is given in Figure 6.5-1.

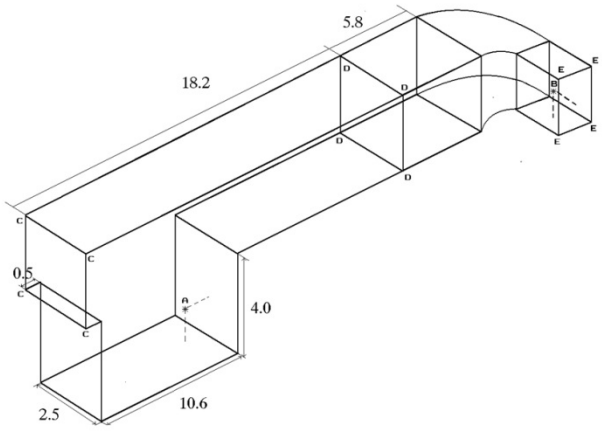

Figure 6.5-1. Geometry of RUT facility.

The size of the RUT facility is in similar to common industrial facilities, so numerical reproduction of detonation waves inside such facility may have very good practical meaning. In the two experiments, both hydrogen concentrations and ignition positions are different. The two ignition points are indicated as A and B in the Figure 6.5-1. The ignition point A is located at the corner of the canyon and the ignition point B at the end of the curved channel. Both ignition points are located 80 cm from the floor and 50 cm from the wall. High explosive charges (TNT) are located in the two ignition points to initiate the detonation wave directly. Details of experiments such as the hydrogen concentrations and the ignition points are given in Table 6.5-1.

Table 6.5-1. Experimental details.

File name	Volume of gas (m^3)	H_2 concentration (%vol)	Ignition point	Mass of the explosive charge (g)
KI-RUT-HYD05	263	20.0	A	200

KI-RUT-HYD09	263	25.5	B	200

The mixture temperature and pressure were 20°C and 1 atm in both experiments. Mixing was assured by fans. Hydrogen concentration and mixture uniformity were checked by taking samples from two points of the experimental volume. It was found that the difference in hydrogen concentration was less than 0.5% vol.

To collect experiment data in the experiments, several pressure transducers are installed in the RUT facility. In Figure 6.5-2, locations of the 11 transducers are given.

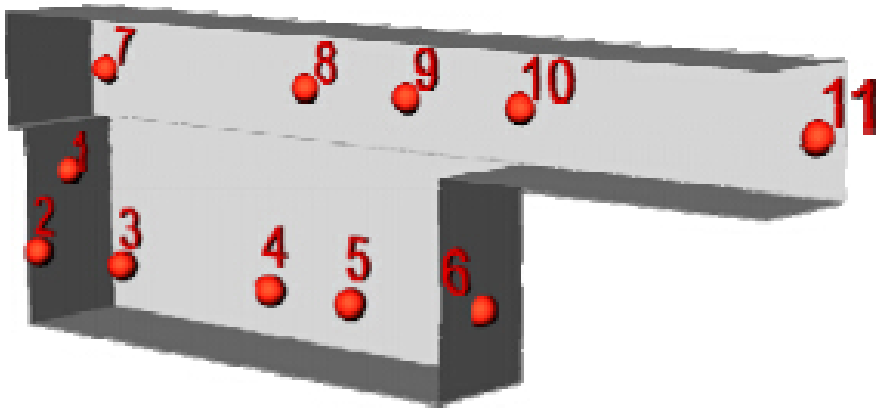

Figure 6.5-2. Transducers in RUT facility.

6.5.1.2 Selection of models and domain setting

As mentioned in Section 4.2.1, the diffusion effects and heat transfer can be ignored in detonation simulations. As a result in the most case, the Euler equations are used to simulate the gas dynamics in detonation wave. In the two industrial scaling detonation problems, the Euler equations are used as well.

In detonation simulation, selection of chemical model and decision of resolution in the computational domain are mutually dependent, and should be considered together. The size of the experimental facility is of the same magnitude as the common industrial facility. To control the total computational efforts a considerably coarse (compared with the thickness of the induction zone and reaction zone of the detonation wave) mesh size should be used. Therefore, as mentioned in detonation section, in order to represent the correct physical phenomena of detonation wave in such coarse resolution the Heaviside detonation model should be used.

As the discussion in the previous paragraph a considerably coarse resolution should be used in the computational domain to control the computational efforts, but to achieve a better performance the mesh of size 0.05 m is used to construct the computational domain. Under the 0.05 m resolution, the domain has the size of 555 x 110 x 126 cells and the total cell number is 7.7 million. In the construction of computational domain, representation of the details of the geometry is another important point that needs to be take care. To produce a numerical simulation being compatible to the reality, it is better to include all the details in the real facility in the computational domain. Figure 6.5-3 and Figure 6.5-4 show the details in canyon and channel of the RUT facility in computational domain with resolution of 0.05 m.

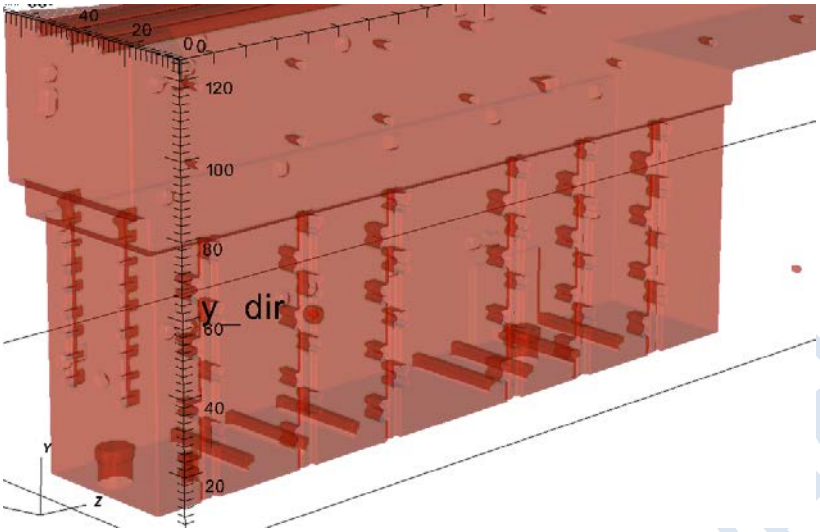

Figure 6.5-3. Details in canyon of RUT facility.

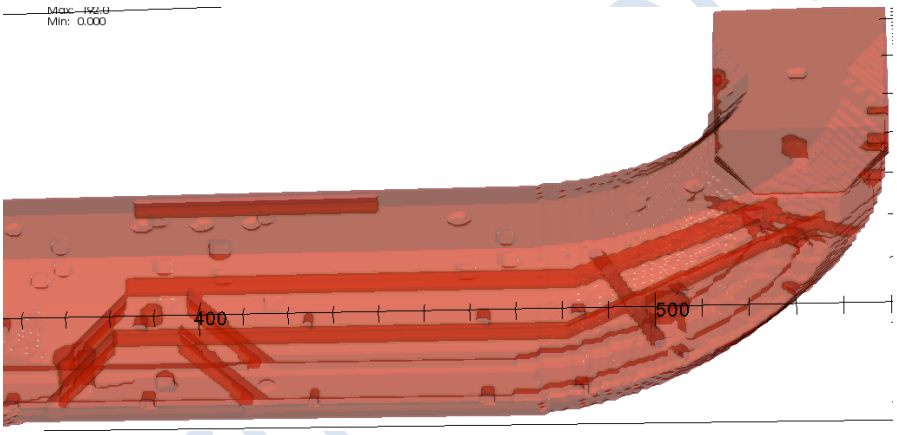

Figure 6.5-4. Details in channel of RUT facility.

From the description of the experiments it is clear that the boundary of the computational domain should be closed, and as the friction and heat transfer are ignored in the simulation of detonation the closed walls can be set as mirror boundary condition (the slipping boundary condition).

6.5.1.3 Setting of initial conditions

As the experiment facility is filled with homogeneous gas, the setting of initial condition should be focused on the ignition of the burnable gas mixture. Description of the experiment procedure shows that the detonation waves are initiated directly by the TNT, so setting a spherical region with high temperature and pressure to present the high energy brought by the explosion of TNT is necessary.

By consulting the energy release by TNT which is about 4.2 kJ per gram, a 0.18m sphere structure region with 100 bar pressure and 3000 K temperature should be given to reach such amount of energy. However, in case of the numerical diffusion brought by the coarse grids and the numerical scheme, larger initiator should be given in the simulation to avoid the decay of detonation wave. By several numerical testing, the sphere structure with the radius of 0.2 m or bigger can initiate the detonation wave successfully. In order to be closed to the reality, the

radius 0.2 m is used in the final simulations. Figure 6.5-5 shows the initiator of detonation in simulation of experiment KI-RUT-HYD05 and Figure 6.5-6 shows the initiator of detonation in simulation of experiment KI-RUT-HYD09.

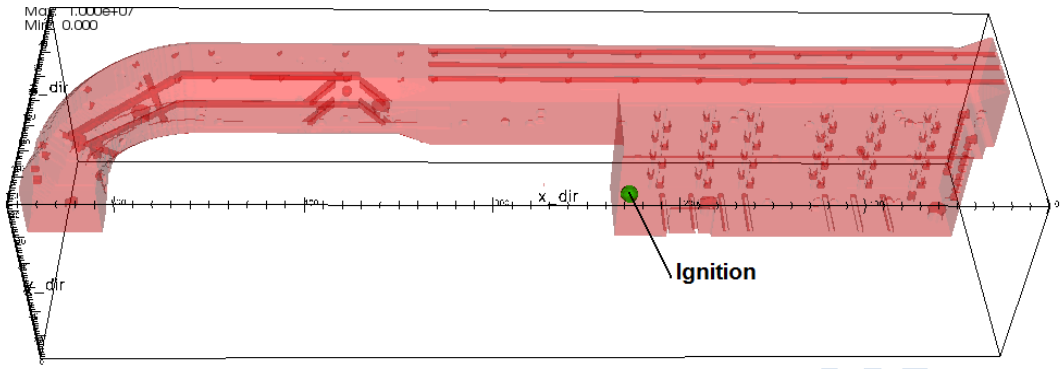

Figure 6.5-5. Initiator for numerical simulation of KI-RUT-HYD05.

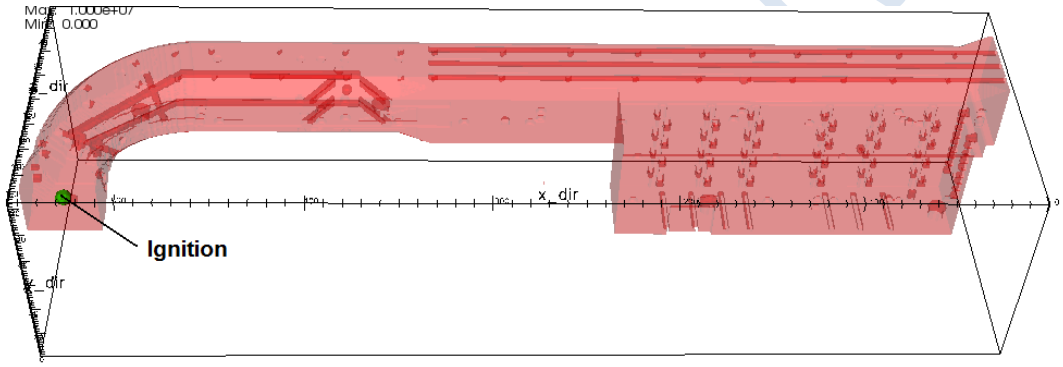

Figure 6.5-6. Initiator for numerical simulation of KI-RUT-HYD09.

6.5.1.4 Results

For KI-RUT-HYD05 experiment, code validation has been focused on the comparison of numerical simulation and experimental data record by the sensors on the lower line (sensor 2, 3, 4 and 5) because the ignition is made at the corner of the canyon.

To avoid the influence of TNT driven detonation flow, synchronization of the numerical result and the experiment is done at the sensor 4. Here the synchronization means the arrival of pressure wave in experiment and simulation are assumed identical in one sensor, then the comparisons at the rest sensors can show if the numerical simulation represent the experiment correctly. The R-t diagram of the comparison is show in Figure 6.5-7. In the figure the horizontal axis presents the time (ms) and the vertical axis present the location of sensors (m), V shape lines shown in the figure present the velocity of detonation wave and velocity of its reflecting wave.

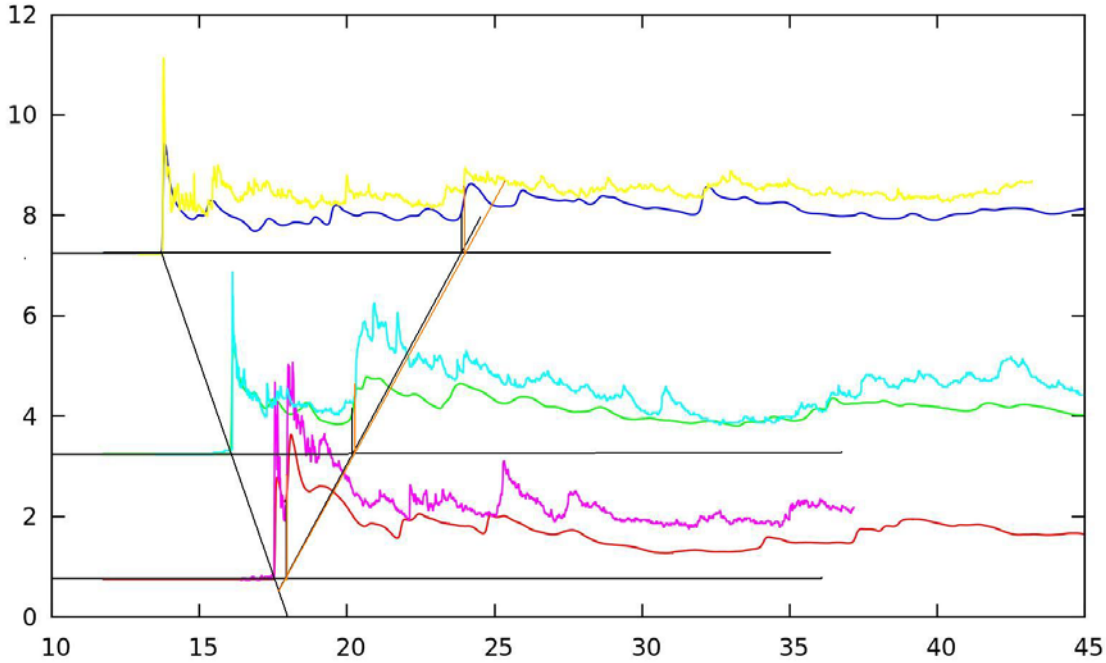

Figure 6.5-7. R-t diagram of KI-RUT-HYD05.

In the figure, comparison between numerical results and experimental results on sensor 4, 3, and 2 are shown from top to bottom. The shock front of the numerical results and experimental results show good agreement on all the three sensors and the slopes of the lines connected by the three shock front (which presents the propagation speed of detonation wave) have almost identical value, so detonation waves in both numerical and experimental results have constant and identical propagation speed. Propagation speed is one important characteristic of detonation wave. Correctly reproduced speed shows that both the chemical part and hydrodynamics of detonation have been represent correctly in the numerical simulation.

In addition, the propagation of the reflecting wave is also analyzed in the R-t diagram. Slopes of the two lines connected by the reflecting wave show slightly different values. Indeed, although heat losses and friction are negligible, they still exist in the experiments and can influence the propagation of shock wave. Therefore, propagation of reflecting shock wave in numerical simulation in which the influence of heat losses and friction are ignored has larger propagation speed.

In total, numerical simulation of experiment KI-RUT-HYD05 shows almost identical detonation propagation speed and a little higher reflecting shock wave speed. Such result shows that the physical model and chemical model selected have the capability to reproduce the real physical phenomena in experiment.

In contrast, since the initiation of detonation in experiment KI-RUT-HYD09 is at the end of upper channel, validation is focused on the comparison of pressure at the sensor 7, 8, 9, 10 and 11. The sensor 11 has a large distance to the TNT explosion position and the influence of the driven effect has disappeared already when the detonation wave reaches the sensor, so the synchronization of numerical simulation and experiment is made at the sensor 11. Following R-t diagram is the comparison of pressure between numerical simulation and experiment.

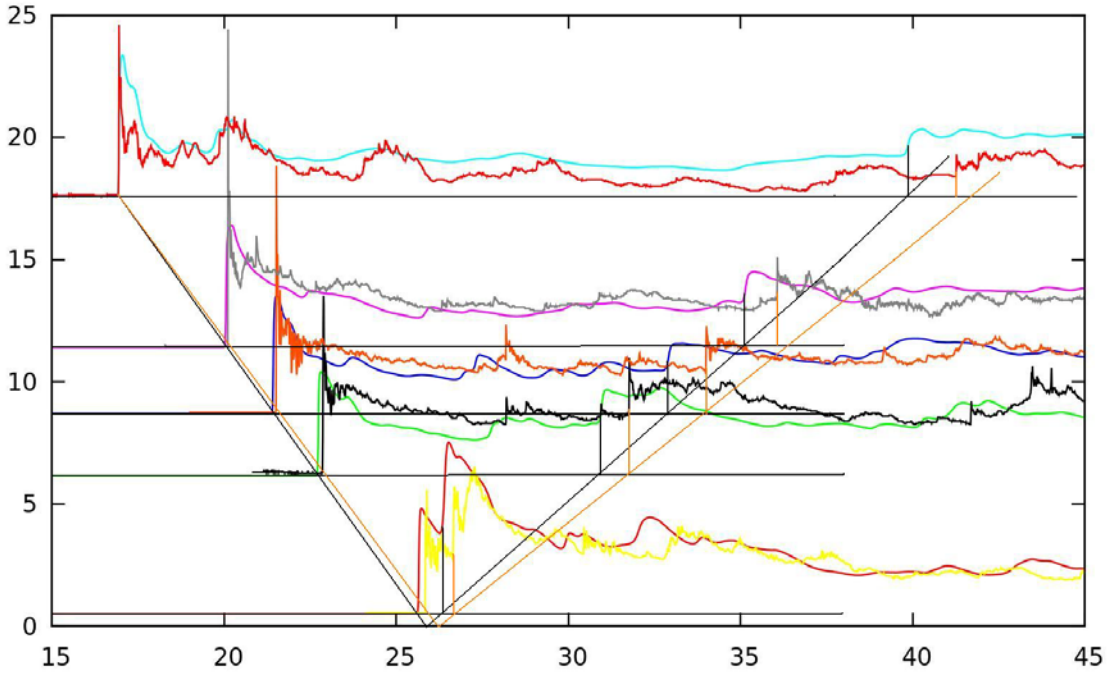

Figure 6.5-8. R-t diagram of KI-RUT-HYD09.

Comparison of pressure between the numerical work and real experiment work on sensor 7, 8 9, 10 and 11 are given from bottom to top on the figure. As we can see in the figure, slopes of the lines which is connected by the detonation shock front are different. Detonation wave in numerical result has a faster propagation speed than the reality. Therefore the difference between the numerical result and experiment grows as the propagation of the wave. As mentioned already, although the heat losses and the friction are negligible the detonation wave can still be influenced and lose energy. Therefore, the propagation speed of detonation in the real experiment work must have a slower speed. Differently from the HYD05 in which the ignition point is at the corner of canyon and the distance to the wall is about 7 meters, the ignition point of experiment HYD09 is at the end of upper channel and the distance between the sensor 11 and wall is about twice which means that the difference between the numerical and the experimental results can be more obvious.

Similarly, influenced by the heat losses and friction, the propagation speed of reflecting wave in experiment is smaller than the numerical simulation, so the difference of reflecting wave in R-t diagram becomes larger and larger.

In general, under the consideration of influence of heat losses and frictions which are ignored in the numerical work, differences of the detonation wave and reflecting shock wave in the R-t diagram is reasonable and acceptable. The result of numerical work for experiment KI-RUT-HYD09 can still show that the physical model and the chemical model selected are capable for the simulation of detonation in industrial scaling facility.

Commonly, the sensitivity of numerical result to resolution should be considered. However the Heaviside detonation chemical model is quite robust to the resolution. In Figure 6.5-9 the comparison of the pressure curve at sensor 11 under different resolution is presented for the simulation of the KI-RUT-HYD09 experiment.

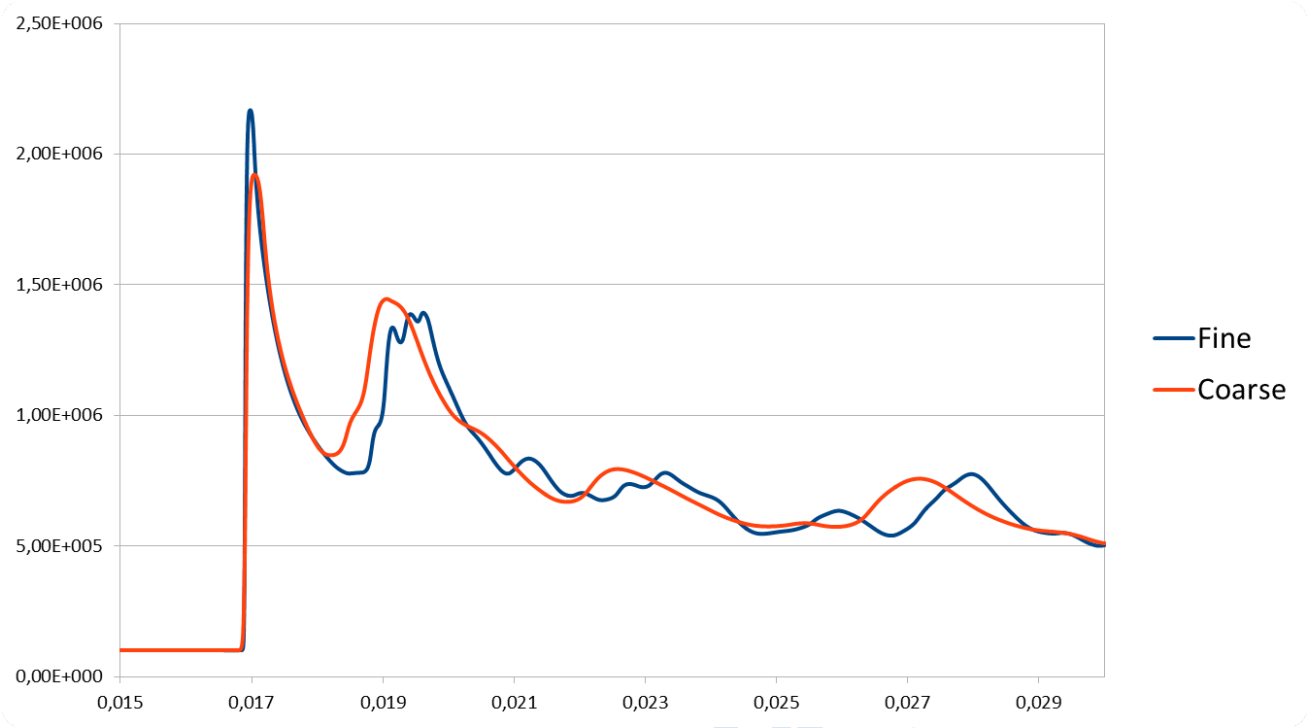

Figure 6.5-9. Comparison of pressure under different resolution on sensor 11 in KI-RUT-HYD09.

"Fine" curve in the figure is achieved by the resolution 0.05 m and the "Coarse" curve is achieved by the resolution 0.1 m. As shown in the figure, the only difference of detonation wave fronts is at the pressure peak values. The coarse grid has much larger numerical diffusion and the pressure value achieved is smaller. Differences in the reflecting waves can be due to the simplification of complex geometry under different resolutions, the differences in spherical ignition regions under different resolutions and the numerical diffusion. To conclude with, comparison shows the robust of Heaviside detonation model under different resolutions. The comparisons at the other sensors are not presented here for reducing the volume of this part.

6.5.1.5 Interpretation of the results

In the former section, analysis of numerical results have been focused on the propagation speed of the detonation wave and its reflecting shock wave. Since the propagation speed is one of the most important parameters in detonation simulation, the numerical reproductions of both experiments are successful. However, when compared with experiment results, some large deviations have not been explained in detail and those explanations will be given in the following parts.

Firstly, the selection of synchronization point in experiment KI-RUT-HYD05 is on sensor 4 instead of sensor 5. Following figure is the R-t diagram in which the synchronization is selection at sensor 5.

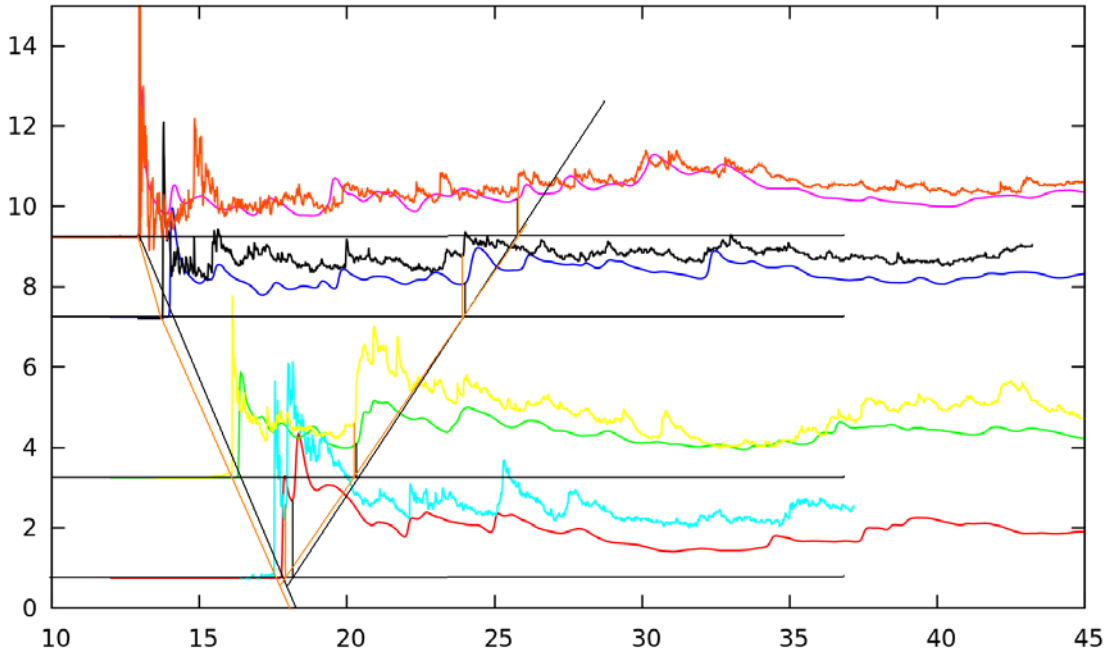

Figure 6.5-10. R-t diagram of HYD05 with synchronization on sensor 5.

As represent by the figure, there is an almost constant shift in the detonation shock wave between the numerical results and experiment results at sensor 2, 3 and 4 if the synchronization is made at sensor 5. In numerical simulation the slopes of the lines connected by the shock front of two neighbouring sensors keep almost the same value, which means that the propagation of detonation in numerical simulation keeps an almost constant value. In contrast, in experiment result, the slopes of line connected by the shock wave front at sensor 5 and 4 is larger than the two other lines. This means that the propagation speed of the detonation wave at the very beginning is larger than the rest of experiment time. Indeed the initial propagation speed of the detonation wave in the experiment is over 2500m/s which is much larger than the detonation in stoichiometric hydrogen-air mixture. In detonation theory the propagation speed of detonation wave depends on the energy released by the chemical reaction and the propagation speed of detonation in stoichiometric hydrogen-air mixture (~29% hydrogen gas) is about 2000m/s. The speed of self-sustained detonation in 20% hydrogen-air mixture should be less. In addition, the sensor 5 is quite near to the TNT explosion point and may be influenced a lot by the TNT detonation. Therefore, the pressure wave detected by sensor 5 is still driven detonation wave and it cannot be used in code validation.

In the former section comparison of pressure curves havr been focused on the position of shock front and reflecting shock. The compatibility of the pressure value between the numerical simulation and experiment has been ignored. Indeed, in the R-t diagram it is not hard to find that there are large errors between the numerical results and experiment results in some sensors. Figure 6.5-11 shows the comparison of pressure at sensor 10 in experiment KI-RUT-HYD09.

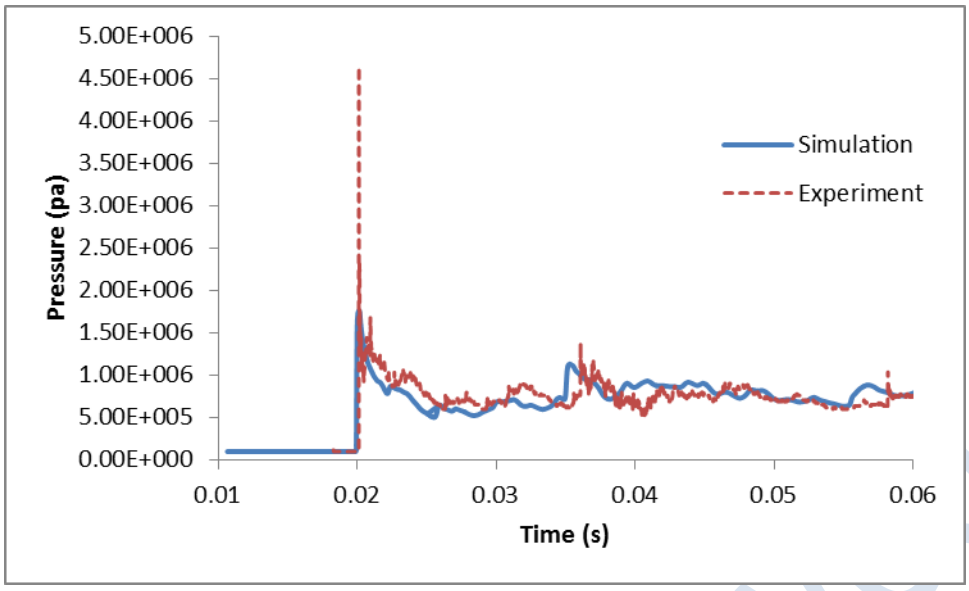

Figure 6.5-11. Pressure comparison at sensor 10 in experiment HYD09.

As we can see, the two shock fronts have very good agreement o each other but the values of pressure peak in the experiment is about 3 times as the numerical results. However, such big difference in pressure peak is still acceptable in the code validation. Firstly, 0.05 m coarse resolution used in the numerical simulation is one main reason why the pressure peak is much smaller than the real experiment. Compared to the thickness of reaction zone of detonation the resolution used in simulation is much larger and as a result the value got in the simulation is an averaged result instead of the real peak value. So, the pressure peak in the numerical simulation should be smaller than the real world measurement. Another reason why the difference in pressure peak is so huge is the physical property of detonation wave. Detonation is a kind of violent supersonic combustion mode and one of the most important characteristics of it is its cellular structure. The cellular structure in the detonation can result in the overlap of the pressure wave and the 3 dimensional overlapping can easily result in a very high pressure value. However, the Heaviside detonation model is a simplified chemical model and in the section of meshing in detonation it has shown already that such model cannot reproduce the cellular structure numerically. As a result, when the sensors are influenced by the triple overlapping pressure wave but the numerical model fails to simulate it, quite big differences between the numerical simulation and experiment in pressure peak will exist. In total, although the compatibility of pressure peak is very bad at some sensor, the validation results can still be accepted if the reproduction of propagation speed is successful.

Last but not the least, the error of detonation propagation speed should be mentioned here again. Heat losses and friction which are ignored in numerical work but really exist in the reality can result in the differences of propagation speed of detonation and its reflecting wave.

6.5.2 Numerical reproduction of detonation cellular structures

One of the most important characteristics of detonation is its cellular strictures. The cell wide of the detonation in 30% volume hydrogen-air mixture is around 12mm. The following simple simulation case will try to reproduce such cell width numerically.

6.5.2.1 Computational domain

Under the consideration of saving computational efforts, reproduction of detonation cellular structure can be done in 2D domain. Figure 6.5-12 shows the size of the computational domain.

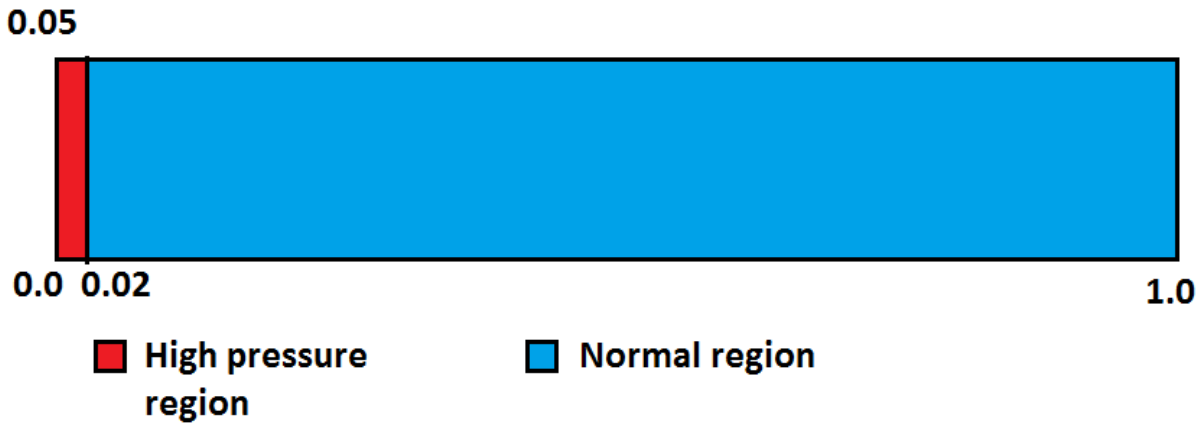

Figure 6.5-12. Size of computational domain for detonation simulation.

As figure shows, computational domain is split into two parts: the high pressure region and the normal region. The high pressure region has very high pressure and temperature to initiated detonation wave directly. The normal region is filled with 30% standard state hydrogen-air mixture. Detailed description of the gas states in the two regions are given in Table 6.5-2.

Table 6.5-2. Gas states of the regions

	High pressure region	Normal region
Size	(0.0, 0.0)X(0.02, 0.05)	(0.02, 0.0)X(1.0, 0.05)
Initial condition	Pressure: 100 bar Temperature: 3000K Velocity: (0, 0) m/s Gas Component (mol ratio): H_2:O_2:N_2:H_2O=2:1:3.76:0	Pressure: 1 bar Temperature: 298K Velocity: (0, 0) m/s Gas Component (mol ratio): H_2:O_2:N_2:H_2O=2:1:3.76:0

The 2D domain is a simple rectangular region, but the computational domain should be constructed quite careful. As mentioned in the former chapter, resolution used in the domain plays quite important role in reproducing detonation cellular structures. Commonly 40 to 50 cells are necessary in width for simulation of one detonation cells, so the resolution used in the computational domain should be less than 0.3mm. If the fine resolution is used in the whole computational domain the numerical simulation will become quite costly. In order to control the computational effort the technique of adaptive local mesh refinement is used in the simulation.

In the section of domain setting in detonation simulation, it has been mentioned that fine resolution is necessary in the chemical reaction part, in the region in front of detonation wave and in the region after the CJ point. According to some numerical experiences, fine resolution can be arranged in a length of half detonation cell length in front of the detonation shock front and in the length of one and half detonation cell length backwards of the shock. In the

simulation, two levels computational domain is used in the detonation simulation, resolution used in the base level is 1 mm and the resolution used in the finer level is 0.25 mm. Figure 6.5-13 shows the computational domain with local mesh refinement, finer resolution cover the regions where the chemical reactions still exits.

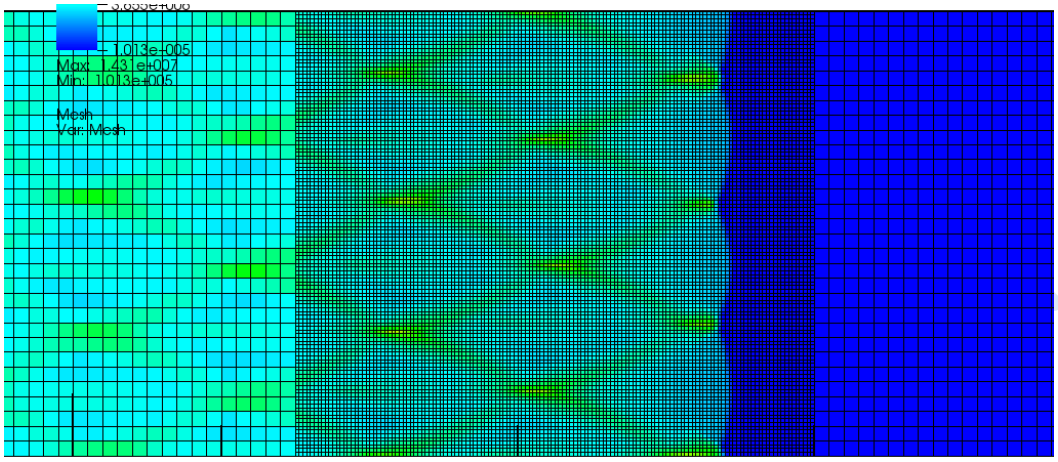

Figure 6.5-13. Setting of local mesh refinement in detonation simulation.

As we can see, refined part covers the region about two and half detonation cell length long behind the shock front and region about half detonation cell length long in front of the shock front. The criterion of finer grid regeneration is the position of detonation shock front. When the detonation wave propagates to the critical position the finer region should be switched forwards. In the grid regeneration it is worth to note that the balance of computational cost and grid regeneration is important in calculation. Finer region should not be too small otherwise the frequent grid regeneration and data redistribution could largely drag down the code efficiency.

Boundary setting of the computational domain is simple, since the viscosity and heat conductivity are totally ignored in the simulation of detonation. The mirror boundary (slipping boundary) is used in the border of the domain.

6.5.2.2 Governing equation

Diffusion is ineligible in propagation of detonation wave, so Euler equations are enough for the simulation of fluid motion. For the numerical production of detonation cellular structures, chemical model can dominate the final results. As mentioned in the section about meshing in detonation simulation, the simplified coarse grid chemical model such as the Heaviside detonation model performs badly in the simulation of cellular structures. Commonly, for simulation of detonation cellular structures, one cheap approach is using the one step Arrhenius method. The following equations show the simplified one step Arrhenius method used in the simulation.

$$\begin{cases} \dfrac{\partial \rho e}{\partial t} = \sum H_i \alpha_i k Y_i \\ \dfrac{\partial Y_i}{\partial t} = \alpha_i k Y_i \\ k = K_{ch} e^{-\frac{E_{ch}}{T}} \end{cases} \tag{6.5.1}$$

In the simulation, for the 30% hydrogen air mixture, the activate energy E_{ch} is set to 8760 K and the factor K_{ch} is set to be 1×10^7.

6.5.2.3 Results

Since the gravity is a quite small perturbation, it will take a long time for the generation of cellular structures. Figure 6.5-14 shows the numerical smoked-foil records at different time. The results shows that till near the ½ length of the computational domain some cellular structures are generated (the numerical smoked-foil records are the maximum pressure records at each cell in the simulation process).

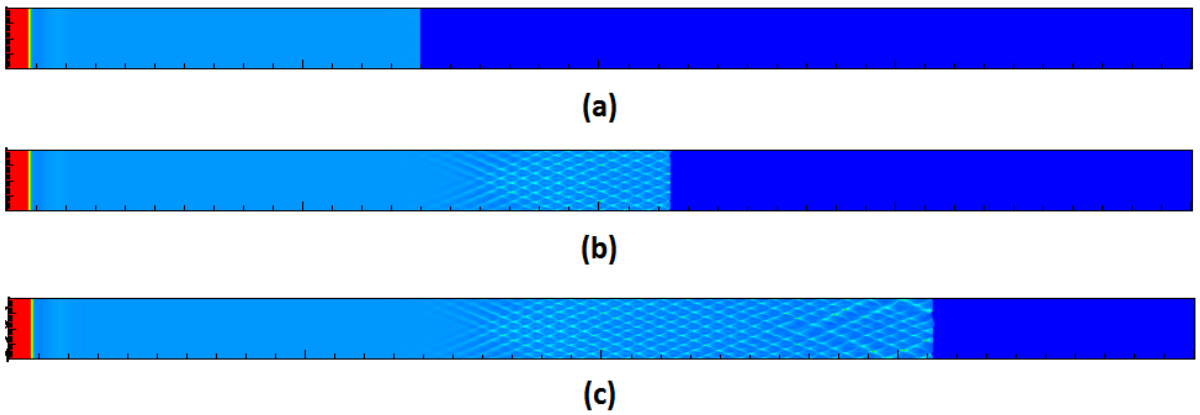

Figure 6.5-14. Smoked-foil records at different times.

Part (a) of the figure shows that the pressure wave still propagates as a flat surface in the front. At this moment the perturbation introduced by gravity is still not so obvious. Then the part (b) shows that some cellular structures appear when the shock front reach near ½ of the 2D channel. Part (c) of the figure shows that the cellular structure becomes irregular in the second half part in the channel.

According to the experimental results, detonation cell width should be around 12mm in the 30% hydrogen-air mixture. However, the cell widths achieved in numerical simulation are different at different stage. Figure 6.5-15 shows the cellular structures at different stages.

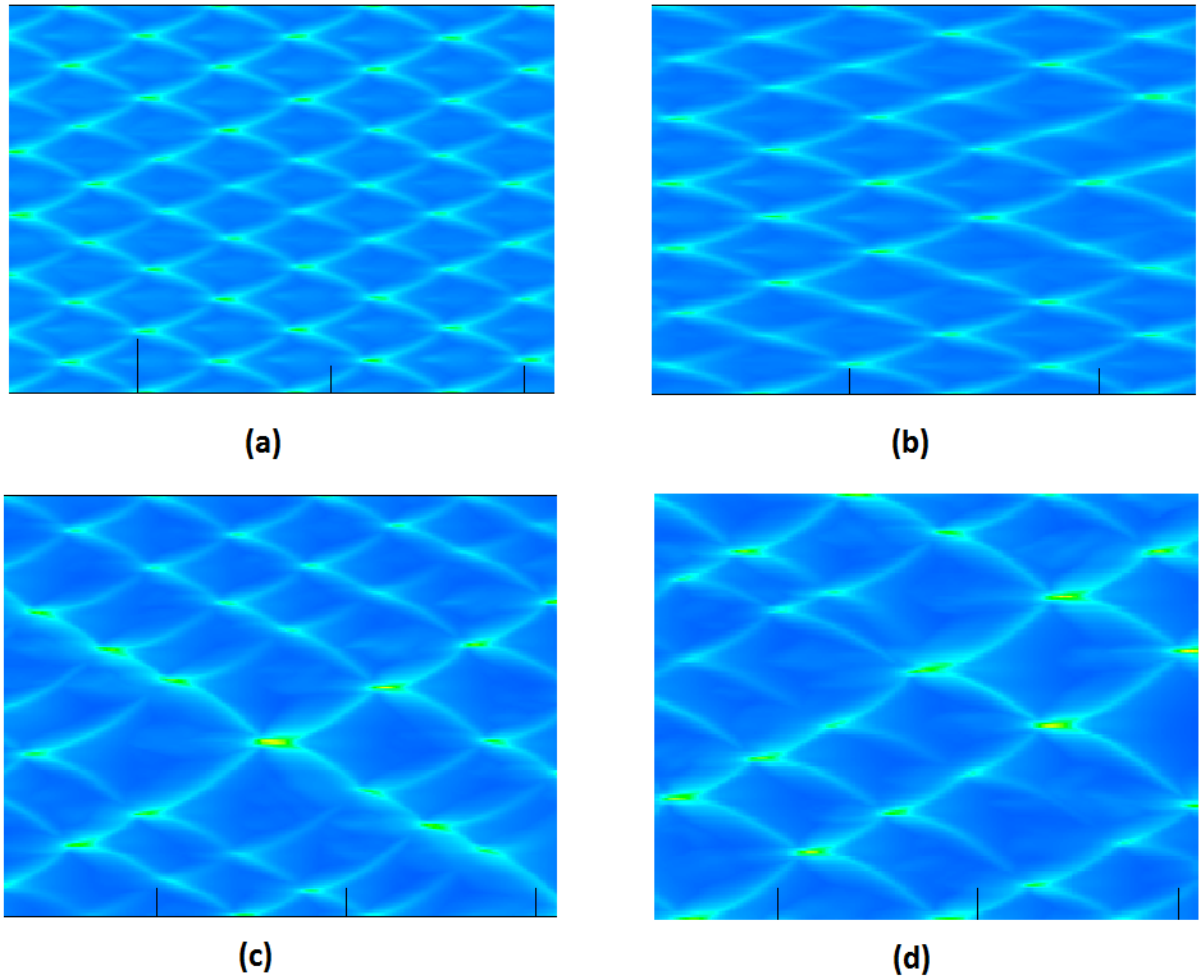

Figure 6.5-15. Cellular structures at different stages.

Part (a) is the cellular structure at the initial stage, six and half cells are generated at 50 mm width channel (which means that the averaged cell width is around 7 mm). Later stage cell width is shown in parts (b), at the moment the cells still maintain the width of 7mm but merging of some cells happens already. At the moment shown by part (c) the cell number reduces to 5, which means that the averaged cell width increases to 10 mm. Part (d) is the cellular structures at the final stage, the cell width goes on increasing to 12mm and reaches a stable limiting.

Shown by the Figure 6.5-15, cellular structures grow as the propagation of the detonation wave and reach the same width as the experiment at the final stage. Cells in the initial stage are much smaller than the experiment but it does not mean that the cells in the initial stage are incorrect. The detonation wave in this numerical simulation is initiated directly by the region with high pressure and high temperature. Energy contained in this region is quite huge. Therefore the detonation in the initial stage is driven detonation instead of self- sustained stable detonation wave. The detonation wave at this stage contains more energy and the cellular structure at this stage is smaller than the stable self-sustained detonation. Since the energy losses are negligible in the simulation, driven effect will last for a considerable long time. The detonation cell width can still reach the size gotten in experiments.

In total, numerical reproduction of detonation cellular structures is successful. The cell width in the stable self-sustained propagation phase has a good agreement against the experiment.

6.5.2.4 Sensitivity study of the results

In simulation of detonation cellular structures, sensitivity of resolution is quite important. The study of resolution sensitivity has been done to show that the 0.25mm resolution is enough for the simulation of hydrogen-air detonation cells. The Figure 6.5-16 the 2D detonation simulation using 0.5mm base level resolution and $3.125X10^{-2}$ mm top level resolution (two finer levels and the refinement ratio of each level is 4) is presented.

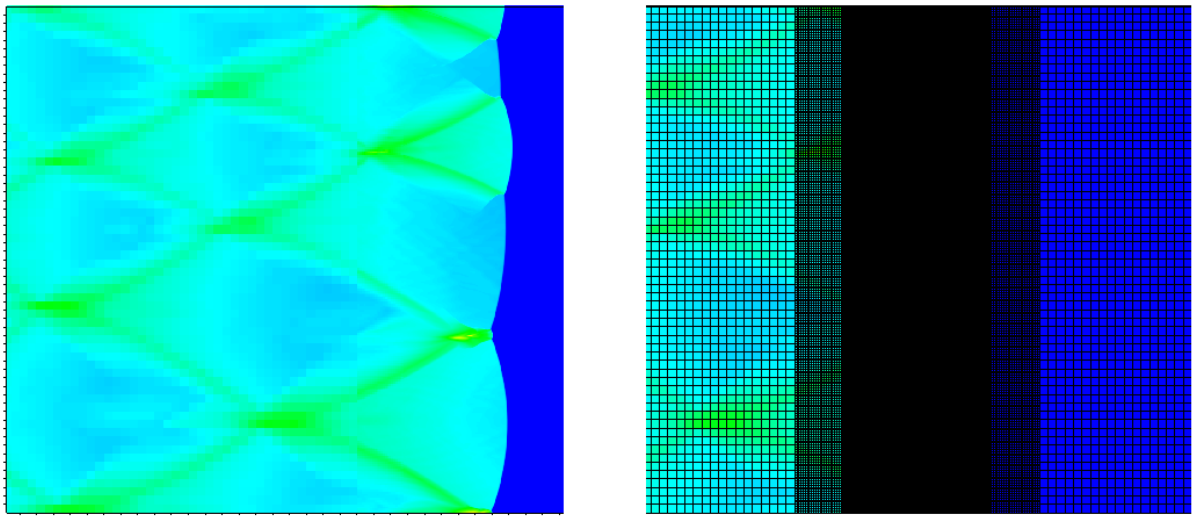

(a) (b)

Figure 6.5-16. Detonation cells and grid in resolution sensitivity study.

Therefore, in the quite high resolution simulation the cell width can still maintain the width of 12 mm. The only difference in the simulations under different resolutions is the appearance of the cellular structures in smoked-foil records. In the high resolution simulations the perturbation can be amplitude more quickly and the appearance of the cellular structure is earlier than the “coarse grid” simulation.

7. References

AIAA Guide (1998) Guide: Guide for the Verification and Validation of Computational Fluid Dynamics Simulations (AIAA G-077-1998(2002)), *In*: *Guide: Guide for the Verification and Validation of Computational Fluid Dynamics Simulations (AIAA G-077-1998(2002)), AIAA Standards*, American Institute of Aeronautics and Astronautics, Inc., Available from: <http://dx.doi.org/10.2514/4.472855.001> [Accessed: 4 December 2015]

Anderson, J.D. (1995), Computational Fluid Dynamics : The Basics With Applications, 6th ed. McGraw-Hill Higher Education, New York, NY, USA.

Angers, B. et al., 2011, *Modelling of hydrogen explosion on a pressure swing adsorption facility*. ICHS2011 - 4th Int. Conf. on Hydrogen Safety, 12-14 September, San Francisco, s.n.

ANSYS Inc. (2009), ANSYS meshing application introduction Appendix A: Mesh quality http://www.scribd.com/doc/105669305/6/Mesh-Quality-Considerations-for-FLUENT.

ANSYS Inc. (2012), FLUENT User Guide, version 14.5.

Antoine, C., 1888, Tensions des vapeurs; nouvelle relation entre les tensions et les températures. [Vapor Pressure: a new relationship between pressure and temperature], Comptes Rendus des Séances de l'Académie des Sciences (in French), 107, pp.681–684, 778–780, 836–837.

Appanaboyina, S., Aung, K. (2004), Development of a VRML application for teaching fluid mechanics, in: ASEE 2004 Annual Conference and Exposition, "Engineering Researchs New Heights", June 20, 2004 - June 23, 2004, ASEE Annual Conference Proceedings. American Society for Engineering Education, pp. 3673–3688.

Arrhenius, S., Über die Reaktionsgeschwindigkeit bei der Inversion von Rohrzucker durch Saunen. Z Phys Chem 4:226 1889.

Arya, S.P., 2001. Introduction to Micrometeorology, Second ed., Academic press.

Aung, K. (2003), Design and implementation of an undergraduate computational fluid dynamics (CFD) course, in: 2003 ASEE Annual Conference and Exposition: Staying in Tune with Engineering Education, June 22, 2003 - June 25, 2003, ASEE Annual Conference Proceedings. American Society for Engineering Education, pp. 121–128.

Badcock, K.J. Richards, B.E. (1999), Educational Requirements for Parallel Computing and Computational Fluid Dynamics, in: Fox, C.A.L.E.P.S. (Ed.), Parallel Computational Fluid Dynamics 1998. North-Holland, Amsterdam, pp. 259–266.

Balsara, D. and Shu, C.W. (2000), Monotonicity preserving weighted essentially non-oscillatory schemes with increasingly high order of accuracy. *J Comput Phys* 2000; 160: 405-52.

Baraldi, D. et al. 2009, An inter-comparison exercise on CFD model capabilities to simulate hydrogen deflagrations in a tunnel. Int. J. Hydrogen Energy, Volume 34, pp. 7862-7872.

Baraldi, D. et al. 2010a, Gap analysis of CFD modelling of accidental hydrogen release and combustion, s.l.: JRC, European Commission.

Baraldi, D. et al. 2010b, An inter-comparison exercise on CFD model capabilities to simulate hydrogen deflagrations with pressure relief vents. Int. J. Hydrogen Energy, Volume 35, pp. 12381-12390.

Bartzis, J.G., Vlachogiannis, D., Sfetsos, A. (2004), Thematic area 5: Best practice advice for environmental flows. The QNET-CFD Network Newsletter, 2, No. 4, pp.34–39.

Bauwens, C., Chaffee, J., Dorofeev, S. (2011), Vented explosion overpressures from combustion of hydrogen and hydrocarbon mixtures. *Intl J of Hydrogen Energy*, Feb. 2011;36(3):2329-2336.

Bauwens, C. R. and Dorofeev, S. B., 2014, Effect of initial turbulence on vented explosion overpressures from lean hydrogen-air deflagrations. *Int. J. Hydrogen Energy*, 39(35), pp. 20509-20515.

Bender, R. and Menter, F. R. (2002). Coupling of Large Eddy Simulation with Eddy Dissipation Model. The 5th Framework Programme (1998-2002), Progress Report, ANSYS CFX Ltd.

Bernard-Michel G, Cariteau B, Ni J, Jallais S, Vyazmina E, Melideo D, Baraldi D, Venetsanos A. (2013), CFD benchmark based on experiments of helium dispersion in a 1 m3 enclosure -intercomparisons for plumes. Proceedings of ICHS 2013, 9-11 September 2013, Brussels, Belgium, paper ID No. 145.

Bhaskaran, R., Collins, L. (2003), Integration of simulation into the undergraduate fluid mechanics curriculum using FLUENT, in: 2003 ASEE Annual Conference and Exposition: Staying in Tune with Engineering Education, June 22, 2003 - June 25, 2003, ASEE Annual Conference Proceedings. American Society for Engineering Education, pp. 9151–9160.

Birch, A. D., Brown, D. R., Dodson, M. G., Swaffield, F. (1984), The structure and concentration decay of high pressure jets of natural gas. *Combustion Science and Technology*, 36, 13.

Birch, A.D., Hughes, D.J. and Swaffield, F. (1987), Velocity decay of high pressure jets. Combustion Science and Technology, 45, pp.161–171.

Boris, J.P. (1990), On Large Eddy Simulation Using Subgrid Turbulence Models, in Whither Turbulence? Turbulence At The Crossroads, J.L. Lumley Ed., Springer, New York, p. 344.

Bragin, M. and Molkov, V. (2009), Physics of spontaneous ignition of high-pressure hydrogen release and transition to jet fire, Proceedings of the 3rd International Conference on Hydrogen Safety, 16-18 September 2009, Ajaccio, France.

Bragin, M.V., Makarov, D.M. and Movkov, V.V. (2013), Pressure limit of hydrogen spontaneous ignition in a T-shaped channel, *Intl J of Hydrogen Energy*, 38 (2013): 8039-8052.

Breitung, W., Kotchourko, A., Veser, A., Scholtyssek, W. (1999), Reactive flow simulation in complex 3D geometries using the COM3D code, in: Proceedings of the Workshop on Severe Accident Research (SARJ-98), 4-6 Nov. 1998, JAERI-Conf 99-005. pp. 462–466.

Brennan, S.L., Makarov, D.M., Molkov, V.V. (2009), LES of high pressure hydrogen fire, *J. of Loss and Prev. in Proc. Ind.*, 22 (2009) 353–359.

Cant, R.S., Mastorakos, E. (2008), An introduction to turbulent reacting flows. Imperial College Press.

CANTERA Toolbox, http://www.galcit.caltech.edu/EDL/public/cantera/html/SD_Toolbox/index.html

Cariteau, B. (2010), Rapport DM2S/SFME/LEEF RT/2010-016/A, CEA.

Cariteau, B. and Tkatschenko, I. (2011), Experimental study of the effects of vent geometry on the dispersion of a buoyant gas in a small enclosure. Proceedings of ICHS 2011, San Francisco, USA, paper ID No. 116.

Cariteau, B. and Tkatschenko, I. (2013), Experimental study of the effects of vent geometry on the dispersion of a buoyant gas in a small enclosure. International Journal of Hydrogen Energy, 38(19), pp.8030–8038.

Casey, M. and Wintergeste, T. (2000), *ERCOFTAC Best Practice Guidelines*, s.l.: European Research Community On Flow Turbulence And Combustion (ERCOFTAC).

Celik, I.B. et al. (2008), Procedure for Estimation and Reporting of Uncertainty Due to Discretization in CFD Applications. Journal of Fluids Engineering, 130.

Chan, T.L. et al. (2002), Validation of a two-dimensional pollutant dispersion model in an isolated street canyon. , 36, pp.861–872.

Chapra, S.C., Canale, R.P. (2001), Numerical Methods for Engineers: With Software and Programming Applications, 4th Revised. ed. McGraw-Hill Publishing Co.

Chen, J. (2015), Practical teaching and learning evaluation of computational fluid dynamics based on traditional chemical engineering curriculum. International Letters of Social and Humanistic Sciences 48, 171 – 179.

Chenoweth, D.R. (1983), Gas-transfer analysis. Section H - Real gas results via the van der Waals equation of state and virial-expansion extensions of its limiting Abel-Noble form. Livermore, CA, Sandia National Laboratories.

Chernyavsky, B. (2012), NSET - A Computational Fluid Dynamics Educational Tool, in: Proceedings of the 2012 International Conference on Modeling, Simulations and Visualization Methods (MSV2012), 16th - 19th July. CSREA Press, Las Vegas Nevada, USA, pp. 102 – 109.

Coleman, H.W. and Steele, W.G. (1999) *Experimentation and Uncertainty Analysis for Engineers*, New York: Wiley

COST (2007), Best practice guideline for the CFD simulation of flows in the urban environment, COST Action 732, European cooperation in science and technology.

Courant, R., Friedrichs, K., Lewy, H. (1967), On the partial difference equations of mathematical physics. *IBM Journal*, 215–234, (English translation of 1928 German original).

Cowan, I.R., Castro, I.P., Robins, A.G. (1997), Numerical considerations for simulations of flow and dispersion around buildings. Journal of Wind Engineering and Industrial Aerodynamics, 67 & 68, pp.535–545.

Cullen, W. D. (1990), *The public inquiry into the Piper Alpha disaster*, London: HMSO.

Cumber, P. S., Fairweather, M., Falle, S. A. E. G., Giddings, J. R. (1995), Predictions of the structure of turbulent, highly under-expanded jets, *J. of Fluids Eng*., 117.

D'Agostino, D. and Congedo, P.M. (2014), CFD modeling and moisture dynamics implications of ventilation scenarios in historical buildings. Building and Environment, 79, pp.181–193.

Davidson, L. (2009), Large Eddy Simulation: How to evaluate resolution, *Intl. J. of Heat and Fluid Flow*, 30(5), 1016-1025.

Dimotakis P. (2005), Turbulent mixing, in *Annu. Rev. Fluid Mech*. 37 (2005), pp. 329–356.

Doring W. (1943), On detonation processes in gases. *Ann Phys.*, 1943, 43: 421–436.

Drikakis, D. (2003), Advances in turbulent flow computations using high-resolution methods. *Progress in Aerospace Sciences*, 39, 405–424.

Echekki, T., Mastorakos, E. (2011), Turbulent Combustion Modeling, Fluid Mechanics and Its Applications 95, Springer Science+Business Media B.V. 2011.

ERCOFTAC (2000), Special Interest Group on Quality and Trust in Industrial CFD: Best Practice Guidelines. Ver. 1.0.

Ewan, B.C.R. and Moodie, K. (1986), Structure and Velocity Measurements in Underexpanded Jets. Combustion Science and Technology, 45(5-6), pp.275–288.

Fairweather, M. and Woolley, R.M. (2003), First-order conditional moment closure modeling of turbulent, nonpremixed hydrogen flames, *Combust Flame*, Jun. 2003;133(4):393-405.

FDS (2016), Fire Dynamics Simulator User's Guide, Sixth Edition, NIST Special Publication 1019, U.S. Department of Commerce, National Institute of Standards and Technology.

Ferziger, J. H. and Peric, M. (2002). *Computational methods for fluid dynamics*. Springer Verlag Berlin Heidelberg New York.

Fluent Inc. (2006), Fluent 6.3 user manual.

FLUENT, 2004. Fluent. Fluent 6.3 documentation. Lebanon, NH: Fluent Inc.; 2006.

Franke, J., Hellsten, A., Schlunzen, H. and Carissimo, B. (2007), Best Practice Guideline for the CFD simulation of flows in the urban environment, s.l.: Quality assurance and improvement of microscale meteorological models, EU COST action 732, https://www.mi.uni-hamburg.de/fileadmin/files/forschung/techmet/cost/cost_732/pdf/BestPractiseGuideline_1-5-2007-www.pdf.

Gallego, E. et al. (2005), *An intercomparison exercise on the capabilities of CFD models to predict deflagration of a large-scale hydrogen-air mixture in open atmosphere.* ICHS2005 - 1st Int. Conf. on Hydrogen Safety, 8-10 September, Pisa.

Gallego, E, Migoya, E, Martín-Valdepeñas, JM, Crespo, A, García, J, Venetsanos, A, Papanikolaou, E, Kumar, S, Studer, E, Dagba, Y, Jordan, T, Jahn, W, Høiset, S, Makarov, D, Piechna, J. (2007), An intercomparison exercise on the capabilities of CFD models to predict distribution and mixing of H2 in a closed vessel, *Intl J of Hydrogen Energy*, 32.13 (2007): 2235-2245

Gant, S.E. (2010), Reliability issues of LES-related approaches in an industrial context. *Flow, turbulence and combustion*, *84*(2), 325-335.

Garcia, J., Baraldi D., Gallego E., Beccantini A., Crespo A., Hansen O.R., Høiset S., Kotchourko, A., Makarov D., Migoya E., Molkov V., Voort M.M., Yanez J. (2010), An intercomparison exercise on the capabilities of CFD models to reproduce a large-scale hydrogen deflagration in open atmosphere, Intl. J. of Hydrogen Energy, 35, 4435–4444.

Germano M., Piomelli U., Moin P., Cabot W. (1991), A dynamic subgrid - scale eddy viscosity model, Physics of Fluids A, 3 (7): 1760–1765.

Geurts, B.J. (2006), Interacting errors in large-eddy simulation: a review of recent developments. *Journal of Turbulence*, (7), N55.

GexCon (2015). FLACS v10.2 User's Manual. January 2015. GexCon AS, Norway.

Giannissi, S.G. et al. (2013), Numerical simulation of LNG dispersion under two-phase release conditions. Journal of Loss Prevention in the Process Industries, 26(1), pp.245–254.

Giannissi, S.G. et al. (2014), CFD modeling of hydrogen dispersion under cryogenic release conditions. Intl Journal of Hydrogen Energy, 39(28), pp.15851–15863.

Giannissi, S.G., Shentsov, V., Melideo, D., Cariteau, B., Baraldi, D., Venetsanos, A. G. and Molkov, V. (2015), CFD benchmark on hydrogen release and dispersion in confined, naturally ventilated space with one vent. *International Journal of Hydrogen Energy*, *40*(5), 2415–2429.

Givoli, D. (1991), Non-reflecting boundary conditions, *Journal of Computational Physics*, 94(1), 1-29.

Golub, V.V., Baklanov, D.I., Golovastov, S.V., Ivanov, M.F., Laskin, I.N., Saveliev, A.S., *et al.* (2008) Mechanisms of High-Pressure Hydrogen Gas Self-Ignition in Tubes, *Journal of Loss Prevention in the Process Industries* 21 (2): 185–198

Golub, V.V., Volodin, V.V., Baklanov, D.I., Golovastov, S.V., Lenkevich, D.A. (2010), Experimental investigation of hydrogen ignition at the discharge into channel filled with air. In: Physics of extreme states of matter, ISBN 978-5-901675-96-0; 2010. p. 110-113. Chernogolovka.

Goodwin, D. (2005), CANTERA – object-oriented software for reacting flows. Technical report, California Institute of Technology, 2005.

Gostintsev Yu.A., Istratov A.G., Shulenin Yu.V. (1988), Self-similar propagation of a free turbulent flame in mixed gas mixtures. *Fizika Goreniya i Vzryva* (Combustion, Explosion and Shock Waves), 1988, 24(5): 63–70.

Gottlieb, D., Orszag, S.A. (1977), Numerical Analysis of Spectral Methods: Theory and Applications. Society for Industrial and Applied Mathematics.

Gran, I.R., Magnussen, B.F. (1996), A numerical study of a bluff-body stabilized diffusion flame. Part 2. Influence of combustion modeling and finite-rate chemistry. *Combust Sci Technol*., Oct. 1996; 119(1-6):191-217.

Guessous, L., Bozinoski, R., Kouba, R., Woodward, D. (2004), Combining experiments with numerical simulations in the teaching of computational fluid dynamics. Computers in Education Journal, Comput. Educ. J. (USA) 14, 21–8.

Gullbrand, J. (2002), Grid-independent large-eddy simulation in turbulent channel using three-dimensional explicit filtering. Center for Turbulence Research Annual Research Briefs.

Gunal, M., Ozcan, A. (2008), Open channel design using Visual Basic. Computer Applications in Engineering Education, Comput. Appl. Eng. Educ. (USA) 16, 127–36. doi:10.1002/cae.20131

Gupta, S., Brinster, J., Studer, E. and Tkatschenko, I. (2009), Hydrogen related risks within a private garage: Concentration measurements in a realistic full scale experimental facility, *International Journal of Hydrogen Energy*, 34(14), pp.5902–5911.

Gutheil, E., Balakrishnan, G. and Williams, F.A. (1993), Structure and extinction of hydrogen-air diffusion flames, In: Reduced kinetic mechanisms for applications in combustion systems (Peters, N. and Rogg, B. Eds.), Springer-Verlag, New York, 1993, p. 179.

Guven, U., Velidi, G. (2011), Utilization of Computational Fluid Dynamics and Computational Engineering Techniques in Mechanical Engineering Streams. Journal of Computational Sciences 48, 22–27.

Hall, R.C. (1997), Evaluation of modelling uncertainty. CFD modelling of near-field atmospheric dispersion. Project EMU final report, (European Commission Directorate–General XII Science, Research and Development Contract EV5V-CT94- 0531, WS Atkins Consultants Ltd., Surrey).

Hanjalic, K. and Launder, B.E (2011), Modelling turbulence in engineering and the environment: Second Moment routes to closure. Cambridge University Press.

Hansen, O.R., Bergonnier, S., Renoult, J. and Van Wingerden, K. (2001), *Phase 3B - Lessons learnt from CFD: FLACS-99r2 simulations, Gexcon report no. Gexcon-01-F36018-1,* Bergen, Norway: s.n.

Hansen, O.R., Renoult, J., Sherman, M. and Tieszen, S. R. (2005), *Valiadtion of FLACS-Hydrogen CFD consequence prediction model against large scale hydrogen explosion experiments in the FLAME facility.* ICHS2005 - 1st Int. Conf. on Hydrogen Safety, 8-10 September, Pisa, s.n.

Hansen, O., Gavelli, F., Davis, S.G. and Middha, P. (2013), Equivalent cloud methods used for explosion risk and consequence studies. *J. Loss Prevention in the Process Industries,* Volume 26, pp. 511-527.

Harlow, F.H. (2004), Fluid dynamics in Group T-3 Los Alamos National Laboratory:(LA-UR-03-3852). Journal of Computational Physics (Elsevier), 195 (2), pp.414–433.

Harten, A. High resolution schemes for hyperbolic conservation-laws. Journal of Computational Physics, 49:357--393, 1983.

Hawkes, E.R. and Cant, R.S. (2001), Implication of a flame surface density approach to large eddy simulation of premixed turbulent combustion, *Combust Flame*, 2001, 126: 1617–1629.

Henderson, B.S., Navaz, H.K., Mukkilmarudhur, R.G. (1998), Bringing Research And New Technology Into The Undergraduate Curriculum: A Course In Computational Fluid Dynamics, in: Proc. 1998 ASEE Annual Conference, 28th June - 1st July. 3.127.1 - 2.127.9, Seattle, Washington, USA.

Hertwig, D. et al. (2012), CFD-RANS model validation of turbulent flow in a semi-idealized urban canopy. Journal of Wind Engineering and Industrial Aerodynamics, 111, pp.61–72.

Hilbert, R. and Thevenin, D. (2002), Autoignition of turbulent non-premixed flames investigated using direct numerical simulations, *Comb. and Flame*, 128 (1-2): 22-37.

Hirsch, C. (Ed.) (2007), Numerical Computation of Internal and External Flows (Second Edition), Second. ed. Butterworth-Heinemann, Oxford.

Hirt, C.W., Amsden, A.A., Cook, J.L. (1974), An arbitrary Lagrangian–Eulerian computing method for all flow speeds , *J. Comput. Phys*. 14 (1974) 227.

Hooker, P., Willoughby, D.B. and Royle, M. (2011), Experimental releases of liquid hydrogen. In *4th Int. Conf. on Hydrogen Safety*. paper 160.

Hooker, P., Hoyes, J.R. and Hall, J. (2014), Accumulation of hydrogen released into an enclosure fitted with passive vents - Experimental results and Simple models. In Institution of Chemical Engineers Symposium Series. Institution of Chemical Engineers. Available at: http://www.scopus.com/inward/record.url?eid=2-s2.0-84908192623&partnerID=tZOtx3y1.

Hooker, P., Hoyes, J.R., Hall, J. and Willoughby, D. (2015). Experimental studies on vented deflagrations in a low strength enclosure. The 6th International Conference on Hydrogen Safety, 19-21 October 2015, Yokohama, Japan.

Houf, W.G., Evans, G.H., Schefer, R.W. (2007), Analysis of jet flames and unignited jets from unintended releases of hydrogen. In: Proceedings of 2nd International conference on hydrogen safety; 11-13 September 2007, Paper ID 1.1.65. San Sebastian, Spain.

Hoyas, S. and Jimenez, J. (2006), Scaling of velocity fluctuations in turbulent channels up to Re_t=2003. *Physics of Fluids A*, 18.

Hoyes, J.R., Ledin, H.S. and Tehrani, A.A.K. (2013). Benchmarking on Hydrogen Deflagrations ISP-49: CFD Modelling Capabilities and Limitations. The 15th International Topical Meeting on Nuclear Reactor Thermal Hydraulics, 12-15 May 2013, Pisa, Italy.

Hu, J., Zhang, L., Xiong, X. (2008), Teaching Computational Fluid Dynamics (CFD) to design engineers, in: 2008 ASEE Annual Conference and Exposition, June 22, 2008 - June 24, 2008, ASEE Annual Conference and Exposition, Conference Proceedings. American Society for Engineering Education.

Ichard, M. et al., (2012), CFD computations of liquid hydrogen releases. International Journal of Hydrogen Energy, 37(22), pp.17380–17389.

International Electrotechnical Commission, Electrical apparatus for explosive gas atmospheres - Part 20: Data for flammable gases and vapours, relating to the use of electrical apparatus, Standard IEC 60079-20:2000.

Ivings, M.J., Lea, C.J. and Ledin, H.S. (2003), Outstanding safety questions concerning the analysis of ventilation and gas dispersion in gas turbine enclosures: Best Practice Guidelines for CFD, Health & Safety Laboratory.

Jallais, S. (2013), Hydrogen vented explosion: experiments, engineering methods and CFD. ICHS2013 - 5th Int. Conf. on Hydrogen Safety, 9-11 September, Brussels, s.n.

Jia, R., Shanjun, X., Songyun, G., Aziz, E.-S., Esche, S., Chassapis, C. (2006), A virtual laboratory on fluid mechanics, in: 113th Annual ASEE Conference and Exposition, 2006, June 18, 2006 - June 21, 2006, ASEE Annual Conference and Exposition, Conference Proceedings. American Society for Engineering Education, p. Dassault Systemes; HP; Lockheed Martin; IBM; Microsoft; et al.

Johnson, D.W. and Woodward, J.L., 2010. Release: a model with data to predict aerosol rainout in accidental releases (Vol. 24). John Wiley & Sons.

Jones, W.P., and Launder, B.E. (1972), The prediction of laminarization with a two-equation model of turbulence, Int. J. Heat Mass Transfer, 15, p301-314.

Kaneko, W., Hayashi, K. and Ishii, K. (2015), An Experimental Study on Mechanism of Self-Ignition of High-Pressure Hydrogen, Proceedings of Int. Conference on Hydrogen Safety, *In*: *6st International Conference on Hydrogen Safety*, Yokohama, Japan.

Kee, R.J., Rupley F.A., Miller J.A. (1989), Chemkin II: a Fortran chemical kinetics package for the analysis of gas-phase chemical kinetics. Sandia National Laboratories Report 1986 No. SAND89–8009.

Keenan, J.J., Makarov, D.V. and Molkov, V.V. (2013), *Rayleigh-Taylor instability: Modelling and effect on coherent deflagrations.* ICHS2013 - 5th Int. Conf. on Hydrogen Safety, 9-11 September, Brussels, s.n.

Keenan, J.J., Makarov, D.V. and Molkov, V.V. (2014), Rayleigh–Taylor instability: Modelling and effect on coherent deflagrations. I*nternational journal of hydrogen energy*, 39(35), 20467-20473.

Kim, W., Shentsov, V., Makarov, D. and Molkov, V. (2015), High Pressure Hydrogen Tank Rupture: Blast Wave and Fireball, In: 6th International Conference on Hydrogen Safety, Yokohama, Japan,

Koutsourakis, N., Venetsanos, A.G. and Bartzis, J.G. (2012a), LES modelling of hydrogen release and accumulation within a non-ventilated ambient pressure garage using the ADREA-HF CFD code, *International journal of hydrogen energy*, 37(22), 17426-17435.

Koutsourakis, N., Tolias, I. C., Venetsanos, A. G. and Bartzis, J. G. (2012b), Evaluation of an LES Code Against a Hydrogen Dispersion Experiment, *CFD Letters*, 4(4), 225-236.

Lamoureux N., Djebaili-Chaumeix N., Paillard C.E. (2002), Laminar flame velocity determination for H2-air-steam mixtures using the spherical bomb method. *J Phys IV* 2002, 12(7): 445–452.

Langtry, RB, Menter, FR (2009), Correlation-based transition modeling for unstructured parallelized computational fluid dynamics codes. AIAA J;47:2894–906.

LaRoche, R.D., Hutchings, B.J., Muralikrishnan, R. (2002), FlowLab: Computational Fluid Dynamics (CFD) framework for undergraduate education, in: 2002 ASEE Annual Conference and Exposition: Vive L'ingenieur, June 16, 2002 - June 19, 2002, ASEE Annual Conference Proceedings. American Society for Engineering Education, pp. 7329–7336.

Laskey, K.J., Oran, E.S., Boris, J.P. (1988), The gradient method for interface tracking, Naval Research Laboratory Memorandum Report 6183; 1988.

Launder, B.E. and Spalding, D.B. (1974), The numerical computation of turbulent flows, *Computer Methods in App Mech and Engg*, 3(2): 269-289.

Lea, C.J., (2010), How to ensure that CFD for Industrial Applications is 'Fit for Purpose'. s.l.:NAFEMS Ltd.

Leachman, J.W., Jacobsen, R.T., Penoncello, S.G. and Lemmon, E.W. (2009), Fundamental equations of state for parahydrogen, normal hydrogen, and orthohydrogen, *Journal of Physical and Chemical Reference Data*, 38(3), 721-748.

Lee, H.S. (2008), The Detonation Phenomenon, ISBN-13 978-0-511-41392-6.

Lee, B.J. and Jeung, I.S. (2009), Numerical study of spontaneous ignition of pressurized hydrogen release by the failure of a rupture disk into a tube, *Intl. J. of Hydrogen Energy*, 34, 2009, pp.8763-8769.

Lemmon, E.W., Huber, M.L. and Leachman, J.W. (2008), Revised standardized equation for hydrogen gas densities for fuel consumption applications, *Journal of Research of the National Institute of Standards and Technology*, 113(6), 341.

L,i J., Zhao, Z ., Kazakov, A., Dryer, F.L. (2004), Int. J. Chem. Kinet. 36: 566-575.

Lilly, D.K. (1992), A proposed modification of the Germano subgrid scale closure model, *Physics of Fluids*, 4, 633–635.

Liuo, M.S. (2006), A sequel to AUSM, Part II: AUSM+up for all speeds. Journal of computational physics 214 137-170.

Luketa-Hanlin, A., Koopman, R.P. and Ermak, D.L. (2007), On the application of computational fluid dynamics codes for liquefied natural gas dispersion. Journal of hazardous materials, 140(3), pp.504–17.

Lund, T.S., Wu, X., Squires, K.D., (1998), Generation of turbulent inflow data for spatially developing boundary layer simulations, *Journal of Computational Physics*, 140(2), pp.233–258.

Magnussen, B.F. and Hjertager, B.H. (1976), On mathematical modelling of turbulent combustion with special emphasis on soot formation and combustion. In: Proceedings of sixteenth symposium (Int.) on combustion. Pittsburgh, PA: The Combustion Institute; 1976. p. 719-729.

Magnussen, B.F. (1981), On structure of turbulence and a generalized eddy dissipation concept for chemical reaction in turbulent flow, presented at 19th AIAA Aerospace Sciences Meeting, 12-15 January 1981, St. Louis, Missouri, USA.

Makarov, D.V., and Molkov, V.V. (2004), Large eddy simulation of gaseous explosion dynamics in an unvented vessel. *Combust Explos Shock Waves*, 2004;40(2):136–44.

Makarov, D., et al. (2009a), An inter-comparison exercise on CFD model capabilities to predict a hydrogen explosion in a simulated vehicle. Int. J. Hydrogen Energy, Volume 34, pp. 2800-2814.

Makarov, D., et al. (2009b), *Modelling of lean uniform and non-uniform hydrogen-air mixture explosions in a closed vessel.* ICHS2009 - 3rd Int. Conf. on Hydrogen Safety, 16-18 September, Ajaccio, Corsica, s.n.

Makarov, D., Verbecke, F., Keenan, J. and Molkov, V., (2010), *On resolved mechanisms of large scale deflagrations in complex geometries.* 6th Int. Seminar on Fire and Explosion Hazards, University of Leeds, April 11-16.

Makarov, D.V. and Molkov, V.V. (2013a), Plane hydrogen jets, *Intl. J. of Hydrogen Energy*, 38 (2013): 8068-8083.

Makarov, M. and Molkov, V., (2013b), Modelling and simulation of lean hydrogen-air deflagrations in 120m3 enclosure. ICHS2013 - 5th Int. Conf. on Hydrogen Safety, 9-11 September, Brussels, s.n.

Markatos, N. and Pericleous, K. (1984), Laminar and turbulent natural convection in an enclosed cavity. International Journal of Heat and Mass, 27(5), pp.755–772.

Mason, H.B. and Spalding, D.B., (1973), Prediction of reaction rates in turbulent premixed boundary layer flows. Combustion Institute European Symposium, 601-612. Academic Press, New York, 1973.

Mastorakos, E., Baritaud, T.A., Poinsot, T.J. (1997), *Numerical simulations of autoignition in turbulent mixing flows, Combust. Flame* 109 (1997) 198–223.

Maxwell, B.M. and Radulescu, M.I. (2011), Ignition Limits of Rapidly Expanding Diffusion Layers: Application to Unsteady Hydrogen Jets, *Combustion and Flame* 158 (10): 1946–1959

Menter, F.R. (1994), Two-Equation Eddy-Viscosity Turbulence Models for Engineering Applications, *AIAA Journal*, 32(8), August 1994, pp. 1598-1605.

Middha, P. and Hansen, O.R. (2009), CFD simulation study to investigate the risk from hydrogen vehicles in tunnels. Int. J. Hydrogen Energy, Volume 34, pp. 5875-5886.

Middha, P. (2010), Development, use, and validation of the CFD tool FLACS for hydrogen safety studies, PhD thesis, University of Bergen, Norway.

Mogi, T., Nishida H., Shiina H., Horiguchi S. (2005a), A study of combustion properties of high-pressure hydrogen gas jet. In: Proceedings of 43rd symposium (Japanese) on combustion; 5-7 December 2005. Tokyo, Japan. p. 164-165.

Mogi, T., Nishida, H. and Horiguchi, S. (2005b) Flame Characteristics of High-Pressure Hydrogen Gas Jet, *In*: *Proceedings of First International Conference on Hydrogen Safety*,

Mogi, T. and Horiguchi S. (2009), Experimental study on the hazards of high pressure hydrogen jet diffusion flame, *J Loss Prev Process Ind* 2009;22:45-51.

Moin, P. and Kim J. (1982), Numerical investigation of turbulent channel flow. *J. of Fluid Mech.*, 118: 341-377.

Molkov, V.V., Makarov, D.V., Grigorash A. (2004), Cellular structure of explosion flames: modelling and large eddy simulation. *Combust Sci Technol*, 2004,176(5–6): 851–85.

Molkov, V.V., Makarov, D.V., Schneider H. (2006), LES modelling of an unconfined large-scale hydrogen-air deflagration. *J Phys D*., Oct. 2006, 39(20):4366-4376.

Molkov, V.V., Makarov, D.V. and Schneider, H., (2007). Hydrogen-air deflagrations in open atmosphere: Large eddy simulation analysis of experimental data. *Int. J. Hydrogen Energy*, Volume 32, pp. 2198-2205.

Molkov, V.V., Bragin, M.V., Brennan, S.B., Makarov, D.M., Verbecke, F., Zbikowski, M. (2008), Progress in modeling and les of hydrogen underexpanded jets and dispersion, spontaneous ignition and jet fires, large scale deflagrations and detonations. UU Report.

Molkov, V.V. and Bragin, M. (2009), High-pressure hydrogen leak through a narrow channel. In: Nonequilibrium Phenomena: Plasma, Combustion, Atmosphere; Torus Press: Moscow, pp. 332-338.

Molkov, V.V., Makarov, D.V., Bragin, M. (2009a), Physics and modelling of under-expanded jets and hydrogen dispersion in atmosphere, in Fortov V.E., et al. (eds), Physics of extreme state of matter 2009. Chernogolovka, Russia, pp. 143-145. ISBN 978-5-901675-89-2.

Molkov, V., Makarov, D. and Bragin, M. (2009b), Physics and Modelling of under-Expanded Jets and Hydrogen Dispersion in Atmosphere, *In*: *Proceedings of the 24th International Conference on Interaction of Intense Energy Fluxes with Matter*, Elbrus, Chernogolovka, pp.143–145

Molkov, V.V. (2012), Fundamentals of hydrogen safety engineering, www.bookboon.com.

Molkov, V. and Shentsov, V. (2014), Numerical and Physical Requirements to Simulation of Gas Release and Dispersion in an Enclosure with One Vent, *International Journal of Hydrogen Energy* 39 (25): 13328–13345

Molkov, V., Shentsov, V., Brennan, S. and Makarov, D. (2014) Hydrogen Non-Premixed Combustion in Enclosure with One Vent and Sustained Release: Numerical Experiments, *International Journal of Hydrogen Energy* 39 (20): 10788–10801

Morris, T. (2005), Quality and Reliability in Engineering CFD Simulations. Fluent News.

Mosedale, A. and Drikakis, D. (2007), Assessment of very high-order of accuracy in LES models *ASME J. of Fluids Engineering*, 129 (12) (2007), pp. 1497–1503.

Moser, R., Kim J., Mansour, N. (1999), Direct numerical simulation of turbulent channel flow up to Re_t=590, *Physics of Fluid*, 11: 943-945.

Nasrifar, K. (2010), Comparative study of eleven equations of state in predicting the thermodynamic properties of hydrogen, *International journal of hydrogen energy*, 35(8), 3802-3811.

National Aeronautics and Space Administration Report, Safety Standard for Hydrogen and Hydrogen Systems, Report NSS 1740.16, 1997, p. A-16.

NEA (2015), Best Practice Guidelines for the use of CFD in Nuclear Reactor Safety Applications – Revision. NEA/CSNI/R(2014)11.

Nettleton, M.A. (1987), Gaseous detonations: their nature, effects and control. New York: Chapman and Hall Ltd.; 1987.

Neumann, Von J. (1942), Theory of detonation waves. In: Taub A.J., editor. John von Neumann, collected works, vol. 6. New York: Macmillan; 1942.

NIST (2016), http://webbook.nist.gov/.

Norris, J.W. and Edwards J.R. (1997), Large eddy simulation of high speed turbulent diffucion flames with detailed chemistry, AIAA paper 97-0370, presented at 35th Aerospace Sciences meeting, Reno, NV, Jan 6-9 1997.

O'Rourke, P.J. and Amsden, A.A. (1986), Implementation of a conjugate residual iteration in the KIVA computer program, Los Alamos National Laboratory report 1986 LA-10849-MS.

OECD (2007), Best practice guidelines for the use of CFD in nuclear reactor safety applications, OECD Nuclear Energy Agency (NEA), Committee on the safety of nuclear installations.

Oran, E.S., Boris, J.P. (2001), Numerical simulation of reactive flow. 2nd ed. Cambridge University Press; 2001.

Orszag, S.A., Yakhot, V., Flannery, W.S., Boysan F., Choudhury D., Maruzewski J. (1993), Renormalization group modeling and turbulence simulations. In: International conference on near-wall turbulent flows; 1993. pp. 1031-1046.

Pantano, C. (2004), Direct simulation of non-premixed flame extinction in a methane-air jet with reduced chemistry, *J. of Fluid Mech*., 514, 231-270, 2004.

Papanikolaou, E.A., Venetsanos, A.G., Heitsch, M., Baraldi D., Huser A., Pujol J., Garcia, J., Markatos, N. (2010), HySafe SBEP-V20: Numerical studies of release experiments inside a naturally ventilated residential garage, *Intl J of Hydrogen Energy*, 35 (10), May 2010, 4747-4757.

Papanikolaou, E.A., Venetsanos, A.G., Cerchiara, G.M., Carcassi. M., Markatos N. (2011), CFD simulations on small hydrogen releases inside a ventilated facility and assessment of ventilation efficiency, *Intl J of Hydrogen Energy*, 36(3), February 2011, 2597-2605.

Patankar, V.S. (1980), Numerical heat transfer and fluid flow, Hemisphere publishing corporation, McGraw-Hill.

Peng, D.Y., Robinson, D.B. (1976), A New Two-Constant Equation of State. Indust. and Engr. Chemistry: Fundamentals 15, p.59.

Peters, N. and Rogg, B. (1993), Reduced kinetic mechanisms for applications in combustion systems, Berlin; New York; Spinger-Verlag, 1993.

Pierce, C. (2001), Progress-variable approach for large-eddy simulation of turbulent combustion. Mech. Eng. Dept. Rep. TF-80. Ph.D. thesis, Stanford University.

Pines, D. (2004), Using computational fluid dynamics to excite undergraduate students about fluid mechanics, in: ASEE 2004 Annual Conference and Exposition, "Engineering Researchs New Heights", June 20, 2004 - June 23, 2004, ASEE Annual Conference Proceedings. American Society for Engineering Education, pp. 14975–14982.

Pinto, D., Aizawa, K., Liu, Y.F., Sato, H., Hayashi, A.K. and Tsuboi, N. (2007), Auto-ignition of high pressure hydrogen release, Proceedings of the 21st International Colloquium on the Dynamics of Explosions and Reactive Systems, 23-27 July 2007, Poitiers.

Poinsot, T. and Veynante, D. (2011), Theoretical and numerical combustion, 2011.

Poling, B.E., Prausnitz, J.M., O'Connell, J.P. (2004). The Properties of Gases and Liquids (5th edition), McGraw-Hill.

Pope, S.B. (1978), An explanation of the turbulent round-jet/plane-jet abnormality, technical note. AIAA J 1978;16(3):279

Pope, S.B. (1997), Computationally efficient implementation of combustion chemistry using in situ adaptive tabulation, *Combust Theory Model* 1997;1:41-63.

Pope, S.B. (2000), Turbulent flows, Cambridge University Press.

Pope, S.B. (2004), Ten questions concerning the large-eddy simulation of turbulent flows, *New Journal of Physics*, 6, 35.

Prudnikov, A. (1967), Combustion of homogeneous fuel-air mixtures in turbulent flows. Physical principles of the working process in combustion chambers of jet engines; 1967, 244-336.

Puttock, J., Chakraborty, D. and Farmayan, W. (2014), *Gas explosion modelling using PDRFOAM.* SUSANA Workshop, 18 September, Athens, s.n.

Goozee, R.J., Jacobs, P.A., Buttsworth, D.R. (2006), Simulation of a complete reflected shock tunnel showing a vortex mechanism for flow contamination, *Shock waves* 15 (3–4) (2006) 165–176.

Rakai, A., Kristof, G. and Franke, J. (2013), Sensitivity analysis of microscale obstacle resolving models for an idealized Central-European city centre, Michel-Stadt, Időjárás. Quarterly Journal of the Hungarian …, 118(1), pp.53–77.

Rayleigh, J.W.S (1883), Investigation of the character of the equilibrium of an incompressible heavy fluid of variable density. In: Proceedings of the London Mathematical Society, 14, 1883, 170-177.

Reynolds, O. (1895), On the Dynamical Theory of Incompressible Viscous Fluids and the Determination of the Criterion, *Phil. Trans. of the Royal Soc of London. A*, v. 186, 123-164.

Reynolds, W.C. (1986), The element-potential method for chemical equilibrium analysis: implementation in the interactive program STANJAN, version 3, Stanford, CA: Department of Mechanical Engineering, Stanford University; 1986.

Richard Courant, Kurt Friedrichs, Hans Lewy: Über die partiellen Differenzengleichungen der mathematischen Physik. In: Mathematische Annalen, Bd. 100 (1928), S. 32–74.

Richardson, L.F. (1911), The approximate arithmetical solution by finite differences of physical problems including differential equations, with an application to the stresses in a masonry dam. Philosophical Transactions of the Royal Society, A 210, pp.307–357.

Richardson, L.F. (1927), The deferred approach to the limit. Philosophical Transactions of the Royal Society A, A 226, pp.299–349.

Roache, P.J. (1994), Perspective: A method for uniform reporting of grid refinement studies. Journal of Fluid Engineering, 116, pp.405–409.

Roache, P.J. (1997), Quantification of uncertainty in computational fluid dynamics, in: Annual Review of Fluid Mechanics. Vol.29. Annual Reviews, Palo Alto, CA, USA, pp. 123–60.

Rodi, W. (1982), Turbulent buoyant jets and plumes. Pergamon Press.

Sathiah, P., Komen, E. and Roekaerts, D. (2014), The role of CFD combustion modelling in hydrogen safety management–III: Validation based on homogeneous hydrogen–air–diluent experiments. *Nuclear Engineering and Design*, 289, 296-310.

Saxena, P., and Williams, F.A. (2006), Testing a small detailed chemicalkinetic mechanism for the combustion of hydrogen and carbon monoxide. *Combust Flame* 2006;145:316–23.

Schefer, R.W., Houf, W.G., Williams, T.C., Bourne, B., Colton, J. (2007), Characterization of high-pressure, under-expanded hydrogen-jet flames, *Intl J. of Hydrogen Energy*, 32(12), 2081–2093.

Schneider, H., and Pförtner, H. (1983), Fraunhofer-ICT Internal Report: PNP-Sichcrheitssofortprogramm, Prozebgasfreisetzung-Explosion in der Gasfabrik und Auswirkungen von Druckwellen auf das Containment, December 1983.

Shah, R.K., Heikal, M.R., Thonon, B., and Tochnon, P. (2001), Progress in the numerical analysis of compact heat exchanger surfaces. In Hartnett, J. P. (Ed.) *Advances in Heat Transfer*, 34, 2001, San Diego, USA, Academic Press.

Shentsov, V., Kim, W., Makarov, D. and Molkov, V. (2016a), Numerical Simulations of Experimental Fireball and Blast Wave from a High-Pressure Tank Rupture in a Fire, In: Proc. of the Eighth International Seminar on Fire & Explosion Hazards (ISFEH8), Hefei, China.

Shentsov, V., Sakarsume, R., Makarov, D., Takeno, K. and Molkov, V. (2016b), Lift-off and Blow-out of under-Expanded Hydrogen Jets: Experiments versus Simulations, In: Proc. of the Eighth International Seminar on Fire & Explosion Hazards (ISFEH8), Hefei, China.

Shi, J., Zhang, Y.T., Shu, C.W. (2003), Resolution of high order WENO schemes for complicated flow structures, *J. Comput. Phys*. 186 (2003) 690–696.

Shirvill, L., Royle, M., Roberts, T. (2007), Hydrogen releases ignited in a simulated vehicle refuelling environment, presented at the 2nd ICHS, San Sebastian, Spain; 2007.

Sklavounos, S., Rigas, F. (2005), Fuel gas dispersion under cryogenic release Conditions. Energy & Fuels, (9), pp.2535–2544.

Smagorinsky, J. (1963), General circulation experiments with the primitive equations I. The Basic Experiment, *Month. Wea. Rev*. 91.3: 99–164.

Smirnov, R., Shi, S., Celik, I. (2001), Random flow generation technique for large eddy simulations and particle-dynamics modelling, *J of Fluids Eng*, 123, 359.

Solberg, D., Pappas, J., Skramstad E. (1981), Observations of flame instabilities in large scale vented gas explosions. Symposium (International) on Combustion, 1981, 18(1): 1607-1614.

Spalding D.B. (1971), Mixing and chemical reaction in steady confined turbulent flames, Thirteenth symposium (international) on combustion, The combustion institute, pp. 649–657, 1971.

Spence D.A. and Woods B.A. (1964), A review of theoretical treatments of shock-tube attenuation, *J Fluid Mech* 1964;19:161-174.

Statharas, J.C., Venetsanos, A.G., Bartzis, J.G., Würtz, J. and Schmidtchen, U. (2000), Analysis of data from spilling experiments performed with liquid hydrogen, *Journal of Hazardous Materials*, 77(1-3), 57–75.

Stern, F., Wilson, R.V., Coleman, H.W., Paterson, E.G. et al. (1999), *Verification and Validation of CFD Simulations*, Iowa Institute of Hydraulic Research, University of Iowa.

Stern, F., Xing, T., Yarbrough, D., Rothmayer, A., Rajagopalan, G., Otta, S.P., Caughey, D., Bhaskaran, R., Smith, S., Hutchings, B., Moeykens, S. (2004), Development of hands-on CFD educational interface for undergraduate engineering courses and laboratories, in: ASEE 2004 Annual Conference and Exposition, "Engineering Researchs New Heights", June 20, 2004 - June 23, 2004, ASEE Annual Conference Proceedings. American Society for Engineering Education, pp. 3719–3749.

Stern, F., Tao Xing, Muste, M., Yarbrough, D., Rothmayer, A., Rajagopalan, G., Caughey, D., Bhaskaran, R., Smith, S., Hutchings, B., Moeykens, S. (2006), Integration of simulation technology into undergraduate engineering courses and laboratories, *International Journal of Learning Technology*, Int. J. Learn. Technol. (Switzerland) 2, 28–48.

Strelets, M. (2001), Detached Eddy Simulation of Massively Separated Flows, AIAA Paper 2001-0879, 39th Aerospace Sciences Meeting and Exhibit, Reno, NV.

SUSANA D2.1 (2016), Review: The state-of-the-art in physical and mathematical modelling of safety phenomena relevant to FCH technologies, Deliverable D2.1, FCH JU SUSANA project, Grant agreement no.: 325386.

SUSANA D2.2 (2016), Critical analysis and requirements to physical and mathematical models, Deliverable D2.2, FCH JU SUSANA project, Grant agreement no.: 325386.

SUSANA D4.2 (2016), Final report on verification and validation procedures, Deliverable D4.2, FCH JU SUSANA project, Grant agreement no.: 325386.

SUSANA D5.2 (2015), Report on model benchmarking exercise 1, Deliverable D5.2, FCH JU SUSANA project, Grant agreement no.: 325386.

SUSANA D5.3 (2016), Report on model benchmarking exercise 2, Deliverable D5.3, FCH JU SUSANA project, Grant agreement no.: 325386.

Taylor, G. (1950), The instability of liquid surfaces when accelerated in a direction perpendicular to their planes, I, in: *Proceedings of the Royal Society of London*, 201, series A, mathematical and physical sciences, no. 1065; Mar. 1950, 192-196.

Tolias, I. C., and Venetsanos, A. G. (2015), Comparison of convective schemes in Hydrogen Impinging Jet CFD simulation. In *6th International Conference on Hydrogen Safety*. Yokohama, Japan.

Tolias, I.C., Venetsanos, A.G., Markatos, N. and Kiranoudis, C.T. (2014), CFD modeling of hydrogen deflagration in a tunnel, *International journal of hydrogen energy*, 39(35), 20538-20546.

Tominaga, Y., Mochida, A., Yoshie, R., Kataoka, H., Nozu, T., Yoshikawa, M., Shirasawa, T. (2008), AIJ guidelines for practical applications of CFD to pedestrian wind environment around buildings, *Wind Engineering and Industrial Aerodynamics*, 96(1749-1761).

Trevino, C., and Mauss, F. (1993), Chapter 10 "Structure and Extinction of Non-Diluted Hydrogen-Air Diffusion Flames", In: Peters, N., Rogg, B., Reduced Kinetic Mechanisms for Applications in Combustion Systems. Lecture Notes in Physics, V. 15. Springer-Verlag, 1993.

Tsuruda, T. and Hirano, T. (1987), Growth of flame front turbulence during flame propagation across an obstacle, *Combust Sci Technol*, 1987, 51(4-6): 323-328.

Tu, J., Yeoh, G.H., Liu, C. (2012), Computational Fluid Dynamics: A Practical Approach, Second. ed. Elsevier Publications, Butterworth-Heinemann.

Venetsanos, A. and Bartzis, J. (2007), CFD modeling of large-scale LH2 spills in open environment, *International Journal of Hydrogen Energy*, 32(13), pp.2171–2177.

Venetsanos, A.G., Papanikolaou, E., Delichatsios, M., Garcia, J., Hansen, O.R., Heitsch, M., Huser, A., Jahn, W., Jordan, T., Lacome, J.M., Ledin, H.S., Makarov, D.M., Middha, P., Studer, E., Tchouvelev, A.V., Teodorczyk, A., Verbecke, F., Van der Voort, M.M. (2009), An inter-comparison exercise on the capabilities of CFD models to predict the short and long term distribution and mixing of hydrogen in a garage. *Intl J. of Hydrogen Energy*, 34.14 (2009): 5912-5923.

Venetsanos, A.G., Papanikolaou, E. and Bartzis, J.G. (2010), The ADREA-HF CFD code for consequence assessment of hydrogen applications, *International journal of hydrogen energy*, 35(8), 3908-3918.

Verfondern, K. (2008), Safety Considerations on Liquid Hydrogen, Forschungszentrum Jülich GmbH.

Versteeg, H., Malalasekera, W. (1997), An Introduction to Computational Fluid Dynamics The Finite Volume Method, 2nd ed. PEARSON, Prentice Hall.

Versteeg, H.K. and Malalasekera, W. (2007), *An introduction to Computational Fluid Dynamics: The finite volume method*. 2nd ed. s.l.:Pearson Education Ltd.

Visser, F.C., Brouwers, J.J.H., Jonker, J.B. (1999), Fluid flow in a rotating low-specific-speed centrifugal impeller passage. Fluid Dynamics Research, Fluid Dyn. Res. (Netherlands) 24, 275–92. doi:10.1016/S0169-5983(98)00033-1

Warnatz, J., Maas, U., Dibble, R.W. (2006), Combustion: Physical and Chemical Fundamentals, Modeling and Simulation, Experiments, Pollutant Formation. 4th Edition, Springer, ISBN 978-3-540-45363-5.

Waterson, N.P., and Deconinck, H. (2007), Design principles for bounded higher-order convection schemes – a unified approach. *Journal of Computational Physics*, *224*(1), 182–207.

Wen, J.X., Xu, B.P. and Tam V.H.Y. (2009), Numerical study on spontaneous ignition of pressurized hydrogen release through a length of tube. *Combust Flame* 2009; 156 (No. 11):2173-2189.

Wen, J.X., Madhav Rao, V.C. and Tam, V.H.Y. (2010), Numerical study of hydrogen explosions in a refuelling environment and in a model storage room, *Int. J. Hydrogen Energy*, Volume 35, pp. 385-394.

Wilcox, D. C. (2008), Formulation of the k-omega Turbulence Model Revisited, *AIAA Journal*, 46(11), 2008, 2823-2838.

Williams, F. (1994), Combustion theory, Westview Press; Second Edition edition (March 21, 1994).

Woolley, R.M., Fairweather, M., Falle, S.A.E.G. and Giddings, J.R. (2013), Prediction of confined, vented methane-hydrogen explosions using a computational fluid dynamic approach, *International Journal of Hydrogen Energy*, 38(16), 6904-6914.

Xu, B.P., Zhang, J.P., Wen, J.X., Dembele, S., and Karwatzki, J. (2005), Numerical study of highly under-expanded hydrogen jet, 1st Intl. Conf. on Hydrogen Safety, Pisa, 2005.

Xu, B.P., El Hima, L., Wen, J.X., Dembele, S., Tam, V.H.Y., Donchev, T. (2007a), Numerical study of spontaneous ignition of pressurized hydrogen release through a tube into air, *J of Loss Prevention in the Process Industries*, 21(2), 205–221.

Xu, B.P., Hima, L.E.L., Wen, J.X., Dembele, S., Tam, V. H. Y. (2007b), Numerical Study of Spontaneous Ignition of Pressurized Hydrogen Release into Air, International Conference on Hydrogen Safety, 11–13 September 2007, San Sebastian, Spain.

Xu, B.P., Wen. J.X., Dembele, S., Tam, V.H.Y. (2008), Effects of the accuracy order of numerical schemes on spontaneous ignition of high-pressure hydrogen release, 32nd International Symposium on Combustion, August 2008, Montreal, Canada.

Xu, B.P., Wen, J.X., Dembele, S., Tam, V.H.Y. and Hawksworth, S.J. (2009a), The effect of pressure boundary rupture rate on spontaneous ignition of pressurized hydrogen release, *J. of Loss Prevention in the Process Industries*, 22, No. 3, 2009, pp. 279-287.

Xu, B.P., El Hima, L., Wen, J.X., Tam, V.H.Y (2009b), Numerical study of spontaneous ignition of pressurized hydrogen release into air, *Int J Hydrogen Energy* 2009; 34:5954-5960.

Xu, B.P., Wen J.X, Tam V.H.Y. (2011), The effect of an obstacle plate on the spontaneous ignition in pressurized hydrogen release: A numerical study, *Intl. J. of Hydrogen Energy*, 2011, 36, 2637-2644.

Xu, B.P. and Wen, J.X. (2012), Numerical study of spontaneous ignition in pressurized hydrogen release through a length of tube with local contraction, *Intl. J. of Hydrogen Energy*, 37 (2012), 17571-17579.

Xu, B.P. and Wen, JX (2014), The effect of tube internal geometry on the propensity to spontaneous ignition in pressurized hydrogen release, *Intl. J. of Hydrogen Energy*, in Press.

Yakhot, V. and Orszag, S. A. (1986), Renormalization group analysis of Turbulence. I. Basic theory. *J. Scientific Computing*, 1(1), pp. 3-51.

Yakhot, V. (1988), Propagation velocity of premixed turbulent flames, *Combust Sci Technol* 1988, 60: 191-214.

Yamada, E., Watanabe, S., Hayashi, A.K., Tsuboi, N. (2009), Numerical analysis on autoignition of a high-pressure hydrogen jet spouting from a tube, *Proceedings of the Combustion Institute*, 32, No. 2, 2009, pp. 2363-2369.

Yanez, J., Kotchourko, K. and Lelyakin, A. (2010), Hydrogen deflagration simulations under typical containment conditions for nuclear safety. CFD for Nuclear Reactor Safety Applications, CFD4NRS-3 Workshop, 14 - 16 September, Bethesda, Maryland, USA, s.n.

Zabetakis, M.G. (1965), Flammability characteristics of combustible gases and vapors, BuMines Bulletin 627, p. 121.

Zamora, B., Kaiser, A.S., Vicente, P.G. (2010), Improvement in learning on fluid mechanics and heat transfer courses using computational fluid dynamics. International Journal of Mechanical Engineering Education, Int. J. Mech. Eng. Educ. (UK) 38, 147–66. doi:10.7227/IJMEE.38.2.6.

Zbikowski, M., Makarov, D.V., Molkov V.V. (2008), LES model of large scale hydrogen–air planar detonations: Verification by the ZND theory, *Intl J of Hydrogen Energy*, 33 (2008), 4884-4892.

Zeldovich, Y.B. (1940), *Zh Eksp Teor Fiz* 1940, 10: 542–568.

Zeldovich, Y., Barenblatt, G., Librovich V., Makhviladze G. (1985), Mathematical theory of combustion and explosions. New York, NY, USA: Consultants Bur; 1985.

Zhang, J., Delichatsios, M.A. and Venetsanos, A.G. (2010), Numerical studies of dispersion and flammable volume of hydrogen in enclosures, *International journal of hydrogen energy*, 35(12), 6431-6437.